



**HAL**  
open science

# MgH<sub>2</sub>-TiH<sub>2</sub> hydrides as negative electrodes of Li-ion batteries

Nicola Berti

► **To cite this version:**

Nicola Berti. MgH<sub>2</sub>-TiH<sub>2</sub> hydrides as negative electrodes of Li-ion batteries. Material chemistry. Université Paris-Est, 2017. English. NNT : 2017PESC1029 . tel-01738335

**HAL Id: tel-01738335**

**<https://theses.hal.science/tel-01738335v1>**

Submitted on 20 Mar 2018

**HAL** is a multi-disciplinary open access archive for the deposit and dissemination of scientific research documents, whether they are published or not. The documents may come from teaching and research institutions in France or abroad, or from public or private research centers.

L'archive ouverte pluridisciplinaire **HAL**, est destinée au dépôt et à la diffusion de documents scientifiques de niveau recherche, publiés ou non, émanant des établissements d'enseignement et de recherche français ou étrangers, des laboratoires publics ou privés.



UNIVERSITÉ —  
— PARIS-EST

## THÈSE

pour obtenir le grade de  
Docteur de l'Université Paris-Est

Spécialité : Sciences des matériaux

présentée et soutenue publiquement par

**Nicola BERTI**

le 13 décembre 2017

## **MgH<sub>2</sub>-TiH<sub>2</sub> hydrides as negative electrodes of Li-ion batteries**

Devant le Jury :

**Mr Marcello BARICCO**

**M<sup>me</sup> Aline ROUGIER**

**M<sup>me</sup> Laetitia LAVERSENNE**

**M<sup>me</sup> Junxian ZHANG**

**Mr Michel LATROCHE**

**Mr Fermín CUEVAS**

Université de Turin (Examinateur)

ICMCB, Bordeaux (Rapporteur)

Institut Néel, Grenoble (Examinateur)

ICMPE, Thiais (Co-encadrant)

ICMPE, Thiais (Co-directeur de thèse)

ICMPE, Thiais (Directeur de thèse)



## Acknowledgments

*First and foremost, I would like to thank my supervisors Fermin Cuevas and Michel Latroche, for giving me the opportunity to work on this project and carrying out my Ph.D. Thesis at ICMPE (Institut de Chimie et des Matériaux Paris-Est) laboratory. Thanks also to my co-supervisor Junxian Zhang for her help and support during my work. To all of you, thanks to have trusted me, keeping me rigorous and patient during these three years of collaboration.*

*I wish to express my greatest gratitude to all the members of the CMTR (Chimie Métallurgie des Terres Rares) for kindly welcomed me in their group and for their support. I would like to thank Eric Alleno, Tahar Azib, Stéphane Bastide, Lofti Bessais, Christine Cachet-Vivier, Jean-Claude Crivello, Jean-Marc Joubert, Eric Leroy, Judith Monnier, Cedric Morin, Yassine Oumellal, Valérie Paul-Boncour, Karine Prostov, Encarnación Torralba-Peñalver, Christian Vard, Karim Zehani, and Claudia Zlotea.*

*A big thanks to all the technicians, Fabrice Couturas, Valérie Lalanne, Léon Pereira, Olivier Rouleau, and Benjamin Villeroy, for their prompt help in solving all the issues occurred during my work.*

*A special thanks to Dominique Alain for helping me in many administrative problems, and for her kindness shown to me in every past day.*

*I would also to acknowledge all the Ph.D. students of the laboratory, Thomas Bartoli, Mohamed Benyahia, Natacha Bourgeois, Wassim Bouzidi, Veronique Charbonnier, Paul Lafaye, Nicolas Madern, Abdelmalek Malouche, Peyman Mirzai, Kamal Nouri, and Pavel Rizo Acosta, wishing them good luck for their future.*

*Many thanks to all the members of the project ECOSTORE, it was a pleasure to spend all these years together.*

*I would like to thank the supervisors of the project, Claudio Pistidda and Martin Dornheim from Helmholtz-Zentrum Geesthacht, Magnus Sørby and Bjørn Hauback from Institutt for Energiteknikk, Torben René Jensen from Aarhus University, Marcello Baricco from Turin University, David Book and Daniel Reed from Birmingham University, Guido Schmitz from Stuttgart University, Georgia Charalambopoulou and Theodore Steriotis of the National Centre for Scientific Research Demokritos, Dorthe Bomholdt Ravnsbæk from University of*

*Southern Denmark, Christian Jordy from SAFT Co., Ulrich Wietelmann from Rockwood Lithium Co., Henning Zoz and Deniz Yigit of ZOZ Co.. A special thanks to Radovan Černý and his group to have hosted me in their laboratory at the University of Geneva for my secondment in Switzerland. I would like to also thank the Japanese partners Shin-ichi Orimo from Tohoku University, and Etsuo Akiba of Kyushu University. A big thanks to Klaus Taube and Sigrid Wulff (HZG) for the coordination of the project.*

*I would like to thank the Post-docs Pedro López-Aranguren and Alberto Biancoli, and many thanks to all my Ph.D. friends, Arash SeyedHosein Payandeh Gharibdoust, Antonio Santoru, Filippo Peru, Matteo Brighi, Priscilla Huen, Efi Hadjixenophontos, Joe Yinzhe Liu, Michael Heere, Anna Wołczyk, and Kate Thi Thu Le. I wish you all the best.*

*A special thanks to my colleague Anh Ha Dao for the time spent working together at ICMPE.*

*Last but not least, a really special thanks to my parents and sister, for always trusting and supporting me in every task of my life, allowing me to achieve great goals such as this dissertation. I love you all*

# Table of contents

<b>Introduction: aim of the thesis</b>	<b>i</b>
<b>CHAPTER 1: General aspects of Li-ion batteries and state of the art</b>	<b>1</b>
1 State of the art	5
2 Conventional Li-ion battery materials	7
2.1 Materials for positive electrodes	8
2.2 Electrolytes	12
2.3 Other components	16
2.4 Materials for negative electrodes	19
3 Metal hydrides for Li-ion batteries	28
References	38
<b>CHAPTER 2: Experimental techniques</b>	<b>51</b>
1 Materials preparation	53
1.1 Reactive ball milling	55
1.2 Plasma-assisted plasma	57
2 Structural and Chemical characterization	58
2.1 X-ray powder diffraction	58
2.2 Transmission electron microscopy	63
2.3 Focused ion beam	65
2.4 Scanning electron microscopy	66
3 Electrochemical analyses	67
3.1 Galvanostatic cycling	67
3.2 Cyclic voltammetry	69
3.3 Electrochemical impedance spectroscopy	70
4 Electrode formulation	72
4.1 MgH <sub>2</sub> thin film electrode	72
4.2 MgH <sub>2</sub> +TiH <sub>2</sub> nanocomposite electrode and formulation optimization	73
References	77

<b>CHAPTER 3: Magnesium hydride thin film as electrode material</b>	<b>79</b>
1 MgH <sub>2</sub> thin films	84
1.1 Structural and Electrochemical properties	84
1.2 Surface barrier and reproducibility	86
2 Al-MgH <sub>2</sub> thin films	88
1.1 Structural properties and Electrochemical cycling	88
1.2 Structural modifications during the first galvanostatic cycle	90
1.3 Microstructural modifications during the first galvanostatic cycle	92
3 Discussion	97
3.1 Effect of the Mg alloying on the conversion reaction	97
3.2 Reversibility of the conversion reaction	100
4 Conclusions	103
References	105

<b>CHAPTER 4: MgH<sub>2</sub>+TiH<sub>2</sub> as anodes of Li-ion batteries</b>	<b>107</b>
1 Synthesis of MgH <sub>2</sub> +TiH <sub>2</sub> nanocomposites	111
1.1 Hydrogenation during RBM	111
1.2 Influence of TiH <sub>2</sub> on Mg hydrogenation kinetics	112
2 Structural properties and Phase distribution of MgH <sub>2</sub> +TiH <sub>2</sub> composites	114
2.1 Structural properties	114
2.2 Phase distribution	118
3 Electrochemical properties	118
3.1 Galvanostatic cycling of pure MgH <sub>2</sub> and TiH <sub>2</sub>	118
3.2 Galvanostatic cycling of MgH <sub>2</sub> +TiH <sub>2</sub> nanocomposites	121
3.3 Detailed electrochemical study of 0.7MgH <sub>2</sub> +0.3TiH <sub>2</sub> composite	121
4 Discussion	132
4.1 Synthesis and structural properties of MgH <sub>2</sub> +TiH <sub>2</sub> nanocomposites	132
4.3 Electrochemical analyses	134
5 Conclusions	145
References	148

<b>CHAPTER 5: All solid-state Li-ion battery</b>	<b>151</b>
1 LiBH <sub>4</sub> as solid electrolyte for Li-ion batteries	155
2 MgH <sub>2</sub> and TiH <sub>2</sub> as electrode materials in LiBH <sub>4</sub> solid-state half-cells	158
2.1 Cycling of MgH <sub>2</sub> pure electrode	158
2.2 Cycling of TiH <sub>2</sub> pure electrode	160
2.3 Cycling of MgH <sub>2</sub> +TiH <sub>2</sub> nanocomposites	161
3 Solid-state metal hydride-sulphur Li-ion battery	165
4 Discussion	167
4.1 Cycle-life of MgH <sub>2</sub> and TiH <sub>2</sub> in LiBH <sub>4</sub> solid half-cells	167
4.2 Cycle-life of solid-state Li-ion battery	170
5 Conclusions	172
References	174
<b>CHAPTER 6: Remarkable conclusions and Outlook</b>	<b>177</b>
1 Conclusions based on our research	179
2 Outlook	183





## Introduction: aim of the thesis

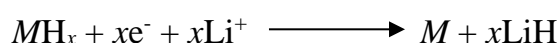
Current concern about greenhouse gasses, climate changes, and depletion of fossil fuel sources, has brought to a rapid development of new renewable energy sources such as sun, wind, tides, *etc.* However, because of the intermittent presence of these sources, efficient energy storage systems are necessary for a sustainable society. Among the various energy conversion/storage systems proposed over the last years, electrochemical storage, and more specifically batteries, seems to be the most suitable candidate for such task.

In a battery, the chemical energy contained in the electrodes is converted to electric energy by means of a redox (reduction-oxidation) reaction. Those batteries in which this reaction is irreversible are called primary cells, and on the other hand, those in which is reversible are called secondary (or rechargeable) cells.

Because of the introduction into the market of several portable devices, such as laptops, smartphones, cameras, *etc.*, much effort has been done to develop rechargeable batteries with high power and long life. Most of these devices, are currently powered by lithium-ion batteries. Due to advantages such as light weight, long cycle life, and low self-discharge compared to other secondary batteries (*i.e.* nickel-cadmium, nickel-metal hydride, lead-acid), Li-ion battery has taken the leadership in the rechargeable energy storage market. However, with the increase demands of electric vehicles and stationary energy storage systems, there is a necessity of further improving the energy density of this battery.

One of the main factor limiting the performance of a Li-ion battery is the anode material. The current negative material used in the commercial batteries is carbon graphite, which provides a theoretical capacity of 372 mAh g<sup>-1</sup>. Hence, for high energy applications, novel materials with higher capacities than graphite are needed.

Among all the compounds actually studied to replace graphite as negative electrode material, metal hydrides have shown to offer a high theoretical capacity through the general conversion reaction:



During the reaction, the metal hydride ( $MH_x$ ) is reduced to its metal ( $M$ ), and lithium hydride ( $LiH$ ) is formed. For each H atom released by the active material, one Li is stored into the electrode, attaining a high energy density. Indeed, the average theoretical capacity provided by most of metal hydrides is in the order of thousands of  $\text{mAh g}^{-1}$ . Furthermore, the lithiation/delithiation reaction occurs at potentials below 1 V vs.  $Li^+/Li$ , suitable for negative electrode materials in high voltage batteries.

However, the sluggish kinetics and the poor reversibility of the conversion reaction still hinder the practical application of metal hydrides in commercial Li-ion batteries.

The remarkable properties of metal hydrides as potential candidates as negative materials for Li-ion batteries are the motivation of this Ph.D. study.

In this thesis,  $MgH_2$  and  $TiH_2$  have been explored as active materials. The reaction with lithium occurs at 0.5 V for  $MgH_2$ , and at 0.2 V for  $TiH_2$ , achieving capacities above 2000 and 1000  $\text{mAh g}^{-1}$  respectively. Moreover, the abundance of magnesium and titanium, and the easy hydrogenation of them by mechanical grinding, promise industrial production and commercial application of these hydrides in Li-ion batteries.

Previous works on these materials have shown that, during the first discharge, both  $MgH_2$  [1] and  $TiH_2$  [2] react with lithium achieving capacities close to their theoretical ones. Nevertheless, the conversion reaction exhibits a poor reversibility [3,4]. In particular, the reformation of  $TiH_2$  has shown to be completely irreversible, and  $MgH_2$  is only partially restored.

The authors of these works have suggested as possible causes of this limited cyclability the volume changes, the poor electric conductivity, and the slow mass transportation. However, none of these hypotheses has been proved with evidences. Thus, a deeper understanding of the reaction mechanisms is needed in order to enhance the performance of these materials for practical applications.

The main goal of this thesis is to improve the knowledge about the factors that hinder the insertion and extraction of lithium from the electrode. The research focuses on the understanding of the issues related to the reversibility of the conversion reaction, suggesting strategies to overcome them, increasing the performance of metal hydrides as negative electrode materials for Li-ion batteries.

This thesis is divided into six chapters. In the first one, the Li-ion battery is described in detail, providing a bibliographic background on the commercial and studied materials used in each component of the battery (*i.e.* negative and positive electrodes, electrolytes, separators, current collectors, and additives). In particular, the conversion reaction of metal hydrides with lithium, and the related literature published until now, are highlighted at the end of this chapter. The second chapter reports the experimental techniques and devices used for the synthesis and characterization of the investigated materials. In the third chapter is devoted to the study of the conversion reaction path during cycling. By means of X-ray diffraction (XRD) and transmission electron microscopy (TEM), the structural and composition properties of  $\text{MgH}_2$  thin films have been analysed at different discharge-charge steps, following the phase distribution within the electrode. The fourth chapter presents a study on the electrode formulation effect on the performance and cycle life of the battery. For this work,  $y\text{MgH}_2-(1-y)\text{TiH}_2$  nanocomposites with different molar content ( $y = 0.2, 0.5, 0.6, 0.7$  and  $0.8$ ) have been synthesized by reactive ball milling under hydrogen pressure and studied as electrode materials. Their structural properties have been investigated by XRD and TEM, and their electrochemical properties have been determined in half cells by galvanostatic and cyclic voltammetry measurements. The fifth chapter deals with the study of  $\text{MgH}_2\text{-TiH}_2$  electrodes in all solid-state Li-ion batteries. Two different solid electrolytes based on lithium borohydride have been chosen for this work, bulk  $\text{LiBH}_4$  and nanoconfined  $\text{LiBH}_4$  in silica scaffold. The last chapter is devoted to a general discussion about the results obtained in this work, and also about the perspectives on the use of metal hydrides in commercial Li-ion batteries.

## References

1. Oumellal, Y., Rougier, A., Nazri, G. A., Tarascon, J.-M. & Aymard, L. Metal hydrides for lithium-ion batteries. *Nat. Mater.* **7**, 916–921 (2008).
2. Oumellal, Y. *et al.* Reactivity of TiH<sub>2</sub> hydride with lithium ion: Evidence for a new conversion mechanism. *Int. J. Hydrogen Energy* **37**, 7831–7835 (2012).
3. Sartori, S., Cuevas, F. & Latroche, M. Metal hydrides used as negative electrode materials for Li-ion batteries. *Appl. Phys. A* **122**, 135 (2016).
4. Aymard, L., Oumellal, Y. & Bonnet, J. P. Metal hydrides: An innovative and challenging conversion reaction anode for lithium-ion batteries. *Beilstein J. Nanotechnol.* **6**, 1821–1839 (2015).

# **CHAPTER 1**

General aspects on Li-ion batteries  
and state of the art



# Content

<b>1</b>	<b>State of the art</b>	<b>5</b>
<b>2</b>	<b>Conventional Li-ion battery materials</b>	<b>7</b>
2.1	Materials for positive electrodes	8
2.1.1	Layered transition metal oxide	8
2.1.2	Three-dimensional compounds	10
2.1.3	Polyanion compounds	11
2.2	Electrolytes	12
2.2.1	Organic solvents	13
2.2.2	Lithium salts	15
2.2.3	Solid electrolyte interphase	15
2.3	Other components	16
2.3.1	Separators	16
2.3.2	Current collectors	17
2.3.3	Additives	18
2.4	Materials for negative electrodes	19
2.4.1	Insertion/intercalation materials	19
2.4.2	Alloying materials	23
2.4.3	Conversion materials	25
<b>3</b>	<b>Metal hydrides for Li-ion batteries</b>	<b>28</b>
3.1	Gravimetric and volumetric storage capacity	28
3.2	Thermodynamics of hydrides as electrode	30
3.3	MgH <sub>2</sub> and TiH <sub>2</sub> as negative electrode materials	32
3.3.1	Reactivity of MgH <sub>2</sub> with lithium	32
3.3.2	Reactivity of TiH <sub>2</sub> with lithium	36
3.3.3	MgH <sub>2</sub> -TiH <sub>2</sub> composite as electrode material	37
	<b>References</b>	<b>38</b>





## 1 State of the art

As the consumption and performance of portable electronic devices, such as smartphones, laptops, cameras, etc., have significantly increased over the past decades, power supplies with higher gravimetric as well volumetric energy density are required. In this context, lithium-ion battery (LIB) technology is the most promising candidate to power future devices, and it is already entering the electric (EV) and hybrid electric (HEV) vehicles market. Compared with other rechargeable energy storage systems, lithium-ion batteries offer very important advantages in terms of cycle-life, flexible design, efficiency, and energy density. A comparison between Li-ion batteries and other know battery types is reported in Figure 1.1 and Table 1.1.

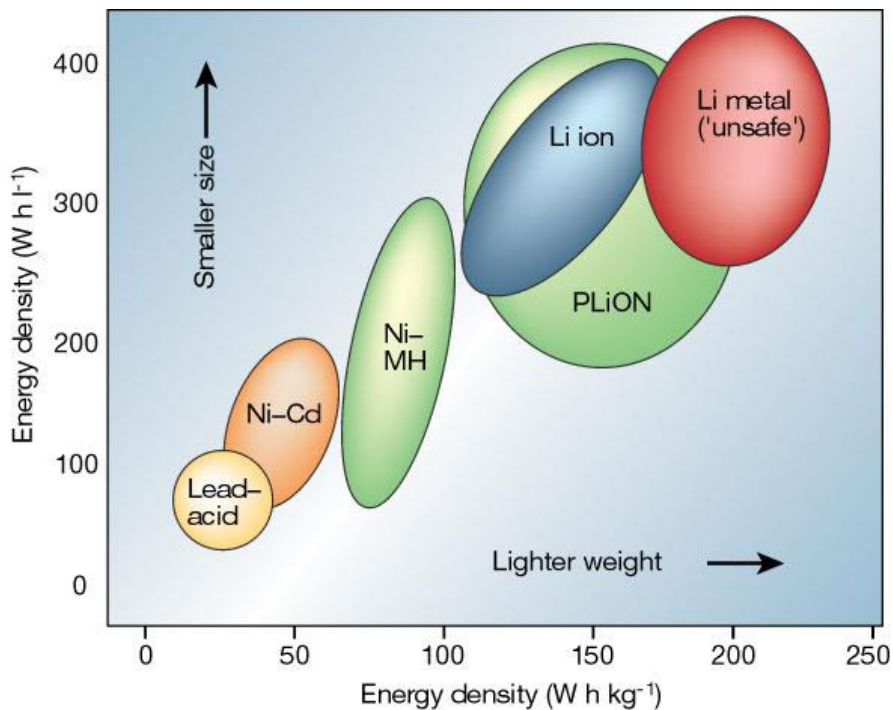


**Figure 1.1.** A comparison of the rechargeable battery technology as a function of volumetric and specific energy density [1].

**Table 1.1.** Different batteries chemistries and characteristics [2,3].

Specs	Li-ion	Lead-acid	Ni-MH	Ni-Cd
Energy density (Wh kg <sup>-1</sup> )	150	30	60	50
Operating voltage (V)	4.0	1.9	1.2	1.2
Average self-discharge rate per month (%)	2-7	2-5	30-50	10
Temperature range (°C)	-20 to 60	-30 to 50	-30 to 70	-40 to 50
Other features	light weight, no memory effect, expensive, fragile	environmental pollution, used for starting cars	memory effect, needs maintenance	memory effect, environmental pollution, needs maintenance

Since the 70's, a lot of attention has been devoted to the use of lithium in batteries. Lithium is an interesting element because it is the lightest solid element at room temperature (molar mass  $M = 6.94 \text{ g mol}^{-1}$ ), with the lowest density ( $\rho = 0.53 \text{ g cm}^{-3}$ ), and the redox couple  $\text{Li}^+/\text{Li}$  has the lowest electrochemical potential value among all the metals ( $-3.04 \text{ V vs. SHE}$ ) [4]. Consequently, batteries using lithium as active material offer the possibility of high voltage and high energy density.

First concepts of rechargeable lithium batteries were based on metallic lithium as negative material, and chalcogenides and oxides as positive materials [5,6]. However, the main drawback of these devices were associated to the use of metallic lithium as electrode, which has the tendency to form dendrites and powder deposits during cycling. These can cause shortcuts and side reactions inside the battery, leading to serious safety issues [7]. Even though the use of a solid electrolyte was suggested to prevent short circuit, this safety issue was the starting point for studying other systems to replace metallic lithium with lithium intercalation compounds.

In the 1980's, Goodenough showed the use of lithium transition metal oxide  $\text{LiCoO}_2$  as intercalation electrode for lithium batteries [8,9], and one year later, Ikeda filed a patent for the use of graphite as intercalation electrode in organic solvent [10]. This led to the development of the first lithium-ion battery prototype by Yoshino of Asahi Kasei Co. in 1985 [11]. Starting from these patents, Sony Co. began to produce commercial cells called Li-ion batteries in 1991 [12].

## 2 Conventional Li-ion battery materials

Lithium-ion batteries consist of two lithium insertion electrodes, separated by means of a thin sheet of microperforated plastic. The negative electrode operates at lower potential, and in its most conventional form is based on carbon, whereas the positive electrode, which works at higher potential, is made of a lithium metal oxide. During the discharge of the battery, lithium ions move from the negative to the positive side through an electrolyte containing a lithium salt. This migration of lithium ions is electronically compensated by the simultaneous flow of electrons into an external circuit, providing energy to any connected device. During the charge, an external electrical power source forces the lithium ions to move back from the positive to the negative electrode, restoring the initial status of the battery. This shuttle of lithium ions has given the name “rocking-chair” cell to the system [13,14]. Schematic discharge and charge mechanisms are illustrated in Figure 1.2.

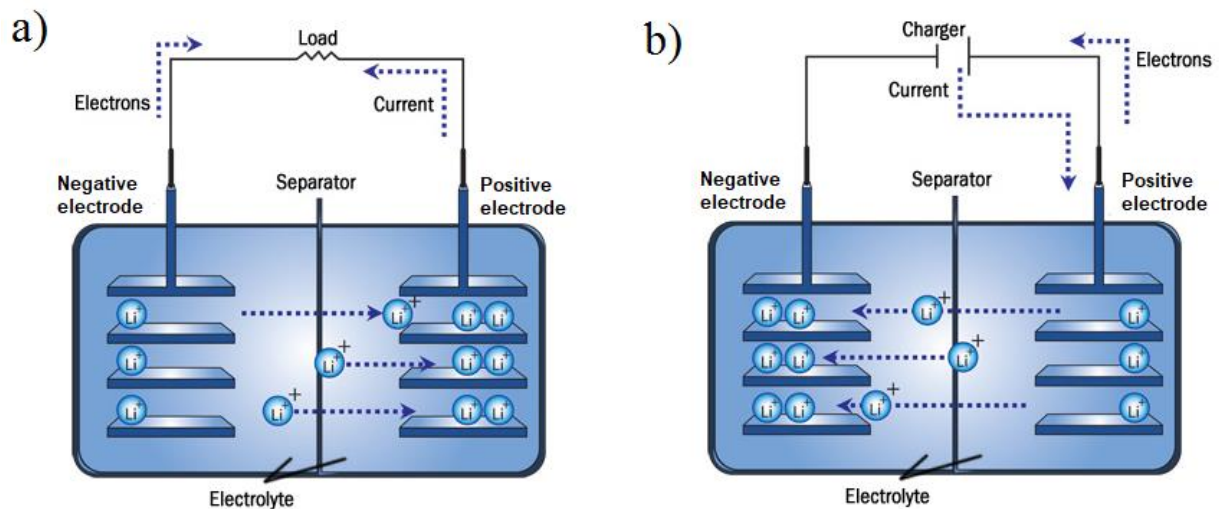
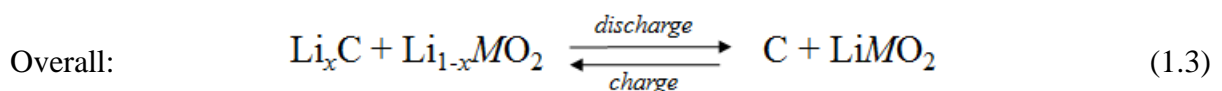
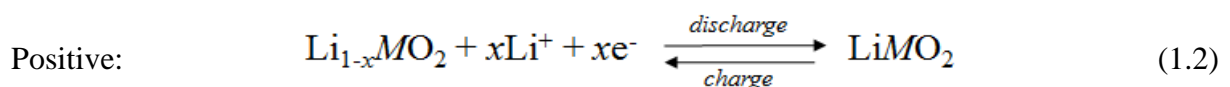
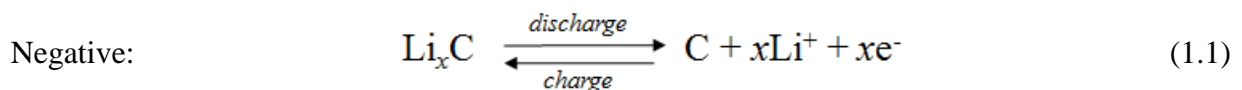


**Figure 1.2.** Schematic representation of the working mechanism of a rechargeable lithium-ion battery. a) Discharge process, b) Charge process.

The electrode reactions and overall reaction for carbon and lithium metal oxide can be written as follows:



The available energy of the battery depends mostly on the capacity of electrochemical reactions and working potentials of both electrodes, but also several other factors affect the performance and cycle-life of the cell. Among these factors the main ones are: raw materials quality, electrode design, electrolyte characteristics and separator features.

## **2.1 Materials for positive electrodes**

The choice of the positive electrode is crucial in terms of energy and power density, cost, safety, and design of the battery. To successfully be used as cathode, a positive material must fulfil several requirements:

- a) The material should host as many Li ions as possible per formula unit, in order to possess a high theoretical capacity;
- b) Extraction/insertion of lithium should occur at high voltage (around 4 V) with minimal or no structural changes;
- c) The material should have good electronic and ionic conductions;
- d) It must be thermally and chemically stable, with a low cost and environmentally benign;

In this Section, the main positive materials used and studied as cathode will be described.

### **2.1.1 Layered transition metal oxide**

Lithium cobalt oxide  $\text{LiCoO}_2$  (LCO) was originally commercialized by Sony Co., and is still used in most commercial lithium-ion batteries as positive electrode. Its structure consists of layers of lithium atoms that lie between planes of octahedrons formed by cobalt and oxygen atoms (Figure 1.3).  $\text{LiCoO}_2$  possess a relatively high theoretical capacity of  $274 \text{ mAh g}^{-1}$ , high discharge voltage curve ( $\sim 4.0 \text{ V vs. Li}^+/\text{Li}$ ), low self-discharge rate and good cycling performance [15,16]. The major limitations come from the cost, low thermal stability, and fast capacity fade at high current rates.

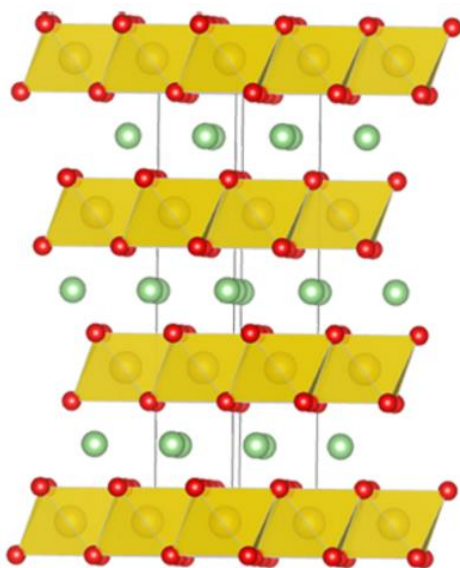


**Figure 1.3.** Crystal structure of  $\text{LiCoO}_2$ . Lithium ions are in green, oxygen in red, and cobalt in yellow.

Practically, its theoretical capacity is never reached, because only 0.5 Li can be reversibly cycled, providing a capacity around  $140 \text{ mAh g}^{-1}$ . This is due to the fact that, when  $x > 0.5$ ,  $\text{Li}_{1-x}\text{CoO}_2$  becomes unstable, releasing oxygen and cobalt. With the purpose of enhancing its performance, different types of metals (*e.g.* Mn, Fe, Cr, Al) were studied as dopants/partial substitutes for Co [17–19]. Coatings of metal oxides (*e.g.*  $\text{Al}_2\text{O}_3$ ,  $\text{B}_2\text{O}_3$ ,  $\text{TiO}_2$ ,  $\text{ZrO}_2$ ) were more effective in enhancing LCO stability and performance [20,21] because chemically and mechanically stable oxides might reduce structural change of LCO and side reactions with electrolyte during cycling. Nevertheless, full delithiation is still not possible without severe cycling losses.

Because of its lower cost compared to  $\text{LiCoO}_2$ , and its possible higher energy density,  $\text{LiNiO}_2$  (LNO) has been also extensively studied as positive material. Nickel is less hazardous and cheaper compared to cobalt, however, because of LNO structural instability it has not been able to be commercialized as cathode in Li-ion batteries. Nominally, it has a crystal structure similar to  $\text{LiCoO}_2$ , but pure LNO are not favourable because  $\text{Ni}^{2+}$  ions have a tendency to substitute  $\text{Li}^+$  sites during synthesis and delithiation, blocking the pathways of Li ions [22]. Partial substitution of Ni with Co was found to be an effective way to reduce cationic disorder [23]. However, LNO is more thermally instable than LCO, because  $\text{Ni}^{3+}$  ions are more readily reduced than  $\text{Co}^{3+}$  ions. The thermal stability can be enhanced by doping LNO with Mg or Al [24]. The only compound based on LNO that found practical applications is  $\text{LiNi}_{0.8}\text{Co}_{0.15}\text{Al}_{0.05}\text{O}_2$  or NCA. The presence of Al in NCA improves both the thermal stability and the electrochemical properties [25]. The good specific capacity ( $190 \text{ mAh g}^{-1}$ )

and power capability make it attractive for several applications, although it is still not considered as inherently safe as other candidates.

### 2.1.2 Three-dimensional compounds

The marked tendency of several manganese oxide phases to convert from layered to spinel structures during lithiation in electrochemical cells (or upon heating with a lithium source) attests the stability of this structure in the Li-Mn-O system. Lithium manganese oxide  $\text{LiMn}_2\text{O}_4$  (LMO) benefits from the cost, abundance, and environmental friendliness of manganese compared to cobalt. In its spinel structure (cubic close-packed, *ccp*), illustrated in Figure 1.4, lithium occupies tetrahedral sites between the octahedrons formed by manganese and oxygen.

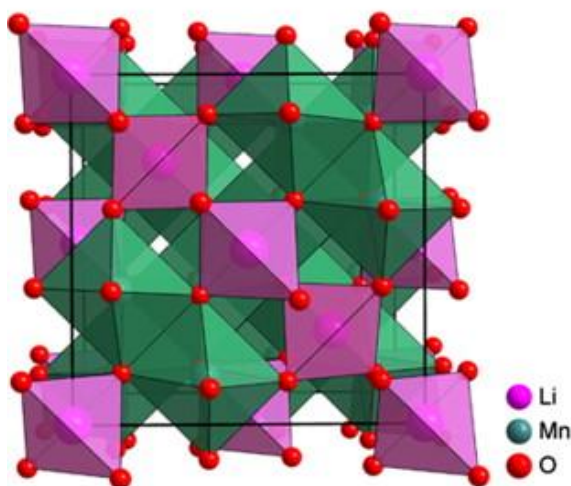


**Figure 1.4.** Crystal structure of spinel  $\text{LiMn}_2\text{O}_4$ .

Theoretically, this material can deliver up to  $285 \text{ mAh g}^{-1}$ , but this capacity is never reached because of structural instability. Indeed, when cycled with a lithium anode, LMO presents two plateau potentials, a first one slightly above 4 V, and a second one below 3 V [26]. During the second plateau, large anisotropic volume changes associated with the formation of tetragonal  $\text{Li}_2\text{Mn}_2\text{O}_4$  occur, leading to particle disintegration and loss of connections within the electrode [27]. This causes a rapid loss in capacity. In contrast, the extraction of lithium above 4 V *vs.*  $\text{Li}^+/\text{Li}$  maintains the cubic structure and results in smaller volume changes. For this reason, the discharge is typically limited around 4 V, providing a capacity of  $120 \text{ mAh g}^{-1}$  with a good reversibility. Moreover, below 4 V also other side reactions occur, decreasing the life of the electrode. These reactions are attributed to the degradation of the electrolyte at high potential, loss of oxygen from the delithiated spinel, and dissolution of Mn.

By using nanoparticles or partial substitution in LMO, the rate performance can be improved due to shorter Li diffusion paths and better electronic transport [28,29]. For these reasons, nearly all commercial LMO cathodes made today are lithium substituted ( $\text{Li}_{1+x}\text{Mn}_{2-x}\text{O}_4$ , where extra Li occupies Mn sites, with maximum  $x = 1/3$ ), providing a capacity between  $100 - 120 \text{ mAh g}^{-1}$  [30].

### 2.1.3 Polyanion compounds

In the last two decades, several compounds with different polyanion groups  $(\text{XO}_4)^{3-}$  with  $X = \text{S, P, Si, As, Mo, W}$ , have been widely investigated [31–34]. Although they possess a lower theoretical capacity compared with layered oxide compounds, they possess a very stable structure operating at high potentials.

In 1997, Goodenough reported the electrochemical properties of a new class of positive materials known as phosphor-olivines [35].  $\text{LiFePO}_4$  (LFP) is the representative material for this group, known for its thermal stability. In its orthorhombic structure, displayed in Figure 1.5,  $\text{FeO}_6$  octahedra share corners, and  $\text{LiO}_6$  octahedra share edges along tunnel down the  $b$ -axis, through which Li ions can diffuse.

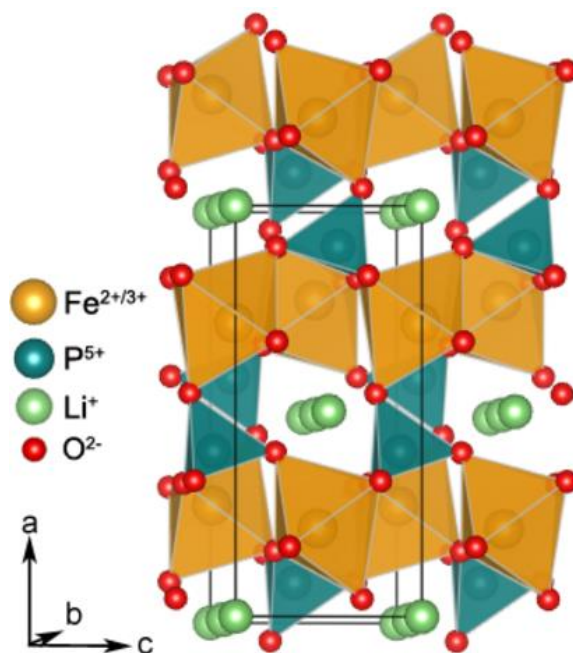


**Figure 1.5.** Olivine structure of  $\text{LiFePO}_4$ .



LFP has a theoretical capacity of 170 mAh g<sup>-1</sup>, and the extraction/insertion of Li occur at an operating voltage of 3.45 V vs. Li<sup>+</sup>/Li [36]. LiFePO<sub>4</sub> and its delithiated phase FePO<sub>4</sub>, are chemically and thermally more stable than oxide materials presented so far. However, the main drawbacks are the relatively low potential, low electrical and ionic conductivity, which limit the reversible capacity. Several strategies have been used to improve the performance of LFP. Reduction of particle size [37] together with carbon coating [38] and cationic doping [39] were found to be effective to increase the rate performance.

In parallel, the partial or total substitution of Fe by other transition metals (Ni, Co, Mn) is used to increase the operating voltage. For instance, the discharge potential of LiMnPO<sub>4</sub> is about 0.5 V higher than LFP vs. Li<sup>+</sup>/Li, increasing the specific energy by about 15% [40]. Unfortunately, it suffers from slow lithium diffusion, and the electronic conductivity is reported to be several orders of magnitude lower than LFP [41]. LiNiPO<sub>4</sub>, LiCoPO<sub>4</sub>, LiNi<sub>0.5</sub>Co<sub>0.5</sub>PO<sub>4</sub> and LiMn<sub>0.33</sub>Fe<sub>0.33</sub>Co<sub>0.33</sub>PO<sub>4</sub> have also been developed showing promising results, but further improvements in power, stability and energy density are still required before practical applications [42,43].

## 2.2 Electrolytes

The electrolyte ensures the conduction of Li ions between the positive and negative electrodes, and together with the separator, acts as a physical barrier for electrons between the two electrodes. In general, every electrolyte is designed for a particular battery application, thus several types of electrolytes have been used in lithium-ion batteries. An ideal electrolyte should fulfil the following requirements:

- a) Large electrochemical potential window, at least 4.5 V for lithium-ion cells with high voltage cathodes;
- b) High ionic conductivity ( $\sigma_{\text{Li}^+} > 10^{-4} \text{ S cm}^{-1}$ ) and low electronic conductivity ( $\sigma_{\text{e}^-} < 10^{-8} \text{ S cm}^{-1}$ ) over a wide range of temperature;
- c) Thermally and chemically stable towards all the cell components;
- d) Should form a stable passivation layer at the surface of the electrodes (see Section 2.2.3 for the solid electrolyte interphase SEI);
- e) Low cost, low toxicity, environmentally friendly, safe, and preferable non-explosive/flammable;

Several types of electrolytes have been used and studied in lithium-ion batteries, such as organic liquid electrolyte, ionic liquids, polymer electrolytes, inorganic solid-state electrolytes, and hybrid electrolytes [44–48].

The organic liquid electrolytes are the most commonly used and longest commercially available. They consist of a solution of a lithium salt dissolved in organic solvents, typically carbonates.

Ionic liquids are solvent-free electrolytes based on molten salts which are in the liquid state at the operating temperature.

Polymer electrolytes have also been used in micro battery devices or in batteries with metallic lithium as electrode. The lithium salts are directly incorporated in a polymer matrix. They can act as separator preventing short cut in the battery. A specific case is the gel polymer electrolyte, which consists of a liquid electrolyte dispersed into a polymer matrix.

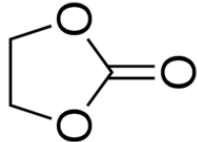
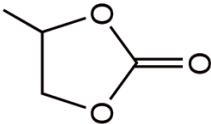
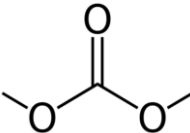
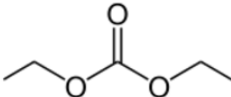
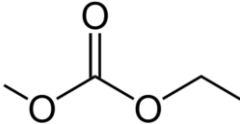
A solid-state electrolyte is a solid compound which can conduct Li ions. Thanks to its mechanical stability, it can drastically improve the safety of the battery. However, they generally suffer of a poor ionic conductivity at room temperature.

Because organic liquid electrolytes are the most used in commercial batteries, they will be discussed in detail in the subsequent sections.

### **2.2.1 Organic solvents**

A good solvent should have a high dielectric constant ( $\epsilon$ ), low viscosity ( $\eta$ ) to facilitate ions transport, be liquid in a wide temperature range, safe, and preferable cheap and non-toxic. In practice, it is difficult to find a single solvent with all these properties, therefore mixtures of different compounds are generally used in commercial batteries. The mixture must contain low amount of water in order to avoid side reactions with lithium. The common solvents used belong to the esters called alkyl carbonates ( $R-O-COOR'$ ), and they are: ethylene carbonate (EC), propylene carbonate (PC), dimethyl carbonate (DMC), diethyl carbonate (DEC), and ethyl methyl carbonate (EMC). The physical and chemical characteristics of these compounds are summarized in Table 1.2.

**Table 1.2.** Main solvents used in non-aqueous liquid electrolytes. Melting point ( $T_m$ ), Boiling point ( $T_b$ ), Viscosity ( $\eta$ ), Dielectric constant ( $\epsilon$ ), Density ( $\rho$ ).

Solvent	Structure	$T_m$ (°C)	$T_b$ (°C)	$\eta$ at 25°C (PI)	$\epsilon$ at 25°C	$\rho$ (g cm <sup>-3</sup> )
EC		37	248	$2.56 \cdot 10^{-3}$	89.78	1.321
PC		-55	240	$2.53 \cdot 10^{-3}$	64.92	1.200
DMC		2 - 4	90	$5.90 \cdot 10^{-4}$	3.107	1.063
DEC		-43	126	$7.50 \cdot 10^{-4}$	2.805	0.969
EMC		-14.5	107	$6.50 \cdot 10^{-4}$	2.958	1.006

Carbonates present a wide electrochemical window between 1.0 V (LUMO, lowest occupied molecular orbital) and 4.7 V (HOMO, highest occupied molecular orbital) vs. Li<sup>+</sup>/Li.

Cyclic carbonates such as EC and PC have higher dielectric constants and higher viscosity than chain-like carbonates such as DMC, DEC, and EMC. EC is almost always used because it provides a better formation of the passivation layer on the surface of the graphite electrode. However, it is solid at room temperature and shows a high viscosity, so it is always coupled with a less viscous carbonate such as DMC and/or DEC. The main weakness of the carbonate is their high flammability.

Inorganic liquid solvents have also been studied, but they present a narrow electrochemical window unsuitable for Li-ion batteries [49].

### 2.2.2 Lithium salts

The lithium salt is essential to ensure the conduction of Li ions in the electrolyte. It must dissolve completely into the solvents without reacting with them, and it must possess a high ionic conductivity. The main lithium salts commonly used in Li-ion batteries are reported in Table 1.3.

**Table 1.3.** Properties of the main lithium salts used in non-aqueous liquid electrolytes. Molar mass ( $M$ ), Melting point ( $T_m$ ), Conductivity ( $\sigma$ ).

Salt	$M$ (g mol <sup>-1</sup> )	$T_m$ (°C)	$\sigma$ (mS cm <sup>-1</sup> ) in 1.0 M at 25°C	
			in PC	in EC/DMC
LiBF <sub>4</sub>	93.9	293	3.4	4.9
LiPF <sub>6</sub>	151.9	200	5.8	10.7
LiAsF <sub>6</sub>	195.9	340	5.7	11.1
LiClO <sub>4</sub>	106.4	236	5.6	8.4

Because of the main drawbacks of the other salts, LiPF<sub>6</sub> is the most used salt in commercialized Li-ion batteries, even if it doesn't possess the highest conductivity. Indeed, LiBF<sub>4</sub> has a very low conductivity, LiAsF<sub>6</sub> is toxic, and LiClO<sub>4</sub> is highly reactive.

### 2.2.3 Solid electrolyte interphase

Because lithiated carbons are not stable in air, a Li-ion battery is always assembled in its discharge state, that means with the positive electrode lithiated. The most used liquid electrolyte, *i.e.* LiPF<sub>6</sub> in EC:DMC, is only stable in the domain from 4.5 V to 0.8 V, as shown in Figure 1.6a. Hence, during the first lithium insertion into the negative electrode, the electrolyte begins to decompose/reduce on the surface of the graphite forming a passivation layer called the solid electrolyte interphase (SEI) [50]. The creation of the SEI consumes an irreversible capacity due to the trapping of Li into the passivation layer (Figure 1.6b). SEI is a very complicated layer comprising inorganic compounds, which are normally salt degradation, as well as organic compounds originated from partial or complete reduction of the solvents [51]. When the SEI totally covers the electrode material and reaches a critical thickness, it prevents the migration of electrons stopping the reduction of the electrolyte and so the formation of new SEI. This is generally achieved during the first lithiation, and so the SEI contribution is not observed in the subsequent cycles. The thickness of the SEI may vary from a few angstroms to tens or hundreds of angstroms [52].

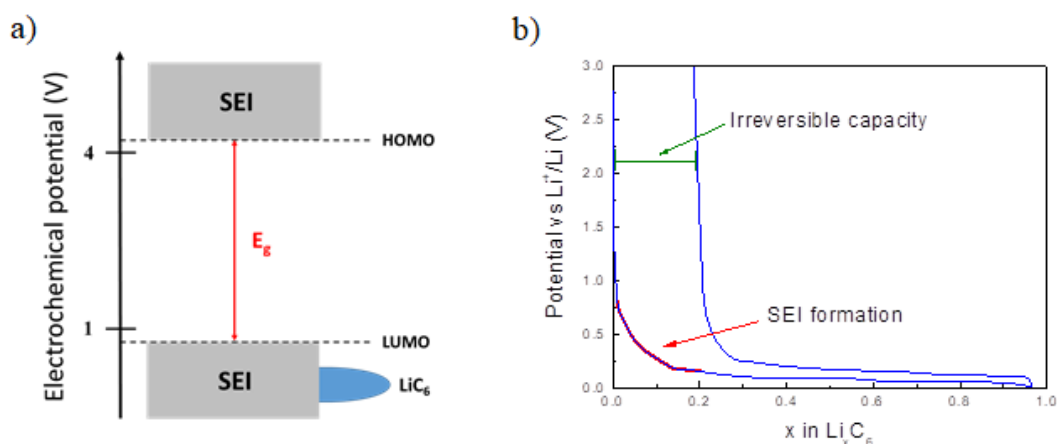


**Figure 1.6.** a) Stability domain ( $E_g$ ) of liquid electrolyte  $\text{LiPF}_6$  in EC:DMC. Readapted from ref [53]. b) SEI formation and irreversible capacity during the first cycle.

Every property of the SEI, such as composition, thickness, morphology, compactness, stability, etc., significantly affects the performance of the battery. The SEI must be electronically insulating but ionically permeable to ensure the intercalation of lithium into the electrode material. It also acts as a physical barrier preventing intercalation of the solvent molecules (especially for propylene carbonate PC [54]) between carbon layers leading to the exfoliation of the electrode [55]. Because SEI can dissolve and/or evolve during cycling deteriorating the battery, having a stable and effective SEI is mandatory for the life and safety of the cell.

## 2.3 Other components

Anode and cathode are indeed the main parts of a battery, because here is where the electrochemical reactions take place in order to provide energy, supported by the presence of the electrolyte. Nevertheless, a large fraction of a Li-ion battery originates from other components, which are necessary in terms of safety, performance, and cost of the battery. In this section, the secondary components of a cell are described.

### 2.3.1 Separators

Separators are an integral part of the performance, safety, and cost of lithium-ion batteries. A separator is a porous membrane placed between the electrodes, and its main function is to keep the negative and positive electrodes apart to prevent electrical short circuits, and at the same time it must allow rapid transport of ions. They should be very good electronic insulators, with sufficient porosity to absorb liquid electrolyte for the high ionic conductivity, and being inert towards the other components of the battery [56]. However, the presence of the separator adds electrical resistance to

the device, affecting the battery performance. Moreover, the separators provide also some protection against overcharge. They exhibit a large increase in impedance at high temperature (around 130 °C) that effectively stops ionic transport under these conditions [57]. The greater the mechanical integrity of the separator at high temperature, the greater the margin of safety it can provide. The greater the mechanical integrity of the separator at high temperature, the greater the margin of safety it can provide.

Battery separators can be divided into three groups: microporous polymer membranes, non-woven fabric mats, and inorganic composite membranes. Because lithium-ion batteries use non-aqueous electrolytes (because of the reactivity of Li in aqueous solutions and because of the high voltage), the most used type of separators are made of microporous membranes of polyolefins.

Table 1.4 shows the different types of separators found in lithium batteries [58].

**Table 1.4.** Types of separators used in different Li-ion batteries.

<b>Battery</b>	<b>Separator</b>	<b>Composition*</b>
Li-ion liquid electrolyte	Microporous	PE, PP, PE+PP
Li-ion gel polymer	Microporous	PVdF
	Microporous	PE, PP, PE+PP coated with PVdF

\*PE polyethylene, PP polypropylene, PVdF polyvinylidene fluoride

### 2.3.2 Current collectors

Generally, the electrode active material does not possess a very high electrical conductivity. Hence, it is necessary to have a current collector, which is usually a metal grid or sheet, where to deposit the active material in order to minimize the resistance. They also act as a physical support for the active material, which otherwise would have a brittle structure. Clearly, the current collector must be stable to chemical reaction with both electrolyte and active material. For most commercial lithium-ion batteries, a copper foil is used for the negative electrode, and aluminium for the positive electrode. Copper is stable at low potential below 3 V vs. Li<sup>+</sup>/Li, whereas aluminium is stable at potentials between 3 V and 5 V [59].

One of the main drawback of the current collectors might be the loss of adhesion during extensive cycling, leading to the degradation of the electrode. Recent research has focused on the use of three-dimensional microporous current collector to improve the performance of the battery. Such current collectors offer a high porosity, high surface area, and a better mechanical stability [60,61].

### 2.3.3 Additives

In commercial Li-ion batteries, additives are always used to improve performance and cycle-life. Generally, conductive materials and binders are added to the electrode, while carbonates are added to the electrolyte solution.

#### 2.3.3.1 Electrode additives

Carbon materials like carbon black and graphite powders are widely used in negative and positive electrodes to increase the inner electrical conductivity [62]. To optimize the energy density of the electrode, the amount of carbon in the total electrode volume needs to be minimized. In real electrodes, the required amount of conductive carbon depends on both the nature of the additive and the active material, as well as on their particle size. Generally, the quantity of carbon added is below 10 wt.% of the total electrode mass. Hence, in relation to the electrochemical capacity of the active material, the carbon contribution can be considered negligible.

A binder is a substance that holds or draws other materials together to form a cohesive whole. They are added to the electrode mixture in order to accommodate volume changes during cycling, and to enhance the contacts between particles. A binder must be chemically and thermally stable, with a good adhesion to the electrode particles without interfering in the motion of both ions and electrons.

Generally, they are polymers, and in commercial Li-ion batteries, the most used binders for the negative electrode are PVdF (polyvinylidene fluoride) and SBR (styrene-butadiene rubber), while for the positive electrode they are PVdF and PTFE (poly-tetrafluoroethylene) [7,63]. However, PVdF is relatively expensive, requires the use of volatile and toxic solvent such as N-methyl pyrrolidone (NMP), and has poor stability towards reducing agents [64]. For these reasons, different binders are currently under investigation. Among these materials, carboxymethyl cellulose (CMC) has shown promising results, for new generation anodes in Li-ion batteries [65,66]. CMC is a derivate of cellulose, and thanks to the carboxymethyl groups ( $-\text{CH}_2\text{-COOH}$ ) is soluble in water, making the electrode production a safer and environmentally process.

The electrodes investigated in this thesis have been prepared adding CMC as binder to the active material powder.

### 2.3.3.2 Electrolyte additives

Carbonate additives can be added with the purpose of improving the formation and stability of the SEI, protecting the electrode from corrosion, stabilizing the lithium salt, improving the safety, etc. [67,68].

Among these additives, VC (vinylene carbonate) has been used in several studies. The results show that, from the decomposition of VC, a SEI with better mechanical properties is formed, enhancing the protection and cohesion of the electrode, achieving better performance during cycling [69].

Works have also been done in order to improve the stability of the lithium salt in the electrolyte. Lewis basic additives [70], such as TTFP (tris 2,2,2-trifluoroethyl), have been added to decrease the reactivity and acidity of  $\text{PF}_5$  formed during the decomposition of  $\text{LiPF}_6$ .

Moreover, other carbonates and new salts to use as additives have also been studied in the past years [71,72].

## 2.4 Materials for negative electrodes

Potential materials for negative electrode must fulfil the following requirements:

- a) React reversibly with lithium;
- b) Accommodate as many Li-ions as possible in order to provide a high capacity;
- c) Insertion/extraction processes should occur at low potential close to  $\text{Li}^+/\text{Li}$  to obtain a large cell voltage;
- d) Good electronic and Li-ion conductivities;
- e) Low cost, environmentally friendly, and safe;

In this part, we will discuss the main materials used and studied as anode in lithium-ion batteries, dividing them in three categories based on their reaction mechanism with Li-ions.

### 2.4.1 Insertion/intercalation materials

Much effort has been directed towards improving lithium-ion batteries, especially in terms of energy and power content, lifetime, safety and cost. Metallic lithium as anode was quickly replaced by carbonaceous material due to safety issues, although several studies are still in progress in order to use lithium metal because of its high theoretical capacity ( $3860 \text{ mAh g}^{-1}$ ) [73]. In the first commercialized lithium-ion batteries carbon coke was used as negative material [74], however, since 1997, it was replaced by graphite. Carbon graphite has a layered, planar structure. In each layer, the carbon atoms are arranged in a honeycomb lattice, with an inter-layer distance of 0.335 nm [75]. Two



different structures of graphite are known: hexagonal called alpha, and rhombohedral called beta. The two structures have very similar physical properties but they differ in the stacking of layers. As shown in Figure 1.7,  $\alpha$ -graphite has an ABAB stacking structure, whereas  $\beta$ -graphite has an ABCABC one.

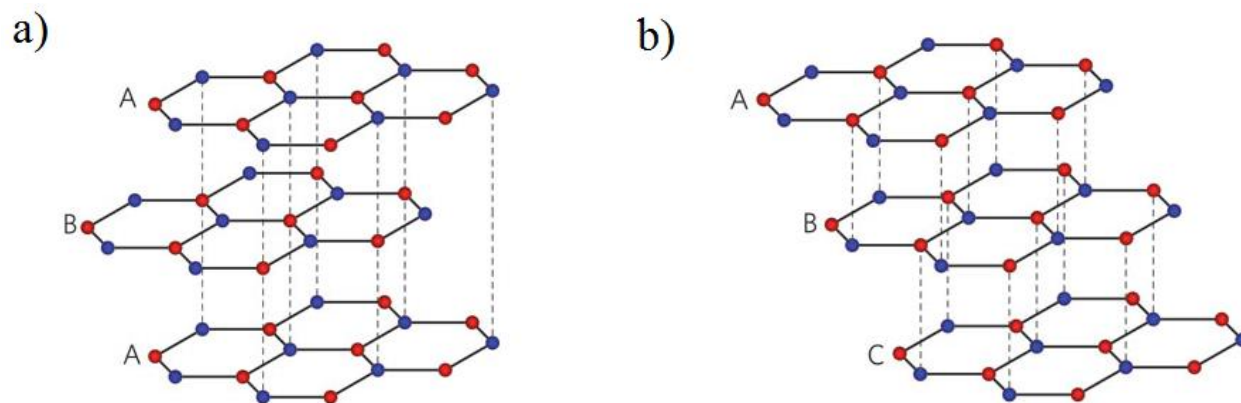


**Figure 1.7.** a) Hexagonal  $\alpha$ -graphite and b) Rhombohedral  $\beta$ -graphite.

Electrochemical activity in graphite comes from the intercalation of lithium ions between carbon planes. Up to 1 Li atom per 6 C atoms can be stored in this way, without affecting the mechanical and electrical properties of the host structure. Graphite has the combined properties of good theoretical capacity, relatively low cost, abundant availability, high electrical conductivity, high lithium diffusivity, low working potential and low volume change during discharge/charge. These properties are listed in Table 1.5.

**Table 1.5.** Graphite anode properties.

Properties	Value	Ref.
Theoretical capacity (mAh g <sup>-1</sup> )	372	[76]
Lithium diffusivity (cm <sup>2</sup> s <sup>-1</sup> )	~10 <sup>-9</sup>	[77]
Discharge potential (V)	~0.1	[78]
Charge potential (V)	~0.2	[78]
Volume change (%)	~10	[79]

Several types of graphite are commercially available, and among these the most used are mesocarbon microbead (MCMB), mesophase-pitch-based carbon fibre (MCF), vapour grown carbon fibre (VGCF), and massive artificial graphite (MAG).

The main drawback of the graphitic compounds (also known as soft carbon) is their low specific capacity (*i.e.* 372 mAh g<sup>-1</sup>), which hinders their use in applications that require a high energy density.

Therefore, new types of carbonaceous materials are studied with the purpose of replacing soft carbons. The differences in crystallinity, size and shape of the particles affect the intercalation process, providing different capacities and insertion potential values.

Presently, the research activity is strongly focused on hard carbons, carbons nanotubes, nanofibers, and graphene, as the most promising based anode materials [80].

Hard carbons have random alignment of graphene sheets, which provides many voids to accommodate lithium. Anode capacities between 200 and 600 mAh g<sup>-1</sup> have been reported in a potential range 0 - 1.5 V vs. Li<sup>+</sup>/Li [81,82]. However, the main weakness of hard carbons is the low initial coulombic efficiency (*i.e.* the ratio between the discharging and charging capacity). Although different strategies to overcome this problem have been suggested, such as fluorination, surface oxidation, and metal coating [83], hard carbons have not yet been introduced on the market as electrode materials.

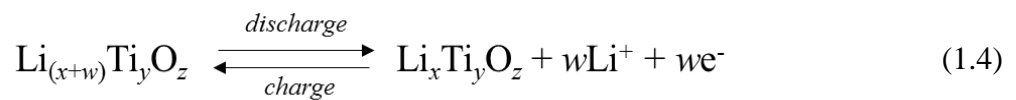
Carbon nanotubes (CNT) can be classified in single (SWCNT) and multiwall carbon nanotubes (MWCNT) depending on the thickness and on the number of coaxial layers. Theoretically, it has been estimated a reversible capacity of 1116 mAh g<sup>-1</sup> for SWNT in the LiC<sub>2</sub> stoichiometry [84,85]. This high capacity, so far the highest among carbonaceous materials, has been attributed to the intercalation of lithium into stable sites located on the surface as well than inside the tube. However, the achievements of complete lithiation and high coulombic efficiency during testing remain still challenging because of the presence of large structure defects and high voltage hysteresis. In order to overcome these issues, research has been focused on the morphological features of CNT, such as wall thickness, shape, diameter, porosity, and doping [86–88]. Anyway, even if several strategies are under study, from the battery industry point of view, the CNT technology is not yet considered mature enough. In fact, open issues regarding the mass production and cost presently hinder their use in Li-ion batteries.

Graphene consists in a honeycomb carbon layer with a single-atom thickness. Because of its astonishing properties, it has been studied in a number of fields such as chemical, physical, biological and engineering sciences. Among these properties, the good electrical conductivity, high surface area, mechanical stability, and high values of charge mobility, make graphene a suitable electrode material for Li-ion batteries [89–91]. Theoretically, graphene has a capacity between 780 and 1116 mAh g<sup>-1</sup>, depending if the storage of Li is considered on both faces of graphene (Li<sub>2</sub>C<sub>6</sub> stoichiometry) or with the ion covalently bond in the benzene ring (LiC<sub>2</sub> stoichiometry), respectively [92,93]. Experimentally, different capacity values above 700 mAh g<sup>-1</sup> are obtained depending on the production methods of graphene [94,95]. Presently, the research is focused on synthesis and functionalization of the surface of graphene. Because of its large area, the surface of graphene is very

reactive, leading to side reactions and so to a large irreversible capacity after the first lithiation. Moreover, the presence of defects can cause a large hysteresis during cycling [96].

As well as active material, graphene can be used as support for other active materials. Materials such as metal, semimetals, oxides, and other carbons, can be dispersed on the surface of graphene in order to obtain a composite electrode with better performance [97–99]. Among the composite graphene-based materials, it is worth to report the promising results of  $\text{Co}_3\text{O}_4/\text{RGO}$  (Reduced Graphene Oxide, *i.e.* graphene oxide in which some oxygen-group has been removed) with a reversible capacity of  $1500 \text{ mAh g}^{-1}$  [100], silicon nanoparticles/RGO with  $1150 \text{ mAh g}^{-1}$  [101], and  $\text{SnO}_2/\text{RGO}$  with  $700 \text{ mAh g}^{-1}$  [102]. Nevertheless, the synthesis of high quality graphene, optimization of structural arrangement during cycling, and weight ratio distribution between the components in the electrode are still key issues that must be achieved for better performance and longer cycle-life [103].

Titanium oxide based materials (LTO) represent the main alternative to carbonaceous compounds for intercalation electrodes. The lithium insertion/extraction process is similar to that occurring in a cathode side in commercial lithium-ion batteries, and the general equation can be written as:



The most widely used titanium oxide is  $\text{Li}_4\text{Ti}_5\text{O}_{12}$  called titanate. Its reaction with lithium is reported in Figure 1.8 [104]:

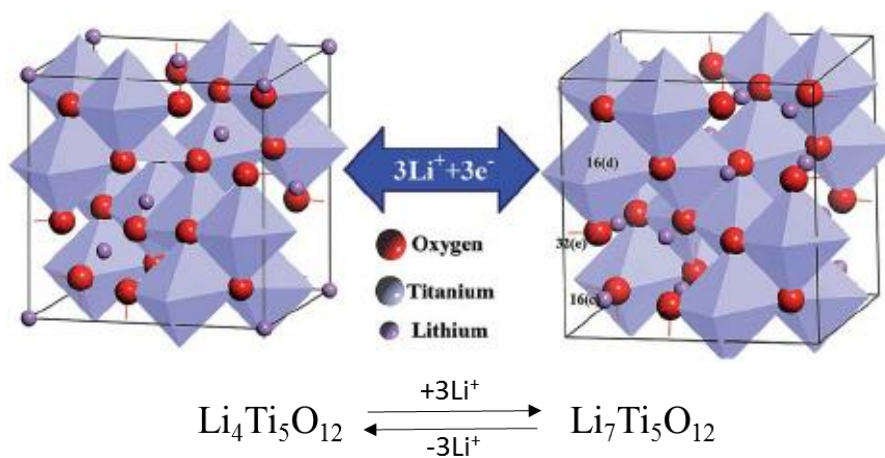


**Figure 1.8.** Illustration of Li insertion/extraction reaction in LTO.

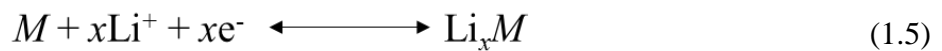
This spinel has a good thermal stability, high cycle-life, and high rate, but on the other hand it suffers from a low capacity (175 mAh g<sup>-1</sup>), reduced cell voltage (1.55 V vs. Li<sup>+</sup>/Li), high cost due to titanium, and poor electronic conductivity (generally Li<sub>4</sub>Ti<sub>5</sub>O<sub>12</sub> is coated with conductive carbon) [105].

High rate and stability originate from the small change in volume (0.2%) during lithiation/delithiation [106,107]. Moreover, because of its high equilibrium potential, the formation of SEI on the surface of carbon additives is avoided. Thanks to these features, LTO was successfully commercialized in 2008, and it is actually used in both mobile and stationary applications.

Other similar compounds are the monoclinic Li<sub>2</sub>Ti<sub>6</sub>O<sub>13</sub> and the ramsdellite Li<sub>2</sub>Ti<sub>3</sub>O<sub>7</sub> [108,109]. Both present better ionic conductivity because of the presence of channels in their structures allowing the fast transport of Li ions. These materials have a theoretical capacity of 200 mAh g<sup>-1</sup> and 235 mAh g<sup>-1</sup> respectively, but they suffer of an important capacity loss during cycling.

#### 2.4.2 Alloying materials

The first electrochemical alloy reaction between lithium and a metal was shown in 1971 [110]. In this reaction, an element *M* reacts at low potential forming an alloy with lithium according to the general equation:



Many metals and semi metals, mainly found in group 13 (Al, Ga, In), 14 (Si, Ge, Sn, Pb) and 15 (As, Sb, Bi) of the periodic table, are reactive towards lithium. The main studied elements are reported in Table 1.6 [111–113].

Generally, they work in a potential range below 1.0 V vs. Li<sup>+</sup>/Li [114], providing much higher volumetric and gravimetric capacities than insertion materials described previously. The combination of the electrochemical properties, as well as the intrinsic characteristics of some elements (such as abundancy, low cost, low toxicity, etc.) explains why much effort has been devoted to develop these types of electrodes.

**Table 1.6.** Characteristics of different lithium alloys  $\text{Li}_x\text{M}$ .  $\text{C}_g$  gravimetric and  $\text{C}_v$  volumetric capacity.

Elements	$x_{\text{Li}}$	$\text{C}_g$ (mAh g <sup>-1</sup> )	$\text{C}_v$ (mAh cm <sup>-3</sup> )
Si	3.75	3579	2194
Sn	4.4	993	2111
Ge	4.25	1568	2260
Pb	4.5	582	2052
Sb	3	660	1771
As	3	1073	2200
Bi	3	385	1662
Al	1	993	1411
Mg	1.95	2150	1658

Unfortunately, they generally suffer from a large irreversible capacity during the first cycles, and so a poor cycle-life, due to the large volume change during discharge/charge cycles.

The alloy formation is accompanied by a large volume expansion, and the successive delithiation/lithiation processes causes high mechanical strains in the particles, leading to the pulverization of the active material, loss in contacts, and damaging the whole electrode structure [115]. These volume changes influence also the formation of the SEI layer. During cycling, the repeated volume expansion causes cracks in the particles, forming new surfaces where the electrolyte decomposes.

Because volume changes are the main issues in this type of electrode, an appropriate design of the microstructure could improve the cycle-life of these materials. The main research activities on alloying materials are turned to developing strategies, such as composite electrodes, nanosized particles, nanostructured materials, etc., in order to alleviate the mechanical strain during cycling [116].

For this thesis, a particular attention is paid for the Mg-Li alloy, because in specific cycling condition (*i.e.* with a cut off potential below 0.1 V vs.  $\text{Li}^+/\text{Li}$ ), this reaction might occur. Indeed, using  $\text{MgH}_2$  as active material, the lithiation leads to the formation of Mg and LiH, and this freshly formed Mg can further react with Li at low potentials. Looking at the binary phase diagram of Mg and Li, reported in Figure 1.9 [117], is possible to notice that at room temperature a Mg-rich phase exists up to 15 atomic Li%, and a Li-rich alloy exists with a minimum of 30 atomic Li%. These regions are separated by a two-coexistence domain. Because the Li-rich solid solution phase extends to lithium metal, the theoretical capacity of Mg is infinite. However, the maximum achieved capacity reported

is 2150 mAh g<sup>-1</sup>, corresponding to a composition about Li<sub>1.95</sub>Mg [118]. Like other metals, magnesium is actually under investigation as possible electrode material. One of the main drawback of Mg is due to the chance of plating lithium on the electrode surface, with the resulting safety issues (expansion and dendrites formation).

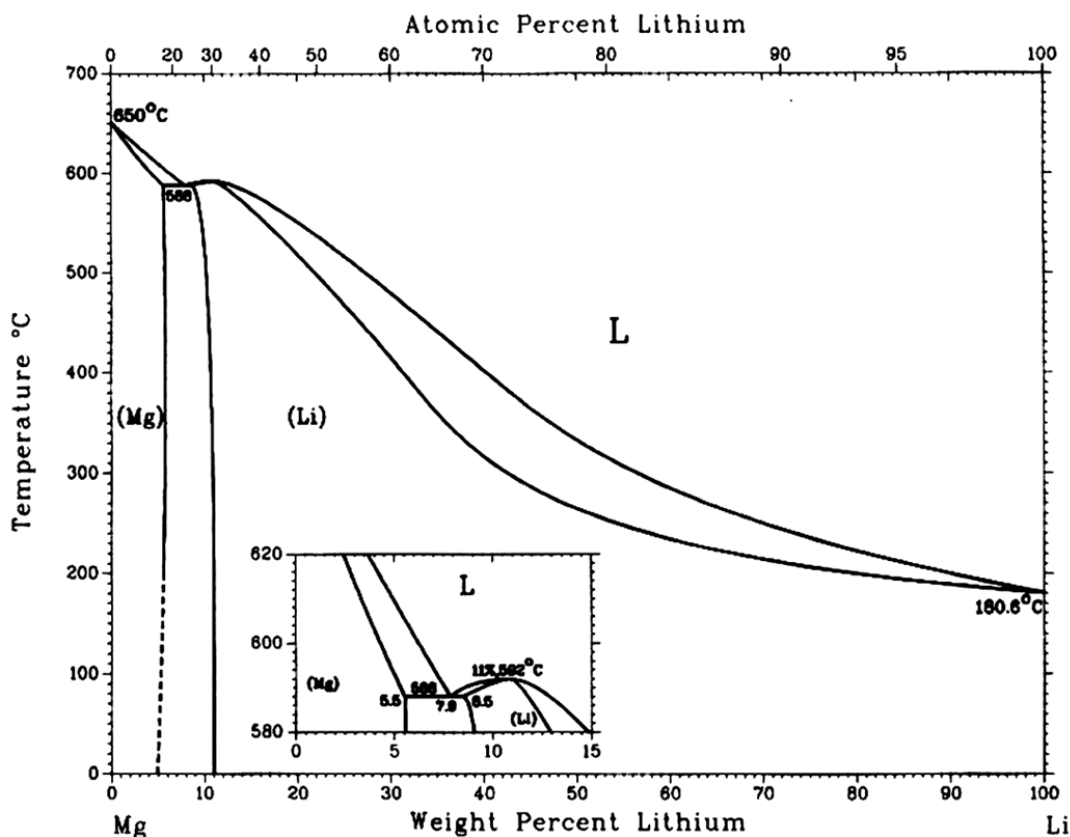
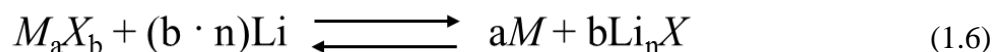


Figure 1.9. Li-Mg binary phase diagram.

### 2.4.3 Conversion materials

The last family of materials investigated as candidates for the negative electrode is referred to as conversion materials. In a general conversion reaction, a compound based on a transition metal ( $M$ ) coupled with an anion ( $X$ ) reacts with lithium as illustrated in Equation 1.6:



During the reaction, the compound  $MX$  is completely reduced to its metallic state  $M$ , forming the lithium binary compound  $LiX$ . Based on the nature of  $MX$ , one or more intermediate phases  $Li-M-X$  can be formed during the lithiation. When the lithiation is completed, nanoparticles of  $M$  are homogeneously embedded in a  $LiX$  matrix. Conversion reactions have been reported for several metal oxides, nitrides, sulphides, fluorides, and recently also for metal hydrides [119–123]. The main

advantage of these materials is the high capacity they can provide compared to graphite. Specific capacities of several material undergoing conversion reaction are displayed in Figure 1.10. Moreover, applications for conversion materials could be found as both negative and positive electrode, because some of them react below 1.0 V *vs.* Li<sup>+</sup>/Li (*e.g.* Cr<sub>2</sub>O<sub>3</sub>, MnS, FeP, etc.), others at potential as high as 2.0 V or 3.0 V (*e.g.* FeF<sub>3</sub> and CuF<sub>2</sub> respectively).

However, as for all the systems illustrated so far, conversion materials present different weaknesses. Strong structural re-organization takes place to accommodate the chemical changes during cycling, inducing volume changes that, as in the case of alloying materials, lead to particles cohesion losses and electrode damage. Moreover, large voltage hysteresis is observed between discharge and charge processes, leading to large loss in energy density.

Several strategies, similar to those studied for alloy electrodes, have been employed to limit these drawbacks, such as composite electrode materials, development of nanostructures, use of polymeric binder, etc. [124].

In this thesis, metal hydrides are studied as active material for lithium-ion batteries, and so their electrochemical properties will be described in detail in Section 3.

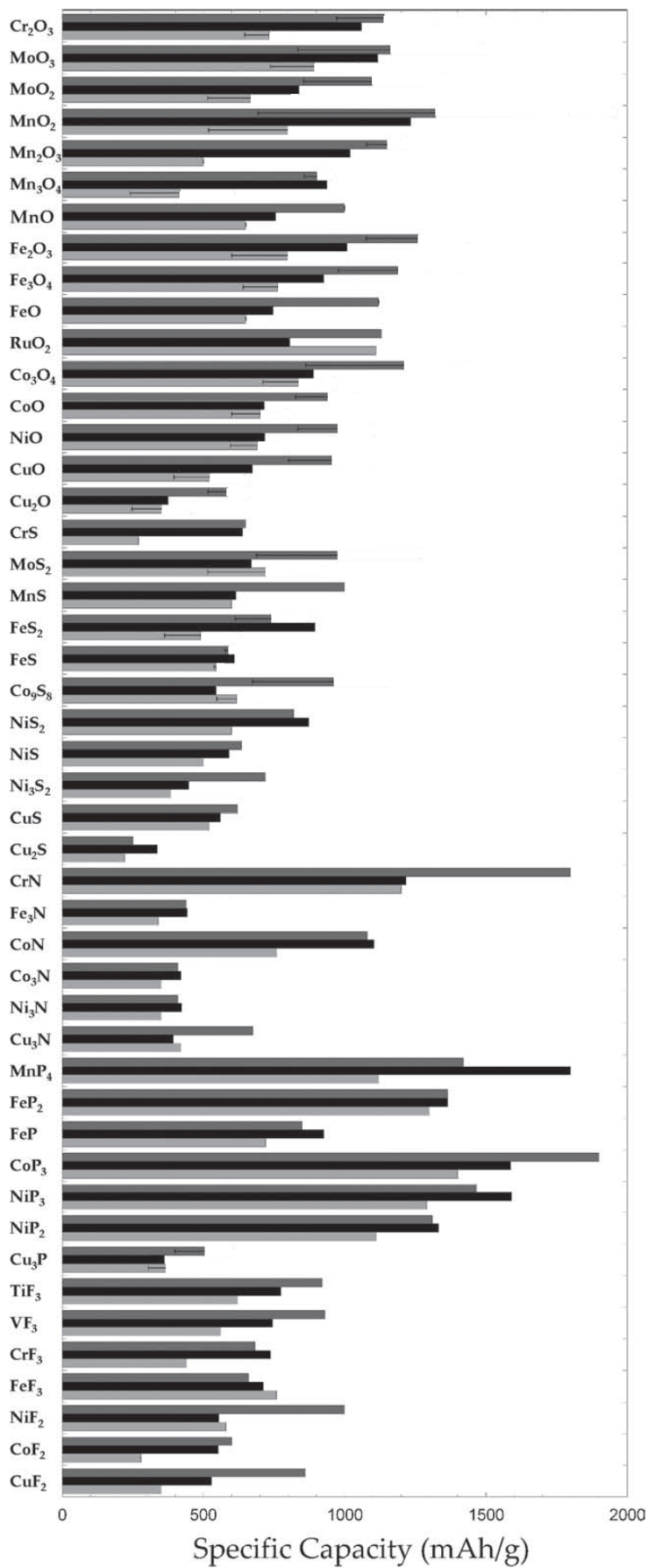
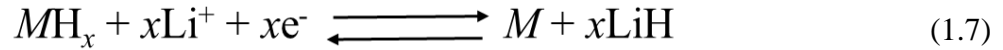


**Figure 1.10.** First discharge (dark grey), theoretical (black) and first charge (light grey) capacities of different compounds undergoing a conversion reaction with lithium. Readapted from ref [119].



### 3 Metal hydrides for Li-ion batteries

In 2008, Oumellal *et al.* proposed for the first time the use of metal hydrides as electrode materials for lithium-ion batteries [125]. As previously cited, metal hydrides belong to the materials undergoing a conversion reaction with lithium according to the general equation:



During the lithiation, the hydride is reduced to metal and lithium hydride (LiH). Based on the nature of the hydride, the lithiation can be completed in one or more steps.

The main advantages that make metal hydrides a promising candidate for future lithium-ion batteries are:

- I. Suitable working potential window, generally between 0.1 and 1.0 V vs. Li<sup>+</sup>/Li;
- II. High theoretical capacity compared to graphite (372 mAh g<sup>-1</sup>). Several hydrides possess a gravimetric capacity in the order of thousands of mAh g<sup>-1</sup>;
- III. Among conversion compounds, metal hydrides show the lowest polarization;

On the other hand, the sluggish kinetics at room temperature and the short cycle-life still remain important issues to overcome in order to use metal hydrides as electrode materials in practical energy storage applications.

In this section, the properties of metal hydrides as conversion electrode materials, their issues, and strategies to improve their performance will be described.

#### 3.1 Gravimetric and volumetric storage capacity

The theoretical capacity of an electrode material for lithium-ion batteries can be calculated from the following equation:

$$C_{theoric} = x \frac{F}{M} \quad (1.8)$$

Where  $x$  is the number of Li atoms exchanged per formula unit,  $F$  is the Faraday constant expressed as 26.801 Ah mol<sup>-1</sup>, and  $M$  is the molar mass of the active material in g mol<sup>-1</sup>.

For a complete lithiation, metal hydrides can form one LiH per each H atom they possess. This, combined with the light weight of several hydrides, explains the high theoretical capacity shown by many metal hydrides. Figure 1.11 shows both the theoretical gravimetric and volumetric capacities of several hydrides.

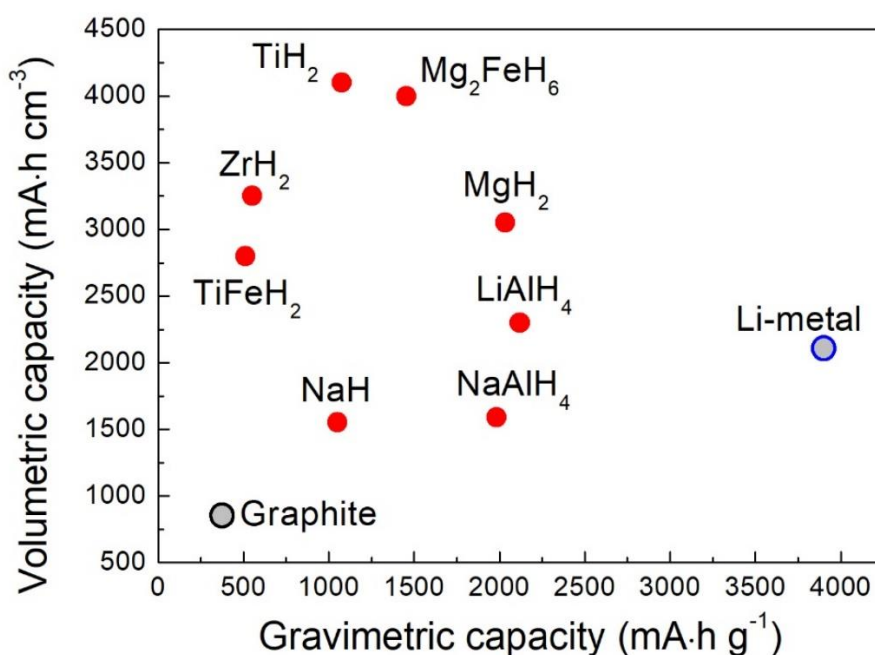


**Figure 1.11.** Gravimetric and volumetric capacities of metal and complex hydrides compared with those of graphite and lithium metal.

Several hydrides can deliver a gravimetric capacity more than twice that of graphite. This is mainly due to the fact that for each atom of H a hydride can store a Li per formula unit, whereas carbon graphite can store a Li every six atoms of C. The highest values are obtained for dihydrides and light complex hydrides, showing a gravimetric capacity of several thousand mAh g<sup>-1</sup>. These large capacities make metal hydrides a good candidate material for negative electrodes in Li-ion batteries for stationary as well as mobile applications.

In the last years, several metallic and complex hydrides have been investigated as negative materials for Li-ion batteries. The main results reported from different groups are summarized in Table 1.7.

**Table 1.7.** Electrochemical properties of binary and complex hydrides towards lithium ions.

Active material	Theoretical capacity		First discharge capacity		Ref.
	mAh g <sup>-1</sup>	<i>x</i> Li	mAh g <sup>-1</sup>	<i>x</i> Li	
	MgH <sub>2</sub>	2038	2	4000	
TiH <sub>2</sub>	1074	2	1072	2	[126]
AlH <sub>3</sub>	2679	3	1625	1.8	[127]
TiNiH	249	1	251	1.07	[128]
Mg <sub>2</sub> NiH <sub>4</sub>	963	4	866	3.6	[129]
Mg <sub>2</sub> CoH <sub>5</sub>	1190	5	1300	5.5	[129]
Mg <sub>2</sub> FeH <sub>6</sub>	1455	6	1577	6.5	[129]
NaAlH <sub>4</sub>	1985	4	1042	2.1	[130]
LiAlH <sub>4</sub>	2119	4	1180	1.7	[131]
Li <sub>3</sub> AlH <sub>6</sub>	1493	6	900	3.6	[131]

From Table 1.7 is possible to notice that for several hydrides the reactivity with lithium ions predicted (*i.e.* theoretical *x*Li) differs from the experimental one. This is due to the multi-step reactions involving the formation of alloys, solid solutions, metastable and/or amorphous phases during discharge and charge [132].

### 3.2 Thermodynamics of hydrides as electrode

The equilibrium potential at which a hydride reacts with lithium can be calculated by using the Nernst law:

$$E_{eq} = -\frac{\Delta_r G^o}{x \cdot F} \quad (1.9)$$

Where  $E_{eq}$  is the equilibrium potential,  $\Delta_r G^o$  is the Gibbs free energy of the reaction between the hydride and lithium,  $x$  is the number of electrons involved in the reaction, and  $F$  is the Faraday constant.

Under standard conditions (*i.e.*  $p = 1$  bar, and  $T = 25^\circ\text{C}$ ), the Gibbs free energy of the reaction in Equation 1.7 can be calculated from the values of Gibbs free energy of formation of reactants and products:

$$\Delta_r G^\circ = [\Delta_f G^\circ(M) + x\Delta_f G^\circ(\text{LiH})] - [\Delta_f G^\circ(\text{MH}_x) + x\Delta_f G^\circ(\text{Li})] \quad (1.10)$$

Because the Gibbs free energy of formation ( $\Delta_f G^\circ$ ) of pure elements, such as  $M$  and  $\text{Li}$ , is zero, Equation 1.10 can be rewritten as follows:

$$\Delta_r G^\circ = x\Delta_f G^\circ(\text{LiH}) - \Delta_f G^\circ(\text{MH}_x) \quad (1.11)$$

Metal hydrides with a positive theoretical equilibrium potential vs.  $\text{Li}^+/\text{Li}$  are possible candidates as negative electrode material for Li-ion batteries. Figure 1.12 shows the calculated equilibrium potential of different hydrides.

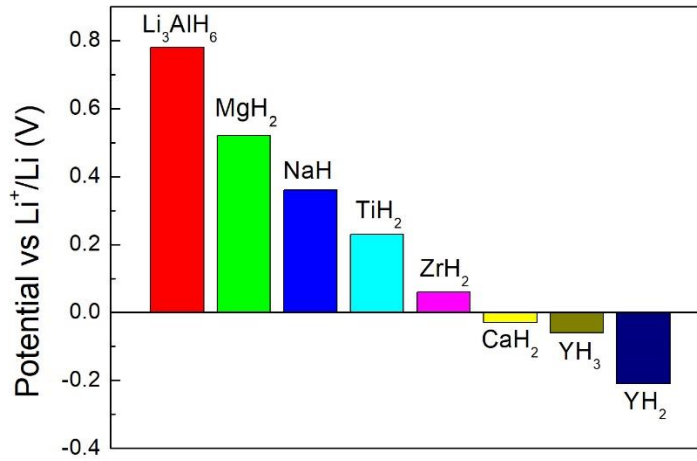


**Figure 1.12.** Theoretical equilibrium potentials vs.  $\text{Li}^+/\text{Li}$  for different metal hydrides.

The hydrides with a negative equilibrium potential cannot undergo the conversion reaction, because they are more stable than the  $\text{LiH}$  phase.

An easier way to evidence which hydride can react with lithium following the path displayed in Eq. 1.7 is to confront its Gibbs free energy of formation with that of lithium hydride. Because  $\text{LiH}$  is formed independently of the hydride taken into account, the reaction is possible when:

$$\frac{\Delta_f G^\circ(\text{MH}_x)}{x} > \Delta_f G^\circ(\text{LiH}) \quad (1.11)$$

Hence, the value of the quotient in Eq. 1.11 should be higher than  $\Delta_f G^\circ(\text{LiH}) = 70 \text{ kJ mol}^{-1}$  [133].

However, during discharge/charge cycling, the plateau curves exhibit potential values different from the theoretical ones. During lithiation the plateau is at lower potential than the theoretical one, whereas during delithiation it is at higher values. This effect is due to internal resistance, polarization, and kinetic limitations. The equilibrium potential of the  $MH_x/Li$  cell can be experimentally obtained by galvanostatic intermittent titration (GITT) in open circuit voltage [134].

### **3.3 MgH<sub>2</sub> and TiH<sub>2</sub> as negative electrode materials**

In this thesis MgH<sub>2</sub>-TiH<sub>2</sub> composites will be the main active materials investigated, so it is worth to report the studies accomplished up to now about these bi-phasic composites and their single-phase counterpart hydrides (MgH<sub>2</sub> and TiH<sub>2</sub>) as electrodes in lithium-ion batteries. They have been chosen because they react with lithium at potentials suitable for negative electrodes (0.5 V for MgH<sub>2</sub> and 0.2 V for TiH<sub>2</sub> vs. Li<sup>+</sup>/Li), providing a high theoretical capacity about 2000 and 1000 mAh g<sup>-1</sup> for MgH<sub>2</sub> and TiH<sub>2</sub> respectively. Moreover, they are easy to synthesize starting from their metals, and when mixed together, some cooperative effect is expected, which can improve the reactivity of the composite.

#### **3.3.1 Reactivity of MgH<sub>2</sub> with lithium**

The reactivity of MgH<sub>2</sub> towards lithium ions was the first example of Li-driven conversion reaction with hydrides reported in literature [125]. Collecting XRD patterns at different reaction steps, Oumellal *et al.* showed the progression of the reaction between MgH<sub>2</sub> and Li. The discharge curve and selected XRD patterns are displayed in Figure 1.13.

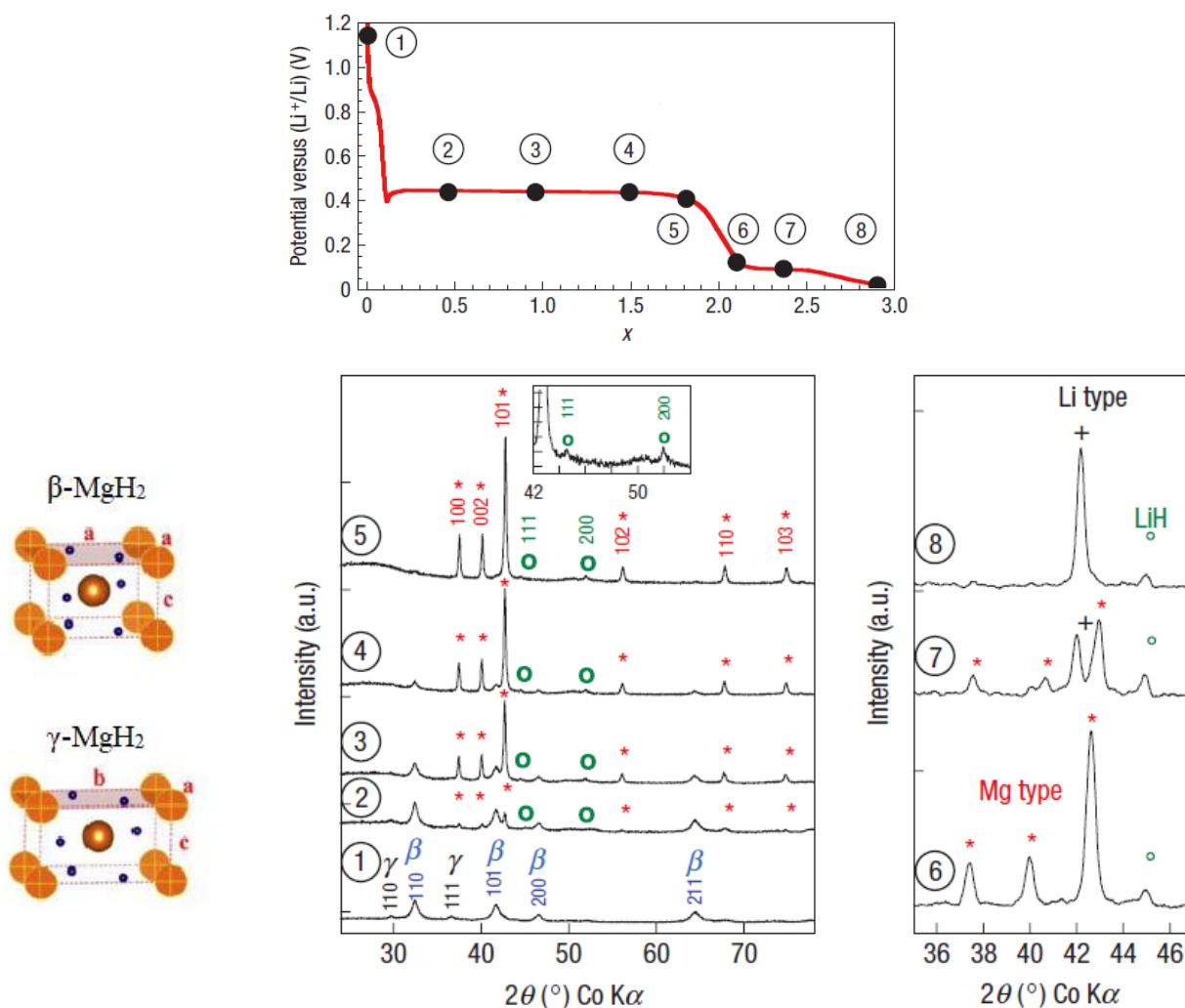
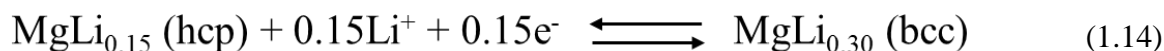
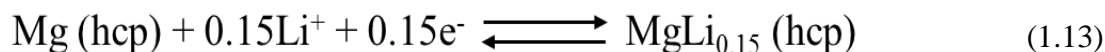


**Figure 1.13.** Discharge curve and XRD patterns acquired at different reaction steps. Readapted from ref [125].

The pristine electrode contains magnesium hydride prepared by ball milling as active material. It exhibits polymorphic  $\beta$  and  $\gamma$ -MgH<sub>2</sub> phases (pattern 1 Figure 1.13). When a cathodic current is applied, the potential drops reaching a plateau at 0.44 V, where the reaction between MgH<sub>2</sub> and Li ions occurs. While the conversion reaction proceeds, patterns 2-4, the intensity of the MgH<sub>2</sub> Bragg peaks decreases, and two new phases are detected, Mg (red asterisks) and LiH (green circles). In pattern 5 only Mg and LiH phases are detected, implying a complete reduction of MgH<sub>2</sub>.

Pursuing further lithiation leads to the alloy reaction between Li ions and the freshly formed Mg. As previously mentioned, the Mg-Li phase diagram exhibits three different domains at room temperature (see Figure 1.9), thus the alloy reaction proceeds in three steps: an initial topotactic reaction up to the Li solubility limit into Mg (Mg-solid solution, pattern 6); a two phases domain, where both a Mg- and Li-solid solutions coexist (pattern 7, with Li-solid solution marked with a black

cross); another topotactic reaction where only the Li-solid solution remains (pattern 8). The overall lithiation reaction of magnesium hydride can be summarized as follows:



Because of alloying reactions, the quantity of lithium stored in the electrode at the end of the discharge exceeds the theoretical value of  $\text{MgH}_2$  (*i.e.*  $x = 2$  for dihydrides).

During the charge lithium should be extracted from both Mg-Li alloy and LiH restoring  $\text{MgH}_2$ . However, experimentally the complete reformation of  $\text{MgH}_2$  has not been achieved yet, implying a large loss in capacity already during the first cycle. In the subsequent cycles the capacity generally drops quite quickly to values below  $300 \text{ mAh g}^{-1}$ . Figure 1.14 shows the capacity loss after the first cycle, and the XRD pattern obtain at the end of the delithiation. Other authors concluded that the main reason of this capacity fading could be attributed to the loss in contact between the particles [135]. Indeed, the reduction of  $\text{MgH}_2$  to Mg and LiH is accompanied by a volume change and a phase rearrangement, which may cause loss of contacts during cycling, hindering the exchange of ions and electrons for the conversion reaction.

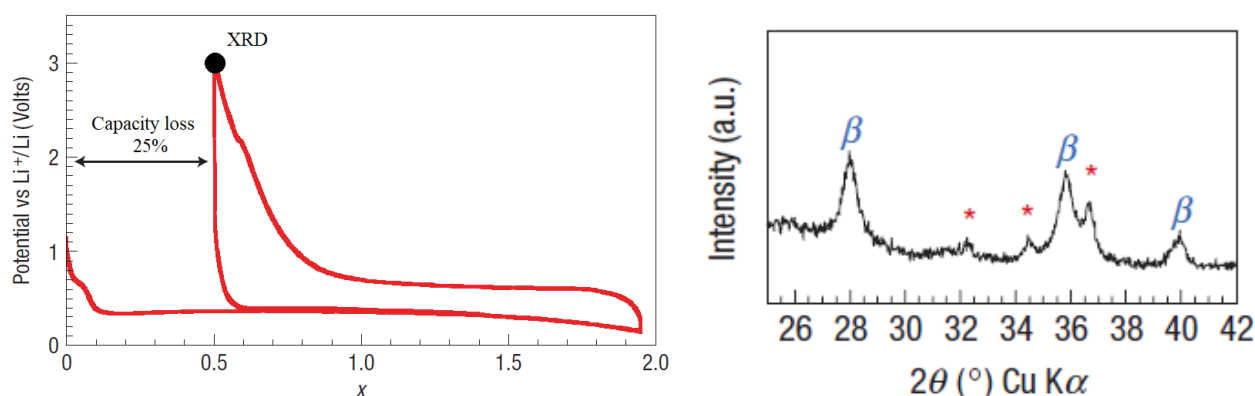


**Figure 1.14.** Capacity loss after the first cycle (left), and XRD pattern (right) performed at the end of the charge (marked with a black dot). In the pattern,  $\beta$  are the tetragonal  $\text{MgH}_2$  phase reformed, and the red asterisk are Mg phase.

With the purpose of enhancing the cycle-life of the electrode, different strategies have been suggested in the last years. Avoiding the Mg alloying reaction by limiting the working potential above 0.1 V has been shown to increase the reversibility of the conversion reaction [136]. This has been credited to a limited volume changes, because the conversion reaction leads to an increase in the volume about 83%, whereas the full lithiation including the alloy reaction reaches 200% volume change.

Depending on the milling conditions and the method to fabricate the electrode, Brutti *et al.* [137,138] obtained different amounts of lithium inserted/extracted, suggesting that nanoparticles homogenously mixed together possess better capacity retention thanks to the high number of interfaces. Related results, about the size effect, were found testing MgH<sub>2</sub> after H<sub>2</sub> absorption/desorption cycles. The particle size of the hydride is reduced through decrepitation during the solid-gas reaction, and once tested as electrode vs. Li<sup>+</sup>/Li MgH<sub>2</sub> showed enhanced reversibility [136].

An approach to tailor the particle morphology of the hydride consisted in preparing composites of MgH<sub>2</sub> nanoparticles dispersed into a porous carbon scaffold. By this method, Oumellal *et al.* [139] enhanced the electrical conductivity in the electrode, preventing also the coarsening of the particles during cycling. These composites were able to deliver a capacity close to 500 mAh g<sup>-1</sup> even after one hundred cycles.

Zaïdi *et al.* [140] studied the effect of carboxymethyl cellulose (CMC) and carboxymethyl cellulose-formate (CMC-f) as binders. These MgH<sub>2</sub> electrodes showed initial reversible capacity about 90% of the theoretical, and a capacity retention of ~20% after 40 cycles. This effect is attributed to the mechanical ability of the binder to accommodate the volume changes during cycling.

Exploring the field of solid electrolytes for lithium-ion batteries, Ikeda [141,142] and Zeng [143,144] investigated the electrochemical properties of MgH<sub>2</sub> in all solid-state batteries. Working at high temperatures (120 °C), solid-state cells showed high discharge capacity even at high current densities, featuring also flatter plateau and smaller polarization effect. Capacities closed to 1000 mAh g<sup>-1</sup> were achieved also after fifty discharge/charge cycles. Among the solid electrolyte there are several hydride-based composites which could be used (*e.g.* LiBH<sub>4</sub>, LiBH<sub>4</sub>-LiNH<sub>2</sub>, LiAlH<sub>4</sub>-Li<sub>3</sub>AlH<sub>6</sub>, etc. [145–148]), opening the possibility of creating in future an all hydride based battery.

Although several strategies, with promising results, have been reported, MgH<sub>2</sub> is not yet ready to be introduced in the market as an electrode material. The poor capacity retention at room temperature still remains the main issue to overcome. Hence, more research efforts are needed to find the right optimization for practical applications.



### 3.3.2 Reactivity of TiH<sub>2</sub> with lithium

After the promising results shown by MgH<sub>2</sub>, other hydrides were investigated as possible candidates for lithium-ion batteries. Due to its high theoretical capacity and electrical conductivity [149], TiH<sub>2</sub> was investigated as electrode material by Oumellal *et al.* [126]. Interestingly, the conversion reaction taking place during the lithiation of TiH<sub>2</sub> was reported to be completely different compared with MgH<sub>2</sub>. XRD analysis of the electrode during the discharge (Figure 1.15) showed that the reactivity of TiH<sub>2</sub> with Li ions cannot be described with a single equation like for MgH<sub>2</sub> (Equation 1.12), but it involves three different steps.

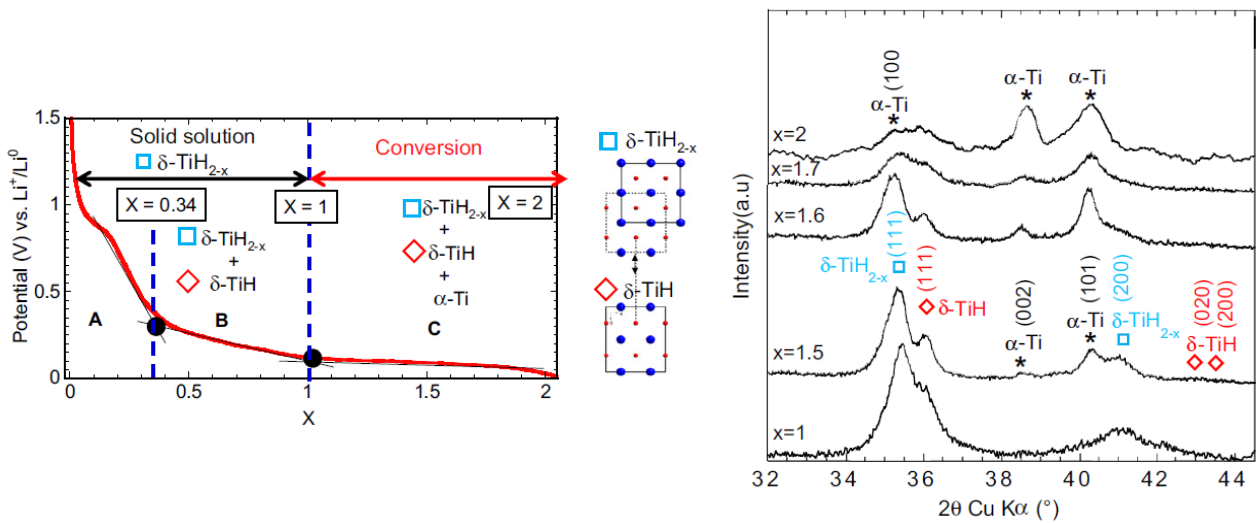


**Figure 1.15.** Discharge curve of TiH<sub>2</sub> (left), and XRD patterns at different lithiation steps. Readapted from ref [126].

The first step of the conversion reaction is related to the slope from  $x = 0$  to  $x = 0.34$ , where TiH<sub>2</sub> reacts with Li ions forming the solid solution  $\delta$ -TiH<sub>2-x</sub> (fcc, marked with blue squares) and LiH. Then, in the subsequent slope from  $x = 0.34$  to  $x = 1$ ,  $\delta$ -TiH<sub>2-x</sub> is partly transformed in  $\delta$ -TiH (fcc, marked with red diamond) and LiH. Finally, the reaction proceeds in a pseudo plateau from  $x = 1$  to  $x = 2$  forming  $\alpha$ -Ti (hcp) and LiH.

Unfortunately, the conversion reaction did not occur during the charge, implying a full irreversible behaviour of the electrode [126,150]. Interestingly, it was observed that, starting from an electrode prepared with ball milled LiH and Ti [151], TiH<sub>2</sub> was partially formed during the charge (~40% of TiH<sub>2</sub>). In the subsequent lithiation, TiH<sub>2</sub> was completely reduced to Ti and LiH, but once again, no electrochemical reversibility was detected in the next charge. Therefore, the fact that TiH<sub>2</sub> is not reformed could be attributed to the large volume expansion during the discharge process (~130%), which leads to electrode pulverization.

Better performances were achieved by Kawahito *et al.* [152] using  $\text{TiH}_2$  in an all solid-state cell with  $\text{LiBH}_4$  as solid electrolyte. The reduction of the hydride was proved to follow a path like in the liquid electrolyte cell, with the formation of intermediate  $\text{TiH}_{2-x}$ . During charge, a high capacity was obtained, and the cell provided a capacity of  $900 \text{ mAh g}^{-1}$  even after fifty cycles. These results could be attributed to an enhanced kinetics of the electrode, with a faster diffusion of species at  $120^\circ\text{C}$  compared to room temperature cycling.

### 3.3.3 $\text{MgH}_2$ - $\text{TiH}_2$ composite as electrode material

Huang *et al.* [153] have recently investigated the composite  $0.7\text{MgH}_2+0.3\text{TiH}_2$  as negative electrode. For hydrogen storage in solid state it is reported in literature that the addition of  $\text{TiH}_2$  to  $\text{MgH}_2$  strongly enhances the transport of hydrogen in the composite [154–156]. During the discharge both hydrides participate in the conversion reaction, showing the plateau of  $\text{MgH}_2$  and the slope of  $\text{TiH}_2$ . In the charge process, the electrode exhibits good electrochemical reversibility, with the partial reformation of both hydrides. This performance was associated to the high electrical conductivity and fast hydrogen kinetics of  $\text{TiH}_2$ . However, after few cycles, the capacity quickly drops to  $500 \text{ mAh g}^{-1}$ , showing the same limits than pure  $\text{MgH}_2$  and  $\text{TiH}_2$  electrodes.

Hence, different  $\text{MgH}_2$ - $\text{TiH}_2$  composites must be studied with the purpose of enhancing the performance of both hydrides. Tailoring the (micro)structure and composition of the electrode could be possible to achieve higher capacities and better reversibility during the cycling.

## References

1. Tarascon, J. M. & Armand, M. Issues and challenges facing rechargeable lithium batteries. *Nature* **414**, 359–67 (2001).
2. Ehrlich, G. M. *Lithium-Ion Batteries. Handbook of Batteries* (2002). doi:10.1016/0378-7753(86)80059-3
3. Winter, M. & Brodd, R. J. What Are Batteries , Fuel Cells , and Supercapacitors? *Chem. Rev.* **104**, 4245–4270 (2004).
4. Lide, D. R. Hardness of Minerals and Ceramics. *CRC Handb. Chem. Phys.* 2313–2314 (2005). doi:10.1021/ja041017a
5. Whittingham, M. S. Electrical Energy Storage and Intercalation Chemistry. *Science*. **192**, 1126 LP-1127 (1976).
6. Whittingham, M. S. Chemistry of intercalation compounds: Metal guests in chalcogenide hosts. *Prog. Solid State Chem.* **12**, 41–99 (1978).
7. Nazri, G.A., Pistoia, G. Lithium batteries: science and technology. *Springer* (2008).
8. Goodenough, J. B. *et al.* Patent US 4,302,518 (1981).
9. Mizushima, K., Jones, P. C., Wiseman, P. J. & Goodenough, J. B.  $\text{Li}_x\text{CoO}_2$  ( $0 < x \leq 1$ ): A new cathode material for batteries of high energy density. *Solid State Ionics* **3–4**, 171–174 (1981).
10. Ikeda, H., Narukawa, K., Nakashim, H. Patent Japan 1769661 (1981).
11. Yoshino, A., Jitsuchika, K., Nakajima, T. Patent Japan 1989293 (1985).
12. Julien, C., Mauger, A., Vijh, A. & Zaghbi, K. Lithium batteries: science and technology. *Springer* (2016).
13. Ohzuku, T. & Brodd, R. J. An overview of positive-electrode materials for advanced lithium-ion batteries. *J. Power Sources* **174**, 449–456 (2007).
14. Scrosati, B. & Garche, J. Lithium batteries: Status, prospects and future. *J. Power Sources* **195**, 2419–2430 (2010).
15. Ozawa, K. Lithium-ion rechargeable batteries with  $\text{LiCoO}_2$  and carbon electrodes: the  $\text{LiCoO}_2/\text{C}$  system. *Solid State Ionics* **69**, 212–221 (1994).

16. Ellis, B. L., Lee, K. T. & Nazar, L. F. Positive electrode materials for Li-Ion and Li-batteries. *Chem. Mater.* **22**, 691–714 (2010).
17. Stoyanova, R., Zhecheva, E. & Zarkova, L. Effect of Mn-substitution for Co on the crystal structure and acid delithiation of  $\text{LiMn}_y\text{Co}_{1-y}\text{O}_2$  solid solutions. *Solid State Ionics* **73**, 233–240 (1994).
18. Alcántara, R. *et al.* X-ray diffraction,  $^{57}\text{Fe}$  Mössbauer and step potential electrochemical spectroscopy study of  $\text{LiFe}_y\text{Co}_{1-y}\text{O}_2$  compounds. *J. Power Sources* **81–82**, 547–553 (1999).
19. Madhavi, S., Subba Rao, G. V., Chowdari, B. V. R. & Li, S. F. Y. Effect of Cr dopant on the cathodic behavior of  $\text{LiCoO}_2$ . *Electrochim. Acta* **48**, 219–226 (2002).
20. Scott, I. D. *et al.* Ultrathin coatings on nano- $\text{LiCoO}_2$  for Li-ion vehicular applications. *Nano Lett.* **11**, 414–418 (2011).
21. Cho, J., Kim, Y. J., Kim, T. J. & Park, B. Zero-strain intercalation cathode for rechargeable Li-Ion cell. *Angew. Chemie - Int. Ed.* **40**, 3367–3369 (2001).
22. Rougier, A., Gravereau, P. & Delmas, C. Optimization of the Composition of the  $\text{Li}_{1-z}\text{Ni}_{1+z}\text{O}_2$  Electrode Materials: Structural, Magnetic, and Electrochemical Studies. *J. Electrochem. Soc.* **143**, 1168–1175 (1996).
23. Kalyani, P. & Kalaiselvi, N. Various aspects of  $\text{LiNiO}_2$  chemistry: A review. *Sci. Technol. Adv. Mater.* **6**, 689–703 (2005).
24. Chowdari, B. V. R., Subba Rao, G. V & Chow, S. Y. Cathodic behavior of (Co, Ti, Mg)-doped  $\text{LiNiO}_2$ . *Solid State Ionics* **140**, 55–62 (2001).
25. Chen, C. H. *et al.* Aluminum-doped lithium nickel cobalt oxide electrodes for high-power lithium-ion batteries. *J. Power Sources* **128**, 278–285 (2004).
26. Lee, H. W. *et al.* Ultrathin spinel  $\text{LiMn}_2\text{O}_4$  nanowires as high power cathode materials for Li-ion batteries. *Nano Lett.* **10**, 3852–3856 (2010).
27. Thackeray, M. M. Spinel Electrodes for Lithium Batteries . *J. Am. Ceram. Soc* **82**, 3347–3354 (1999).
28. Kakuda, T., Uematsu, K., Toda, K. & Sato, M. Electrochemical performance of Al-doped  $\text{LiMn}_2\text{O}_4$  prepared by different methods in solid-state reaction. *J. Power Sources* **167**, 499–503 (2007).

29. Numata, T., Amemiya, C., Kumeuchi, T., Shirakata, M. & Yonezawa, M. Advantages of blending  $\text{LiNi}_{0.8}\text{Co}_{0.2}\text{O}_2$  into  $\text{Li}_{1+x}\text{Mn}_{2-x}\text{O}_4$  cathodes. *J. Power Sources* **97**, 358–360 (2001).
30. Jiao, F., Bao, J., Hill, A. H. & Bruce, P. G. Synthesis of Ordered Mesoporous Li-Mn-O Spinel as a Positive Electrode for Rechargeable Lithium Batteries. *Angew. Chemie* **120**, 9857–9862 (2008).
31. Manthiram, A. & Goodenough, J. B. Lithium insertion into  $\text{Fe}_2(\text{MO}_4)_3$  frameworks: Comparison of  $\text{M} = \text{W}$  with  $\text{M} = \text{Mo}$ . *J. Solid State Chem.* **71**, 349–360 (1987).
32. Chung, S.-Y., Bloking, J. T. & Chiang, Y.-M. Electronically conductive phospho-olivines as lithium storage electrodes. *Nat Mater* **1**, 123–128 (2002).
33. Gong, Z. & Yang, Y. Recent advances in the research of polyanion-type cathode materials for Li-ion batteries. *Energy Environ. Sci.* **4**, 3223 (2011).
34. Xu, B., Qian, D., Wang, Z. & Meng, Y. S. Recent progress in cathode materials research for advanced lithium ion batteries. *Mater. Sci. Eng. R Reports* **73**, 51–65 (2012).
35. Padhi, A. K., Nanjundaswamy, K. S. & Goodenough, J. B. Phospho-olivines as Positive-Electrode Materials for Rechargeable Lithium Batteries. *J. Electrochem. Soc.* **144**, 1188–1194 (1997).
36. Yamada, A., Chung, S. C. & Hinokuma, K. Optimized  $\text{LiFePO}_4$  for Lithium Battery Cathodes. *J. Electrochem. Soc.* **148**, A224 (2001).
37. Delacourt, C., Poizot, P., Levasseur, S. & Masquelier, C. Size Effects on Carbon-Free  $\text{LiFePO}_4$  Powders. *Electrochem. Solid-State Lett.* **9**, A352 (2006).
38. Chen, Z. & Dahn, J. R. Reducing Carbon in  $\text{LiFePO}_4/\text{C}$  Composite Electrodes to Maximize Specific Energy, Volumetric Energy, and Tap Density. *J. Electrochem. Soc.* **149**, A1184 (2002).
39. Ni, J. F., Zhou, H. H., Chen, J. T. & Zhang, X. X.  $\text{LiFePO}_4$  doped with ions prepared by co-precipitation method. *Mater. Lett.* **59**, 2361–2365 (2005).
40. Delacourt, C. *et al.* Toward Understanding of Electrical Limitations (Electronic, Ionic) in  $\text{LiMPO}_4$  ( $\text{M}=\text{Fe}, \text{Mn}$ ) Electrode Materials. *J. Electrochem. Soc.* **152**, A913 (2005).
41. Yonemura, M., Yamada, A., Takei, Y., Sonoyama, N. & Kanno, R. Comparative Kinetic Study of Olivine  $\text{Li}_x\text{MPO}_4$  ( $\text{M}=\text{Fe}, \text{Mn}$ ). *J. Electrochem. Soc.* **151**, A1352 (2004).

42. Wolfenstine, J. & Allen, J. LiNiPO<sub>4</sub>–LiCoPO<sub>4</sub> solid solutions as cathodes. *J. Power Sources* **136**, 150–153 (2004).
43. Okada, S. *et al.* Cathode properties of phospho-olivine LiMPO<sub>4</sub> for lithium secondary batteries. *J. Power Sources* **97–98**, 430–432 (2001).
44. Goodenough, J. B. & Kim, Y. Challenges for rechargeable Li batteries. *Chem. Mater.* **22**, 587–603 (2010).
45. Xu, K. Nonaqueous liquid electrolytes for lithium-based rechargeable batteries. *Chem. Rev.* **104**, 4303–4417 (2004).
46. Armand, M., Endres, F., MacFarlane, D. R., Ohno, H. & Scrosati, B. Ionic-liquid materials for the electrochemical challenges of the future. *Nat. Mater.* **8**, 621–629 (2009).
47. Agrawal, R. C. & Pandey, G. P. Solid polymer electrolytes: materials designing and all-solid-state battery applications: an overview. *J. Phys. D. Appl. Phys.* **41**, 223001 (2008).
48. Fergus, J. W. Ceramic and polymeric solid electrolytes for lithium-ion batteries. *J. Power Sources* **195**, 4554–4569 (2010).
49. Stassen, I. & Hambitzer, G. Metallic lithium batteries for high power applications. *J. Power Sources* **105**, 145–150 (2002).
50. Balbuena, P. B., Wang, Y. Lithium-ion Batteries: Solid-Electrolyte Interphase. *Imperial College Press* (2004).
51. Verma, P., Maire, P. & Novák, P. A review of the features and analyses of the solid electrolyte interphase in Li-ion batteries. *Electrochim. Acta* **55**, 6332–6341 (2010).
52. Edström, K., Herstedt, M. & Abraham, D. P. A new look at the solid electrolyte interphase on graphite anodes in Li-ion batteries. *J. Power Sources* **153**, 380–384 (2006).
53. Zhu, Y., He, X. & Mo, Y. Origin of Outstanding Stability in the Lithium Solid Electrolyte Materials: Insights from Thermodynamic Analyses Based on First-Principles Calculations. *ACS Appl. Mater. Interfaces* **7**, 23685–23693 (2015).
54. Aurbach, D., Markovsky, B., Weissman, I., Levi, E. & Ein-Eli, Y. On the correlation between surface chemistry and performance of graphite negative electrodes for Li ion batteries. *Electrochim. Acta* **45**, 67–86 (1999).
55. Chung, G.-C. *et al.* Origin of Graphite Exfoliation An Investigation of the Important Role of

- Solvent Cointercalation. *J. Electrochem. Soc.* **147**, 4391 (2000).
56. Zhang, S. S. A review on the separators of liquid electrolyte Li-ion batteries. *J. Power Sources* **164**, 351–364 (2007).
  57. Lissy, N. & Mills, G. Patent US 5,516,962 (1996).
  58. Arora, P. & Zhang, Z. Battery separators. *Chem. Rev.* **104**, 4419–4462 (2004).
  59. Myung, S.-T., Hitoshi, Y. & Sun, Y.-K. Electrochemical behavior and passivation of current collectors in lithium-ion batteries. *J. Mater. Chem.* **21**, 9891 (2011).
  60. Yao, M. *et al.* LiFePO<sub>4</sub>-based electrode using micro-porous current collector for high power lithium ion battery. *J. Power Sources* **173**, 545–549 (2007).
  61. Yang, C. *et al.* Nickel foam supported Sn–Co alloy film as anode for lithium ion batteries. *J. Power Sources* **196**, 10673–10678 (2011).
  62. Kinoshita, K. Carbon: Electrochemical and Physicochemical Properties. *Wiley* (1988).
  63. Fransson, L., Eriksson, T., Edström, K., Gustafsson, T. & Thomas, J. O. Influence of carbon black and binder on Li-ion batteries. *J. Power Sources* **101**, 1–9 (2001).
  64. Li, J. *et al.* Investigations on cellulose-based high voltage composite cathodes for lithium ion batteries. *J. Power Sources* **196**, 7687–7691 (2011).
  65. Senda, H. Sodium Carboxymethyl Cellulose. *J. Synth. Org. Chem. Japan* **43**, 382–383 (1985).
  66. Lestriez, B., Bahri, S., Sandu, I., Roué, L. & Guyomard, D. On the binding mechanism of CMC in Si negative electrodes for Li-ion batteries. *Electrochem. commun.* **9**, 2801–2806 (2007).
  67. Blomgren, G. E. Liquid electrolytes for lithium and lithium-ion batteries. *J. Power Sources* **119**, 326–329 (2003).
  68. Zhang, S. S. A review on electrolyte additives for lithium-ion batteries. *J. Power Sources* **162**, 1379–1394 (2006).
  69. Aurbach, D. *et al.* On the use of vinylene carbonate (VC) as an additive to electrolyte solutions for Li-ion batteries. *Electrochim. Acta* **47**, 1423–1439 (2002).
  70. Zhang, S. S., Xu, K. & Jow, T. R. Tris(2,2,2-trifluoroethyl) phosphite as a co-solvent for

- nonflammable electrolytes in Li-ion batteries. *J. Power Sources* **113**, 166–172 (2003).
71. Herstedt, M., Rensmo, H., Siegbahn, H. & Edström, K. Electrolyte additives for enhanced thermal stability of the graphite anode interface in a Li-ion battery. *Electrochim. Acta* **49**, 2351–2359 (2004).
  72. El Ouatani, L. *et al.* The Effect of Vinylene Carbonate Additive on Surface Film Formation on Both Electrodes in Li-Ion Batteries. *J. Electrochem. Soc.* **156**, A103 (2009).
  73. Qian, J. *et al.* High rate and stable cycling of lithium metal anode. *Nat. Commun.* **6**, 6362 (2015).
  74. Li, H., Wang, Z., Chen, L. & Huang, X. Research on advanced materials for Li-ion batteries. *Adv. Mater.* **21**, 4593–4607 (2009).
  75. carbon book.
  76. Kaskhedikar, N. A. & Maier, J. Lithium storage in carbon nanostructures. *Adv. Mater.* **21**, 2664–2680 (2009).
  77. Persson, K. *et al.* Lithium diffusion in graphitic carbon. *J. Phys. Chem. Lett.* **1**, 1176–1180 (2010).
  78. Shu, Z. X., Mcmillan, R. S. & Murray, J. J. Electrochemical Intercalation of Lithium into Graphite. *J. Electrochem. Soc.* **140**, 922 (1993).
  79. Qi, Y. & Harris, S. J. In Situ Observation of Strains during Lithiation of a Graphite Electrode. *J. Electrochem. Soc.* **157**, A741 (2010).
  80. Goriparti, S. *et al.* Review on recent progress of nanostructured anode materials for Li-ion batteries. *J. Power Sources* **257**, 421–443 (2014).
  81. Yang, J., Zhou, X., Li, J., Zou, Y. & Tang, J. Study of nano-porous hard carbons as anode materials for lithium ion batteries. *Mater. Chem. Phys.* **135**, 445–450 (2012).
  82. Fujimoto, H., Tokumitsu, K., Mabuchi, A., Chinnasamy, N. & Kasuh, T. The anode performance of the hard carbon for the lithium ion battery derived from the oxygen-containing aromatic precursors. *J. Power Sources* **195**, 7452–7456 (2010).
  83. Wang, J., Liu, J.-L., Wang, Y.-G., Wang, C.-X. & Xia, Y.-Y. Pitch modified hard carbons as negative materials for lithium-ion batteries. *Electrochim. Acta* **74**, 1–7 (2012).
  84. Meunier, V., Kephart, J., Roland, C. & Bernholc, J. *Ab Initio* Investigations of Lithium



- Diffusion in Carbon Nanotube Systems. *Phys. Rev. Lett.* **88**, 75506 (2002).
85. Schauerman, C. M. *et al.* Recycling single-wall carbon nanotube anodes from lithium ion batteries. *J. Mater. Chem.* **22**, 12008 (2012).
  86. Dileo, R. A. *et al.* Enhanced capacity and rate capability of carbon nanotube based anodes with titanium contacts for lithium ion batteries. *ACS Nano* **4**, 6121–6131 (2010).
  87. de las Casas, C. & Li, W. A review of application of carbon nanotubes for lithium ion battery anode material. *J. Power Sources* **208**, 74–85 (2012).
  88. Oktaviano, H. S., Yamada, K. & Waki, K. Nano-drilled multiwalled carbon nanotubes: characterizations and application for LIB anode materials. *J. Mater. Chem.* **22**, 25167 (2012).
  89. Huang, X., Qi, X., Boey, F. & Zhang, H. Graphene-based composites. *Chem. Soc. Rev.* **41**, 666–686 (2012).
  90. Hou, J., Shao, Y., Ellis, M. W., Moore, R. B. & Yi, B. Graphene-based electrochemical energy conversion and storage: fuel cells, supercapacitors and lithium ion batteries. *Phys. Chem. Chem. Phys.* **13**, 15384 (2011).
  91. Liang, M. & Zhi, L. Graphene-based electrode materials for rechargeable lithium batteries. *J. Mater. Chem.* **19**, 5871 (2009).
  92. Pan, D. *et al.* Li storage properties of disordered graphene nanosheets. *Chem. Mater.* **21**, 3136–3142 (2009).
  93. Hwang, H. J. *et al.* Multilayer Graphynes for Lithium Ion Battery Anode. *J. Phys. Chem. C.* **17**, 6919-6923 (2013).
  94. Lian, P. *et al.* Large reversible capacity of high quality graphene sheets as an anode material for lithium-ion batteries. *Electrochim. Acta* **55**, 3909–3914 (2010).
  95. Wang, Z.-L., Xu, D., Wang, H.-G., Wu, Z. & Zhang, X.-B. In Situ Fabrication of Porous Graphene Electrodes for High-Performance Energy Storage. *ACS Nano* **7**, 2422–2430 (2013).
  96. Raccichini, R., Varzi, A., Passerini, S. & Scrosati, B. The role of graphene for electrochemical energy storage. *Nat. Mater.* **14**, 271–279 (2014).
  97. Xia, H., Zhu, D., Fu, Y. & Wang, X. CoFe<sub>2</sub>O<sub>4</sub>-graphene nanocomposite as a high-capacity anode material for lithium-ion batteries. *Electrochim. Acta* **83**, 166–174 (2012).

98. Li, X. *et al.* A nanocomposite of graphene/MnO<sub>2</sub> nanoplatelets for high-capacity lithium storage. *J. Appl. Electrochem.* **42**, 1065–1070 (2012).
99. Pham, V. H. *et al.* Liquid phase co-exfoliated MoS<sub>2</sub>–graphene composites as anode materials for lithium ion batteries. *J. Power Sources* **244**, 280–286 (2013).
100. Lee, W. W. & Lee, J.-M. Novel synthesis of high performance anode materials for lithium-ion batteries (LIBs). *J. Mater. Chem. A* **2**, 1589–1626 (2014).
101. Zhou, X., Yin, Y.-X., Wan, L.-J. & Guo, Y.-G. Facile synthesis of silicon nanoparticles inserted into graphene sheets as improved anode materials for lithium-ion batteries. *Chem. Commun.* **48**, 2198 (2012).
102. Chen, J. S. & Lou, X. W. SnO<sub>2</sub>-based nanomaterials: Synthesis and application in lithium-ion batteries. *Small* **9**, 1877–1893 (2013).
103. Wu, Z.-S. *et al.* Graphene/metal oxide composite electrode materials for energy storage. *Nano Energy* **1**, 107–131 (2012).
104. Sun, X. *et al.* Structure and electrochemical properties of spinel Li<sub>4</sub>Ti<sub>5</sub>O<sub>12</sub> nanocomposites as anode for lithium-ion battery. *Int. J. Electrochem. Sci.* **9**, 1583–1596 (2014).
105. Yang, Z. *et al.* Nanostructures and lithium electrochemical reactivity of lithium titanites and titanium oxides: A review. *J. Power Sources* **192**, 588–598 (2009).
106. Scharner, S. Evidence of Two-Phase Formation upon Lithium Insertion into the Li<sub>1.33</sub>Ti<sub>1.67</sub>O<sub>4</sub> Spinel. *J. Electrochem. Soc.* **146**, 857 (1999).
107. Colin, J.-F., Godbole, V. & Novák, P. In situ neutron diffraction study of Li insertion in Li<sub>4</sub>Ti<sub>5</sub>O<sub>12</sub>. *Electrochem. commun.* **12**, 804–807 (2010).
108. Pérez-Flores, J. C., Kuhn, A. & García-Alvarado, F. A Structural and Electrochemical Study of Li<sub>2</sub>Ti<sub>6</sub>O<sub>13</sub>. *MRS Proc.* **1313**, mrsf10-1313-kk05-09 (2011).
109. de Dompablo, M. E. A. y, Morán, E., Várez, A. & García-Alvarado, F. Electrochemical lithium intercalation in Li<sub>2</sub>Ti<sub>3</sub>O<sub>7</sub>-ramsdellite structure. *Mater. Res. Bull.* **32**, 993–1001 (1997).
110. Dey, a. N. Electrochemical Alloying of Lithium in Organic Electrolytes. *J. Electrochem. Soc.* **118**, 1547 (1971).
111. Park, C.-M., Kim, J.-H., Kim, H. & Sohn, H.-J. Li-alloy based anode materials for Li

- secondary batteries. *Chem. Soc. Rev.* **39**, 3115 (2010).
112. Obrovac, M. N. & Chevrier, V. L. Alloy Negative Electrodes for Li-Ion Batteries. *Chem. Rev.* **114**, 11444–11502 (2014).
  113. Zhang, W. J. A review of the electrochemical performance of alloy anodes for lithium-ion batteries. *J. Power Sources* **196**, 13–24 (2011).
  114. Larcher, D. *et al.* Recent findings and prospects in the field of pure metals as negative electrodes for Li-ion batteries. *J. Mater. Chem.* **17**, 3759 (2007).
  115. Chen, Z., Christensen, L. & Dahn, J. R. Large-volume-change electrodes for Li-ion batteries of amorphous alloy particles held by elastomeric tethers. *Electrochem. commun.* **5**, 919–923 (2003).
  116. Wu, H. & Cui, Y. Designing nanostructured Si anodes for high energy lithium ion batteries. *Nano Today* **7**, 414–429 (2012).
  117. Okamoto, H. Desk Handbook Phase Diagrams for Binary Alloys. *ASM International* (2000).
  118. Kim, H., Park, B., Sohn, H. J. & Kang, T. Electrochemical characteristics of Mg-Ni alloys as anode materials for secondary Li batteries. *J. Power Sources* **90**, 59–63 (2000).
  119. Cabana, J., Monconduit, L., Larcher, D. & Palacín, M. R. Beyond intercalation-based Li-ion batteries: The state of the art and challenges of electrode materials reacting through conversion reactions. *Adv. Mater.* **22**, 170–192 (2010).
  120. Palacín, M. R. Recent advances in rechargeable battery materials: a chemist's perspective. *Chem. Soc. Rev.* **38**, 2565 (2009).
  121. Tarascon, J., Poizot, P., Laruelle, S., Grugeon, S. & Dupont, L. Nano-sized transition-metal oxides as negative-electrode materials for lithium-ion batteries. *Nature* **407**, 496–499 (2000).
  122. Reddy, M. V., Subba Rao, G. V & Chowdari, B. V. Metal oxides and oxysalts as anode materials for Li ion batteries. *Chem Rev* **113**, 5364–5457 (2013).
  123. Croguennec, L. & Palacin, M. R. Recent achievements on inorganic electrode materials for lithium-ion batteries. *J. Am. Chem. Soc.* **137**, 3140–3156 (2015).
  124. Wu, H. Bin, Chen, J. S., Hng, H. H. & Wen (David) Lou, X. Nanostructured metal oxide-based materials as advanced anodes for lithium-ion batteries. *Nanoscale* **4**, 2526 (2012).
  125. Oumellal, Y., Rougier, A., Nazri, G. A., Tarascon, J.-M. & Aymard, L. Metal hydrides for

- lithium-ion batteries. *Nat. Mater.* **7**, 916–921 (2008).
126. Oumellal, Y. *et al.* Reactivity of TiH<sub>2</sub> hydride with lithium ion: Evidence for a new conversion mechanism. *Int. J. Hydrogen Energy* **37**, 7831–7835 (2012).
  127. Teprovich, J. A. *et al.* Li-driven electrochemical conversion reaction of AlH<sub>3</sub>, LiAlH<sub>4</sub>, and NaAlH<sub>4</sub>. *J. Phys. Chem. C* **119**, 4666–4674 (2015).
  128. Bououdina, M. *et al.* Lithium storage in amorphous TiNi hydride: Electrode for rechargeable lithium-ion batteries. *Mater. Chem. Phys.* **141**, 348–354 (2013).
  129. Zaïdi, W. *et al.* Reactivity of complex hydrides Mg<sub>2</sub>FeH<sub>6</sub>, Mg<sub>2</sub>CoH<sub>5</sub> and Mg<sub>2</sub>NiH<sub>4</sub> with lithium ion: Far from equilibrium electrochemically driven conversion reactions. *Int. J. Hydrogen Energy* **38**, 4798–4808 (2013).
  130. Silvestri, L. *et al.* Reactivity of Sodium Alanates in Lithium Batteries. *J. Phys. Chem. C* **119**, 28766–28775 (2015).
  131. Silvestri, L. *et al.* Lithium Alanates as Negative Electrodes in Lithium-Ion Batteries. *ChemElectroChem* **2**, 877–886 (2015).
  132. Sartori, S., Cuevas, F. & Latroche, M. Metal hydrides used as negative electrode materials for Li-ion batteries. *Appl. Phys. A* **122**, 135 (2016).
  133. Manchester, F.D. Phase Diagrams of Binary Hydrogen Alloys. *ASM International* (2000).
  134. Meggiolaro, D. *et al.* Origin of the Voltage Hysteresis of MgH<sub>2</sub> Electrodes in Lithium Batteries. *J. Phys. Chem. C* **119**, 17044–17052 (2015).
  135. Aymard, L., Oumellal, Y. & Bonnet, J. P. Metal hydrides: An innovative and challenging conversion reaction anode for lithium-ion batteries. *Beilstein J. Nanotechnol.* **6**, 1821–1839 (2015).
  136. Oumellal, Y. *Réactivité électrochimique des hydrures métalliques vis-à-vis du lithium: Electrodes negatives pour batteries Li-ion: Stockage de l'hydrogène par voie solide-gaz.* Ph.D. Thesis, Université de Picardie, Jules Verne (2009).
  137. Brutti, S., Mulas, G., Piciollo, E., Panero, S. & Reale, P. Magnesium hydride as a high capacity negative electrode for lithium ion batteries. *J. Mater. Chem.* **22**, 14531 (2012).
  138. Meggiolaro, D., Gigli, G., Paolone, A., Vitucci, F. & Brutti, S. Incorporation of lithium by MgH<sub>2</sub>: An ab initio study. *J. Phys. Chem. C* **117**, 22467–22477 (2013).

139. Oumellal, Y. *et al.* Bottom-up preparation of MgH<sub>2</sub> nanoparticles with enhanced cycle life stability during electrochemical conversion in Li-ion batteries. *Nanoscale* **6**, 14459–14466 (2014).
140. Zaïdi, W. *et al.* Carboxymethylcellulose and carboxymethylcellulose-formate as binders in MgH<sub>2</sub>-carbon composites negative electrode for lithium-ion batteries. *J. Power Sources* **196**, 2854–2857 (2011).
141. Ikeda, S. *et al.* Anode properties of magnesium hydride catalyzed with niobium oxide for an all solid-state lithium-ion battery. *Chem Commun* **49**, 7174–7176 (2013).
142. Ikeda, S. *et al.* Anode properties of Al<sub>2</sub>O<sub>3</sub>-added MgH<sub>2</sub> for all-solid-state lithium-ion batteries. *J. Solid State Electrochem.* **19**, 3639–3644 (2015).
143. Zeng, L. *et al.* Metal hydride-based materials towards high performance negative electrodes for all-solid-state lithium-ion batteries. *Chem. Commun.* **51**, 9773–9776 (2015).
144. Zeng, L., Ichikawa, T., Kawahito, K., Miyaoka, H. & Kojima, Y. Bulk-Type all-solid-state lithium-ion batteries: Remarkable performances of a carbon nanofiber-supported MgH<sub>2</sub> composite electrode. *ACS Appl. Mater. Interfaces* **9**, 2261–2266 (2017).
145. Matsuo, M. & Orimo, S. I. Lithium fast-ionic conduction in complex hydrides: Review and prospects. *Adv. Energy Mater.* **1**, 161–172 (2011).
146. Matsuo, M. *et al.* Complex hydrides with (BH<sub>4</sub>)<sup>-</sup> and (NH<sub>2</sub>)<sup>-</sup> anions as new lithium fast-ion conductors. *J. Am. Chem. Soc.* **131**, 16389–16391 (2009).
147. Maekawa, H. *et al.* Halide-stabilized LiBH<sub>4</sub>, a room-temperature lithium fast-ion conductor. *J. Am. Chem. Soc.* **131**, 894–895 (2009).
148. Oguchi, H. *et al.* Lithium-ion conduction in complex hydrides LiAlH<sub>4</sub> and Li<sub>3</sub>AlH<sub>6</sub>. *J. Appl. Phys.* **107**, 4–7 (2010).
149. Ito, M. *et al.* Electrical and thermal properties of titanium hydrides. *J. Alloys Compd.* **420**, 25–28 (2006).
150. Vitucci, F. M. *et al.* H<sub>2</sub> thermal desorption and hydride conversion reactions in Li cells of TiH<sub>2</sub>/C amorphous nanocomposites. *J. Alloys Compd.* **645**, S46–S50 (2015).
151. Oumellal, Y., Rougier, A., Tarascon, J. M. & Aymard, L. 2LiH + M (M = Mg, Ti): New concept of negative electrode for rechargeable lithium-ion batteries. *J. Power Sources* **192**,

698–702 (2009).

152. Kawahito, K., Zeng, L., Ichikawa, T., Miyaoka, H. & Kojima, Y. Electrochemical Performance of Titanium Hydride for Bulk-Type All-Solid-State Lithium-Ion Batteries. *Mater. Trans.* **57**, 755–757 (2016).
153. Huang, L., Aymard, L. & Bonnet, J.-P. MgH<sub>2</sub>–TiH<sub>2</sub> mixture as an anode for lithium-ion batteries: synergic enhancement of the conversion electrode electrochemical performance. *J. Mater. Chem. A* **3**, 15091–15096 (2015).
154. Song, Y., Guo, Z. X. & Yang, R. Influence of titanium on the hydrogen storage characteristics of magnesium hydride: A first principles investigation. *Mater. Sci. Eng. A* **365**, 73–79 (2004).
155. Cuevas, F., Korablov, D. & Latroche, M. Synthesis, structural and hydrogenation properties of Mg-rich MgH<sub>2</sub>–TiH<sub>2</sub> nanocomposites prepared by reactive ball milling under hydrogen gas. *Phys. Chem. Chem. Phys.* **14**, 1200–1211 (2012).
156. Ponthieu, M. *et al.* Structural properties and reversible deuterium loading of MgD<sub>2</sub>-TiD<sub>2</sub> nanocomposites. *Journal of Physical Chemistry C* **117**, 18851–18862 (2013).



# **CHAPTER 2**

Experimental techniques





# Content

<b>1</b>	<b>Materials preparation</b>	<b>55</b>
1.1	Reactive ball milling	55
1.2	Plasma-assisted sputtering	57
<b>2</b>	<b>Structural and Chemical characterization</b>	<b>58</b>
2.1	X-ray powder diffraction	58
2.1.1	Diffraction analysis: the Rietveld method	59
2.2	Transmission electron microscopy	63
2.3	Focused ion beam	65
2.4	Scanning electron microscopy	66
<b>3</b>	<b>Electrochemical analyses</b>	<b>67</b>
3.1	Galvanostatic cycling	67
3.2	Cyclic voltammetry	69
3.3	Electrochemical impedance spectroscopy	70
<b>4</b>	<b>Electrode formulation</b>	<b>72</b>
4.1	MgH <sub>2</sub> thin film electrode	72
4.2	MgH <sub>2</sub> +TiH <sub>2</sub> nanocomposite electrode and formulation optimization	73
4.2.1	Half-cell with liquid electrolyte	73
4.2.2	Half-cells with LiBH <sub>4</sub> as solid electrolyte	74
4.2.3	Complete solid-state metal hydride-sulphur Li-ion battery	75
	<b>References</b>	<b>77</b>



In this chapter, we describe the techniques that have been used to prepare and characterize the materials throughout this thesis. First, the synthesis of the composites and thin films used as active materials, as well as the nanoconfined solid electrolyte, will be presented, then we will describe the techniques employed to characterize their structural, microstructural, chemical, and electrochemical properties.

## 1 Materials preparation

### 1.1 Reactive ball milling

Different  $\text{MgH}_2+\text{TiH}_2$  nanocomposites have been prepared in this work by reactive ball milling (RBM) of elemental Mg and Ti powders. This technique, schematically reported in Figure 2.1, allows the formation of fine hydride powders at room temperature [1]. The mechanical grinding induces the formation of fresh surfaces available for the absorption of hydrogen. Moreover, the highly energetic impacts permit a homogeneous mixing of the solid constituents at the nanoscale.

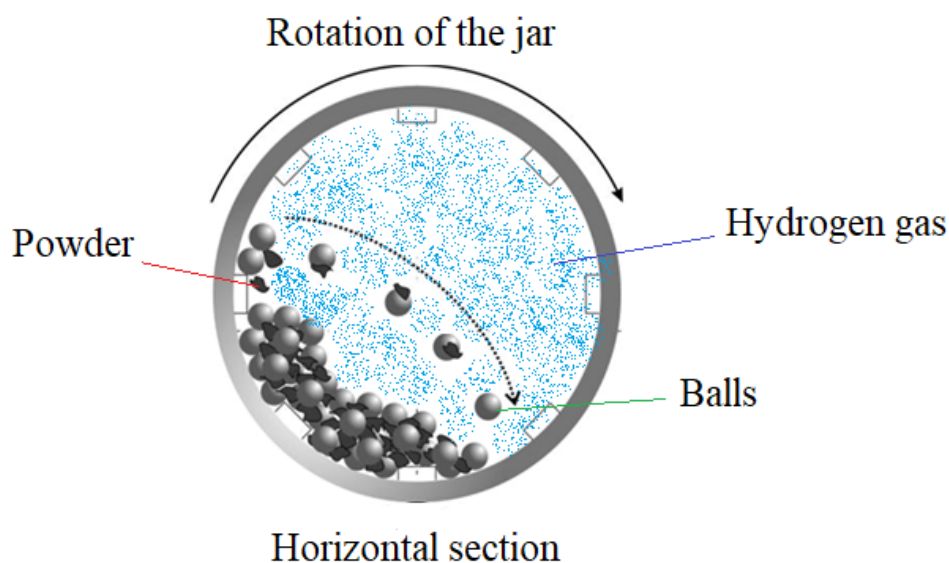


**Figure 2.1.** Motions of the balls and the powder inside a jar during ball milling under hydrogen atmosphere.

Reactive ball milling experiments under hydrogen pressure have been performed in a planetary Fritsch Pulverisette 4 using a high-pressure vial commercialized by Evicomagnetics [2] (Figure 2.2a and 2.2b respectively). This vial is equipped with sensors for monitoring both pressure and temperature during the synthesis.

To evaluate the uptake of hydrogen with high accuracy, an experimental method which considers the real gas behaviour of hydrogen is used [3].

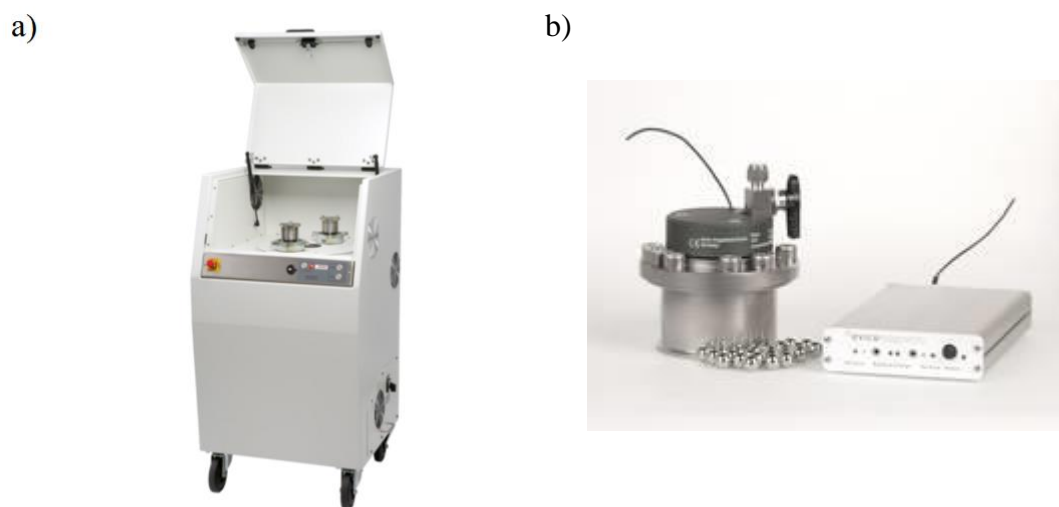


**Figure 2.2.** a) Planetary ball mill Fritsch Pulverisette 4. b) Evicomagnetics milling vial and the telemetric receptor.

For each  $\text{MgH}_2+\text{TiH}_2$  nanocomposite, 5 g of Mg/Ti mixture and 40 stainless steel balls (diameter 12 mm) were placed in the milling vial inside the glove box. The balls to powder mass ratio was 60:1 in all experiments. Next, the vial was connected to a manometric hydrogenation apparatus, in order to remove the argon from the vial and introduce hydrogen at a pressure of 9 MPa (Alphagaz, 6N). The milling was carried out in two cycles of 120 minutes with 120 minutes of pause in between for cooling down the mill. A rotation speed of 400 rpm was chosen for the disk, and an opposite 800 rpm speed for the vial. Hydrogenation is completed during the first cycle, and the purpose of the second one is only for calibration of the temperature of hydrogen gas during milling. At the end of the synthesis, the remaining hydrogen gas was evacuated and the vial unloaded inside the glove box.

## 1.2 Plasma-assisted sputtering

The deposition of thin films was performed by Dr. Ana Lacoste from LPSC laboratory (Grenoble, France). Two different magnesium hydride thin films were prepared by reactive plasma-assisted microwave/radio frequency sputtering [4,5], namely  $\text{MgH}_2$ , and  $\text{MgH}_2$  covered with Al. In a chamber at low argon/hydrogen pressure (0.2 Pa for both gasses), plasma is created by means of multi-dipolar microwave couplers. Magnesium ions are produced from targets (99.99% Mg) and then accelerated applying a potential difference towards the copper substrates (squares of 6.7 cm side, with a thickness of  $\sim 16 \mu\text{m}$ ). During the process, the temperature of the substrate did not exceed  $55 \text{ }^\circ\text{C}$ , avoiding any thermal-driven reaction between the deposit material and the substrate.

For the covered thin films, after the formation of the hydride, a protective layer of Al ( $\sim 13 \text{ nm}$ ) was deposited on top of the films with the purpose of preventing contamination of  $\text{MgH}_2$  from moisture and air. The cross section thin film as prepared is illustrated in Figure 2.3 below. Two different layers are noticed in the cross section of the thin film. The top layer is  $\text{MgH}_2$  phase, which exhibits an average thickness around  $1 \mu\text{m}$ , and the bottom part is the Cu current collector. The copper foils possess a rough surface, hence the  $\text{MgH}_2$  film is not a flat layer. These Cu foils are used as current collectors in commercial Li-ion batteries (they have been provided by SAFT Co.), and this roughness allows a better attachment of the active material on the surface of the Cu, enhancing both the contacts between particles and the mechanical stability of the electrode.

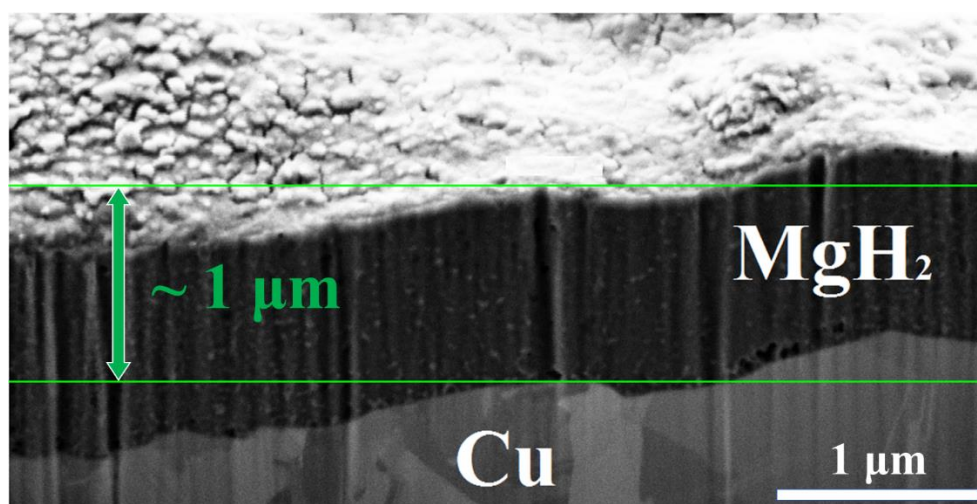


**Figure 2.3.** SEM image of the cross section of the  $\text{MgH}_2$  thin film as deposited. In green is reported the average thickness of the hydride deposited.

## 2 Structural and Chemical characterization

### 2.1 X-ray powder diffraction

The X-ray diffraction method (XRD) was used to investigate the structural properties of the electrode materials. A diffractometer produces waves at a known frequency (depend on the X-ray source) which interact with the electron cloud of the atoms of the sample [8]. From this interaction, scattered radiations will propagate in all directions. When the Bragg's law is fulfilled (Equation 2.1) a constructive interference occurs at particular angles. By measuring the intensity of these interactions within a range of angles, a diffraction pattern is observed.

$$n\lambda = 2d \sin\theta \quad (2.1)$$

Equation 2.1 describes the Bragg's law, where  $n$  is a positive integer,  $\lambda$  is the wavelength of the incident X-rays,  $d$  is the interplanar spacing between successive atomic planes in the crystal, and  $\theta$  is the angle between the incident wave and the atomic planes (Figure 2.4).

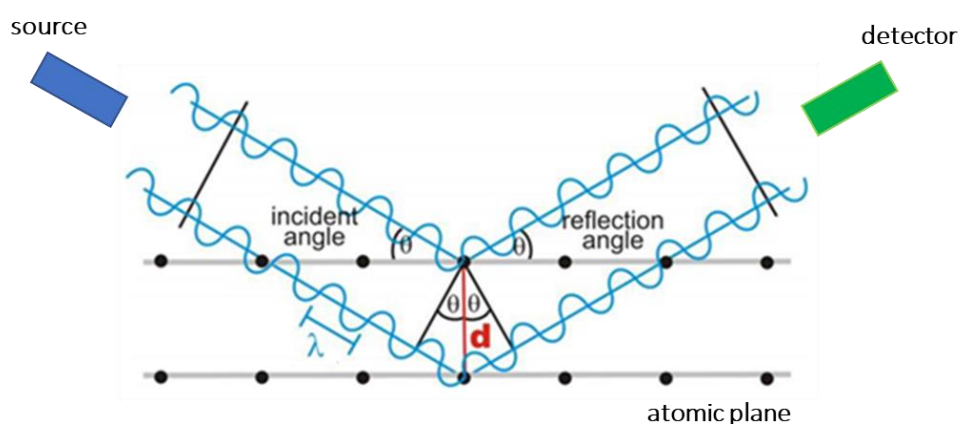


**Figure 2.4.** Incident radiation with wavelength  $\lambda$  interacts in a constructive way with atomic planes (atoms represented by black circles) of a sample at angle  $\theta$ , fulfilling the Bragg's law. The emergent radiation is acquired by the detector.

XRD analysis were performed on a Bruker D8 Advance in a  $\theta$ - $\theta$  Bragg-Brentano geometry, with a Cu- $K_{\alpha}$  radiation ( $\lambda_{K\alpha 1} = 1.54051 \text{ \AA}$ ,  $\lambda_{K\alpha 2} = 1.54433 \text{ \AA}$ ). In  $\theta$ - $\theta$  geometry, the sample is fixed while both the X-ray source and detector move symmetrically along the angles range chosen by the operator (Figure 2.5). Because of the reactivity of the hydrides

with air and moisture, a special air-tight sample-holder commercialized by Bruker was used for all the XRD analysis.

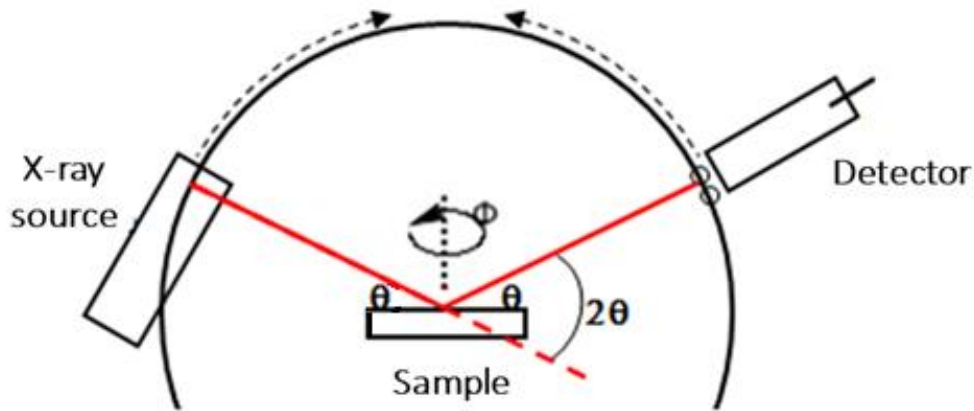


**Figure 2.5.** Schematic representation of the  $\theta$ - $\theta$  Bragg-Brentano geometry in Bruker D8. The sample spins on itself with a given speed ( $\phi$ ) in a stable position while source and detector move together with the same step.

### 2.1.1 Diffractogram analysis: the Rietveld method

The X-ray diffraction of powder samples results in a pattern characterized by reflections (peaks in intensity) at certain positions. The height, width and position of these reflections can be used to determine different aspects of the material, such as crystal structure, crystallites size, microstrain, and phase abundance. This method was developed by Hugo Rietveld in 1969 [9]. This method uses a least square approach to refine the structural parameters (lattice parameters, atomic positions, site occupancy, and Debye-Waller factors), the scale factor, the background signal and the shape factor of a theoretical diffractogram until it matches as much as possible to the experimental pattern [10]. This is done by minimizing the function  $M$ :

$$M = \sum_i w_i (y_{i,obs} - y_{i,calc})^2 \quad (2.2)$$

In Equation 2.2  $w_i$  is a statistical weight given by the inverse of the calculated intensity  $y_{i,calc}$ , and  $y_{i,obs}$  is the observed intensity at a given angular position  $i$ .



The intensity  $y_{i,calc}$  at a position  $i$  is calculated as the sum of all the Bragg peak contribution from the different phases and the background contribution in this point:

$$y_{i,calc} = y_{bi} + \sum_{\Phi} S_{\Phi} \sum_k j_{\Phi k} \cdot Lp_{\Phi k} \cdot |F_{\Phi k}|^2 \cdot \Omega_{i\Phi k} \quad (2.3)$$

Where  $y_{bi}$  is the background contribution,  $S_{\Phi}$  is the scale factor of the phase  $\Phi$ ,  $j_{\Phi k}$  is the multiplicity of the reflection  $k$ ,  $Lp_{\Phi k}$  is the Lorentz-polarization factor,  $F_{\Phi k}$  is the structure factor of the reflection  $k$ , and  $\Omega_{i\Phi k}$  is the profile shape function.

The first summation is related to all the crystalline phases  $\Phi$  present in the sample, and the second one concerns all the reflections  $k$  contributing to point  $i$ .

The structure factor  $F_{\Phi k}$  relates the intensity of the reflection  $k$  to the atomic arrangement of the diffraction structure:

$$F_{\Phi k} = \sum_{j=1}^n f_j \cdot \exp(i2\pi \cdot \vec{k} \cdot \vec{r}_j) \cdot \exp\left(-B_j \cdot \sin^2\left(\frac{\theta}{\lambda^2}\right)\right) \quad (2.4)$$

Where  $f_j$  is the form factor of atom  $j$ ,  $\vec{k}$  is the direction of the diffraction,  $\vec{r}_j$  is the position of atom  $j$ , and  $B_j$  is the Debye-Waller factor for atom  $j$ . This latter factor is associated with the thermal vibration of an atom around its crystallographic position, and in case of isotropic vibration it can be written as:

$$B = 8\pi^2 \cdot U_{iso} \quad (2.5)$$

With  $U_{iso}$  as average quadratic amplitude of the vibration.

All patterns were refined here using a function called ‘‘Thomas-Cox-Hastings pseudo-Voigt’’ [11], which considers the peak profile  $\Omega_{i\Phi k}$  as a weighted sum of a Gaussian and Lorentzian functions:

$$\Omega = \eta L + (1 - \eta) G \quad (2.6)$$

Where  $\eta$  is the balance between the L and G components.

The full-width at half maximum (FWHM) of the Gaussian and Lorentzian components is given respectively as:

$$H_G = (U \tan^2\theta + V \tan\theta + W)^2 \quad (2.7)$$

$$H_L = X \tan\theta + Y \cos\theta \quad (2.8)$$

The parameter  $U$  is largely affected by peak broadening induced by microstrains in the sample, while  $Y$  depends on the crystallite size. On the other hand, parameters  $V$ ,  $W$  and  $X$  are related to the contribution of the diffractometer. Because only  $U$  and  $Y$  are correlated to the sample characteristics, from their refinement it is possible to determinate the microstrain and crystallite size in the material analysed.

The microstrain is obtained from the Gaussian contribution to the peak broadening by the following equation:

$$\varepsilon = \frac{\pi^{3/2}}{1.8 \cdot 8\sqrt{\ln 2}} \cdot \sqrt{U - U_0} \quad (2.9)$$

With  $\varepsilon$  as the average microstrain in percentage, and  $U_0$  as the instrumental contribution to the Gaussian component.

The estimation of the crystallite size is determined from the Lorentzian broadening contribution and the Scherrer equation:

$$D = \frac{360}{\pi^2} \cdot \frac{\lambda}{Y - Y_0} \quad (2.10)$$

Where  $D$  is the diameter in angstrom ( $\text{\AA}$ ) of the crystallite considered isotropic,  $\lambda$  is the wavelength in  $\text{\AA}$  and  $Y_0$  is the instrumental contribution to the Lorentzian component in degrees.

To evaluate the validity of a diffraction profile refinement several reliability factors are calculated. These factors measure the agreement between the experimental pattern and the calculated one. The Bragg factor ( $R_B$ ) assesses the validity of the refinement for a given phase:

$$R_B = 100 \cdot \frac{\sum_k |I_{k,obs} - I_{k,calc}|}{\sum_k |I_{k,obs}|} \quad (2.11)$$

With  $I_k = j_k \cdot F_k^2$ .

The profile factor  $R_p$  and the weighted profile factor  $R_{wp}$  characterize the quality of the global refinement:

$$R_p = 100 \cdot \frac{\sum_i |y_{i,obs} - y_{i,calc}|}{\sum_k |y_{i,obs}|} \quad (2.12)$$

$$R_{wp} = 100 \cdot \left( \frac{\sum_i w_i (y_{i,obs} - y_{i,calc})^2}{\sum_i w_i (y_{i,obs})^2} \right)^{1/2} \quad (2.13)$$

The expected weighted profile factor ( $R_{exp}$ ) reflects the statistical quality of the data:

$$R_{exp} = 100 \cdot \left( \frac{n - p + c}{\sum_i w_i (y_{i,obs})^2} \right)^{1/2} \quad (2.14)$$

Where  $n$  is the number of points used in the refinement,  $p$  is the number of refined parameters and  $c$  is the number of constraints.

Finally, the goodness of the fit is expressed by the reduced chi-square parameter  $\chi$ :

$$\chi^2 = \left( \frac{R_{wp}}{R_{exp}} \right)^2 \quad (2.15)$$

This statistical parameter should be as close as possible to 1.

The X-ray diffraction patterns were analysed using Rietveld method with the Fullprof Suite software [12].

## 2.2 Transmission electron microscopy

In a transmission electron microscope (TEM), a high energy beam of electrons (from 100 keV to 1 MeV) is shone through a very thin sample (generally < 200 nm), and the interactions between the electrons and the atoms is used to obtain information on structures, defects, interfaces, grain boundaries, *etc.* with atomic scale resolution [13]. The electrons generated by a field emission gun are focused into a small, thin, coherent beam by the use of the condenser lenses. This beam is restricted by a condenser aperture, which excludes high angle electrons. The beam then strikes the specimen and parts of it is transmitted and focused by the objective lens into a fluorescent screen, creating an image on a couple device camera (CCD). Figure 2.6 shows the column structure of a TEM equipment.

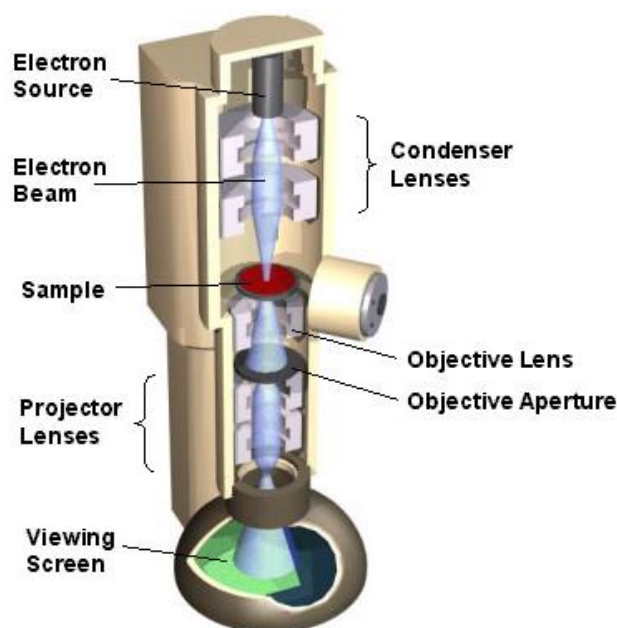


**Figure 2.6.** Schematic cross section displaying the typical layout of optical components in the TEM.

Two different samples were investigated by TEM: powder hydrides and MgH<sub>2</sub> thin films.

Powder metal hydrides were investigated in a 200 kV FEI Tecnai F20 microscope. The samples were dispersed in dimethyl carbonate, with the purpose of preventing air contamination. A few drops of this solution were placed on a sample-holder made by a carbon grid, and immediately transferred inside the microscope. Once in the TEM, the organic solvent was removed by applying high vacuum.

In the case of MgH<sub>2</sub> thin films, their thickness (> 15 μm) did not allow their investigation without a proper preparation. As described in paragraph 2.3, suitable samples for microscope analysis were prepared by means of focused ion beam (FIB). Because of their small size and reactivity under the electron beam, a sample-holder cooled with liquid nitrogen was used for their investigation at 200 kV in a Philips CM200 microscope.

To acquire information about the different structures in the samples techniques such as bright field (BF), dark field (DF), and electron diffraction (ED) were employed, whereas high angle annular dark field (HAADF) was used to map the spatial distribution of the phases.

### 2.3 Focused ion beam

In a focused ion beam (FIB) equipment, a beam of ions is used to shape a sample via sputtering process [14]. The milling action of the ions can be controlled at nanometre precision, removing unwanted material and shaping the substrate as required. It is generally coupled with a scanning electron microscope, which allows a visual control during the preparation. The preparation of lamellas from  $\text{MgH}_2$  thin films, and the subsequent TEM analysis, were performed by Efi Hadjixenophontos (ITN ECOSTORE fellow) in Stuttgart University (Germany) using a SCIOS-FEI dual beam FIB/SEM equipment.

The main steps of the sample preparation are shown in Figure 2.7. Prior to the cross sectioning, a layer of  $\sim 2 \mu\text{m}$  of platinum was deposited on top of the thin film to protect the area of interest from the Ga-ion beam. Next, the thin film is excavated around the selected area, creating a thin lamella. The width of the lamella, *i.e.* the thickness through which TEM radiation should pass perpendicularly to the cross section, is less than 100 nm. Finally, the lamella is removed from the thin film and placed in a sample-holder to be stored in a glovebox.

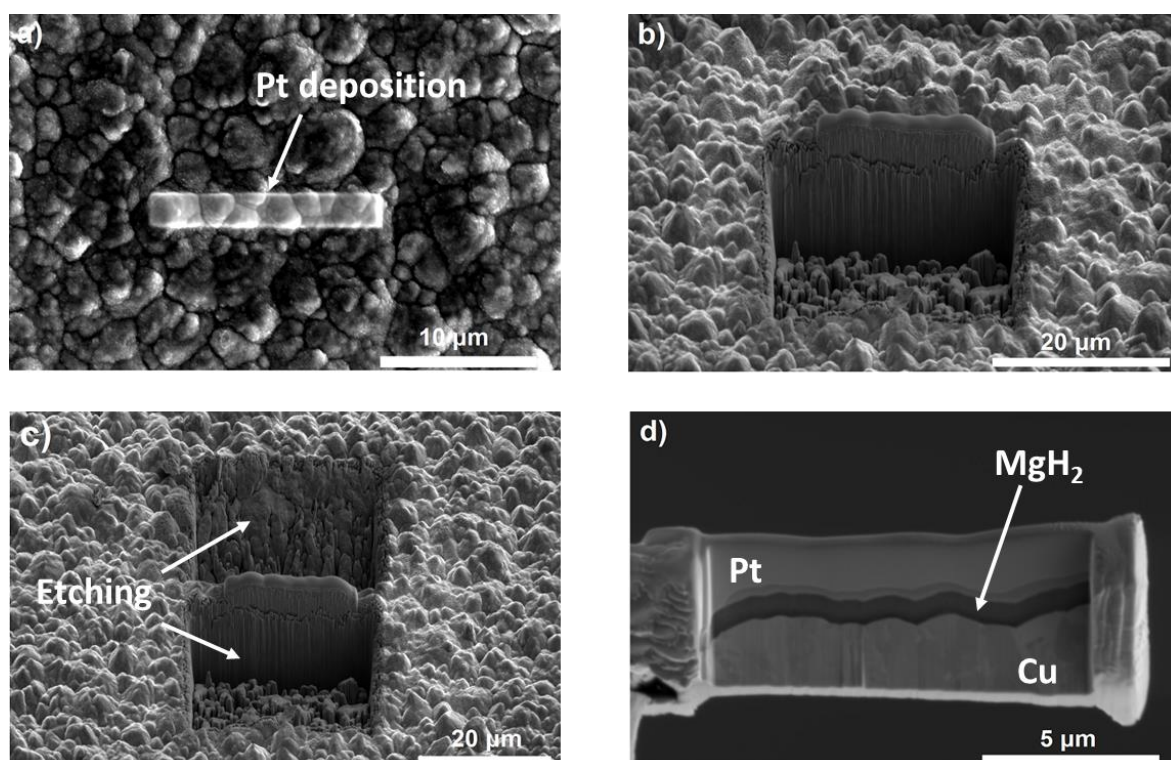


**Figure 2.7.** SEM images during the preparation of a lamella. a) Deposition of Pt on the selected area. b) and c) Removal of material around the lamella. d) Obtained lamella.

## 2.4 Scanning electron microscopy

The scanning electron microscope (SEM) uses a focused beam of high energy electrons (from 0.3 to 30 keV) to create a variety of signals at the surface of a solid specimen [15]. A schematic illustration of these interactions is reported in Figure 2.8. These signals come from the interactions between the electrons of the beam and the atoms of the sample at different depths, and they contain information about morphology and composition of the specimen. The size of the interaction volume depends on the electron energy, the atomic number of the sample and its density. The electrons (and electromagnetic radiations) emitted are detected by specialized detectors.

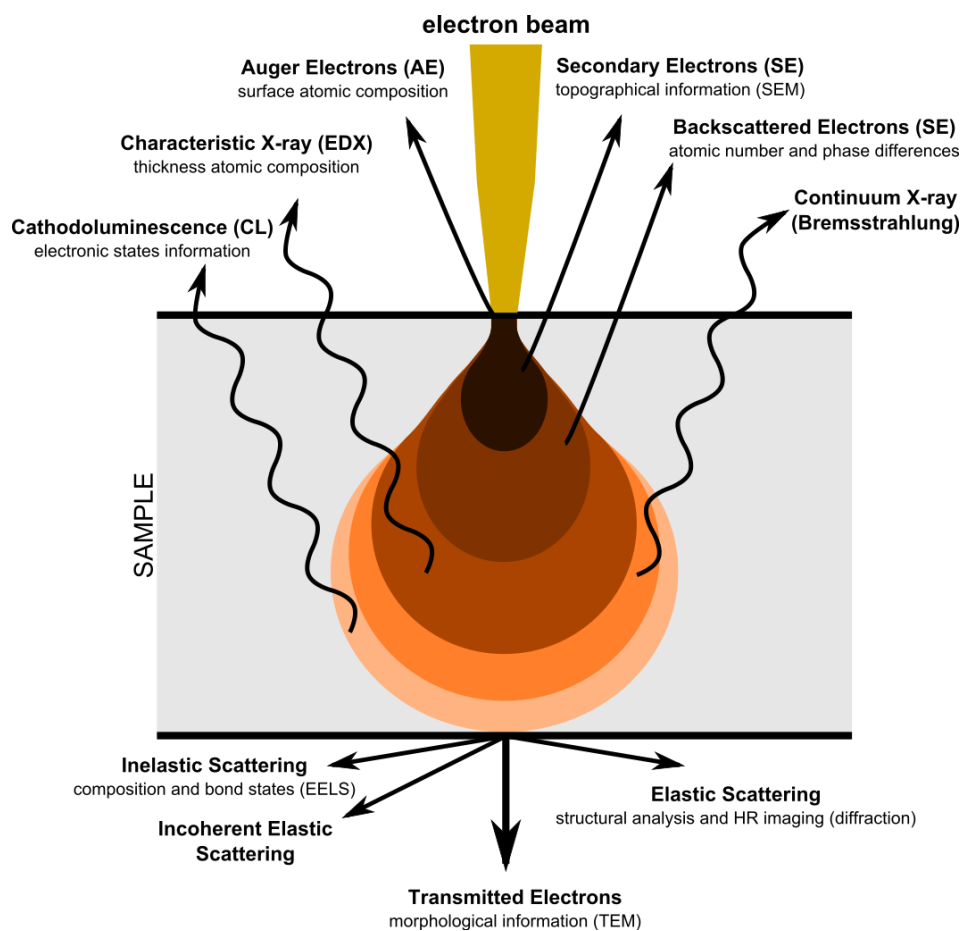


**Figure 2.8.** Different signals produced by the interaction of the SEM electron beam with a sample.

In the most common detection mode (SEI, secondary electron imaging), secondary electrons are used to create an image of the sample surface. Secondary electrons result from the inelastic interactions between the primary electrons from the beam and the atoms of the sample. Because of their low energy, they are emitted within a few nanometres from the

sample surface. Consequently, this technique produces high resolution images of a specimen surface, containing information about morphology and topography.

### **3 Electrochemical analyses**

All the electrochemical measurements were conducted using a Bio-Logic VMP3 multichannel potentiostat. For electrochemical analysis, the reactivity of a working electrode (WE) is studied against a counter electrode (CE) and/or a reference electrode (RE). The working electrode is the electrode in which the reaction of interest is occurring (*i.e.* the sample studied), whereas the counter electrode is an electrode used to close the current circuit in the electrochemical cell. It is also possible to have a third reference electrode (RE), to control the potential during the measurements. For all the electrochemical experiment in this thesis, the setup used only two electrodes, where the CE and RE are shorted on one electrode while the WE is the opposite electrode.

The different techniques used to investigate the electrochemical properties of the batteries are described in detail in this section.

#### **3.1 Galvanostatic cycling**

In galvanostatic cycling a constant current is imposed through the electrolytic cell, and the resulting potential between the WE and CE is measured as a function of time [16]. The constant anodic/cathodic current causes the active species in the electrodes to be oxidized/reduced at a constant rate. During cycling, the current switches from cathodic to anodic in order to introduce (discharge) and extract (charge) lithium from the WE. The switch in current can be done at specific time (*i.e.* changing current direction at set time-intervals) or electrode potential (*i.e.* when the WE reaches a given potential value). The typical galvanostatic discharge/charge profile is shown in Figure 2.9.



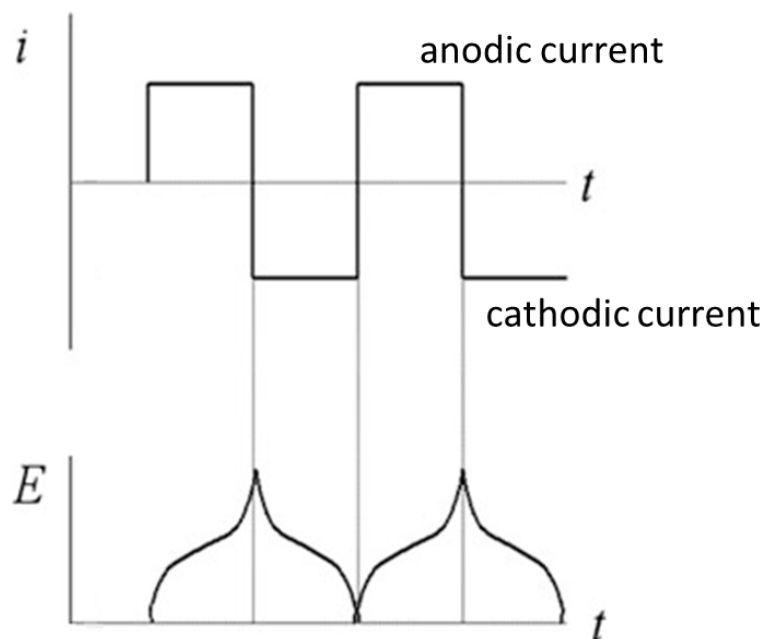


**Figure 2.9.** Current ( $i$ ) and potential ( $E$ ) during galvanostatic discharge/charge as a function of time ( $t$ ). For anodic currents the potential increases (delithiation), and for cathodic currents it decreases (lithiation).

The value of the current depends on the rate at which the battery is fully discharged/charge, and this rate is called C-rate. In the battery field,  $C/n$  rate means that the discharge/charge is complete in  $n$  hours. For instance, with a C-rate of  $2C$  the discharge/charge is complete in half an hour, and with a  $0.5C$  (or  $C/2$ ) it takes 2 hours. If not specified, the galvanostatic experiments reported in this thesis have been carried out with a C-rate of  $C/50$ , *i.e.* 50 hours per discharge/charge.

The total quantity of electricity per mass available from a fully charged cell (or storable in a fully discharged cell) can be calculated at a specific C-rate from the charge transferred during the discharging (or charging) process in terms of  $C/g$  or  $\text{mAh g}^{-1}$ .

### 3.2 Cyclic voltammetry

In a cyclic voltammetry experiment, one sweeps the potential of the working electrode with a specific sweep rate (V/s), recording the resulting current as a function of time [17]. For a reversible electrode, a chosen potential range is scanned for both cathodic and anodic currents, in order to detect as peaks the reduction and oxidation reactions. Each peak corresponds to a specific reaction during the reduction and oxidation of the WE. Since the sweep rate is constant and the initial and switching potentials are known, it is possible to convert time to potential, and the usual protocol is to record current *vs.* applied potential. The resulting current *vs.* applied potential graph is called cyclic voltammogram. For an ideal reversible system, a cyclic voltammogram is shown in Figure 2.10 is obtained.

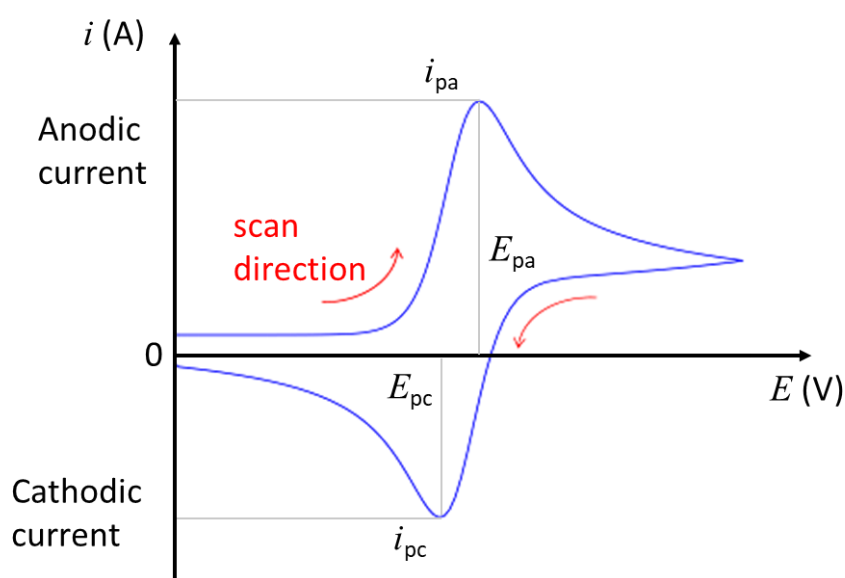


**Figure 2.10.** A cyclic voltammogram. For cathodic current, the reduction reaction occurs at potential  $E_{pc}$  providing the current  $i_{pc}$ . For anodic current the oxidation reaction at  $E_{pa}$  providing  $i_{pa}$ .

### 3.3 Electrochemical impedance spectroscopy

Electrochemical impedance spectroscopy (EIS) is a powerful method for the characterization of electrode materials. It is a non-destructive technique that can provide information about the corrosion, absorption/desorption at the electrode surface, catalytic reaction kinetics, charge transfer and diffusion, *etc.* [18]. For this thesis, EIS has been used to investigate the resistance of the electrodes, and the ionic conductivity of solid electrolytes. EIS is based on the application of a sinusoidal voltage (or current) to an electrochemical cell. If this perturbation is small enough, the response is a sinusoidal signal with the same frequency ( $f$ ) of the perturbation, but shifted ( $\phi$ ) in phase. The ratio between the perturbation and the answer is a frequency-dependant complex number called impedance ( $Z$ ). Thus, impedance represents the opposition of a circuit to a current when a voltage is applied.

$$Z(t) = \frac{V(t)}{I(t)} = \frac{V_0 \sin(\omega t)}{I_0 \sin(\omega t - \phi)} \quad (2.16)$$

Whereas  $V_0$  and  $I_0$  are the amplitudes of the perturbation and the response respectively, and  $\omega$  is the radial frequency ( $\omega = 2\pi f$ ). Using the Euler's relationship  $\exp(iN) = \cos N - i \sin N$  ( $N$  is a real number,  $i$  is an imaginary unit), the previous equation can be written as follow:

$$Z(t) = \frac{V_0 \exp(i\omega t)}{I_0 \exp(i\omega t - \phi)} = \frac{V_0}{I_0} \exp(i\phi) = Z_0 (\cos\phi - i \sin\phi) \quad (2.17)$$

Therefore, the impedance is given by a magnitude,  $Z_0$ , and the real and imaginary parts of the phase shift.

The measured impedance  $Z$  is generally depicted with the real part on the  $X$  axis, and the imaginary part on the  $Y$  axis of a chart called Nyquist plot. The shape of this graphic depends on the complexity of the cell circuit.

In this thesis,  $\text{LiBH}_4$  have been studied as solid electrolyte for Li-ion batteries. In a typical test for evaluating the ionic conductivity, the solid electrolyte was pelletized in a die (8 mm diameter) at 200 MPa, and then placed in a Swagelok cell between two Li disks (8 mm diameter). The perturbation current was 0.1  $\mu\text{A}$ , in a frequency range between 0.1 Hz and 1 MHz. The Nyquist plot of a cell with this configuration is schematically illustrated in Figure 2.11. Owing its shape, with a single semicircle, the equivalent circuit of the cell

can be written as  $C_{dl}/R_{electr}$ , where  $C_{dl}$  is the double layer capacitance, and  $R_{electr}$  is the bulk resistance of the electrolyte.

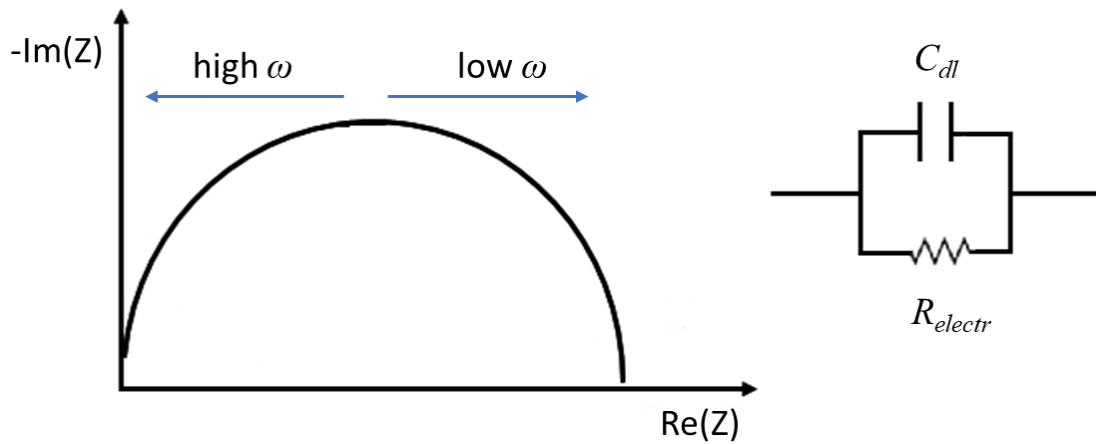


**Figure 2.11.** Nyquist plot of a Li || solid electrolyte || Li cell, and its relative circuit. The blue arrows show the frequency ( $\omega$ ) domain.

The potentiostat software EC-Lab allows to fit the Nyquist plot, obtaining the values of each component in the equivalent circuit, *i.e.*  $C_{dl}$  and  $R_{electr}$ . From the value of  $R_{electr}$  is possible to calculate the conductivity ( $\sigma$ ) of the solid electrolyte with the following equations:

$$\rho = R_{elec} \frac{A}{l} \quad (2.18)$$

$$\sigma = \frac{1}{\rho} \quad (2.19)$$

Where  $\rho$  is the ionic resistivity, and  $l$  and  $A$  are the thickness and the area of the pelletized electrolyte. Because the electric conductivity of  $\text{LiBH}_4$  is assumed negligible, the value of  $\sigma$  is attributed to the mobility of lithium ions, and so it is called ionic conductivity.

## 4 Electrode formulation

For electrochemical analyses, half-cells were assembled testing  $\text{MgH}_2$  thin films and  $\text{MgH}_2+\text{TiH}_2$  nanocomposites against a lithium counter electrode. Thin film electrodes were studied only in liquid electrolyte, while the nanocomposites were tested in both liquid and solid electrolytes.

### 4.1 $\text{MgH}_2$ thin film electrode

After the deposition of  $\text{MgH}_2$ , squares of 6.7 cm side were recovered from the sputtering chamber and stored under argon atmosphere (see Figure 2.12). From these squares, electrodes were prepared by cutting the thin film into smaller squares of side 9 mm, which were placed in a Swagelok cell as working electrode. Two Whatman glass fibre filters imbued with liquid electrolyte 1.0 M  $\text{LiPF}_6$  (in 1:1 dimethyl carbonate : ethylene carbonate) were used as separators, and lithium foil (9 mm disk) as counter electrode.

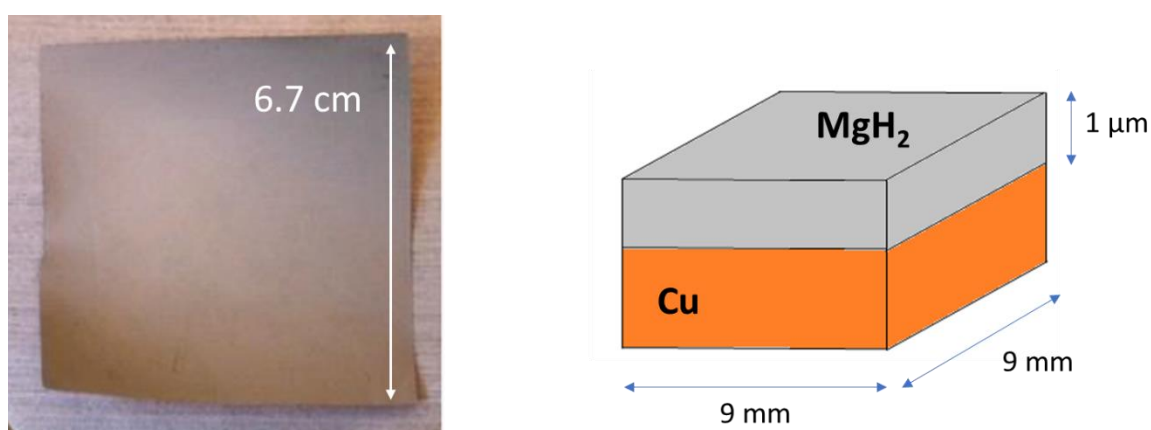


**Figure 2.12.** Thin film as obtained from the sputtering chamber (left), and schematic illustration of the electrode placed into the cell (right).

For the purpose of calculating how much active material was present in each electrode, it was assumed a volume of  $\text{MgH}_2$  of  $8.1 \cdot 10^{-5}\ \text{cm}^3$  ( $9\ \text{mm} \times 9\ \text{mm} \times 1\ \mu\text{m}$ ) with a density of  $1.45\ \text{g/cm}^3$ , hence a mass of active material of 0.12 mg.

## 4.2 MgH<sub>2</sub>+TiH<sub>2</sub> nanocomposite electrode and formulation optimization

### 4.2.1 Half-cell with liquid electrolyte

Working electrodes were prepared by hand mixing the nanocomposites synthesized by ball milling with Carbon Super P (SP) and carboxymethyl cellulose (CMC) in a weight ratio of 1:1:1. Carbon Super P is added to increase the electric conductivity inside the electrode [19], and CMC is a binder able to accommodate the volume expansion during cycling [20]. The mixture was placed on a nickel foam disk, (9 mm diameter) used as current collector, and pressed at 150 MPa. The effects of these additives are shown in Figure 2.13. The so-prepared working electrode was then placed in a Swagelok half-cell for electrochemical tests. Lithium foil (9 mm diameter disk) was used as negative electrode and two Whatman filters saturated with electrolyte 1.0 M LiPF<sub>6</sub> (in 1:1 DMC:EC) were used as separators. All sample handling was done in a purified argon-filled glovebox.

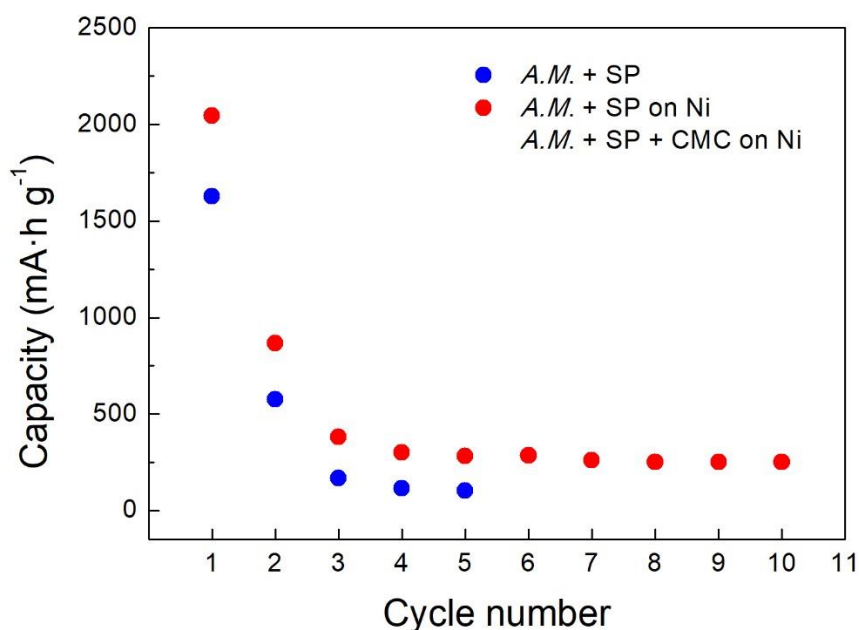


**Figure 2.13.** Discharge capacity during cycling of electrodes with different formulations. *A.M.* is the 0.5MgH<sub>2</sub>+0.5TiH<sub>2</sub> active material.

Figure 2.13 shows the importance of the contacts inside the electrode. When loose powder (black dots) is placed into the cell, the complete lithiation of the active material is not obtained (1275 vs. 1405 mAh g<sup>-1</sup>), moreover the capacity quickly drops to low values in the subsequent cycle and then the electrode stops working. The main reason of this

performance is attributed to the poor contacts within the electrode. Pressing the mixture (A.M. + SP) on a nickel current collector increases the contacts between particles, and also provides a better mechanical stability compared to loose powder. As result (blue dots), the electrode is full lithiated during the first discharge (the excess in capacity is due to the formation of SEI and Mg-Li alloy), and the cycle-life slightly increases. Finally, when the binder CMC is added to the mixture (red dots), the electrode achieves a higher capacity, which decreases slower during cycling, stabilizing around 300 mAh g<sup>-1</sup> for several cycles.

#### **4.2.2 Half-cells with LiBH<sub>4</sub> as solid electrolyte**

The work on solid-state cells was done in part at ICMPE and partly at SAFT Co. (Bordeaux), in collaboration with Dr. Pedro López-Aranguren and Anh Ha Dao (ECOSTORE fellows). At ICMPE MgH<sub>2</sub> and TiH<sub>2</sub> have been investigated as electrode materials in half-cells, whereas at SAFT MgH<sub>2</sub>+TiH<sub>2</sub> nanocomposites have been studied in both half-cells and complete battery using Li<sub>2</sub>S as cathode material.

Because the solid electrolyte cannot impregnate into the electrode like a liquid electrolyte, active material and solid electrolyte were mixed together to form the electrode with the purpose of increasing the number of interfaces between these materials.

For MgH<sub>2</sub> and TiH<sub>2</sub>, the electrode mixture was prepared by ball milling the active material with carbon Super P and commercial LiBH<sub>4</sub> in a weight ratio of 35:20:45 respectively. This ratio was chosen based on initial results compared to other ratios. In a planetary mill Fritsch Pulverisette 7, electrode mixture were loaded in a vial with 60 stainless steel balls (7 mm diameter) with a balls to powder mass ratio of 60:1. The composite was milled at 200 rpm for a total of 2 hours, in cycles of 30 minutes with a break of 15 minutes. The effect of the ball mill on the electrode activity is shown in Figure 2.14. Not only the ball milled electrode exhibits a higher quantity of Li stored during the first discharge (1.9 vs. 1.5 Li), but the capacity retention is clearly better than the hand made one. These results undoubtedly demonstrate the importance of the mixing process when using a solid electrolyte. However, the theoretical capacity of 2 Li is not reached yet, so further optimization can be achieved.

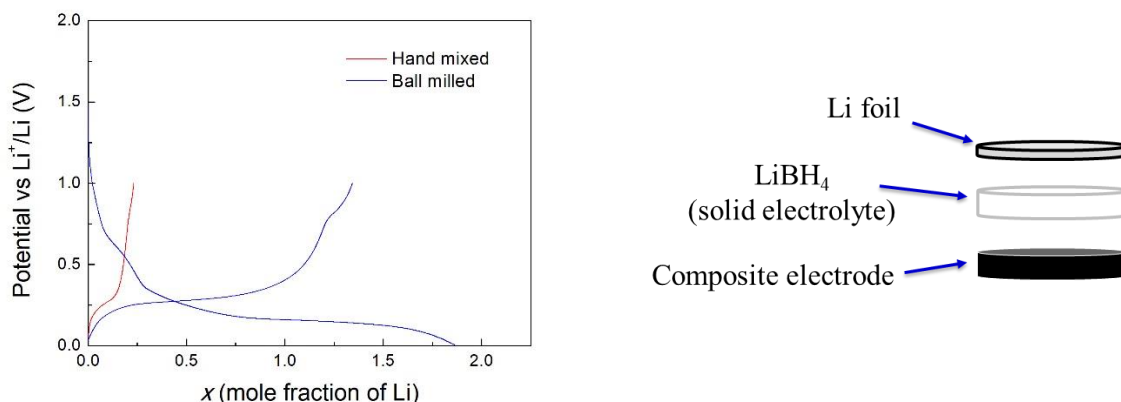


**Figure 2.14.** First galvanostatic cycle of a solid cell with  $\text{TiH}_2\text{:SP:LiBH}_4$  as electrode composite prepared hand mixing (red) and by ball mill (blue). On the right, an illustration of the three-layered pellet.

For the  $\text{MgH}_2+\text{TiH}_2$  nanocomposites, it was used carbon C65 to prepare the working electrode. Active material, carbon and  $\text{LiBH}_4$  were mixed in a ball mill with a weight ratio of 30:20:50. The components were milled for 2 hours at 300 rpm with a 40:1 balls to powder ratio, with a resting time of 5 minutes each 15 minutes of milling.

To prepare the cell, first, 25 mg of commercial  $\text{LiBH}_4$  were loaded into an 8-mm diameter die and uniaxially pressed at 60 MPa. Subsequently, 4 mg of the composite electrode powder were transferred onto the pressed electrolyte still present in the die, and uniaxially pressed at 200 MPa to obtain a single pellet comprised of the electrode mixture and the solid electrolyte. Li foil (5 mm diameter) was placed on the side of the pellet opposite to the working electrode. Prior to all the measurements, the cells were kept at 120 °C for 5 hours to ensure a homogeneous temperature inside the Swagelok.

#### 4.2.3 Complete solid-state metal hydride-sulphur Li-ion battery

To assembly a complete solid-state Li-ion battery it was chosen to use  $0.8\text{MgH}_2+0.2\text{TiH}_2$  composite as negative material, and  $\text{Li}_2\text{S}$  as positive material. To produce  $\text{Li}_2\text{S}$  it was mandatory to lithiate sulphur by means of galvanostatic discharge in a half-cell.

Sulphur powder (S) was mechanical mixed with carbon Ketjen-Black EC 300J (KB) in a weight ratio of 1:1 for 3 hours at 300 rpm. 25 stainless steel balls (7 mm diameter) were used in order to have a balls to powder ratio of 29:1. The recovered mixture was then



dried overnight at 55 °C. To prepare the electrode composite for the lithiation in a half-cell, LiBH<sub>4</sub> was added to S-KB to attain the weight percent ratio of 25S:25C:25LiBH<sub>4</sub>, and mixed by hand in a mortar for 10 minutes. A pellet was created from a 10-mm die. First, 10 mg of composite were pressed at 25 MPa, then 25 mg of LiBH<sub>4</sub> were loaded into the die and uniaxially pressed on top of the composite at 250 MPa. A disk of lithium (9 mm) was placed as counter electrode. The so prepared S:KB:LiBH<sub>4</sub> || LiBH<sub>4</sub> || Li half-cell was discharged at 120 °C up to 1 V with a C-rate of C/50, obtaining the full lithiated Li<sub>2</sub>S composite. The working electrode was then recovered scratching the powder from the pellet.

The complete battery was prepared pressing 60mg of LiBH<sub>4</sub> at 250 MPa between 10 mg of positive material (Li<sub>2</sub>S:KB:LiBH<sub>4</sub>) and 3 mg of negative material (0.8MgH<sub>2</sub>+0.2TiH<sub>2</sub>:C65:LiBH<sub>4</sub>). Figure 2.15 shows the final pellet investigated at 120 °C in a Swagelok cell during galvanostatic cycling.

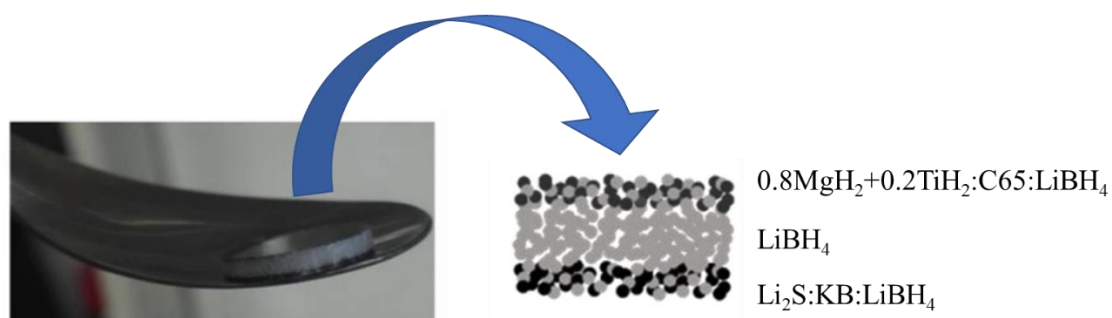


**Figure 2.15.** Image of the final pellet (left) and its schematic representation (right) studied as complete solid-state metal hydride-sulphur Li-ion battery.

## References

1. Huot, J. *et al.* Mechanochemical synthesis of hydrogen storage materials. *Prog. Mater. Sci.* **58**, 30–75 (2013).
2. Doppiu, S., Schultz, L. & Gutfleisch, O. In situ pressure and temperature monitoring during the conversion of Mg into MgH<sub>2</sub> by high-pressure reactive ball milling. *427*, 204–208 (2007).
3. Zhang, J. *et al.* Highlighting of a single reaction path during reactive ball milling of Mg and TM by quantitative H<sub>2</sub> gas sorption analysis to form ternary complex hydrides (TM = Fe, Co, Ni). *J. Phys. Chem. C* **115**, 4971–4979 (2011).
4. Le-Quoc, H. *et al.* MgH<sub>2</sub> thin films deposited by one-step reactive plasma sputtering. *Int. J. Hydrogen Energy* **39**, 17718–17725 (2014).
5. Platzer-Björkman, C. *et al.* Deposition of magnesium hydride thin films using radio frequency reactive sputtering. *Thin Solid Films* **519**, 5949–5954 (2011).
6. Eggenhuisen, T. M., Steenbergen, M. J. Van, Talsma, H., Jongh, P. E. De & Jong, K. P. De. Impregnation of Mesoporous Silica for Catalyst Preparation Studied with Differential Scanning Calorimetry. 16785–16791 (2009).
7. Ngene, P., Adelhelm, P., Beale, A. M., Jong, K. P. De & Jongh, P. E. De. LiBH<sub>4</sub>/SBA-15 Nanocomposites Prepared by Melt Infiltration under Hydrogen Pressure : Synthesis and Hydrogen Sorption Properties. *J. Phys. Chem. C* **114**, 6163–6168 (2010).
8. Bish, D.L., Post, J.E. Modern powder diffraction. *Mineralogical Society of America* (1989).
9. Rietveld, H. M. A profile refinement method for nuclear and magnetic structures. *J. Appl. Crystallogr.* **2**, 65–71 (1969).
10. McCusker, L. B., Von Dreele, R. B., Cox, D. E., Louër, D. & Scardi, P. Rietveld refinement guidelines. *J. Appl. Crystallogr.* **32**, 36–50 (1999).
11. Ares, J. R. & Cuevas, F. Mechanical milling and subsequent annealing effects on the microstructural and hydrogenation properties of multisubstituted LaNi<sub>5</sub> alloy. **53**, 2157–2167 (2005).

12. Rodriguez-carvajal, J. WinPLOTTR : A Windows tool for powder diffraction pattern analysis. (2013). doi:10.4028/www.scientific.net/MSF.378-381.118
13. Williams, D.B., Carter, C-B. Transition Electron Microscopy – A textbook for Material Science. *Springer* (2009).
14. Giannuzzi, L. A. & Stevie, F. A. A review of focused ion beam milling techniques for TEM specimen preparation. **30**, 197–204 (1999).
15. Egerton, R. Physical Principles of Electron Microscopy – An introduction to TEM, SEM, and AEM. *Springer* (2005).
16. Bard, A.J., Faulkner, L.R. Electrochemical Methods: Fundamentals and Applications. *Wiley* (2001).
17. Somasundaran, P. Encyclopedia of Surface and Colloid Science. *Marcel Dekker* (2004).
18. Barsoukov, E., Macdonald, J.R. Impedance Spectroscopy: Theory, Experiment, and Application. *Wiley* (2005).
19. Oumellal, Y. *Réactivité électrochimique des hydrures métalliques vis-à-vis du lithium: Electrodes negatives pour batteries Li-ion: Stockage de l'hydrogène par voie solide-gaz*. Ph.D. Thesis, Université de Picardie, Jules Verne (2009).
20. Zaïdi, W. *et al.* Carboxymethylcellulose and carboxymethylcellulose-formate as binders in MgH<sub>2</sub>-carbon composites negative electrode for lithium-ion batteries. *J. Power Sources* **196**, 2854–2857 (2011).

# **CHAPTER 3**

Magnesium hydride thin film  
as electrode material



# Content

<b>1</b>	<b>MgH<sub>2</sub> thin films</b>	<b>84</b>
1.1	Structural and Electrochemical properties	84
1.2	Surface barrier and reproducibility	86
<b>2</b>	<b>Al-coated MgH<sub>2</sub> thin films</b>	<b>88</b>
2.1	Structural properties and Electrochemical cycling	88
2.2	Structural modifications during the first galvanostatic cycle	90
2.3	Microstructural modifications during the first galvanostatic cycle	92
<b>3</b>	<b>Discussion</b>	<b>97</b>
3.1	Effect of the Mg alloying on the conversion reaction	97
3.2	Reversibility of the conversion reaction	100
<b>4</b>	<b>Conclusions</b>	<b>103</b>
	<b>References</b>	<b>105</b>



Magnesium hydride in thin film morphology has been widely studied for hydrogen storage and optical application [1–5]. In this work,  $\text{MgH}_2$  thin films are used as working electrodes in lithium-ion half-cells, with the purpose of better understanding the reversibility of the conversion reaction between  $\text{MgH}_2$  and lithium. Thanks to their well-defined 2D morphology, thin films are ideal systems to study the effect of the conversion reaction on the electrode morphology. Moreover, with the help of image tools, the mechanism and spatial localization of the conversion reaction can be determined.

$\text{MgH}_2$  thin films have been synthesized on copper foil by reactive sputtering. Their conversion reaction with lithium has been studied by galvanostatic and cyclic voltammetry measurements. Structural and morphological properties during discharge and charge processes have been investigated by means of X-ray diffraction (XRD) and transmission electron microscopy (TEM).

The deposition of thin films has been performed by Dr. Ana Lacoste from LPSC laboratory (Grenoble, France). The TEM investigation has been carried out by Efi Hadjixenophontos from Stuttgart University (Stuttgart, Germany).



# 1 MgH<sub>2</sub> thin films

## 1.1 Structural and Electrochemical properties

Magnesium hydride thin films were prepared by reactive plasma-assisted microwave/radio frequency sputtering on copper substrates (see Chapter 2 section 1.2). The X-ray diffraction pattern obtained from the as-prepared thin film is reported in Figure 3.1.

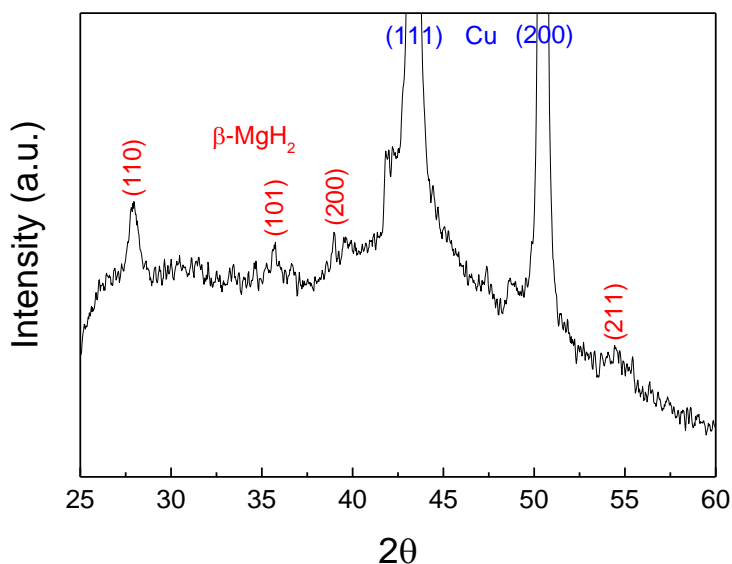


**Figure 3.1.** XRD pattern and peak indexation of MgH<sub>2</sub> thin film deposited on copper.

The X-ray diffraction pattern of the sample can be indexed with two phases: MgH<sub>2</sub> and Cu. Magnesium hydride crystallizes in the tetragonal rutile-type polymorph β-MgH<sub>2</sub>, with space group  $P4_2/mnm$ . Copper crystallizes as cubic with space group  $Fm\bar{3}m$ . It is worth to notice that no diffraction peak related to hcp-Mg is detected in the pattern.

Square electrodes (9 mm side) have been cut from the as-prepared MgH<sub>2</sub> thin films, placed into a Swagelok cell (MgH<sub>2</sub> || LiPF<sub>6</sub>:EC:DMC || Li), and tested in galvanostatic mode with a C-rate of C/50. The evolution of the potential as a function of time during cycling between 0.005 V to 1.5 V is shown in Figure 3.2

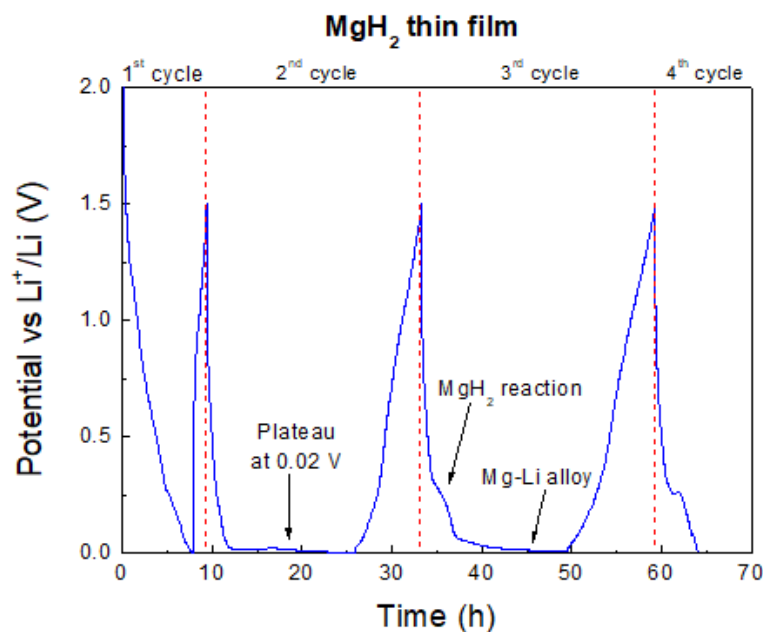


**Figure 3.2.** Potential profile during the first four galvanostatic cycles of MgH<sub>2</sub> thin film electrode.

During the first eight hours of discharge (*i.e.* lithiation), the potential decreases till the cut-off potential,  $V_{\text{cut-off}}$ , of 5 mV. The plateau potential characteristic of the MgH<sub>2</sub> conversion reaction (expected around 0.3 – 0.5 V) is not observed. On charge (*i.e.* delithiation), no plateaus are found. During the second cycle, the potential quickly drops without any signal of the conversion reaction, but interestingly, the potential displays a plateau at ~0.02 V. This plateau could be related to the reaction of MgH<sub>2</sub> with Li, occurring at very low potential because of a high overpotential. Such difference in the potential plateau (0.5 V theoretically *vs.* 0.02 V experimentally) might be due to a surface barrier, which delays the conversion reaction. This hypothesis is clarified taking a look at the subsequent cycle. In the third cycle, two different plateaus are detected at 0.3 and 0.06 V during the discharge. The plateau at 0.3 V is related to the conversion reaction of MgH<sub>2</sub> with Li, forming Mg and LiH [6]. The second one at 0.06 V is the Mg alloying reaction with lithium [6,7]. The conversion reaction signal is also found, though at a lower extent, in the subsequent cycle.

The previous result shows that the MgH<sub>2</sub> conversion reaction detected in cycles 3<sup>rd</sup> and 4<sup>th</sup> is preceded by an activation process that operates during the two first cycles. This process is attributed to the reduction of surface contaminants, likely MgO or Mg(OH)<sub>2</sub> [8], that are formed over the thin film during its transfer from the deposition chamber to the glovebox. The thickness of this passivation layer should be small as it was not detected by

XRD. To verify the hypothesis of a surface barrier, further experiments about the activation of the thin film have been carried out.

## 1.2 Surface barrier and reproducibility

The fact that the plateau found at 0.02 V is related to the reduction of a surface passivation layer was checked in a second experiment. As displayed in Figure 3.3, a  $\text{MgH}_2$  thin film was cycled under the same conditions as before but increasing  $V_{\text{cut-off}}$  to 0.1 V. It can be clearly seen that the conversion reaction of  $\text{MgH}_2$  does not occur in this experiment: the cut-off voltage of 0.1 V is too high to allow the reduction of the passivation layer.

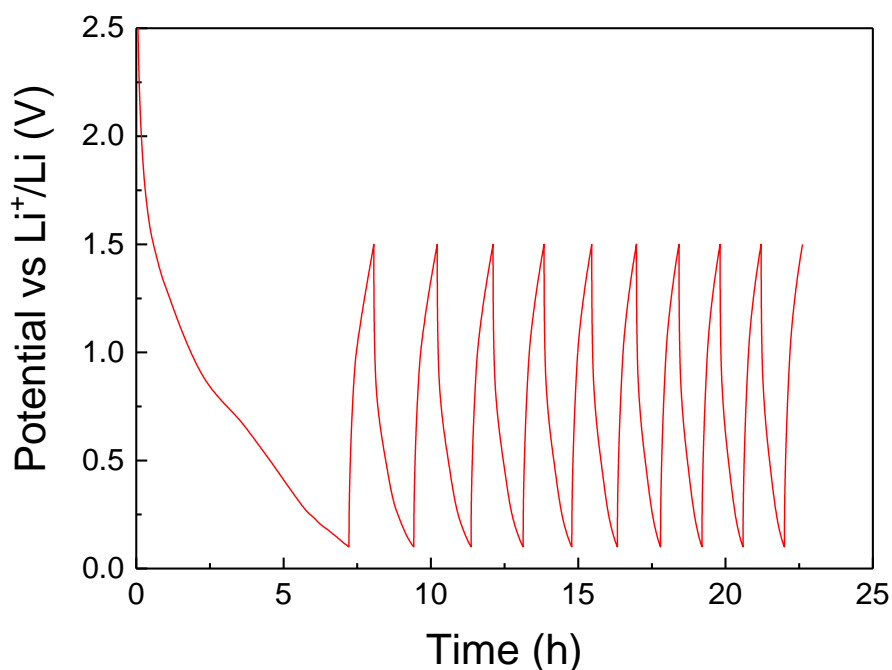


**Figure 3.3.** Galvanostatic cycling of  $\text{MgH}_2$  thin film between 0.1 – 1.5 V with a C-rate of C/50.

With the purpose of gaining a better understanding of the activation process, a thin film was discharged in galvanostatic mode down to 0.02 V. Once the potential reached this value, it was hold in potentiostatic mode for one week (168 hours). After this time, the cell was switched back to galvanostatic mode to determine whether the conversion reaction takes place during the subsequent discharge/charge cycles. The results of this experiment are shown in Figure 3.4.

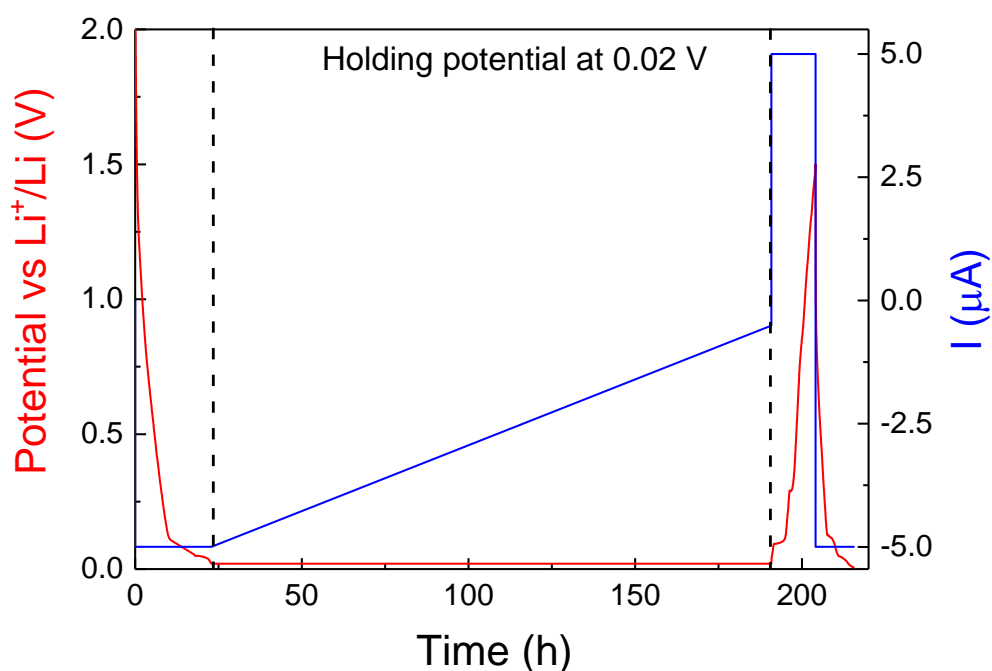


**Figure 3.4.** Evolution of the potential (red line) and the current (blue line) as a function of time (h) during an experiment to activate a MgH<sub>2</sub> thin film.

During the first galvanostatic discharge, the potential quickly decreases to 0.02 V without displaying any clear evidence of the reduction of MgH<sub>2</sub>. Next, during the potentiostatic discharge for 168 hours, the current decreases (in absolute value) linearly with time. Then, galvanostatic cycling (charge/discharge) is imposed but the signal of the conversion reaction of MgH<sub>2</sub> is not detected. This indicates that the thin film could not be activated by this electrochemical treatment, contrary to the results shown in Figure 3.2. Likely, passivation layers formed on MgH<sub>2</sub> are not uniform (either in thickness and/or composition) and activation processes are not reproducible. To solve this issue, we prepared new thin films while protecting hydride MgH<sub>2</sub> from surface contaminants. This was achieved by depositing a protective layer of aluminium on top of MgH<sub>2</sub>.

## 2 Al-coated MgH<sub>2</sub> thin films

### 2.1 Structural properties and Electrochemical cycling

Aluminium was chosen as protective layer because it is active towards lithium and exhibits a high electric conductivity [9,10], allowing Li ions to move through the layer reaching the hydride. Because the thin films were exposed to air while transferring from the sputtering chamber to the glovebox, the oxidation of aluminium, forming Al<sub>2</sub>O<sub>3</sub>, is expected. However, Al<sub>2</sub>O<sub>3</sub> is not a passivating layer, and it is studied as coating material for Li-ion battery electrodes [11–13].

Figure 3.5 shows the XRD pattern of this covered thin film. As for the previous sample, the main diffraction peaks can be indexed with two phases: rutile-type  $\beta$ -MgH<sub>2</sub> and copper. No diffraction peaks related to pure aluminium or aluminium oxide are detected, due either to their low amount or poor crystallinity.

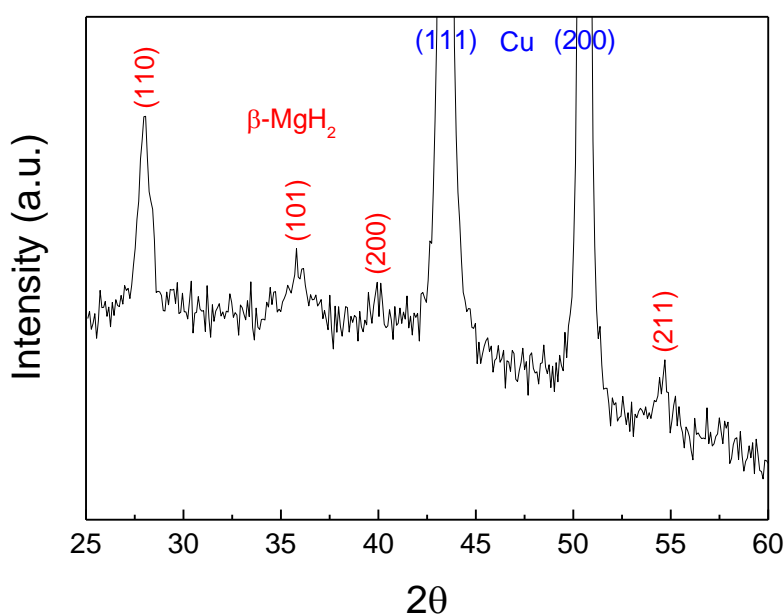


**Figure 3.5.** XRD pattern of Al-coated MgH<sub>2</sub> thin film deposited over Cu current collector.

Galvanostatic cycling of Al-coated MgH<sub>2</sub> thin films has been studied in two potential ranges: from 0.1 to 1 V and from 0.005 to 1 V. In the former range, we target the MgH<sub>2</sub> conversion reaction, whereas in the latter one both MgH<sub>2</sub> conversion and Mg alloying reactions are expected to occur. The potential *vs.* compositions (*x*) profiles for the first

discharge/charge cycle are shown in Figure 3.6. Here  $x$  stands for the mole fraction of Li that reacts with the electrode.

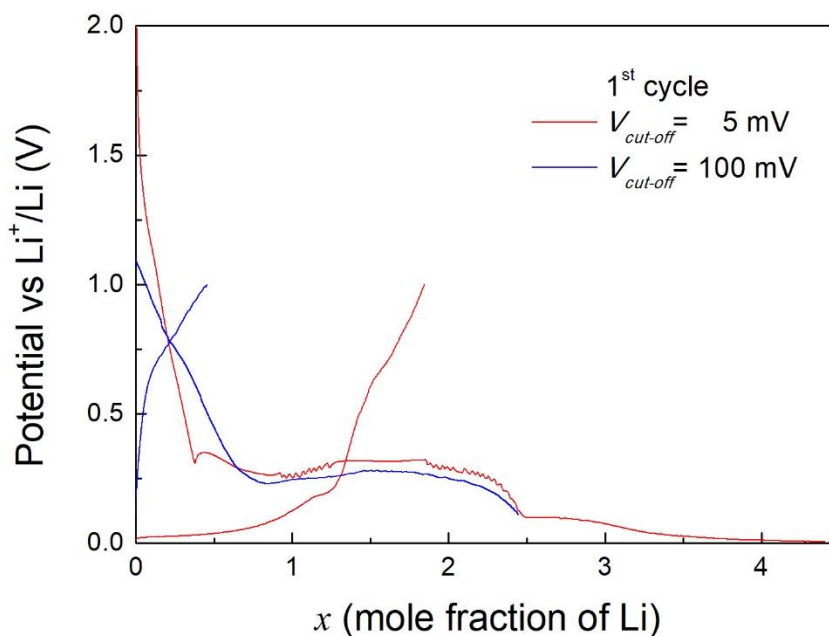


**Figure 3.6.** Evolution of the potential (V) as a function of  $x$  (mole fraction of Li) for Al covered thin films in the first galvanostatic cycle with a C-rate of C/50.  $V_{\text{cut-off}} = 5$  mV (red line, Mg alloying) and 100 mV (blue line, without Mg alloying).

Under both cycling conditions, the first discharge curve consists of a sloping voltage profile followed by a flat plateau around 0.3 V. As demonstrated by Liu *et al.* [12], the initial slope is due to the irreversible lithiation of the surface aluminium oxide, forming a Li-Al-O glass layer. These authors have attributed to  $\text{Al}_2\text{O}_3$  a theoretical capacity around  $530 \text{ mAh g}^{-1}$ , since the oxide is 53% Al by mass. Because of the low amount of oxide in each electrode ( $\sim 4 \cdot 10^{-6} \text{ g}$ ), its contribution to the final capacity is considered negligible. Moreover, it should be also noted that no plateau potential related to the lithiation of pure Al, expected around 0.2 V [7], is observed. This likely relates to the fact that the amount of Al is small, and part of it is also oxidized into  $\text{Al}_2\text{O}_3$ . On the other hand, the plateau observed between  $0.5 < x < 2.5$  is related to the conversion reaction of  $\text{MgH}_2$  to Mg and  $2\text{LiH}$ . Since  $\Delta x$  is  $\sim 2$ , it can be asserted that the conversion reaction is completed. It is worth noting that the conversion reaction occurs already at the first cycle with no significant

overpotential as compared to an activated  $\text{MgH}_2$  thin film (3<sup>rd</sup> cycle in Figure 3.2). The Al-coating is very effective to avoid the formation of surface passivation barriers over  $\text{MgH}_2$ .

For the thin film lithiated down to 5 mV (red line in Figure 3.6), a short plateau appears at  $\sim 95$  mV followed by a sloping potential trace till the cut-off potential. This allows for an additional capacity of  $\Delta x \sim 2$  that is attributed to Mg alloying reactions.

During the first charge step, different potential traces are observed depending on the lithiation cut-off voltage  $V_{\text{cut-off}}$ . For the film cycled with  $V_{\text{cut-off}} = 0.1$  V (blue line), the potential gradually increases till reaching a sloping plateau that starts at  $\sim 0.7$  V. This sloping plateau is attributed to the reformation of  $\text{MgH}_2$  from Mg and LiH. The quantity of  $\text{MgH}_2$  restored is  $\Delta x \sim 0.5$ , implying a poor reversibility of the conversion reaction in thin films ( $\sim 25\%$ ). For the film cycled down to lower potentials ( $V_{\text{cut-off}} = 5$  mV, red line), the potential trace on charging shows first a gradual increase of the potential followed by a short plateau at 0.2 V. These features are attributed to de-alloying of Mg-Li compounds. Finally, above 0.2 V, the potential trace is analogous as for the film cycled with  $V_{\text{cut-off}} = 0.1$  V, revealing limited reformation of  $\text{MgH}_2$ .

## 2.2 Structural modifications during the first galvanostatic cycle

With the purpose of studying the structural changes in the  $\text{MgH}_2$  thin film during lithiation and delithiation sweeps within the first galvanostatic cycle, six electrodes have been prepared stopping the electrochemical reaction at different stages of (dis)charge (Figure 3.7) carried out with C/50. The cells have been taken into the glovebox, where the electrodes have been recovered, washed in dimethyl carbonate (DMC), and dried in vacuum. Because the main aim of this Thesis is to study the hydride conversion reaction, the Mg alloying reaction has been avoided by fixing  $V_{\text{cut-off}}$  to 0.1 V. As illustrated in Figure 3.7, the samples prepared are:

- a) Pristine Al-coated thin film;
- b) Beginning of the conversion reaction;
- c) Middle of the conversion reaction;
- d) Near complete lithiation;
- e) Complete discharge;
- f) End of charge at 1 V;

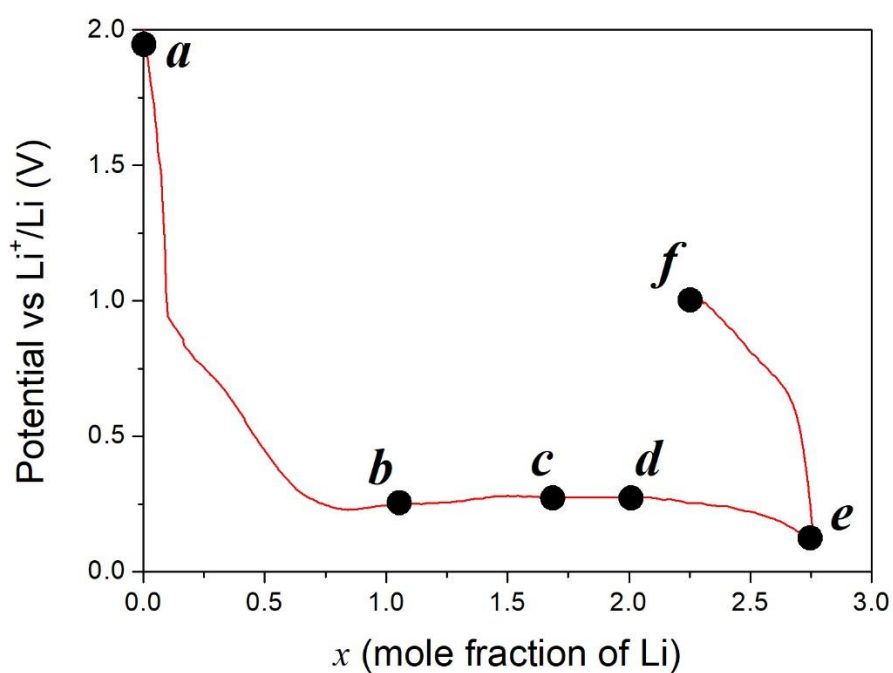


**Figure 3.7.** Evolution of potential (V) as a function of  $x$  (mole fraction of Li). The black circles represent the points at which the electrodes have been recovered from the cells.

For each sample, the quantity of Li stored ( $x$ ) has been evaluated subtracting the contribution of the initial slope due to the lithiation of the protective layer (*i.e.* 0.75 Li), obtaining: zero for the pristine film *a*, 0.35 Li for *b*, 1 for *c*, 1.25 for *d*, 2 for *e*, and during delithiation 0.5 Li have been recovered, implying a quantity of 1.5 Li still into the electrode *f*.

Subsequently, the electrodes have been investigated by XRD, and the obtained patterns are displayed in Figure 3.8.



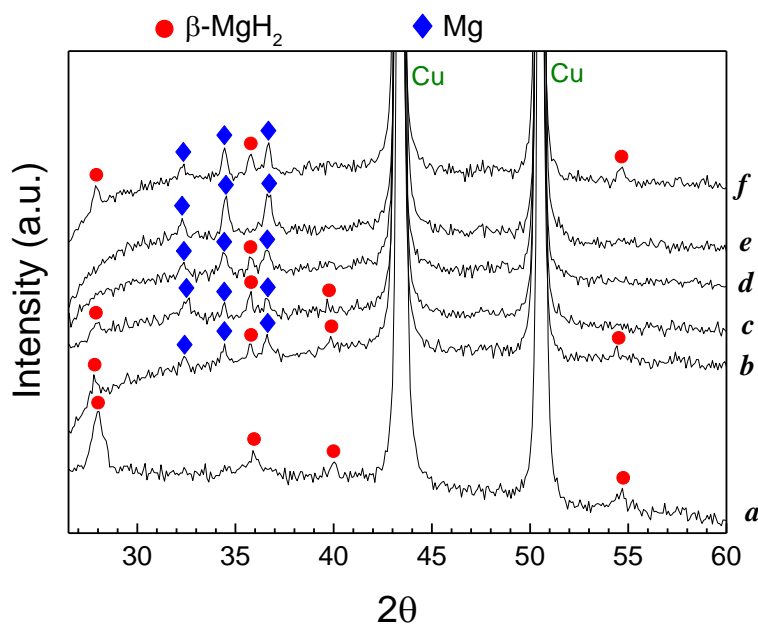


**Figure 3.8.** XRD patterns obtained at different steps of discharge/charge: *a*  $x=0$ , *b*  $x=0.35$ , *c*  $x=1$ , *d*  $x=1.25$ , *e*  $x=2$ , and *f*  $x=1.5$  Li.

As previously described, the active phase in the pristine thin film (*a*) is  $\beta$ -MgH<sub>2</sub>. On discharge (*b*, *c*, and *d* patterns), the intensity of the diffraction peaks of MgH<sub>2</sub> phase decreases while those of Mg grow up with lithium loading. When the thin film is fully lithiated (*e*), only the peaks of hexagonal Mg (space group  $P6_3/mmc$ ) are visible, confirming the complete conversion of the hydride. The electrode is then partially delithiated during the charge, thus both MgH<sub>2</sub> and Mg diffraction peaks are detected in the latter pattern (*f*). LiH formed during the conversion reaction could not be detected by XRD, likely because of its low scattering power.

### 2.3 Microstructural modifications during the first galvanostatic cycle

XRD patterns acquired at different reaction steps within the first galvanostatic cycle have shown the complete conversion of MgH<sub>2</sub> to Mg and then, after delithiation, the partial reformation of the hydride (Figure 3.8). Being a light hydride, LiH was not detected by X-ray. XRD provides information about the formation and crystal structure of crystalline phases into the thin film electrode, but to study their spatial distribution and therefore to better understand irreversibility phenomena, other characterization techniques are needed. For this reason, the same thin films analyzed by XRD analysis have been later analyzed by

TEM. Lamellas with a thickness of ~80 nm have been cut from the thin films by FIB and the cross sections were observed under the microscope.

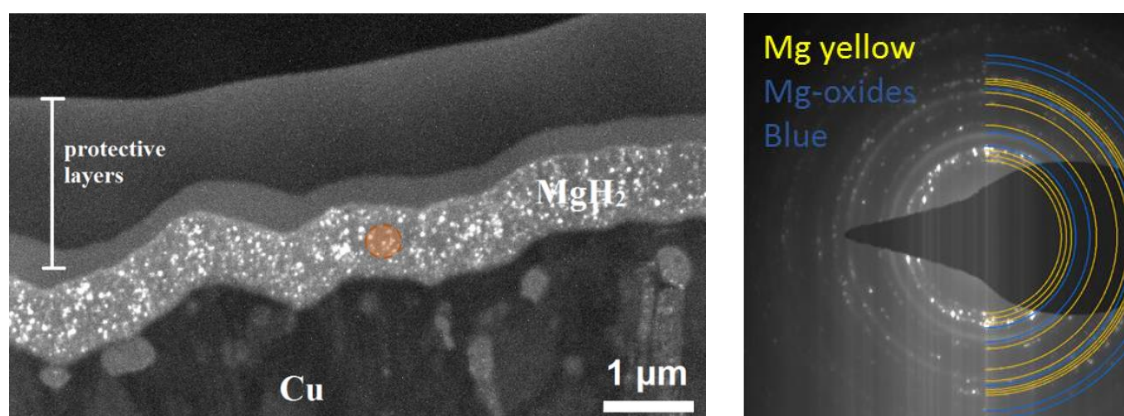


**Figure 3.9.** TEM dark field image of the cross section of pristine Al-covered MgH<sub>2</sub> thin film (left), and SAED pattern (right) performed on the selected orange area displayed in TEM image.

Figure 3.9 shows the TEM image of the pristine thin film (sample *a* in Figure 3.7 and 3.8). Four different layers can be observed. Starting from the top, the two first layers are due to platinum coating that was deposited during the FIB preparation for protecting the film from ionic-milling. They have different tonality because they were deposited in different ways. This first layer in contact with the thin film has been deposited by electron beam, whereas the second by ion beam. This is done because electron beam-induced deposition is less harmful on the thin film surface compared to ion beam deposition. Below the two FIB protective layers, the MgH<sub>2</sub> thin film and the copper substrate are observed. The Al layer on top of MgH<sub>2</sub> is not observed. The SAED electron diffraction rings of the thin film can be indexed with two phases: magnesium and magnesium oxide. Magnesium oxide is formed during the exposition of the thin film to air while transferring it into the microscope. In addition, magnesium is observed instead of magnesium hydride. This can be explained by the fact that MgH<sub>2</sub> is not stable in high vacuum, and when illuminated by the electron beam it desorbs hydrogen promoting the nucleation of Mg [14,15].

The evolution of the thin film microstructure at different steps of the lithiation sweep is displayed in Figure 3.10.

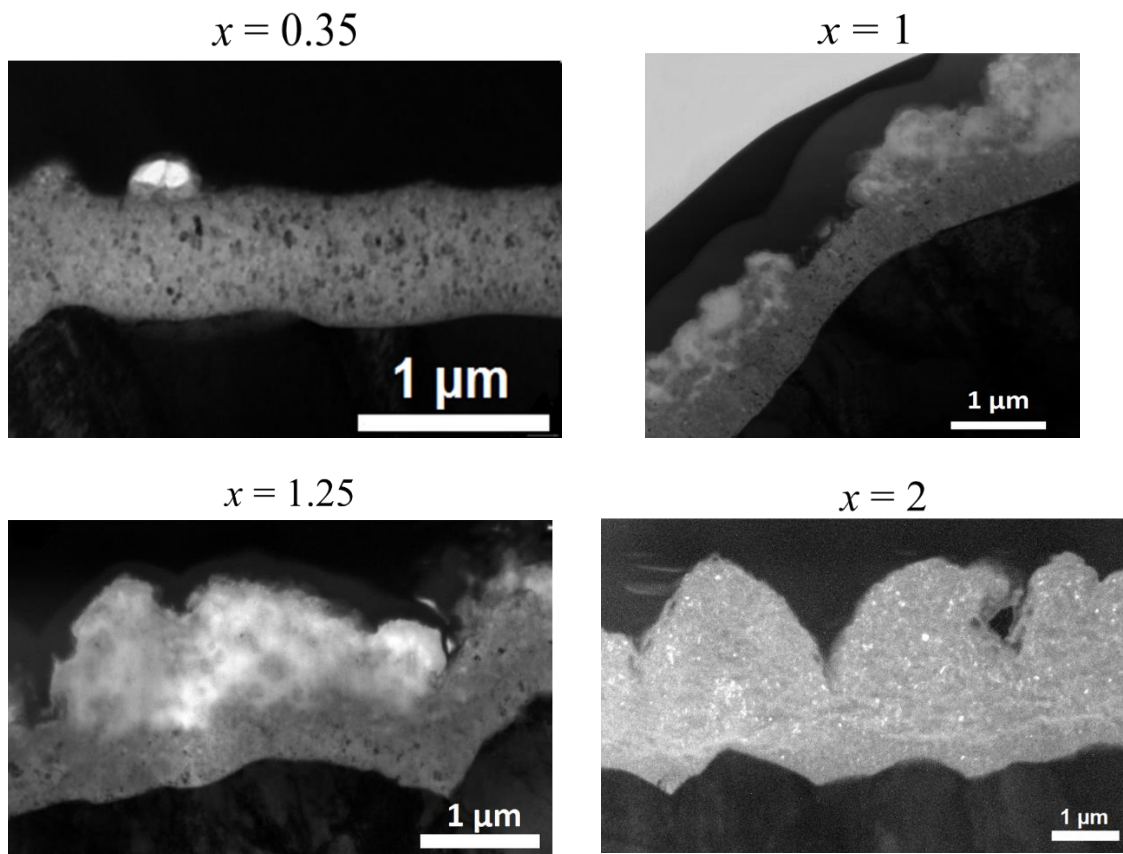


**Figure 3.10.** TEM bright field images of the cross sections of electrodes at different lithiation steps.

At the beginning of the lithiation ( $x = 0.35$ ), white areas appear at specific locations on the top of the  $\text{MgH}_2$  layer. These areas are attributed to  $\text{LiH}$  formation. Because they are found only in some part of the thin film, this suggests that the formation of  $\text{LiH}$  occurs with a nucleation reaction. Next, on increasing Li content ( $x = 1$  and  $1.25$ ), the conversion reaction progresses as an irregular front from the top to the bottom of the thin film, until the electrode is fully lithiated ( $x = 2$ ). It is worth to notice how the morphology significantly differs between pristine and lithiated thin film. The thickness of the lithiated film is much more irregular and its average value is much higher (*ca.*  $2.3 \mu\text{m}$ ). Film expansion relates to the volume variation that accompanies the conversion reaction when  $\text{MgH}_2$  (unit cell  $31 \text{ \AA}^3$ ) transforms into  $\text{Mg}$  ( $23 \text{ \AA}^3$ ) and  $2\text{LiH}$  ( $2 \times 17 \text{ \AA}^3$ ), involving an expansion of 83% in volume. The fact that the thickness of the film shows an expansion above 83% ( $1 \mu\text{m}$  vs.  $2.3 \mu\text{m}$ ) could be attributed to a preferential expansion orientation due to the substrate constraints. However, despite such a high volume expansions, neither cracks nor decohesion between the film and the substrate are observed.

The presence of LiH in the lithiated parts has been confirmed by SAED analysis performed on  $x = 1.25$  close to the top and bottom of the sample. As shown in Figure 3.11, the SAED diffraction image from the brighter areas on top of the film can be indexed by the occurrence of Mg and LiH phases. In contrast, at the bottom of the thin film Mg and MgO are detected as for the pristine thin film (Figure 3.9).

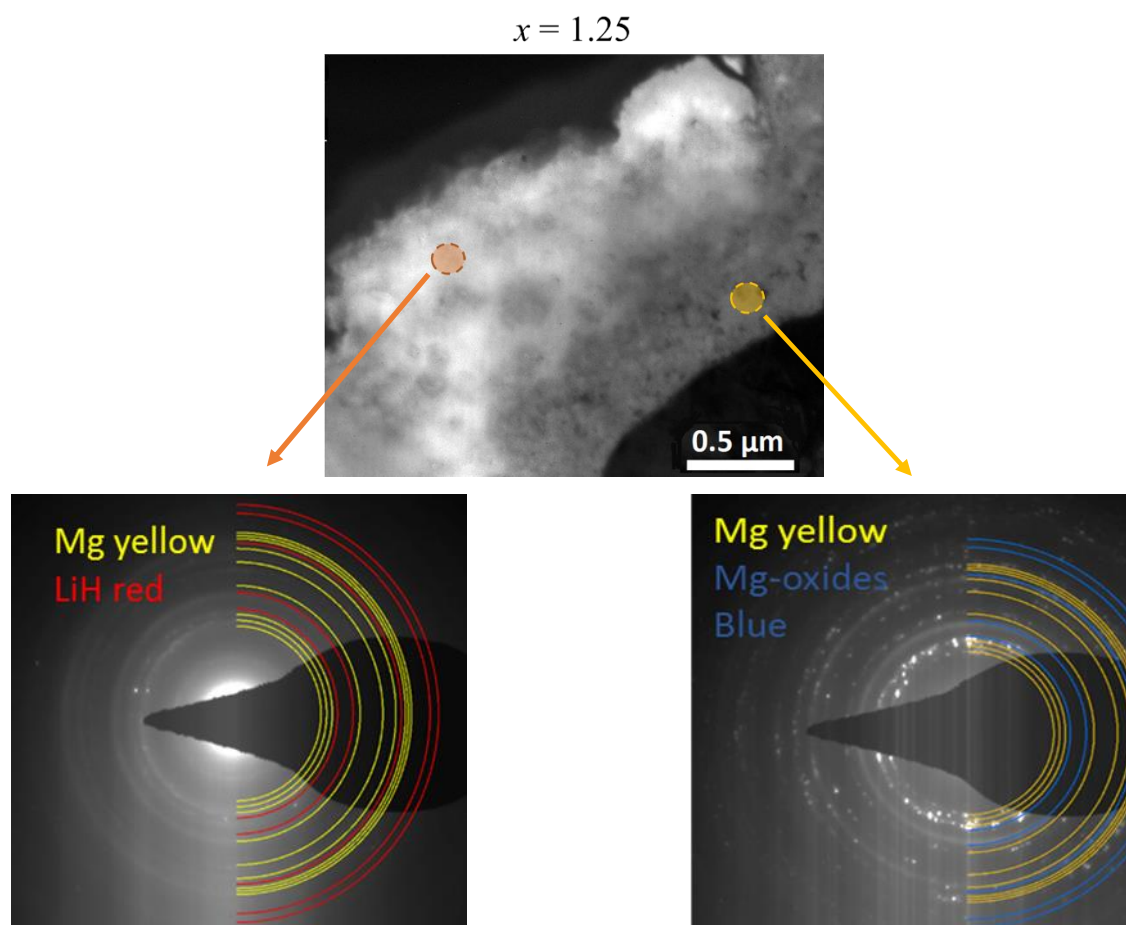


**Figure 3.11.** TEM bright field of electrode  $x = 1.25$  with SAED performed on the lithiated part (orange) and  $\text{MgH}_2$  (yellow).

Moreover, SEAD performed in different regions of the full lithiated sample  $x = 2$ , Figure 3.12, has detected the presence of LiH beside Mg, confirming the complete conversion of  $\text{MgH}_2$ , in agreement with the previous XRD analyses (Figure 3.8 pattern *e*).

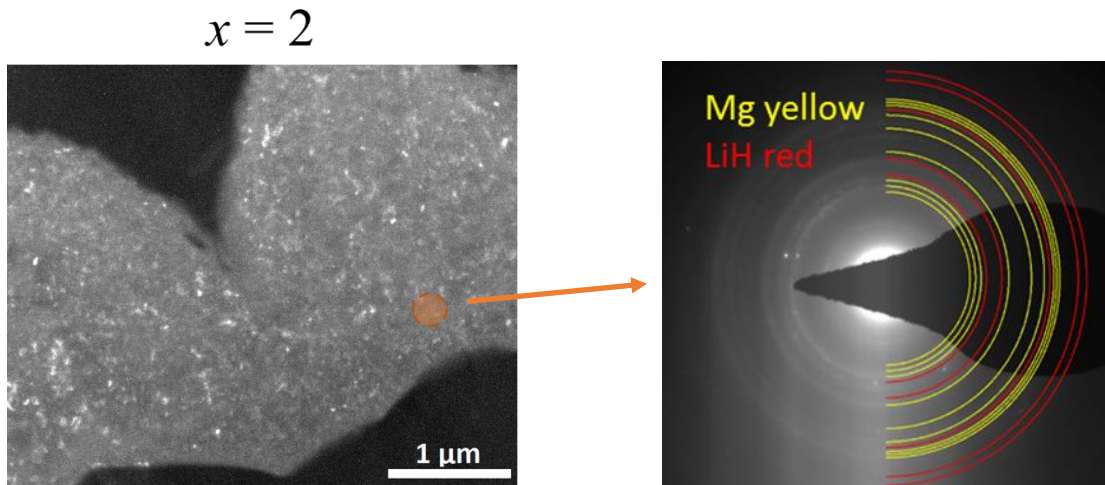


**Figure 3.12.** TEM dark field image of electrode  $x = 2$  with SEAD performed on the selected region (orange).

After the charge process, the thin film is partially recovered back to  $\text{MgH}_2$ , thus its cross section shows zones with different morphology. From the electrode, it was estimated a quantity of Li recovered of 0.5, hence its cross section should be comparable with sample  $x = 1.25$ . However, as shown in Figure 3.13, these two electrodes exhibit different cross sections.

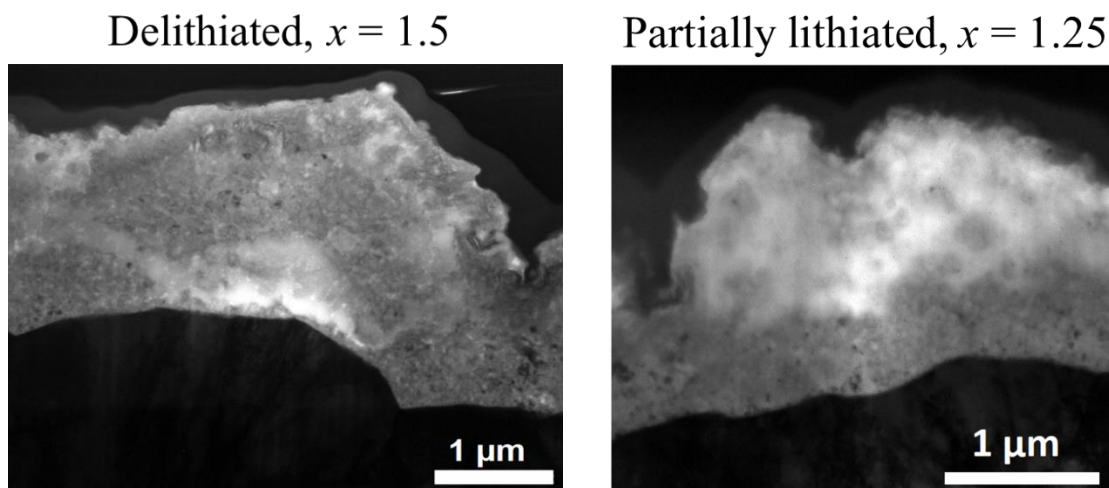


**Figure 3.13.** Comparison between the TEM bright field images of the cross sections of the delithiated (left) and the partially lithiated (right) thin films.

In Figure 3.13 is possible to notice that the white lithiated zones are randomly distributed along the cross section after the charge process (left image), whereas during the

lithiation a bright front was found starting on top of the thin film (right image). The average thickness of the delithiated sample is  $\sim 2 \mu\text{m}$ , while the partially lithiated is  $\sim 1.4 \mu\text{m}$ . This is in agreement with the fact that the electrode after the charge still has 1.5 Li stored, hence its volume is larger than  $x = 1.25$ . Moreover, it is worth to notice that the electrode has contracted with the extraction of lithium in comparison with the full lithiated sample (Figure 3.10,  $x = 2$ ), but no voids or detachment from the Cu current collector are found in the TEM image.

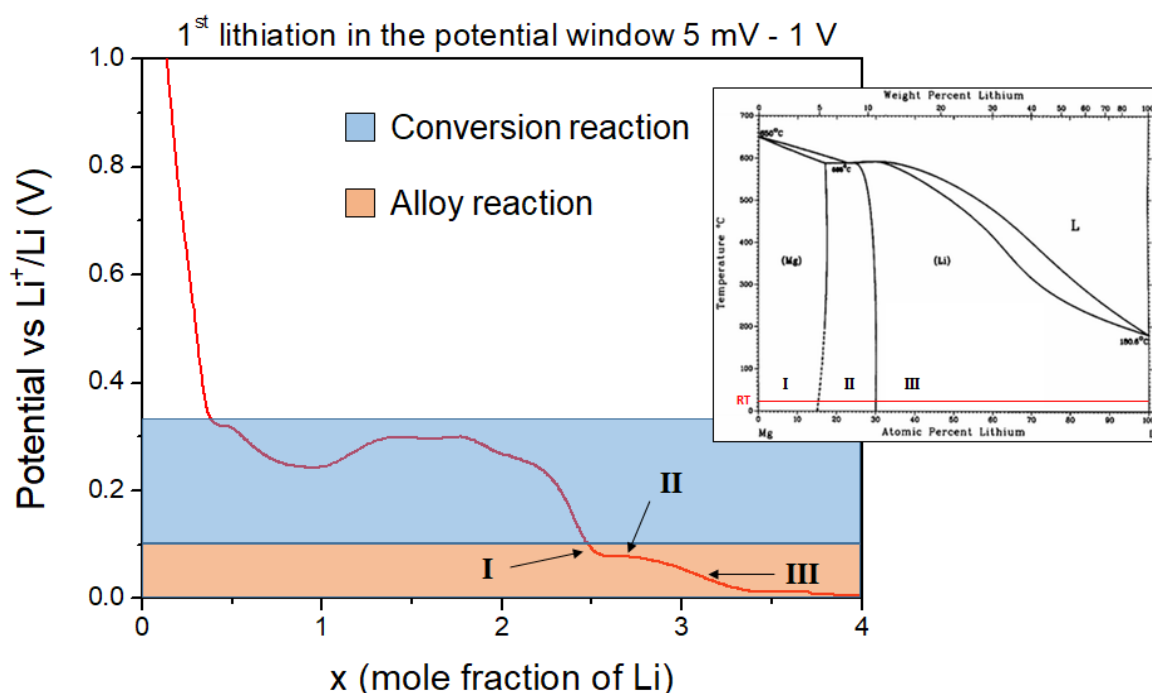
### 3 Discussion

MgH<sub>2</sub> thin films have been investigated as electrode material for Li-ion battery applications. The experiments have shown that to obtain the full lithiation of the electrode during the first discharge of the half-cell it is necessary to avoid the contamination of the hydrides by moisture and air. A protective aluminium layer on top of MgH<sub>2</sub> films has shown to properly evade the oxidation of the hydride, allowing the full conversion of MgH<sub>2</sub> to Mg and LiH. However, the conversion reaction has exhibited a poor reversibility already in the first cycle (Figure 3.6). Further investigation has been carried out with the purpose of understanding the causes of the loss in capacity. The main issues that can be hypothesized are: side reactions, such as Mg-Li alloying, interfering with the conversion reaction, cracks and voids due to the volume changes during lithiation/delithiation, poor electric conductivity because of the formation of LiH at the end of the discharge, poor mass transport during cycling.

#### 3.1 Effect of the Mg alloying on the conversion reaction

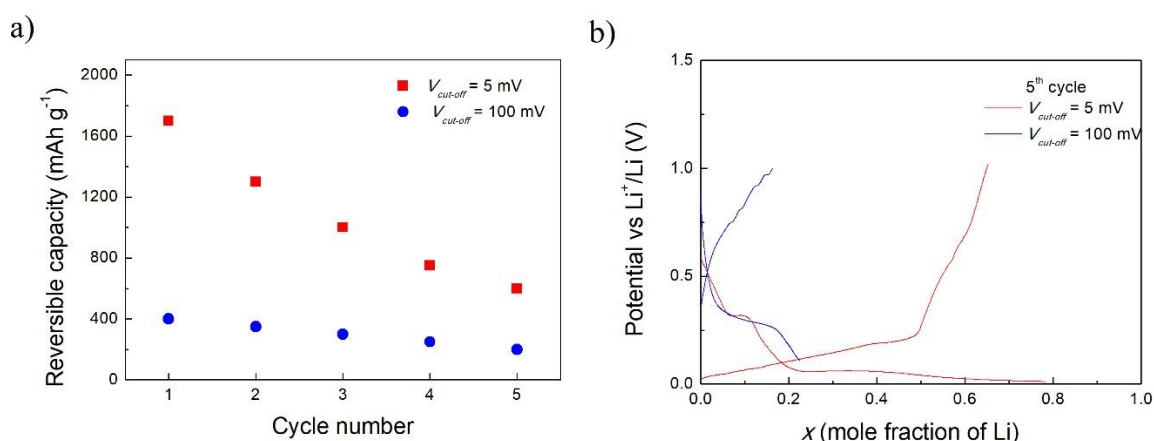
It was shown in Figure 3.6 that MgH<sub>2</sub> can store more than 2 Li atoms thanks to the contribution of Mg alloying. Looking in detail to the first lithiation of the thin film cycled down to  $V_{\text{cut-off}} = 5 \text{ mV}$ , it is possible to estimate the Mg alloying contribution and how it affects the conversion reaction. In Figure 3.14, which displays the potential profile of the first lithiation curve, we notice that, after the plateau of MgH<sub>2</sub> reduction at  $\sim 0.3 \text{ V}$ , the Mg alloying reaction is characterized by two slopes (marked as I and III) with a plateau (II) between them. This profile shape of the alloying can be understood at the light of the Mg-Li alloy phase diagram [16]. As reported by Park *et al.* [7], the alloying reaction begins around 0.1 V, and the first slope I is attributed, from the phase diagram, to solid solution of

Li in Mg up to 15% atomic Li content (*i.e.*  $\text{Mg}_{85}\text{Li}_{15}$ ). Then, a two-phase domain with both Mg and Li structures is found between 15% and 30% Li content (*i.e.* from  $\text{Mg}_{85}\text{Li}_{15}$  to  $\text{Mg}_{70}\text{Li}_{30}$ ), attributed to the plateau reaction II. Finally, for a quantity of Li above 30% into the alloy, a solid solution of Mg in Li is found, providing the last slope III of the reaction. At the end of the first discharge the quantity of lithium stored into the alloy is  $\Delta x = 1.5$  Li, forming  $\text{MgLi}_{1.5}$  (*i.e.*  $\text{Mg}_{40}\text{Li}_{60}$ ).



**Figure 3.14.** First lithiation of a  $\text{MgH}_2$  thin film with the contribution of the Mg alloying. The potential range of the conversion reaction is highlighted in blue, and for the alloy reaction in orange. The three steps of the alloy formation are marked as I, II and III. Insert: Mg-Li phase diagram, with the domains of the alloying reactions steps at room temperature (red line).

Mg alloying with lithium is a reversible reaction. Hence, as a benefit, it contributes to the reversible capacity stored on cycling. On the other hand, it leads to additional volume expansion and phase re-arrangement into the electrode. Therefore, we decided to study whether Mg alloying affects the reversibility of the conversion reaction. To this aim, thin films were cycled in different potential ranges to compare the reversible electrochemical capacities with ( $V_{\text{cut-off}} = 5$  mV) and without ( $V_{\text{cut-off}} = 0.1$  V) Mg alloying. Results are displayed in Figure 3.15.



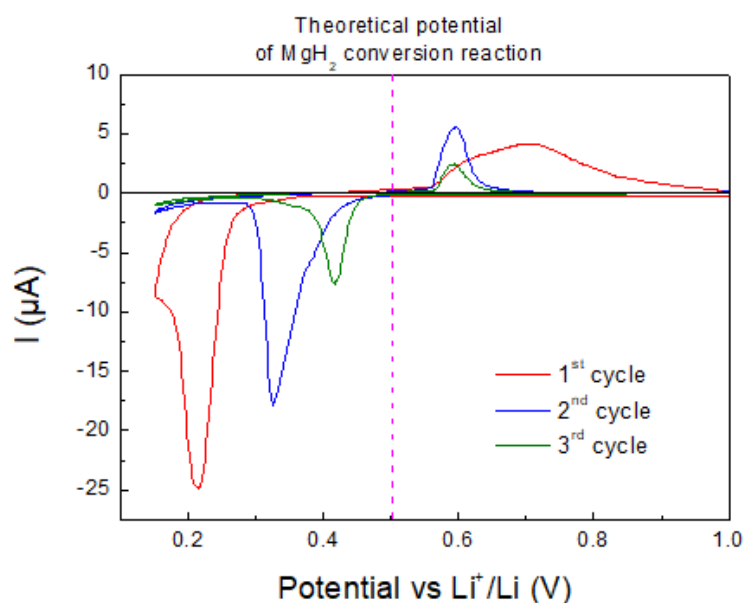
**Figure 3.15.** a) Reversible capacity of MgH<sub>2</sub> thin films on cycling with ( $V_{\text{cut-off}} = 5 \text{ mV}$ , red squares) and without ( $V_{\text{cut-off}} = 0.1 \text{ V}$ , blue circles) Mg-Li alloying. b) Potential vs. composition profile of both experiments in the fifth cycle.

Figure 3.15a shows the evolution of the reversible capacity with cycling for the two potential ranges. When Mg alloying occurs (red squares), the initial reversible capacity is  $1700 \text{ mAh g}^{-1}$ , and then decreases in the subsequent cycles. In contrast, without the alloying reaction (blue circles), the capacity in the first cycle is only  $400 \text{ mAh g}^{-1}$ . After five cycles, the capacity with the Mg-Li alloying decreases to  $600 \text{ mAh g}^{-1}$ , implying a loss of 65%, while the electrode without the side reaction exhibits a capacity of  $200 \text{ mAh g}^{-1}$ , *i.e.* 50% of the initial one. Not only the capacity decreases with a higher decay in presence of the alloy, but in Figure 3.15b can be also noticed that the extent of the potential plateau of the conversion reaction is shorter compared to the electrode with  $V_{\text{cut-off}} = 0.1 \text{ V}$ . The electrode with the alloying reaction exhibits a higher capacity ( $600 \text{ vs. } 200 \text{ mAh g}^{-1}$ ), but the main contribution comes from the Mg-Li reaction (0.7 Li), and 0.1 Li from the conversion reaction. On the other hand, without the alloy, 0.2 Li are stored thanks to the reaction between MgH<sub>2</sub> and Li. This suggests that Mg alloying is detrimental for the conversion or reformation of the hydride. Probably, the additional volume expansion caused by the Mg-Li alloying leads to mechanical damage and loss in contacts within the electrode. However, as shown in Figure 3.6, with or without the alloying reaction, the electrode exhibits a poor reversibility already in the first cycle, hence the Mg-Li formation cannot be asserted as one of the main issues for the reformation of MgH<sub>2</sub>.



### 3.2 Reversibility of the conversion reaction

The cyclic voltammetry of a thin film cycled between 0.1 V (*i.e.* without Mg alloying) and 1 V is shown in Figure 3.16. In the first cycle, a single cathodic peak related to the reduction of MgH<sub>2</sub> is observed at 0.21 V whereas a broad anodic peak attributed to its reformation is detected around 0.7 V. While cycling, both cathodic and anodic peaks shift to potentials closer to the theoretical one, *i.e.* 0.5 V (dashed line), implying an easier lithiation/delithiation compared to the first cycle. It is worth to notice that the first lithiation reaction exhibits an overpotential around 0.3 V, whereas the delithiation shows 0.2 V, compared to the theoretical potential of the conversion reaction. Moreover, the anodic peak shifts only between the first and second cycle, and then it is stable at 0.6 V. On the other hand, the cathodic peak shifts also in the third cycle, reaching 0.42 V. The fact that the lithiation reaction exhibits, during the first cycles, a higher overpotential compared to the delithiation reaction, might be due to the Al protective layer, which needs to be reduced before letting lithium to penetrate into the film and reacting with MgH<sub>2</sub>. Furthermore, the lithiation of the hydride implies nucleation and rearrangement of new phases (*i.e.* Mg and LiH), which require additional energy.



**Figure 3.16.** Cyclic voltammetry of Al-covered MgH<sub>2</sub> thin film in the potential range 0.1 – 1.0 V, performed with a scan rate of 0.3 mV min<sup>-1</sup>.

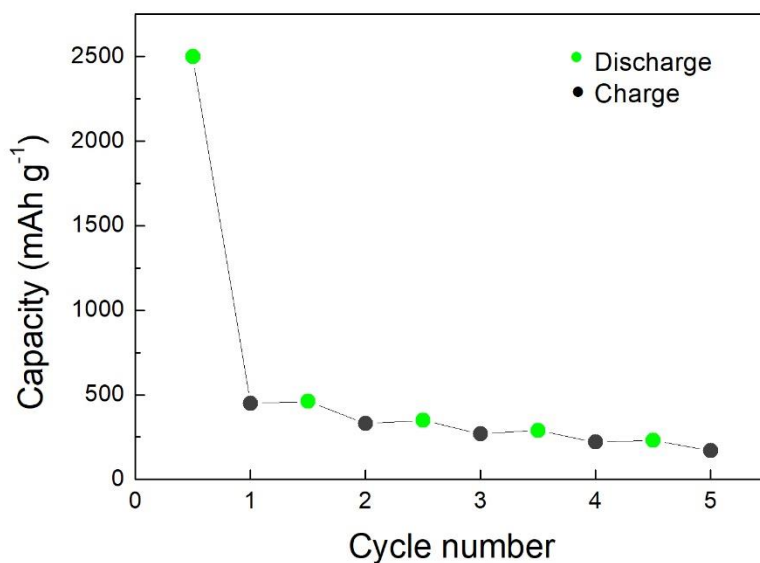


**Figure 3.17.** Electrochemical capacity during lithiation (green circles) and delithiation (black circles) of Al-covered MgH<sub>2</sub> thin film in galvanostatic analysis with C/50.

Figure 3.17 displays the capacity provided by the electrode during discharge/charge cycling. At the end of the first discharge the electrode is fully lithiated ( $>2000 \text{ mAh g}^{-1}$ ), but only a small part of MgH<sub>2</sub> is restored during the charge ( $450 \text{ mAh g}^{-1}$ ). This implies that the extraction of Li from the thin film in the first cycle is a key issue. Note for all cycles in Figure 3.17 that the charge capacity obtained during delithiation (green circles) is comparable to the capacity achieved in the subsequent lithiation (black circles). This means that the quantity of extracted Li can be fully re-stored into the electrode in the successive cycle. On the other hand, after a lithiation, the capacity value always decreases. These results highlight the fact that lithium can always move into the electrode, but at each lithiation some structural modification occurs, which impedes the recovering of Li during the next delithiation.

These structural modifications might include cracks and voids, phase segregation, and growth of domains (*e.g.* large insulating LiH domains) which don't allow a proper mass transport. TEM investigation of the cross section of the thin film (Figure 3.10 and 3.13) has shown the changes in the morphology during the first galvanostatic cycle. Indeed, the thin film expands during lithiation because of the formation of Mg and LiH, and it shrinks while Li is extracted. However, no cracks or detachment from the Cu current collector have been noticed during the different steps of discharge/charge, suggesting that the electrode

damaging cannot be one of the main cause of the poor reversibility at least during the first cycle. To evaluate possible change in conductivity due to the formation of LiH, EIS measurements have been performed during the first discharge/charge cycle. Figure 3.18 shows the Nyquist plots acquired on the pristine thin film (black line), at the end of the lithiation (red line), and after the delithiation (blue line).

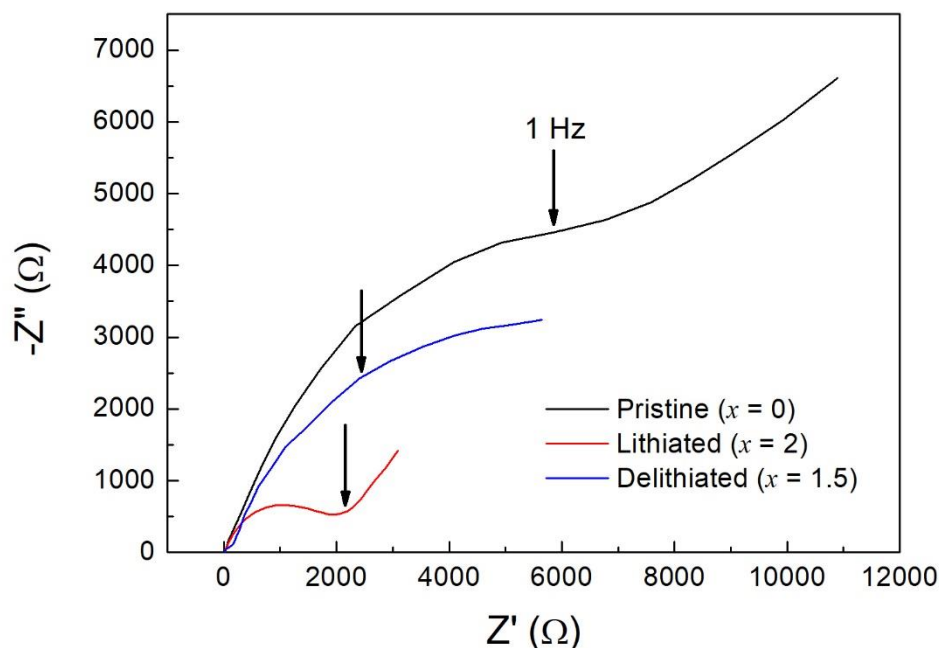


**Figure 3.18.** Impedance profiles of the thin film obtained at different reaction steps within the first galvanostatic cycle. Frequency range from 0.1 Hz to 1 MHz.

For the analysis, because of the complexity of the system (which consists in different solid phases, Cu current collector, liquid electrolyte, etc.), only the overall cell resistance is considered. The pristine thin film exhibits a high impedance ( $Z$ ), which decreases when lithium is provided within the electrode, implying that the lithiated electrode Mg+LiH has a lower electric resistance than pure  $\text{MgH}_2$ . After the delithiation,  $\text{MgH}_2$  is partially restored, and so the overall resistance increases. Because of the presence of Mg, the delithiated electrode still exhibits an impedance lower compared to the pristine thin film. Owing the fact that the lithiation was complete when the cell possessed the highest resistance, the poor reversibility cannot be attributed to the presence of insulating LiH phase, since Mg phase provides a good electronic path (*i.e.* low resistance).

## 4 Conclusions

Magnesium hydride has been deposited on copper foil by means of reactive plasma-assisted microwave/radio frequency sputtering, preparing thin films with a thickness of 1  $\mu\text{m}$ . The as-deposited thin films have been studied as positive electrodes in Li-ion half-cells. Galvanostatic cycling tests have shown that the electrochemical reactivity of the  $\text{MgH}_2$  thin film strongly depends on its surface state. Indeed, thin films covered with a nanometric layer, 13 nm in thickness, of aluminium do undergo a conversion reaction with lithium during the first discharge, whereas uncovered thin films have a limited reactivity. Uncovered electrodes needed an activation process previous to the conversion reaction evidencing the presence of a passivation layer on the surface of the electrode. The formation of this layer has been attributed to the oxidation of  $\text{MgH}_2$  [8] thin films during the handling of the samples outside the sputtering chamber.

Al-coated thin films electrodes showed a complete lithiation during the first discharge, storing 2.5 Li. The excess in capacity has been credited to the reaction of the Al overlayer with lithium forming a Li-Al-O composite [12]. As for the charge sweep, lithium could only be partially extracted (25%) from the film, which evidences a poor reversibility of the conversion reaction. Beside the conversion reaction of  $\text{MgH}_2$  with lithium, the so formed Mg undergoes an alloying reaction with lithium when the potential decreases below 0.1 V vs.  $\text{Li}^+/\text{Li}$ . This reaction can provide additional capacity during cycling, but its occurrence has revealed to slightly hinder the conversion reaction.

XRD and TEM analysis have been carried out to investigate the conversion reaction path and the electrode morphology, respectively, in the first discharge/charge cycle. The reaction between  $\text{MgH}_2$  and Li has been noticed to start from the top of the film, and then proceeding to the bottom. The thickness of the thin film increases with the quantity of Li stored due to expansion caused by the formation of Mg and LiH phases. Compared to the pristine film (1  $\mu\text{m}$  thick), the lithiated electrode has shown an average thickness of 2.3  $\mu\text{m}$ , implying an expansion greater than the theoretical one (130% vs. 83%, respectively). This effect has been attributed to the typical preferential growth of thin films along the Z-axis.

At the end of the discharge  $\text{MgH}_2$  is no longer detected, and the electrode is composed exclusively by Mg surrounded by a LiH matrix, which confirms the complete lithiation of the hydride. During delithiation  $\text{MgH}_2$  is partially restored, and it is detected beside Mg and LiH phases.

In many cases, the poor reversibility of hydride conversion reactions is attributed to the loss of electronic contact, low conductivity inside the electrode and cracks due to the volume changes during cycling. Here, we have shown that despite a high irreversibility in the conversion reaction (75% capacity lost in the first cycle), no cracks, voids or detachment of the thin film from the current collector occur in the first cycle. Moreover, the internal resistance has shown to decrease during lithiation, implying a better electronic conductivity at the end of the discharge. In the light of these results, the main reason for the poor reversibility of the conversion reaction might be attributed to the limited mobility of species, such as H, and Mg within the electrode.

## References

1. Higuchi, K. *et al.* In situ study of hydriding–dehydriding properties in some Pd/Mg thin films with different degree of Mg crystallization. **295**, 484–489 (1999).
2. Borgschulte, A., Rector, J. H., Schreuders, H., Dam, B. & Griessen, R. Electrohydrogenation of MgH<sub>2</sub>-thin films. *Appl. Phys. Lett.* **90**, 71912 (2007).
3. Isidorsson, J., Arwin, H. & Griessen, R. Optical properties of MgH<sub>2</sub> measured in situ in a novel gas cell for ellipsometry/spectrophotometry. *Phys. Rev. B.* **68**, 115112 (2014).
4. Letters, A. P. & Columbia, B. Hydrogen storage cycling of MgH<sub>2</sub> thin film nanocomposites catalyzed by bimetallic CrTi. *Appl. Phys. Lett.* **97**, 083106 (2010). doi:10.1063/1.3479914
5. Giebels, I. A. M. E., Isidorsson, J. & Griessen, R. Highly absorbing black Mg and rare-earth-Mg switchable mirrors. *Phys. Rev. B.* **69**, 205111 (2004). doi:10.1103/PhysRevB.69.205111
6. Oumellal, Y., Rougier, A., Nazri, G. A., Tarascon, J.-M. & Aymard, L. Metal hydrides for lithium-ion batteries. *Nat. Mater.* **7**, 916–921 (2008).
7. Park, C. M., Kim, Y. U., Kim, H. & Sohn, H. J. Enhancement of the rate capability and cyclability of an Mg-C composite electrode for Li secondary batteries. *J. Power Sources* **158**, 1451–1455 (2006).
8. Klassen, T., Bormann, R. & Ferna, A. Chemical and microstructural study of the oxygen passivation behaviour of nanocrystalline Mg and MgH<sub>2</sub>. *Appl. Surf. Sci.* **252**, 2334–2345 (2006).
9. Li, S. *et al.* High-rate aluminium yolk-shell nanoparticle anode for Li-ion battery with long cycle life and ultrahigh capacity. *Nat. Commun.* **6**, 7872 (2015). doi:10.1038/ncomms8872
10. Hamon, Y. *et al.* Aluminum negative electrode in lithium ion batteries. *J. Power Sources* **97–98**, 185–187 (2001).
11. Cho, J., Kim, Y. J. & Park, B. Novel LiCoO<sub>2</sub> Cathode Material with Al<sub>2</sub>O<sub>3</sub> Coating for a Li Ion Cell. **4**, 3788–3791 (2016).

12. Liu, Y. *et al.* In Situ Transmission Electron Microscopy Observation of Pulverization of Aluminum Nanowires and Evolution of the Thin Surface Al<sub>2</sub>O<sub>3</sub> Layers during Lithiation and Delithiation Cycles. *Nano* **11**, 4188–94 (2011).
13. Nguyen, H. T. *et al.* Alumina-coated silicon-based nanowire arrays for high quality Li-ion battery anodes. *J. Mater. Chem.* **22**, 24618 (2012).
14. Paik, B., Jones, I. P., Walton, A., Mann, V. & Book, D. MgH<sub>2</sub> → Mg phase transformation driven by a high-energy electron beam : An in situ transmission electron microscopy study. *Philos. Mag. Lett.* **90**, 1–7 (2010).  
doi:10.1080/09500830903272892
15. Surrey, A., Schultz, L. & Rellinghaus, B. Electron beam induced dehydrogenation of MgH<sub>2</sub> studied by VEELS. *Adv. Struct. Chem. Imaging* 1–9 (2016).  
doi:10.1186/s40679-016-0022-1
16. Manchester, F.D. Phase Diagrams of Binary Hydrogen Alloys. *ASM International* (2000).

# CHAPTER 4

MgH<sub>2</sub>+TiH<sub>2</sub> as anodes  
of Li-ion batteries





# Content

<b>1</b>	<b>Synthesis of MgH<sub>2</sub>+TiH<sub>2</sub> nanocomposites</b>	<b>111</b>
1.1	Hydrogenation during RBM	111
1.2	Influence of TiH <sub>2</sub> on Mg hydrogenation kinetics	112
<b>2</b>	<b>Structural properties and Phase distribution of MgH<sub>2</sub>+TiH<sub>2</sub> composites</b>	<b>114</b>
2.1	Structural properties	114
2.2	Phase distribution	118
<b>3</b>	<b>Electrochemical properties</b>	<b>118</b>
3.1	Galvanostatic cycling of pure MgH <sub>2</sub> and TiH <sub>2</sub>	118
3.2	Galvanostatic cycling of MgH <sub>2</sub> +TiH <sub>2</sub> nanocomposites	121
3.2.1	First discharge/charge cycle	121
3.2.2	Reversibility of the conversion reaction for MgH <sub>2</sub> and TiH <sub>2</sub> phases	123
3.2.2.1	Cycling of MgH <sub>2</sub> phase	123
3.2.2.2	Cycling of TiH <sub>2</sub> phase	125
3.2.2.3	Effect of Mg alloying on the cycling of MgH <sub>2</sub> +TiH <sub>2</sub> composites	126
3.3	Detailed electrochemical study of 0.7MgH <sub>2</sub> +0.3TiH <sub>2</sub> composite	129
3.3.1	Reversibility of the overall conversion reaction	129
3.3.2	Reversibility and cycle-life of MgH <sub>2</sub> conversion reaction	130
3.3.3	Reversibility and cycle-life of TiH <sub>2</sub> conversion reaction	131
<b>4</b>	<b>Discussion</b>	<b>132</b>
4.1	Synthesis and structural properties of MgH <sub>2</sub> +TiH <sub>2</sub> nanocomposites	132
4.2	Electrochemical analyses	134
4.2.1	Reversibility of each hydride phase	135
4.2.1.1	Influence of TiH <sub>2</sub> on the reversibility of MgH <sub>2</sub> conversion reaction	135
4.2.1.2	Enhanced reversibility of TiH <sub>2</sub> phase in a Mg-rich electrode	137
4.2.1.3	Influence of Mg-Li alloying on the overall conversion reaction	142
<b>5</b>	<b>Conclusions</b>	<b>145</b>
	<b>References</b>	<b>148</b>



The objective of this chapter is to investigate the electrochemical properties of several  $\text{MgH}_2+\text{TiH}_2$  composites used as active materials in lithium-ion cells. These are dihydride compounds with well-known structural and chemical properties and high theoretical capacity: 2036 and 1074  $\text{mAh g}^{-1}$  for  $\text{MgH}_2$  and  $\text{TiH}_2$ , respectively. Moreover, synergetic effects between them are expected as reported in the literature for hydrogen storage applications [1–3], which could enhance the electrochemical activity as compared to single hydride ( $\text{MgH}_2$  or  $\text{TiH}_2$ ) electrodes. The composites have been synthesized by reactive ball milling (RBM), and their structural properties investigated by X-ray diffraction (XRD) and transmission electron microscopy (TEM). Galvanostatic and cyclic voltammetry tests have been carried out in different potential windows in order to evaluate the electrochemical properties of the composites as a function of their composition, as well as the contribution of each hydride as electrode material.

## **1 Synthesis of $\text{MgH}_2+\text{TiH}_2$ nanocomposites**

### **1.1 Hydrogenation during RBM**

The synthesis of  $\text{MgH}_2+\text{TiH}_2$  composites was achieved by reactive ball milling (RBM) under hydrogen atmosphere as described in Chapter 2, section 1.1. Thanks to the monitoring system, it was possible to recorder the evolution of pressure and temperature into the vial as a function of time during the milling process. A typical pressure/temperature evolution recorded during the formation of one  $\text{MgH}_2+\text{TiH}_2$  composite is shown in Figure 4.1. The milling was carried out in two cycles of 120 minutes with 120 minutes rest in between for cooling down the vial. At the beginning of the process, the temperature increases because of the frictions and collisions of the stainless-steel balls with the walls of the jar. This leads also to an increase of the pressure due to thermal gas expansion. After that, the pressure drops because hydrogen is absorbed during the formation of the hydride phases. When the hydrogenation is completed, a pressure plateau is observed. At the end of the first milling cycle, both pressure and temperature decrease to equilibrium values at ambient conditions during the rest time. The second cycle does not show any additional hydrogen absorption, being the change in pressure due to thermal variations induced by milling and resting. Thus, the second cycle can be used to calibrate the gas temperature that differs from the measured vial temperature. In this way, it is possible to calculate accurately the hydrogen uptake corresponding to the pressure change observed during the first cycle [4].

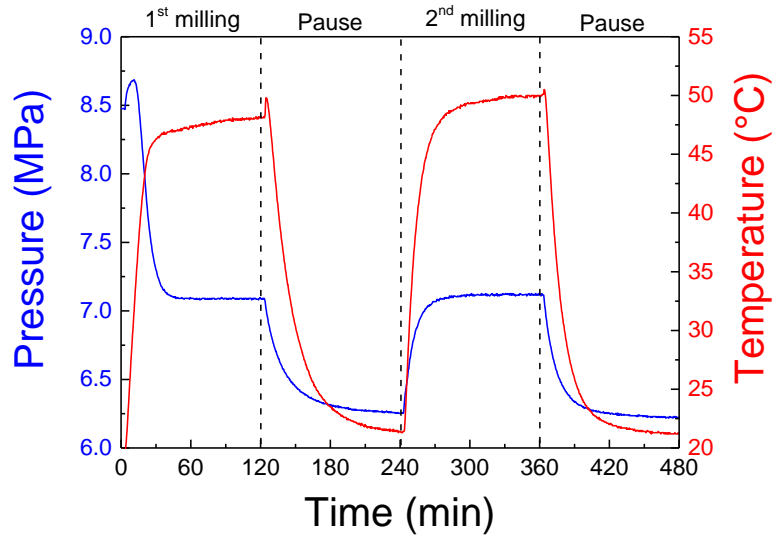


**Figure 4.1.** Evolution of the hydrogen pressure (blue line) and the vial temperature (red line) as a function of milling time during the synthesis of the composite  $0.5\text{MgH}_2+0.5\text{TiH}_2$ .

## 1.2 Influence of $\text{TiH}_2$ on Mg hydrogenation kinetics

Different  $y\text{MgH}_2+(1-y)\text{TiH}_2$  mixtures, with molar compositions  $y = 0, 0.2, 0.5, 0.6, 0.7, 0.8,$  and  $1,$  were synthesized for this study. The corresponding absorption curves are displayed in Figure 4.2. Clearly, overall hydrogenation kinetics of Ti-rich composites are faster than Mg-rich ones. This is due to the initial formation of  $\text{TiH}_2$ , which enhances the kinetics of Mg hydrogenation. Indeed, the formation of  $\text{TiH}_2$  occurs during the first minutes of ball milling, and being a brittle phase [5] creates fresh clean surfaces in Mg that facilitate hydrogen absorption. Moreover, because of the highest mobility of hydrogen in  $\text{TiH}_2$  than  $\text{MgH}_2$  [6,7], titanium hydride can act as a gateway for a faster diffusion of hydrogen towards Mg phase.

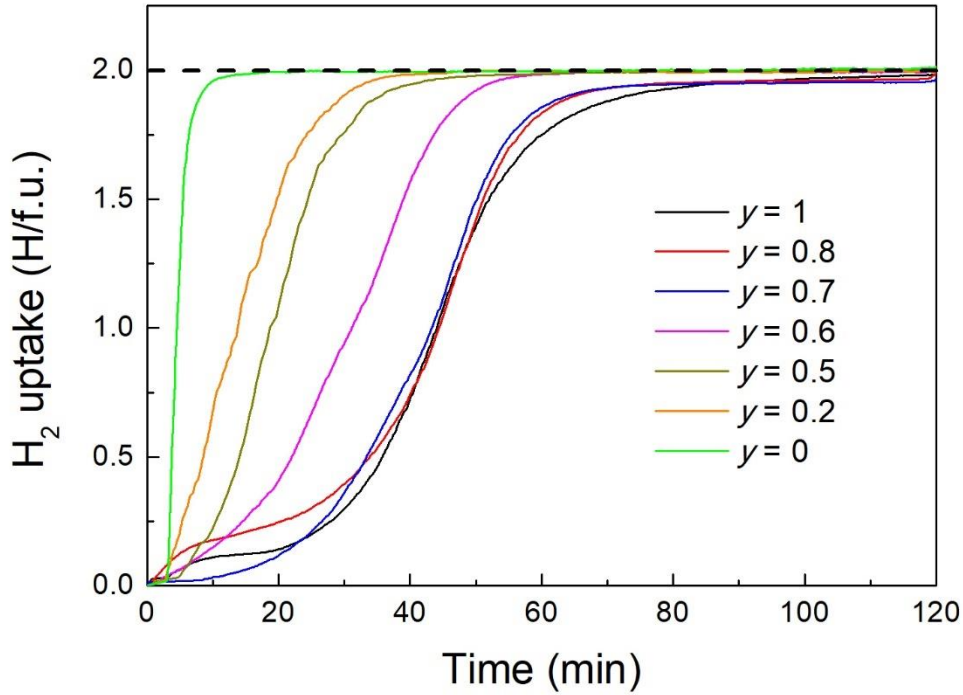


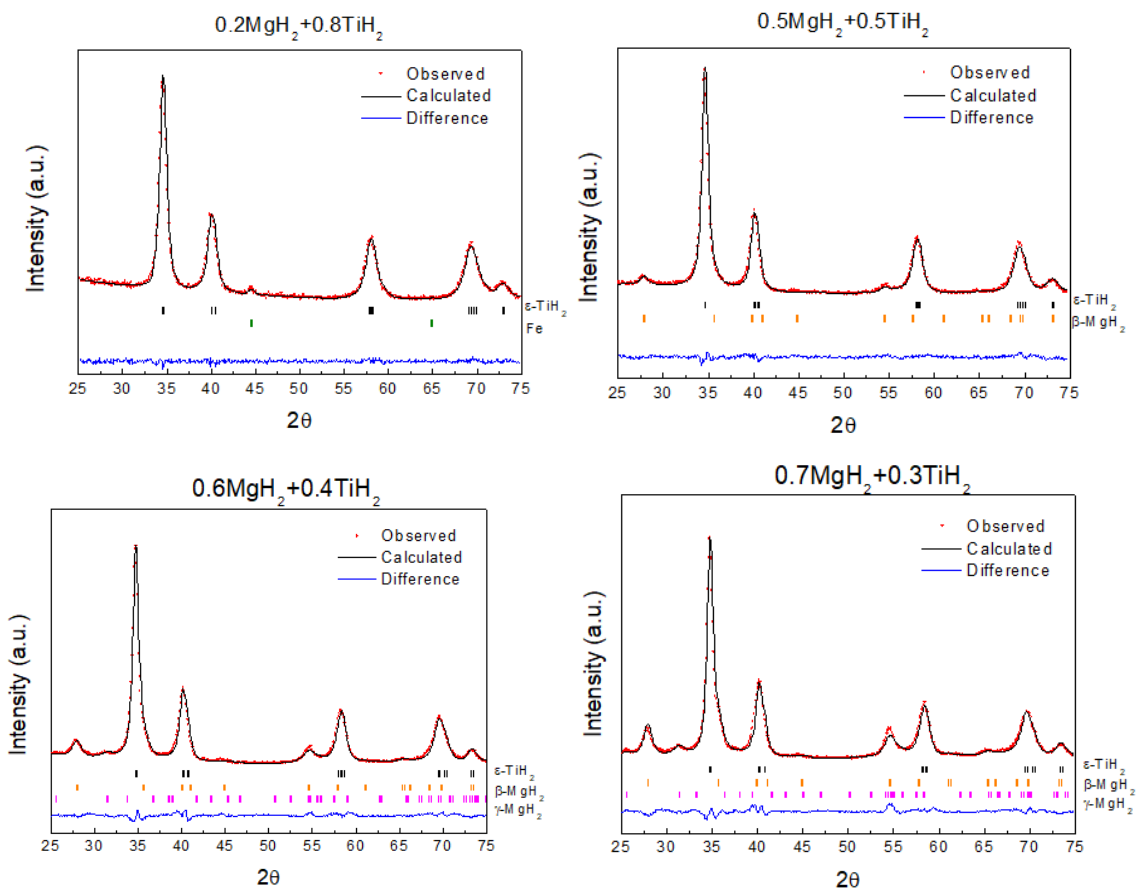
**Figure 4.2.** Hydrogen absorption curves measured during synthesis of  $y\text{MgH}_2+(1-y)\text{TiH}_2$  composites by RBM of Mg and Ti under hydrogen gas.

The overall hydrogen uptake during the composite formation varies between 1.96 and 2.0 H/f.u.. This confirms the full hydrogenation of both Ti and Mg. The faster absorption kinetics of the Ti-rich composites compared to the Mg-rich is remarkable. Indeed, the hydrogenation of sample  $0.2\text{MgH}_2+0.8\text{TiH}_2$  (*i.e.*  $y = 0.2$ ) is completed in less than 50 minutes, whereas that of composite  $0.8\text{MgH}_2+0.2\text{TiH}_2$  (*i.e.*  $y = 0.8$ ) takes almost 80 minutes.

## 2 Structural properties and Phase distribution of $\text{MgH}_2+\text{TiH}_2$ composites

### 2.1 Structural properties

The structural properties of the composites prepared by reactive ball milling were investigated by means of X-ray diffraction. Information about lattice parameters, crystallite size and phase amount were calculated for each composite applying the Rietveld method. The XRD patterns and Rietveld analysis, as well as their crystallographic data, are reported in Figure 4.3 and Table 4.1 respectively.



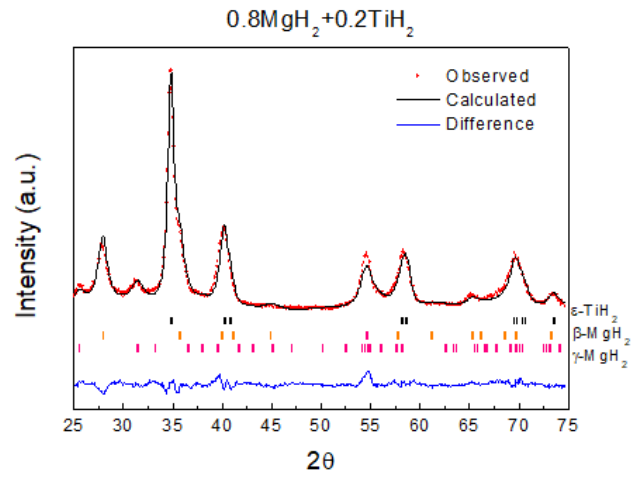


**Figure 4.3.** Rietveld analysis of XRD patterns for the  $\text{MgH}_2 + \text{TiH}_2$  composites.



**Table 4.1.** Crystallography data from Rietveld refinements of the XRD patterns of the as milled  $\gamma$ MgH<sub>2</sub>-(1- $\gamma$ )TiH<sub>2</sub> composites, where  $D$  is the average crystallite size,  $R$  the factors for the quality of the refinement, and  $\chi^2$  the chi-square (see Chapter 2 section 2.1.1 for details).

Composite	Phase	Space group	Amount (%)	Lattice parameters (Å)			$D$ (nm)	$R_B$	$R_p$	$R_{WP}$	$R_{exp}$	$\chi^2$
				$a$	$b$	$c$						
$\gamma = 0.2$	$\epsilon$ -TiH <sub>2</sub>	$I4/mmm$	99	3.187	3.187	4.461	8	0.6	7.1	7.1	6.1	1.35
	$\alpha$ -Fe	$Fm\bar{3}m$	1	2.875	2.875	2.875	/	1.6				
$\gamma = 0.5$	$\epsilon$ -TiH <sub>2</sub>	$I4/mmm$	89	3.182	3.182	4.455	10	1.9	8.1	8.3	5.0	2.77
	$\beta$ -MgH <sub>2</sub>	$P4_2/nmm$	11	4.523	4.523	3.036	7	5.3				
$\gamma = 0.6$	$\epsilon$ -TiH <sub>2</sub>	$I4/mmm$	54	3.176	3.176	4.432	9	2.7	6.2	7.7	3.5	4.86
	$\beta$ -MgH <sub>2</sub>	$P4_2/nmm$	23	4.510	4.510	3.037	5	2.4				
	$\gamma$ -MgH <sub>2</sub>	$Pbcn$	23	4.624	5.311	4.897	3	1.6				
$\gamma = 0.7$	$\epsilon$ -TiH <sub>2</sub>	$I4/mmm$	46	3.173	3.173	4.424	10	3.0	7.2	9.1	3.2	7.96
	$\beta$ -MgH <sub>2</sub>	$P4_2/nmm$	33	4.515	4.515	3.031	5	5.1				
	$\gamma$ -MgH <sub>2</sub>	$Pbcn$	21	4.572	5.387	4.942	4	2.8				
$\gamma = 0.8$	$\epsilon$ -TiH <sub>2</sub>	$I4/mmm$	43	3.171	3.171	4.419	11	1.7	7.0	8.1	4.2	3.73
	$\beta$ -MgH <sub>2</sub>	$P4_2/nmm$	41	4.518	4.518	3.029	6	2.4				
	$\gamma$ -MgH <sub>2</sub>	$Pbcn$	16	4.564	5.399	4.925	4	3.4				

For the Ti-rich composite  $y = 0.2$ , the main phase is identified as tetragonal  $\epsilon$ -TiH<sub>2</sub>. In addition,  $\alpha$ -Fe is observed as a minor secondary phase. Its presence is attributed to the highly abrasive properties of titanium hydride, which continuously scratches the walls of the jar during milling. For this composite, MgH<sub>2</sub> phase contribution is not detected likely due its low amount, poor crystallinity and low scattering power of Mg compared to Ti. For the equimolar mixture  $y = 0.5$ , the XRD pattern can be indexed with two phases:  $\epsilon$ -TiH<sub>2</sub> and the tetragonal rutile-type  $\beta$ -MgH<sub>2</sub>. Here,  $\alpha$ -Fe is not detected revealing lower iron contamination due to reduced abrasion by the milled material on increasing the MgH<sub>2</sub> amount. Besides the two previous hydride phases, orthorhombic  $\gamma$ -MgH<sub>2</sub> is detected for Mg-rich composites  $y = 0.6, 0.7$  and  $0.8$ .  $\gamma$ -MgH<sub>2</sub> is a metastable polymorph of magnesium hydride commonly found in ball-milled magnesium hydride, which formation is stabilized by mechanical strain [8].

The average crystallite size ( $D$ ) of the different phases calculated from the Scherrer equation is comprised between 3 nm and 11 nm. Moreover, it should be noticed that all composites contained only MgH<sub>2</sub> and TiH<sub>2</sub> pure hydrides with no occurrence of ternary Mg-Ti-H phases. Therefore, all milled materials can be denoted as MgH<sub>2</sub>+TiH<sub>2</sub> nanocomposites. Nanostructuring is a significant feature of these composites. As described in Chapter 1 section 3, metal hydrides as electrode materials suffer from sluggish kinetics at room temperature, but the reactivity can be enhanced by nanostructuring, providing a high surface area and short diffusion paths for the reactants.

## 2.2 Phase distribution

With the purpose of getting information about the spatial distribution of the hydride phases within the nanocomposites, HAADF TEM was used for the as-milled Ti-rich ( $y = 0.2$ ), equimolar ( $y = 0.5$ ), and Mg-rich ( $y = 0.8$ ) composites. The images are displayed in Figure 4.4.

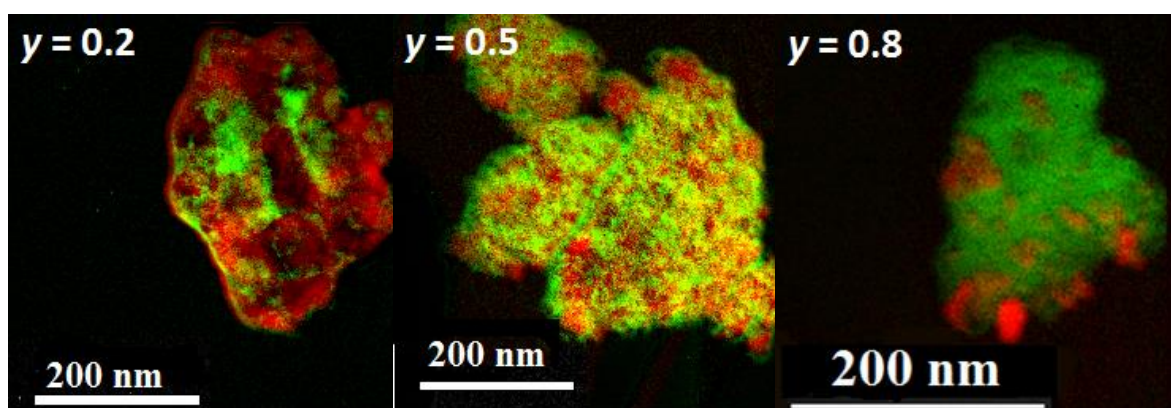


**Figure 4.4.** HAADF TEM images of as-milled nanocomposites  $y = 0.2$  (left),  $0.5$  (middle), and  $0.8$  (right).  $\text{TiH}_2$  phase is coloured in red, and  $\text{MgH}_2$  phase in green.

For all composites, the TEM analysis confirms the formation of the hydride phases  $\text{TiH}_2$  and  $\text{MgH}_2$ . Both phases are intimately mixed at the nanoscale forming particles of the order of hundreds of nanometres. In contrast to XRD analysis, the  $\text{MgH}_2$  phase is detected as expected for the Ti-rich ( $y = 0.2$ ) composite.

## 3 Electrochemical properties

### 3.1 Galvanostatic cycling of pure $\text{MgH}_2$ and $\text{TiH}_2$

Pure  $\text{MgH}_2$  ( $y = 1$ ) and  $\text{TiH}_2$  ( $y = 0$ ) synthesized by RBM have been studied separately as active materials in Li-ion half-cells. The first galvanostatic cycle, performed with C/50, of  $\text{MgH}_2$  and  $\text{TiH}_2$  is reported in Figure 4.5 and 4.6 respectively.

In Figure 4.5 shows the first discharge/charge cycle of  $\text{MgH}_2$  electrode in two different potential windows. In red is shown the cycle in which, beside the conversion reaction of the hydride, also the Mg-Li alloying reaction occurs ( $V_{\text{cut-off}} = 5$  mV). In blue, there is the cycle without the contribution of the alloying reaction ( $V_{\text{cut-off}} = 0.15$  V).

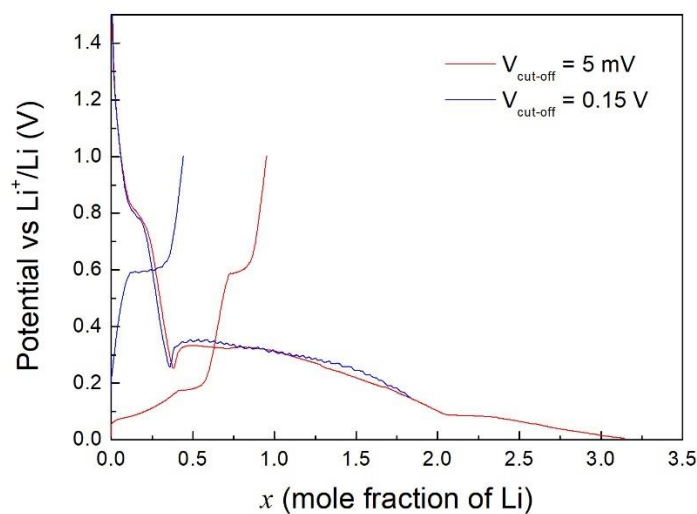


**Figure 4.5.** Evolution of the potential (V) as a function of  $x$  (mole fraction of Li) during the first discharge/charge cycle of  $\text{MgH}_2$  electrode. The half-cells have been cycled in the potential window 5 mV – 1 V (red line), and 0.15 V – 1 V (blue line), with a regime of C/50.

During the lithiation of  $\text{MgH}_2$  electrode, a shoulder, related to the irreversible decomposition of the liquid electrolyte on the surface of the conductive carbon forming the solid electrolyte interface (SEI) [9,10], is noticed around 0.8 V. Afterwards, a plateau for the conversion reaction of  $\text{MgH}_2$  with Li is found at 0.33 V. When further lithium is provided (red line), the alloying reaction between the freshly formed Mg and Li occurs [11–13]. Like for the  $\text{MgH}_2$  thin film (Chapter 3, section 2), this reaction occurs below 0.1 V, and exhibits a first slope, followed by a plateau around 0.08 V, and then a final slope down to  $V_{\text{cut-off}}$ . When the discharge is interrupted at 0.15 V (blue line), the quantity of lithium stored into the electrode ( $x$ , Li equivalents) is 1.8 Li, implying a not complete conversion of  $\text{MgH}_2$ . On the other hand, because of the contribution of Mg-Li alloying, 3.1 Li are stored when the electrode is cycled down to 5 mV, suggesting a complete lithiation ( $x > 2$ ).

On delithiation, Mg is recovered from the alloy below 0.2 V, and for both electrodes, the reformation of  $\text{MgH}_2$  is found as a plateau at 0.6 V. At the end of the charge, 0.44 Li and 0.95 Li are extracted for  $V_{\text{cut-off}} = 0.15$  V and 5 mV, implying a reversibility within the first cycle of 25% and 31% respectively. However, it is worth to notice that the extent of the plateau related to the restoring of the hydride is longer for the half-cell with

$V_{\text{cut-off}} = 0.15 \text{ V}$ , 0.44 Li vs. 0.38 Li, respectively. These results are in agreement with the previous assertions on  $\text{MgH}_2$  thin film, *i.e.* the occurring of the Mg-Li alloying reaction slightly decreases the reformation of  $\text{MgH}_2$  during cycling.

Figure 4.6 shows the potential vs. composition curves of  $\text{TiH}_2$  electrode cycled in a potential window between 5 mV and 1 V, with a C-rate of C/50.

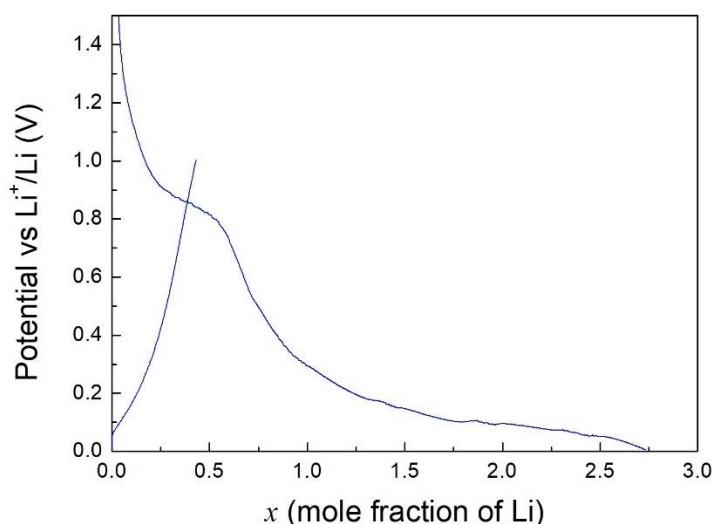


**Figure 4.6.** First galvanostatic cycle of  $\text{TiH}_2$  electrode in a Li-ion half-cell, performed in the range 5 mV to 1 V, with C/50.

On lithiation, after the SEI formation at 0.8 V, a slope followed by a pseudo-plateau are observed for a  $\text{TiH}_2$  electrode. As demonstrated by Oumellal *et al.* [14], the conversion reaction of  $\text{TiH}_2$  cannot be explained as a single-step reaction. Indeed, the slope in the range 0.5 – 0.2 V is attributed to the formation of  $\delta\text{-TiH}_{2-x}$  cubic solid solution. Pursuing the lithiation,  $\delta\text{-TiH}_{2-x}$  is completely dehydrogenated during the pseudo-plateau, achieving a quantity of lithium stored into the electrode of 2.75 Li.

During the charge, no plateau reaction is observed, implying that the reformation of the hydride from Ti and LiH did not occur, leading to a complete irreversibility of the conversion reaction.

## 3.2 Galvanostatic cycling of MgH<sub>2</sub>+TiH<sub>2</sub> nanocomposites

### 3.2.1 First discharge/charge cycle

The potential vs. composition profiles of the nanocomposites on lithiation (discharge) and delithiation (charge) for the first galvanostatic cycle in the potential window 5 mV to 1 V are shown in Figure 4.7.

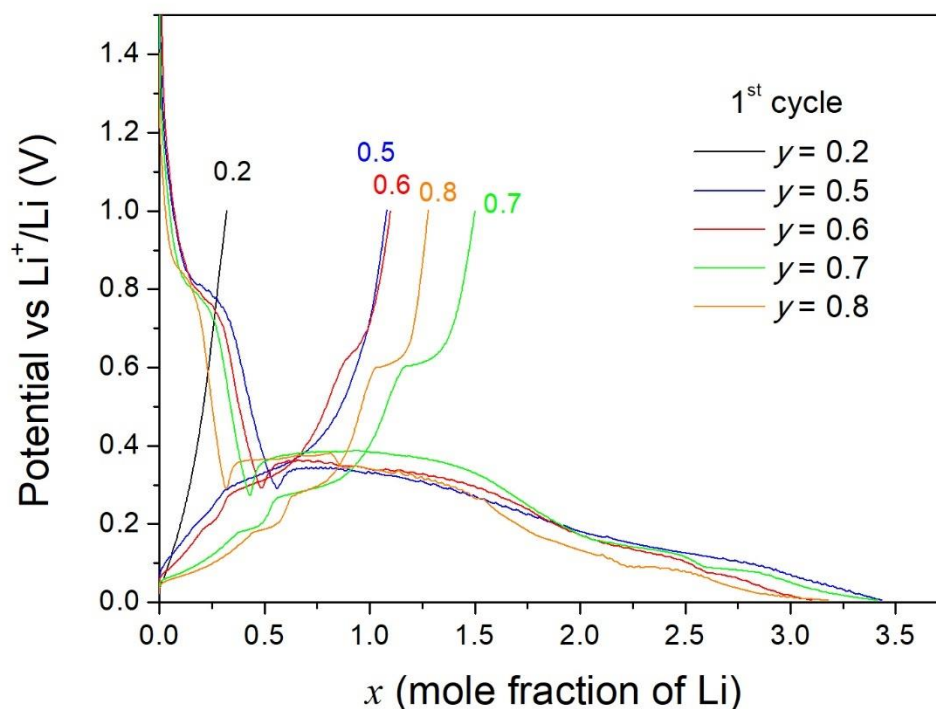


**Figure 4.7.** Evolution of the potential as a function of the mole fraction of Li ( $x$ ) during the first discharge-charge cycle at C/50 for all composites.

During lithiation, all the composites react with lithium exhibiting several plateau potentials. The first plateau detected at  $\sim 0.8$  V is attributed to the SEI formation. Then, two consecutive potential plateaus are observed at  $\sim 0.35$  V and  $\sim 0.10$  V respectively. They are assigned to the conversion reaction of MgH<sub>2</sub> and TiH<sub>2</sub>. Below 0.10 V, the profile slowly decreases down to the cut-off potential because of the lithiation of the freshly formed magnesium. As result of the SEI and Mg-Li alloy formation, the total amount of Li stored in the electrodes exceeds the value expected for the fully conversion reaction of the hydrides, *i.e.*  $x = 2$ . Because the quantity of carbon is the same for each electrode, the contribution of the SEI formation is the same for all the composites, around 0.5 Li. However, the overall capacity increases with Mg-content in the composites due to the growing contribution of the Mg-Li alloy reaction.

On delithiation, contrary to the discharge sweep, the potential profiles strongly depend on the composition of the nanocomposites. For the Ti-rich composite ( $y = 0.2$ ) no clear plateau is noticeable during the charge process, leading to a limited amount of lithium recovery ( $x < 0.5$  Li). Higher reversibility is obtained for the other composites, especially for the Mg-rich  $y = 0.7$  and  $0.8$  ( $x \geq 1.3$  Li). The equimolar composite  $y = 0.5$  displays a unique plateau potential at  $\sim 0.3$  V, whereas Mg-rich composites  $y = 0.6, 0.7$  and  $0.8$  exhibit two potentials plateaus at  $\sim 0.3$  and  $0.6$  V. These plateaus are assigned to the restoring of  $\text{MgH}_2$  and  $\text{TiH}_2$  phases, respectively.

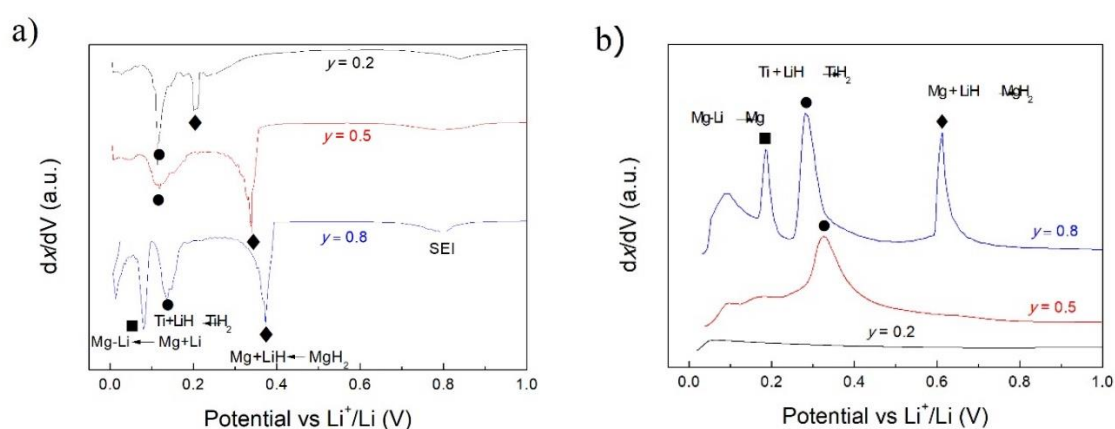


**Figure 4.8.** Differential capacity plots of the  $\text{MgH}_2+\text{TiH}_2$  electrodes during first lithiation (a), and delithiation (b). Diamonds and circles stand for  $\text{MgH}_2$  and  $\text{TiH}_2$  conversion reactions, respectively, squares for Mg alloying reaction. Full and empty symbols stand for lithiation and delithiation, respectively.

A clearer picture of the electrochemical reactions can be gained from the differential capacity plots ( $dx/dV$  vs. V). They are displayed in Figure 4.8. Because the Mg-rich composites  $y \geq 0.6$  exhibit almost identical profiles, only  $y = 0.8$  is displayed in the figure. On lithiation (Figure 4.8a), four potential peaks are typically evidenced. On sweeping from high to low potentials, they correspond to the SEI formation on carbon ( $\sim 0.8$  V), lithiation of  $\text{MgH}_2$  ( $\sim 0.35$  V), lithiation of  $\text{TiH}_2$  ( $\sim 0.1$  V), and alloying reaction of Mg with Li ( $< 0.07$  V). The small signal around the cut off potential ( $\sim 0.005$  V) is attributed to the plating of lithium coming from the counter electrode. It is worth noting that for the Ti-rich composite ( $y = 0.2$ ), the lithiation of  $\text{MgH}_2$  phase occurs at lower potentials ( $\sim 0.2$  V) as compared to the other electrodes ( $\sim 0.35$  V), which evidences the occurrence of large kinetic barriers for  $\text{MgH}_2$  lithiation at high  $\text{TiH}_2$  contents.

The derivate plots on delithiation (Figure 4.8b) deserve much more interest. For Ti-rich composite  $y = 0.2$ , no peak potentials are observed during the process, suggesting that the reformation of both  $\text{MgH}_2$  and  $\text{TiH}_2$  did not occur. For the equimolar composite  $y = 0.5$ , a unique peak is detected at 0.33 V, related to the restoring of the  $\text{TiH}_2$  phase, while no signature of  $\text{MgH}_2$  phase is observed. For the Mg-rich composite  $y = 0.8$  two peaks are detected at 0.27 V and 0.61 V. They are attributed to the reformation of  $\text{TiH}_2$  and  $\text{MgH}_2$  phases respectively. For Mg-rich composites, the area of the anodic peak corresponding to  $\text{TiH}_2$  reformation is larger than that of  $\text{MgH}_2$ , even though  $\text{TiH}_2$  molar amount in the composite is lower than that of  $\text{MgH}_2$  one. This fact demonstrates that the reversibility of the conversion reaction is better for  $\text{TiH}_2$  than  $\text{MgH}_2$  for Mg-rich composites.

### **3.2.2 Reversibility of the conversion reaction for $\text{MgH}_2$ and $\text{TiH}_2$ phases**

In order to study the reversibility of each phase in the composite, and how each conversion reaction affects that of the other phases, electrochemical cycling within selected potential windows has been carried out. By this way, we could identify under which cycling conditions and for which electrode composition the best performances are found.

#### **3.2.2.1 Cycling of $\text{MgH}_2$ phase**

Magnesium hydride is reduced by Li ions during half-cell discharge at a potential around 0.3 V. Next, during the charge, its reformation from Mg and LiH is observed around 0.6 V. On the other hand, lithiation of titanium hydride occurs around 0.1 V, and its reformation around 0.3 V. Thus, to study the reversibility of  $\text{MgH}_2$  conversion alone, galvanostatic cycling has been restrained to a potential window between 0.17 and 1 V. As the  $\text{TiH}_2$  conversion reaction is avoided, the calculated capacity during cycling refers to the  $\text{MgH}_2$  conversion reaction alone. The capacities provided during the first two cycles are reported in Table 4.2.



**Table 4.2.** Capacities and reversibility of MgH<sub>2</sub> conversion reaction in yMgH<sub>2</sub>+(1-y)TiH<sub>2</sub> electrodes (potential window: 0.17 – 1 V).

<b>Composite y</b>	<b>Calculated capacity of yMgH<sub>2</sub> (mAh g<sup>-1</sup>)</b>	<b>Charge capacity 1<sup>st</sup> cycle (mAh g<sup>-1</sup>)</b>	<b>Reversible capacity 1<sup>st</sup> cycle vs. calculated (%)</b>	<b>Charge capacity 2<sup>nd</sup> cycle (mAh g<sup>-1</sup>)</b>	<b>Capacity retention 2<sup>nd</sup>/1<sup>st</sup> cycle (%)</b>
0.2	228	/	/	/	/
0.5	685	301	44	192	64
0.6	880	349	40	292	84
0.7	1100	562	51	467	83
0.8	1363	566	42	445	79

After the complete lithiation of the electrodes, the reformation of MgH<sub>2</sub> has been clearly observed only in Mg-rich composites  $y \geq 0.6$  (Figure 4.8b). The MgH<sub>2</sub> conversion reaction is still irreversible in Ti-rich composite  $y = 0.2$  even when the conversion reaction of TiH<sub>2</sub> is avoided by limiting the potential to  $V_{\text{cut-off}} = 0.17$  V. In contrast, for the composite  $y = 0.5$ , the signal from the reformation of MgH<sub>2</sub> is detected by cycling in the constrained potential window (Figure 4.9).

The best reversibility for MgH<sub>2</sub> conversion reaction is obtained for electrode  $y = 0.7$ , where 51% of the hydride is reformed during the first charge. In the subsequent cycle, the MgH<sub>2</sub>-rich electrodes ( $y = 0.6, 0.7$  and  $0.8$ ) exhibit a capacity retention of  $\sim 80\%$  compared to the first cycle.

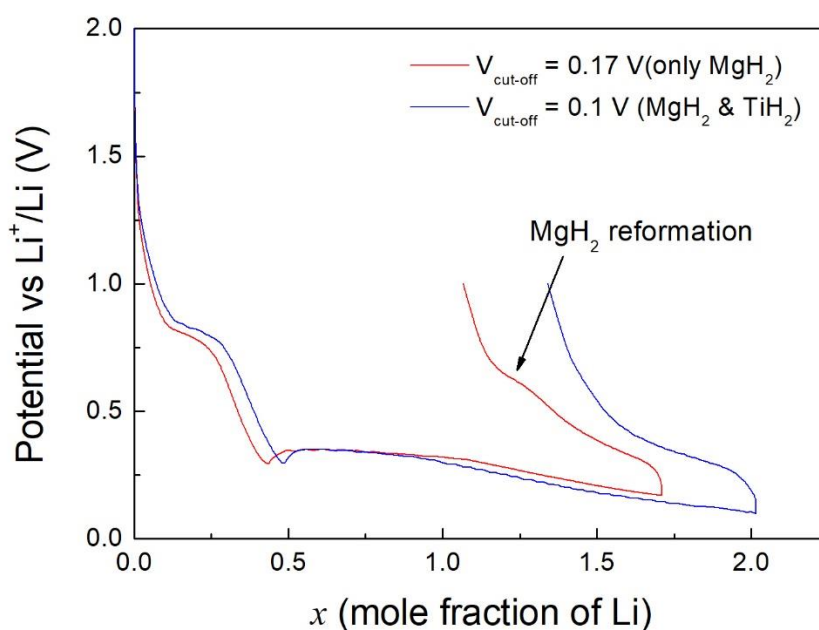


**Figure 4.9.** First cycle of electrode  $y = 0.5$ , in red in the potential window 0.17 – 1 V (only MgH<sub>2</sub> reaction) and in blue between 0.1 – 1 V (both hydrides reaction).

### 3.2.2.2 Cycling of TiH<sub>2</sub> phase

For the investigation of the reversibility of the TiH<sub>2</sub> phase, a potential window between 0.1 and 0.45 V has been chosen. By this way, both the reformation of MgH<sub>2</sub> and the Mg-Li alloy reaction are avoided. One should note however that on the first discharge from 1.0 to 0.1 V, the lithiation reaction of MgH<sub>2</sub> into Mg and LiH takes place. Consequently, the two latter phases coexist during the TiH<sub>2</sub> conversion reaction. The capacities obtained during the first cycles are displayed in Table 4.3.

**Table 4.3.** Capacities and reversibility of TiH<sub>2</sub> conversion reaction in yMgH<sub>2</sub>+(1-y)TiH<sub>2</sub> electrodes (potential window: 0.10 – 0.45 V).

Composite y	Calculated capacity of 1-yTiH <sub>2</sub> (mAh g <sup>-1</sup> )	Charge capacity 1 <sup>st</sup> cycle (mAh g <sup>-1</sup> )	Reversible capacity 1 <sup>st</sup> cycle vs. calculated (%)	Charge capacity 2 <sup>nd</sup> cycle (mAh g <sup>-1</sup> )	Capacity retention 2 <sup>nd</sup> /1 <sup>st</sup> cycle (%)
0.2	957	/	/	/	/
0.5	720	357	50	214	60
0.6	613	384	63	356	93
0.7	495	467	94	446	96
0.8	355	268	76	257	96

For the Ti-rich composite ( $y = 0.2$ ), the restoring of the TiH<sub>2</sub> phase is not observed after the lithiation of the electrode. In the equimolar composite, 50% of TiH<sub>2</sub> is recovered in the first charge. Better performances are achieved in Mg-rich electrodes, especially for  $y = 0.7$ , with a reversibility of 94% as compared to the calculated capacity of TiH<sub>2</sub> counterpart. Moreover, Mg-rich composites ( $y = 0.6, 0.7$  and  $0.8$ ) have a capacity retention in the second cycle above 90% of the first one.

### 3.2.2.3 Effect of Mg alloying on the cycling of MgH<sub>2</sub>+TiH<sub>2</sub> composites

The alloying reaction between Mg, formed by the reduction of MgH<sub>2</sub>, and Li provides additional capacity, but it also causes additional volume expansion. Moreover, if the reversibility of the alloying reaction is low, the retained Mg-Li alloy may not undergo the conversion reaction into MgH<sub>2</sub> and Li during the oxidation sweep. With the purpose of investigating the effect of Mg alloying on the cycle-life of the electrode, the conversion reaction has been studied in two different potential windows: 0.005 – 1 V (with alloying reaction) and 0.1 – 1 V (without alloying reaction). Reversible capacities in both cases are gathered in Table 4.4 for all the studied composites.

**Table 4.4.** Capacities and reversibility of  $\text{MgH}_2$ -TiH<sub>2</sub> electrodes, with and without the Mg-Li alloying reaction.

Composite $y$	Calculated capacity of $y\text{MgH}_2+(1-y)\text{TiH}_2$ (mAh g <sup>-1</sup> )	With Mg-Li alloy reaction (5 mV - 1 V)				Without Mg-Li alloy reaction (0.1 V - 1 V)			
		Charge capacity 1 <sup>st</sup> cycle (mAh g <sup>-1</sup> )	Reversible capacity, 1 <sup>st</sup> cycle vs. calculated (%)	Charge capacity 2 <sup>nd</sup> cycle (mAh g <sup>-1</sup> )	Capacity retention 2 <sup>nd</sup> /1 <sup>st</sup> cycle (%)	Charge capacity 1 <sup>st</sup> cycle (mAh g <sup>-1</sup> )	Reversible capacity, 1 <sup>st</sup> cycle vs. calculated (%)	Charge capacity 2 <sup>nd</sup> cycle (mAh g <sup>-1</sup> )	Capacity retention 2 <sup>nd</sup> /1 <sup>st</sup> cycle (%)
0.2	1185	/	/	/	/	/	/	/	/
0.5	1405	764	54	347	45	560	40	226	40
0.6	1493	826	55	590	71	721	48	607	84
0.7	1608	1203	75	853	71	898	56	741	83
0.8	1718	1250	73	851	68	717	42	559	78

From the comparison of the electrodes studied in different potential windows is possible to notice that a higher charge capacity is obtained during the first delithiation for the composites cycled down to  $V_{\text{cut-off}} = 5 \text{ mV}$ . This is due to the formation of the Mg-Li alloy, which is able to store additional lithium during the discharge of the electrodes. However, in the subsequent cycle, the electrodes cycled without the alloying reaction show a better capacity retention. Except for the equimolar composite  $y = 0.5$ , which exhibits a capacity retention around 40% in both potential windows, all the Mg-rich electrodes  $y \geq 0.6$  display a retention at least 10% higher when the Mg-Li alloy is avoided (*i.e.* for  $V_{\text{cut-off}} = 0.1 \text{ V}$ ). These results are in agreement with both the  $\text{MgH}_2$  thin film and the pure  $\text{MgH}_2$  experiments, where we asserted that the formation of the Mg-Li alloy limits the reversibility of the conversion reaction.

### 3.3 Detailed electrochemical study of 0.7MgH<sub>2</sub>+0.3TiH<sub>2</sub> composite

Electrodes prepared with composite  $y = 0.7$  have shown the best capacity retention among all the composites. For this reason, it has been chosen for further electrochemical characterization. The electrochemical capacity and cycle-life have been investigated by galvanostatic cycling and cyclic voltammetry.

#### 3.3.1 Reversibility of the overall conversion reaction

The reversibility of redox reactions for composite  $y = 0.7$  has been studied by cyclic voltammetry in the potential window 0.1 – 1 V, with a scan rate of 0.3 mV min<sup>-1</sup>. Results are shown in Figure 4.10a.

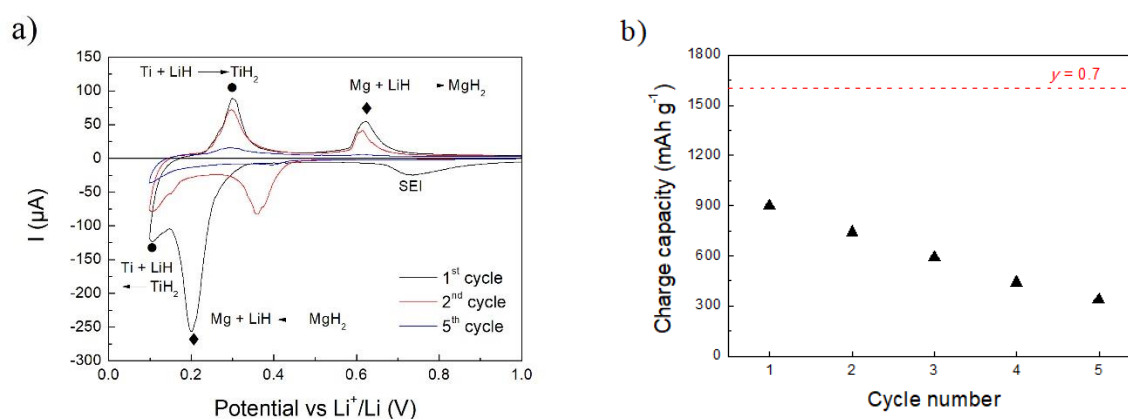


**Figure 4.10.** a) Cyclic voltammetry of composite  $y = 0.7$  in the range 0.1 – 1 V at 0.3 mV min<sup>-1</sup>. b) Evolution of the charge capacity upon cycling. The upper dashed line corresponds to the calculated capacity of the composite.

For cathodic currents, the first sweep shows the irreversible formation of the SEI, followed by the peaks of MgH<sub>2</sub> and TiH<sub>2</sub> lithiation. The overlapping of these peaks is less pronounced in the subsequent cycles, for which the reaction of MgH<sub>2</sub> shifts to 0.36 V, while TiH<sub>2</sub> remains at 0.11 V. As for anodic currents, two oxidation peaks are found at 0.30 and 0.62 V, corresponding to the reformation of TiH<sub>2</sub> and MgH<sub>2</sub> from LiH and metallic Ti and Mg, respectively. It is worth to notice that the area of the oxidation peak related to the MgH<sub>2</sub> reformation is smaller than that corresponding to TiH<sub>2</sub> restoring, even if the MgH<sub>2</sub> molar amount in the composite is higher. This suggests a better reversibility of the conversion reaction for TiH<sub>2</sub> as compared to MgH<sub>2</sub>. Indeed, the reversibility of MgH<sub>2</sub> has been evaluated to ~ 40%, whereas that of TiH<sub>2</sub> is ~ 90%. Interestingly, the reversibility of

MgH<sub>2</sub> and TiH<sub>2</sub> achieved when cycled alone in a narrow potential window (Table 4.2 and 4.3, respectively) were higher, suggesting a lower capacity retention when both hydrides undergo the conversion reaction.

During the subsequent cycles, the intensities of the cathodic and anodic peaks related to the conversion reaction of both hydrides gradually decrease, especially for MgH<sub>2</sub>. Figure 4.10b shows that the charge capacity in the first cycle is ~ 55 % of the calculated value for  $y = 0.7$ , and then it slowly decreases. Indeed, 700 mAh g<sup>-1</sup> are lost within the first cycle, whereas an average of 140 mAh g<sup>-1</sup> are lost in the others, showing that the largest part of capacity is lost in the first discharge/charge cycle.

### 3.3.2 Reversibility and cycle-life of MgH<sub>2</sub> conversion reaction

Figure 4.11a shows the cyclic voltammetry of composite  $y = 0.7$  in the potential range 0.17 – 1.0 V (*i.e.* the TiH<sub>2</sub> conversion reaction is avoided). During the first sweep from higher to lower potentials, after the formation of the SEI at 0.8 V, a single cathodic peak due to the conversion reaction of MgH<sub>2</sub> into Mg and LiH is found at 0.25 V. The anodic peak for the reverse reaction during delithiation is detected at 0.65 V. Note that the area of the anodic peak is much smaller compared to the cathodic one. This indicates an irreversible capacity loss of 535 mAh g<sup>-1</sup> (*i.e.* only 51% of MgH<sub>2</sub> is reformed) in the first cycle. Afterwards, the cathodic peak shifts to 0.35 V, suggesting an easier lithiation of MgH<sub>2</sub> in the subsequent cycles. The anodic peak does not shift significantly during cycling. Compared with the first cycle, the area of both cathodic and anodic peaks decreases slower in the subsequent cycles. The reversible capacity at each cycle is displayed in Figure 4.11b. After the large loss in the first cycle, the capacity decreases with an average of 75 mAh g<sup>-1</sup> per cycle.

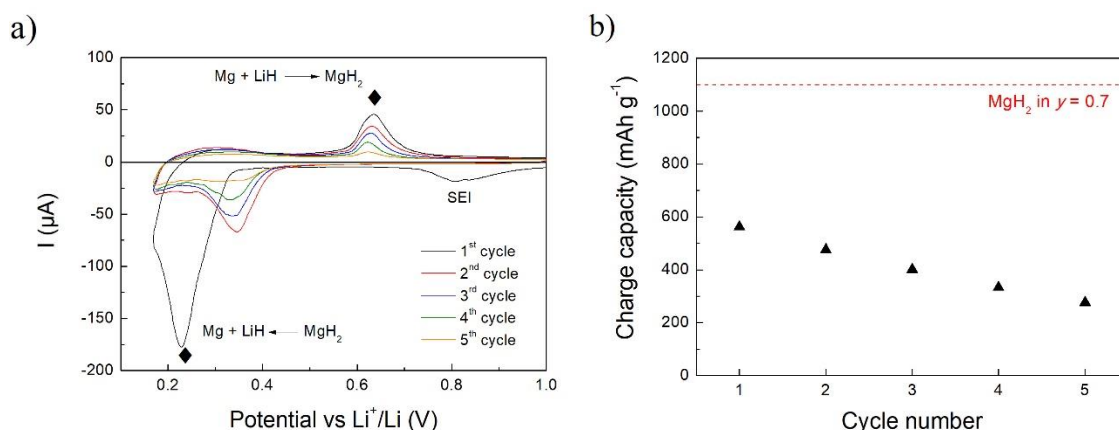


**Figure 4.11.** a) Cyclic voltammetry of  $y = 0.7$  composite in the potential window 0.17 – 1 V at  $0.3 \text{ mV min}^{-1}$ . b) Evolution of the charge capacity with cycling. The upper dashed line corresponds to the theoretical capacity of  $\text{MgH}_2$  phase in  $y = 0.7$ .

### 3.3.3 Reversibility and cycle-life of $\text{TiH}_2$ conversion reaction

Analogous studies were performed in the 0.1 – 0.45 V potential window to exclusively study the reversibility of the  $\text{TiH}_2$  conversion reaction. Cyclic voltammetry results after the first discharge of the electrode down to 0.1 V, in which both hydrides are reduced to lithium hydride and their respective metal elements, are displayed in Figure 4.12a. For anodic currents, a single peak at 0.3 V for the reformation of  $\text{TiH}_2$  is observed, while for cathodic currents, a peak at 0.11 V is found. During cycling, the intensity of both peaks gradually decreases, implying a rather good reversibility of the conversion reaction. The capacity provided by the electrode during cycling is displayed in Figure 4.12b. The initial reversible capacity is evaluated at  $467 \text{ mAh g}^{-1}$ , which, assuming the full lithiation of  $\text{TiH}_2$  ( $495 \text{ mAh g}^{-1}$ ) during the discharge, represents a reversibility of 94%. After ten cycles, the capacity slowly decreases to  $315 \text{ mAh g}^{-1}$ , indicating an average capacity loss per cycle of  $18 \text{ mAh g}^{-1}$ , *i.e.* at each cycle 3.6% of the capacity is lost.



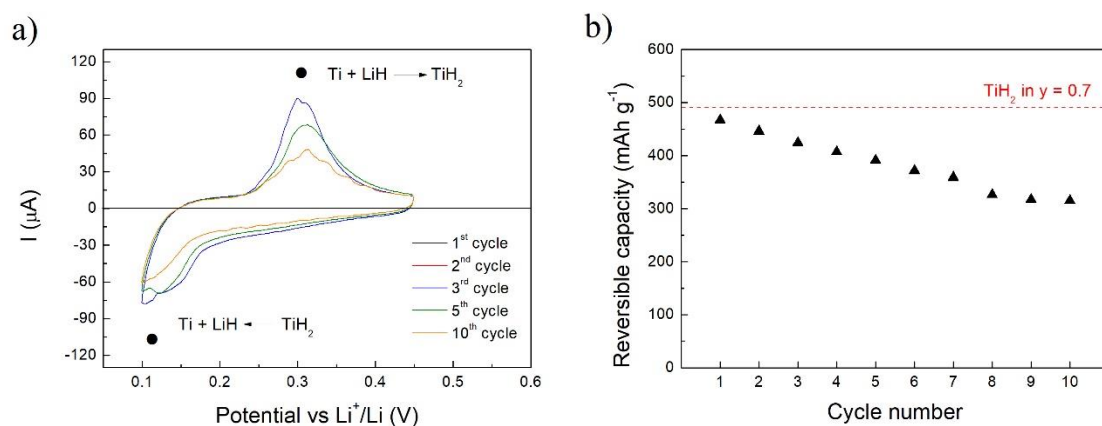


**Figure 4.12.** a) Cyclic voltammetry for the composite  $y = 0.7$  in the range  $0.1 - 0.45$  V, at  $0.3 \text{ mV min}^{-1}$  b) Evolution of the charge capacity on cycling. The upper red dashed line corresponds to the theoretical capacity of the  $\text{TiH}_2$  conversion reaction for composite  $y = 0.7$ .

## 4 Discussion

### 4.1 Synthesis and structural properties of $\text{MgH}_2 + \text{TiH}_2$ nanocomposites

At the light of the structural characterizations, we can conclude that all materials obtained by RBM of Mg and Ti elements under  $\text{H}_2$  are composites made of  $\text{MgH}_2$  and  $\text{TiH}_2$ . The monitored RBM hydrogen absorption curves (Figure 4.2) have shown that the kinetics of composite formation depends on the Mg/Ti molar ratio. The derivative of the absorption curves with respect to the milling time (Figure 4.13) allows a deeper understanding of the formation mechanism. Figure 4.13 clearly shows two consecutive steps evidenced by two absorption peaks during the milling process. The first peak is attributed to the formation of  $\text{TiH}_2$ , whereas the second peak corresponds to the formation of  $\text{MgH}_2$ . Note that, not only  $\text{TiH}_2$  is formed before  $\text{MgH}_2$ , but also the peak related to  $\text{MgH}_2$  formation shifts to shorter time with the increase of Ti-amount in the composite. The faster hydrogenation of magnesium in presence of  $\text{TiH}_2$  may be explained by at least two specific properties of  $\text{TiH}_2$ . First, the highly abrasive character of  $\text{TiH}_2$  which would facilitate the grinding of Mg powder into fine and reactive particles. Second, the fact that  $\text{TiH}_2$  may act as a gateway for hydrogen absorption in Mg: the hydrogen gas would dissociate at  $\text{TiH}_2$  surfaces and atomically transferred through  $\text{TiH}_2$  towards the Mg phase where  $\text{MgH}_2$  nucleates. This mechanism would be favoured by the large diffusion coefficient of H in  $\text{TiH}_2$  phase [15].

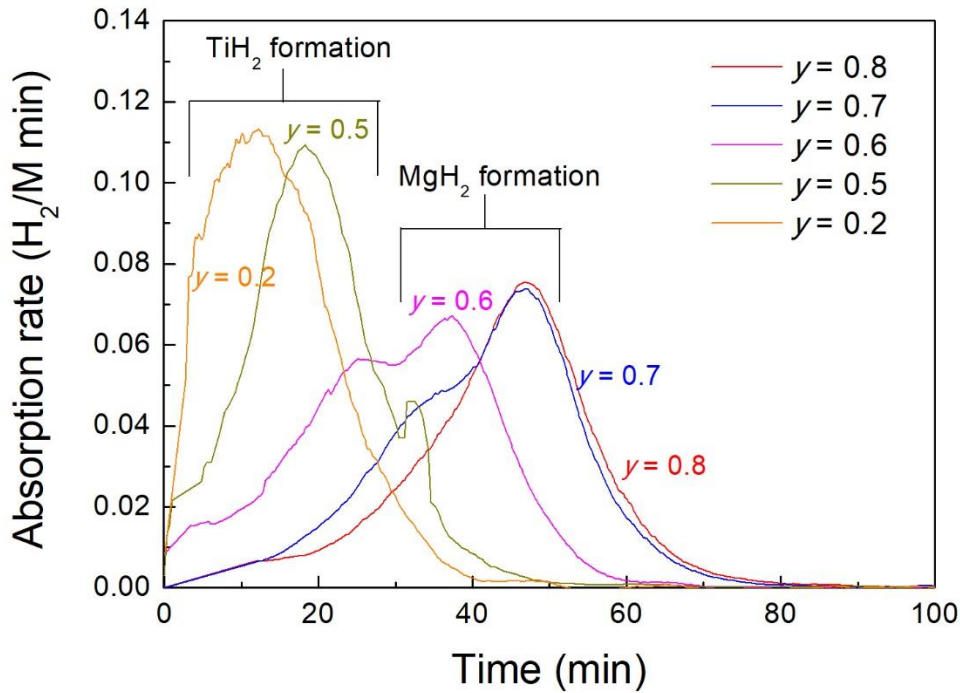


**Figure 4.13.** Time-derivative plots of the absorption curves of MgH<sub>2</sub>+TiH<sub>2</sub> composites.

The presence of the two hydrides MgH<sub>2</sub> and TH<sub>2</sub> in the composites is confirmed by XRD analysis except for the Ti-rich ( $y = 0.2$ ) one for which only TiH<sub>2</sub> is detected. The contribution of MgH<sub>2</sub> is not detected because of its low amount, poor crystallinity and low scattering power of Mg atoms compared to Ti ones. Nonetheless, TEM investigation confirms the formation of MgH<sub>2</sub> in  $y = 0.2$ , supported also by the quantity of hydrogen absorbed per formula unit (Figure 4.2) close to 2 for all the composites. The analyses show the formation of an intimate mixture of MgH<sub>2</sub> and TiH<sub>2</sub> for all composites, with an average crystallite size between 3 and 11 nm. Neither Mg-Ti alloy nor Mg-Ti-H ternary phase are found, suggesting that hydrogenation absorption during mechanical milling leads to a phase configuration close to thermodynamic equilibrium. Definitely, in the Mg-Ti phase diagram [16], solubility of each metal to another is less than 2 atomic%, and intermetallic compounds are not found. Successful preparations of Mg-Ti alloy have been reported by using electron beam deposition [17], or extreme milling of metal powders under argon atmosphere [18]. Ternary Mg-Ti-H compounds are not formed by simply mixing MgH<sub>2</sub> and TiH<sub>2</sub> together, they require more energetic techniques as shown by Kyoi *et al.* [19], which synthesized a ternary Mg-Ti-hydride by means of a high-pressure anvil at high

temperature. Thus, in our working conditions (4 hours of milling, at 50 °C and 9 MPa H<sub>2</sub> gas) is unlikely to obtain such compounds. Our results are in good agreement with previous works reported in literature about the synthesis of MgH<sub>2</sub>+TiH<sub>2</sub> composites by RBM [8].

## 4.2 Electrochemical analyses

To ensure the operation of any active material in a Li-ion battery, both high mobility of Li ions and electrons are required. Furthermore, for conversion reaction electrodes, reactivity between solid species within the electrode should occur at enough rate. In the particular case of metallic hydrides *MH*, the transport of metal atoms *M* (here *M* = Mg and Ti) and H in atomic form is required. The volume variation during lithiation/delithiation must also be managed in order to maintain good interface and contact between solid phases. To mitigate the issues of the active material related to electronic conductivity and volume changes in the electrode on discharge/charge cycling, the nanocomposites have been mixed with carbon Super P and CMC to prepare the working electrodes.

During the first discharge, all electrodes can fully react with lithium, accomplishing the conversion reaction. In previous studies [20,21], a full lithiation was not achieved for commercial hydrides, and the authors identified the main cause as the grain size and/or surface contamination (such as metal-oxide layers). Thanks to the nanostructuring obtained during ball milling (average crystallite size ≤ 11 nm) both MgH<sub>2</sub> and TiH<sub>2</sub> are completely reduced to Mg and Ti accompanied by LiH formation. These results evidence the importance of nanostructuring in the accomplishment of the conversion reaction of hydrides with lithium. However, the reversibility upon delithiation strongly depends on the composition (Figure 4.7), being much higher for Mg-rich than for Ti-rich electrodes. Therefore, nanostructuring is necessary to attain full lithiation but not sufficient to ensure the restoration of the hydride phases.

Indeed, the low reversibility of the Ti-rich composite (*y* = 0.2) concurs with previous finding of Oumellal *et al.* for single-phase TiH<sub>2</sub> electrodes [14]. These authors reported that, after full lithiation, the restoring of the TiH<sub>2</sub> phase could not be obtained. Interestingly, same authors showed that the reversibility can be partially achieved starting from an intimate mixture of Ti and LiH prepared by mechanochemical reaction of TiH<sub>2</sub> and Li [22]. This demonstrates the key role of *M* and LiH phase distribution or the properties of *M*/LiH interfaces on the reversibility of the conversion reaction.

In the equimolar composite ( $y = 0.5$ ),  $\text{TiH}_2$  is recovered during the first charge, but the signal of the reformation of  $\text{MgH}_2$  is not detected (Figure 4.8b). One may hypothesise that the restoring of  $\text{TiH}_2$  may hamper the subsequent restoring of  $\text{MgH}_2$ . Indeed, the brittleness and high volume change associated to the conversion reaction of  $\text{TiH}_2$  can induce loss of electronic contact within the electrode. This hypothesis is supported by the fact that the signal of  $\text{MgH}_2$  reformation during the delithiation is clearly detected when the conversion reaction of  $\text{TiH}_2$  is excluded selecting an appropriate potential window (*i.e.* cycling between 0.17 – 1 V, Figure 4.9).

A better overall reversibility has been obtained in Mg-rich electrodes ( $y \geq 0.6$ ), especially in composite 0.7. Here, both hydrides are reformed during the charge, with  $\text{TiH}_2$  exhibiting a higher reversibility compared to  $\text{MgH}_2$  within the first cycle, 90% vs. 40% respectively. Interestingly, the conversion reaction of  $\text{TiH}_2$ , which was not reversible when the hydride is the only [14] or major phase ( $y = 0.2$ ), shows a high reversibility in Mg-rich electrodes.

#### **4.2.1 Reversibility of each hydride phase**

In view of the better performance of the composite  $y = 0.7$ , it was chosen for further investigations. Studies in different potential windows have been carried out with the purpose of evaluating the contribution of each phase, their reversibility, and the influence of the Mg alloying reaction at low potentials.

##### **4.2.1.1 Influence of $\text{TiH}_2$ on the reversibility of $\text{MgH}_2$ conversion reaction**

Galvanostatic cycling in the range 0.17 – 1 V (*i.e.* for  $\text{MgH}_2$  conversion reaction, Figure 4.11b) is characterized by significant irreversibility in the first cycle, with only 51% of  $\text{MgH}_2$  restored during the charge. Moreover, the capacity drops in the subsequent cycles (6.8% of capacity lost per cycle). For better understanding of the reversibility of  $\text{MgH}_2$  in presence of  $\text{TiH}_2$ , it is worth comparing with an electrode prepared with only  $\text{MgH}_2$ .

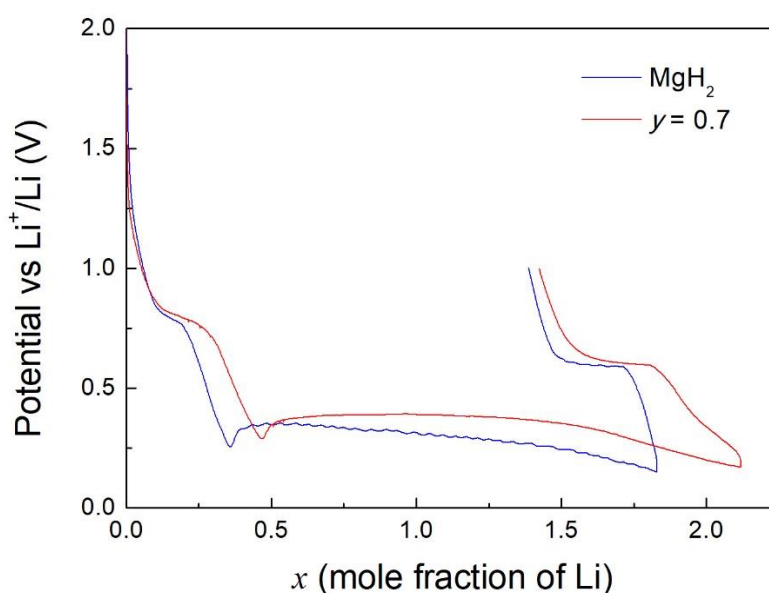


**Figure 4.14.** First cycle of electrodes prepared with composite  $y = 0.7$  (red line), and electrode prepared with  $\text{MgH}_2$  (blue line), in the potential window 0.17 – 1 V with a C-rate of C/50.

Figure 4.14 shows a comparison between composite  $y = 0.7$  and pure  $\text{MgH}_2$  electrodes cycled in the same potential window at C/50. The capacity of these two electrodes should reach  $x = 1.4$  and 2 for  $y = 0.7$  and  $\text{MgH}_2$  respectively. However, taking into account the additional contribution of the SEI formation,  $x \sim 0.5$  Li, only the composite  $y = 0.7$  stores a quantity of lithium close to its theoretical value. Moreover, the potential plateau reaction of  $y = 0.7$  is flatter and at higher potential than pure  $\text{MgH}_2$  electrode, implying a smaller polarization and so a better kinetics. During the charge, the extraction of lithium occurs at the same potential, with a quantity of Li larger for  $y = 0.7$ . These results are in good agreement with the experiments reported in literature. Indeed, Huang *et al.* [23] investigated the electrochemical properties of  $0.7\text{MgH}_2+0.3\text{TiH}_2$  mixture at different C-rates, showing that lower polarization and better reversibility are obtained for the composite in comparison with pure  $\text{MgH}_2$ . The authors attributed the better electrochemical properties of the composite to its higher electronic conductivity and faster hydrogen transport due to the presence of  $\text{TiH}_2$  [15,24].

#### 4.2.1.2 Enhanced reversibility of TiH<sub>2</sub> phase in a Mg-rich electrode

As illustrated in Figure 4.15, the highest reversibility is obtained cycling the minor phase (*i.e.* TiH<sub>2</sub>) in composite  $y = 0.7$ . Indeed, while cycling both hydrides (black squares), or MgH<sub>2</sub> alone (red circles), less than 60% of the capacity is recovered in the first cycle, and quickly it drops below 30%. On the other hand, TiH<sub>2</sub> alone (blue triangles) exhibits more than 90% of its capacity during the first cycle, and slowly decreases losing an average of 3.6% per cycle.

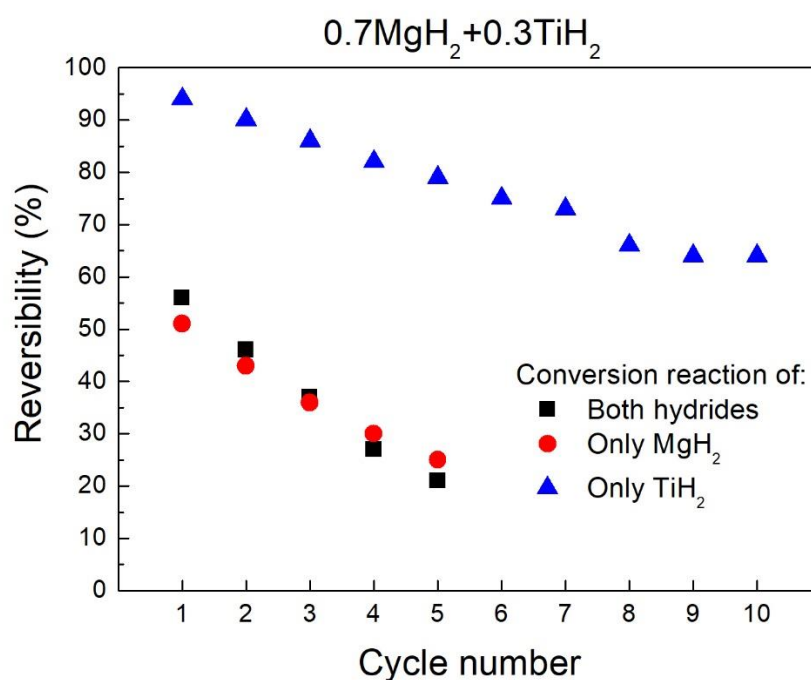


**Figure 4.15.** Reversibility of electrode 0.7MgH<sub>2</sub>+0.3TiH<sub>2</sub> achieved cycling both hydrides (black squares), only MgH<sub>2</sub> phase (red circles), and only TiH<sub>2</sub> phase (blue triangles).

It is worth to notice that  $\text{TiH}_2$  undergoes the conversion reaction while embedded within a two-phase  $\text{Mg}+\text{LiH}$  matrix. Therefore, the improvement in cycle-life is assigned to manifold factors, namely:

- i) The presence of major Mg metallic phase, which enhances the electrical conductivity of the electrode;
- ii) The presence of major LiH phase, which creates a high density of Ti/LiH interfaces that facilitate the restoring of  $\text{TiH}_2$  upon delithiation;
- iii) The embedding of a minor amount of active material ( $0.3\text{TiH}_2$ ) in a buffering matrix ( $\text{Mg}+\text{LiH}$ ) that accommodate the volume changes induced by the conversion reaction;

With the purpose of understanding which of these factors plays a major role for the reversibility, we synthesized a composite material that consist of  $\text{TiH}_2$  embedded in a Mg metallic matrix. For this experiment, the composite  $0.8\text{MgH}_2+0.2\text{TiH}_2$  was heated at  $180^\circ\text{C}$  under dynamic vacuum ( $10^{-3}$  mbar). Such a moderate temperature was selected to get hydrogen desorption exclusively from  $\text{MgH}_2$  phase while limiting Mg crystal growth. The residual pressure was monitored over time to determine the dehydrogenation completion. Figure 4.16a shows the XRD before and after this treatment.

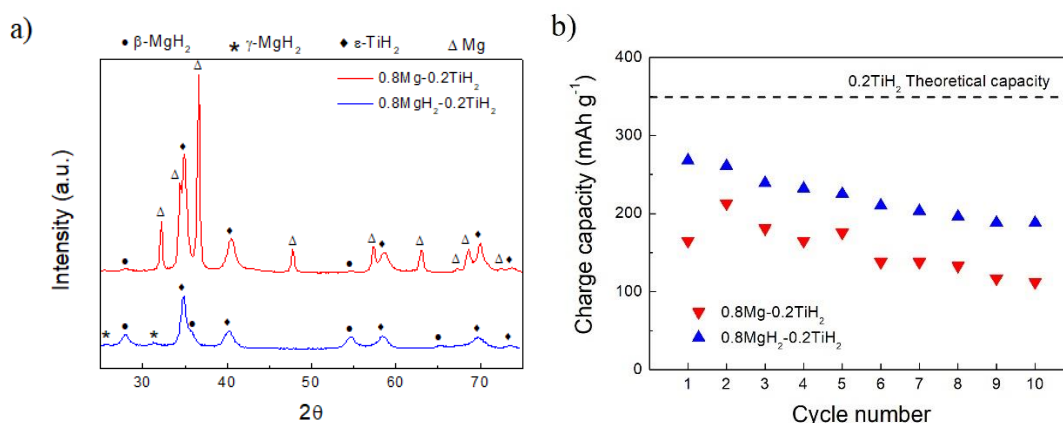


**Figure 4.16.** a) XRD patterns of the  $0.8\text{MgH}_2+0.2\text{TiH}_2$  composite before (blue line) and after (red line)  $\text{MgH}_2$  dehydrogenation. b) Evolution of the charge capacity of the  $\text{TiH}_2$  phase with cycling.

The crystallographic data obtained from the patterns analysis before and after the dehydrogenation are shown in Table 4.5. After dehydrogenation, the pattern shows mainly Mg (60%) and  $\epsilon$ -TiH<sub>2</sub> (37%). Trace of  $\beta$ -MgH<sub>2</sub> is still found (3%). The main difference found in the crystallographic data is the increase of the average crystallite size ( $D$ ) after the treatment at 180 °C to remove hydrogen from the MgH<sub>2</sub> phase. Indeed, TiH<sub>2</sub> grows from 11 to 21 nm, and the freshly formed Mg exhibits an average of 35 nm.



**Table 4.5.** Crystallographic data from Rietveld refinements of the XRD patterns of the composite  $\gamma = 0.8$  before and after dehydrogenation of  $\text{MgH}_2$  phase.

Composite	Phase	Space group	Amount (%)	Lattice parameters (Å)			$D$ (nm)	$R_B$	$R_P$	$R_{WP}$	$R_{exp}$	$\chi^2$
				$a$	$b$	$c$						
0.8MgH <sub>2</sub> +0.2TiH <sub>2</sub>	$\epsilon$ -TiH <sub>2</sub>	$I4/mmm$	43	3.171	3.171	4.419	11	1.7				
	$\beta$ -MgH <sub>2</sub>	$P4_2/mmm$	41	4.518	4.518	3.029	6	2.4	7.0	8.1	4.2	3.73
	$\gamma$ -MgH <sub>2</sub>	$Pbcn$	16	4.564	5.399	4.925	4	3.4				
0.8Mg+0.2TiH <sub>2</sub>	$\epsilon$ -TiH <sub>2</sub>	$I4/mmm$	37	3.161	3.161	4.408	21	5.8				
	$\beta$ -MgH <sub>2</sub>	$P4_2/mmm$	3	4.521	4.521	3.001	8	10.0	9.4	11.0	2.7	16.9
	Mg	$P6_3/mmc$	60	3.212	3.212	5.217	35	3.8				

Figure 4.16b displays a comparison between the cycle-life of electrodes prepared with  $0.8\text{Mg}+0.2\text{TiH}_2$  and  $0.8\text{MgH}_2+0.2\text{TiH}_2$ , both cycled in the potential window where only the conversion reaction of  $\text{TiH}_2$  occurs (*i.e.* 0.1 – 0.45 V). Both electrodes show a capacity decay around 30% during ten cycles, but the composite  $0.8\text{MgH}_2+0.2\text{TiH}_2$  provides a higher capacity than  $0.8\text{Mg}+0.2\text{TiH}_2$ , implying a better reactivity of  $\text{TiH}_2$  in the two-hydride composite.

To understand why such a difference in the reversibility, we looked at the electrode compositions. A schematic illustration is given in Figure 4.17. In the case of the dehydrogenated sample,  $\text{TiH}_2$  is surrounded by a Mg matrix during the conversion reaction. On the other hand, for the two-hydride composite, the conversion reaction of  $\text{TiH}_2$  occurs in a matrix of  $\text{Mg}+\text{LiH}$  as result of the initial lithiation of the  $\text{MgH}_2$  phase. Therefore, the quantity of  $\text{LiH}$  within the electrode for the restoring of the  $\text{TiH}_2$  phase is much higher for the original  $0.8\text{MgH}_2+0.2\text{TiH}_2$  composite than for the dehydrogenated  $0.8\text{Mg}+0.2\text{TiH}_2$  one. The conversion reaction might occur where the active phases and electrons meet (green dots called Triple points in Figure 4.17), enable the exchange of material. In the two-hydride composite the density of  $\text{Ti}/\text{LiH}$  interfaces in contact with Mg (which conducts the electrons) are higher than for the dehydrogenated composite, hence  $0.8\text{MgH}_2+0.2\text{TiH}_2$  electrode exhibits a higher reversibility. This experiment demonstrates that the main factor that enhanced the reversibility of the  $\text{TiH}_2$  phase in a Mg-rich composite is the high density of the interfaces that enable the reformation of the hydride.

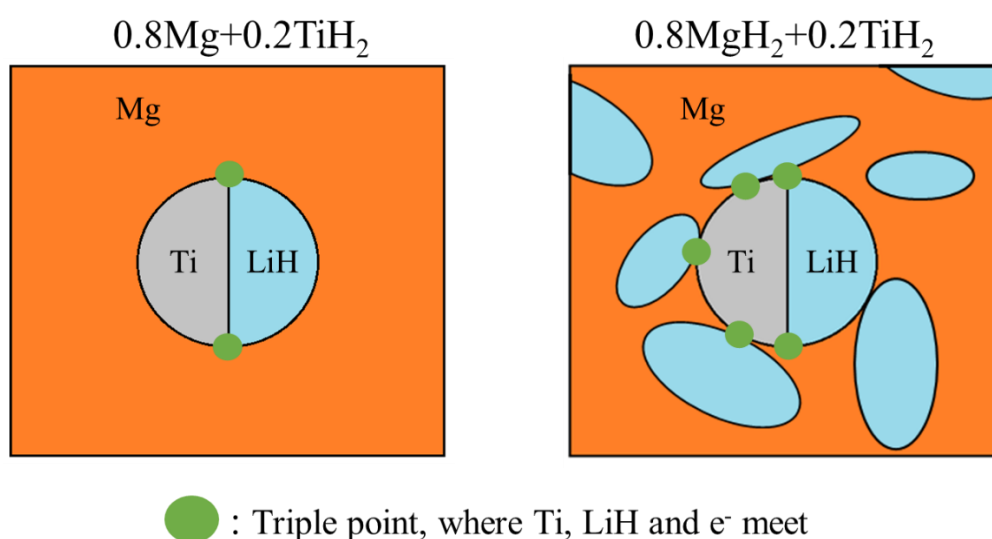


**Figure 4.17.** Schematic illustration of the composition of electrodes  $0.8\text{Mg}+0.2\text{TiH}_2$  (left), and  $0.8\text{MgH}_2+0.2\text{TiH}_2$  (right) while cycling.

### 4.2.1.3 Influence of Mg-Li alloying on the overall conversion reaction

Electrodes studied in the potential window 5 mV – 1 V have shown the highest capacities during the first cycles (Table 4.4). This is due to the formation of the Mg-Li alloy at potentials lower than 0.1 V. But during cycling, the capacity decay of these electrodes was 7% higher compared to the composites cycled without the contribution of the alloy reaction. To better understand the effect of the Mg-Li alloying reaction on the reversibility of the conversion reaction, one can look at the difference in the reversible capacity of the electrodes while cycling. A comparison between  $y = 0.7$  electrodes cycled with ( $V_{\text{cut-off}} = 5$  mV) and without the alloying reaction ( $V_{\text{cut-off}} = 0.1$  V) at a kinetics regime of C/50 is shown in Figure 4.18.

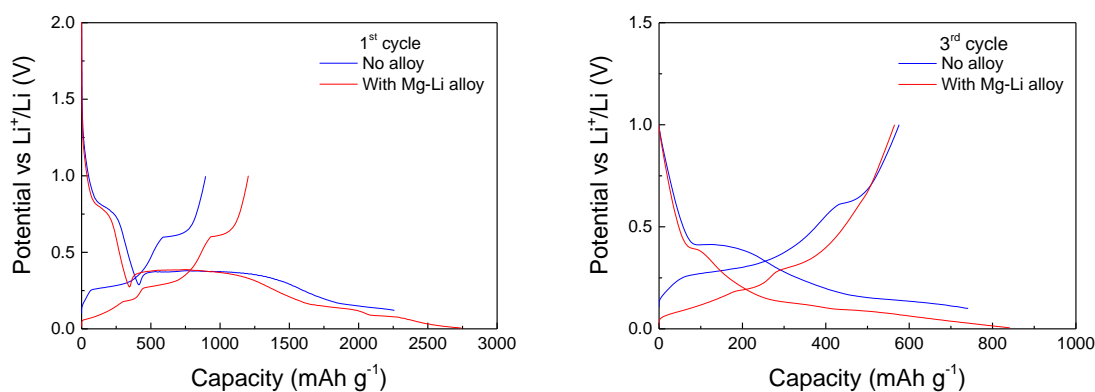


**Figure 4.18.** Comparison between the potential profiles of the electrode  $y = 0.7$  undergoing Mg-Li alloying (red curve,  $V_{\text{cut-off}} = 5$  mV) and without Mg alloying (blue curve,  $V_{\text{cut-off}} = 0.1$  V), during the first cycle (left) and third cycle (right).

In both experiments, the composite  $y = 0.7$  exhibits during the first lithiation, a first plateau potential at 0.8 V for the SEI formation, a second one at 0.36 V for the reduction of  $\text{MgH}_2$  and a sloping plateau at 0.16 V for the reaction of  $\text{TiH}_2$  with lithium. Then, for the electrode cycled down to 5 mV, the contribution of the Mg-Li alloy reaction is found below 0.1 V. Because of this alloy reaction, the electrode reaches a larger capacity (2740 vs. 2260  $\text{mAh g}^{-1}$ ). The quantity of lithium stored into the electrode below 0.1 V is actually 0.94 Li, implying the formation of the alloy  $\text{Li}_{0.94}\text{Mg}_{0.7}$ . During delithiation, the reformation of  $\text{MgH}_2$  and  $\text{TiH}_2$  is observed at 0.60 V and 0.29 V respectively, while the extraction of Mg from the alloy occurs at 0.18 V. Except for a larger capacity, no major differences are found in the two profile curves, suggesting that the alloying reaction has no detrimental effect on the electrode within the first cycle.

Much more interest deserve the profiles of the third cycle. During lithiation, the potential plateau of the  $\text{MgH}_2$  conversion reaction ( $\sim 0.36$  V) is much longer for the electrode cycled without the alloy reaction, implying a better reversibility during cycling of this electrode. Below 0.1 V the alloy reaction still provides additional capacity, but its extent is shorter compared with the first discharge. During the delithiation, the composite undergoing Mg-Li alloying exhibits only two plateaus. At low potential ( $\sim 0.20$  V), there is the de-alloying reaction, and at 0.30 V the reformation of  $\text{TiH}_2$ . Interestingly, the extent of this latter reaction is longer in the composite cycled without the alloying, *i.e.* there is a higher reversibility of the  $\text{TiH}_2$  conversion reaction when the Mg-Li alloying is avoided. At higher potential, no plateau related to the  $\text{MgH}_2$  reformation is detected for the electrode undergoing the alloying reaction. Since the Mg de-alloying reaction is still found around 0.20 V, the difficulty to restore  $\text{MgH}_2$  cannot be attributed to isolation of Mg domains, nor persistence of large Mg-Li phases. Likely, the additional volume expansion due to the alloy reaction leads to loss in contacts and separation between Mg and LiH phases, preventing the conversion reaction. This hypothesis concurs, as illustrated in Figure 4.19, with the capacity fade of this electrode undergoing the alloy reaction during cycling. The electrode undergoing Mg alloying shows a higher charge capacity thanks to the contribution of the de-alloying reaction. However, this electrode loses an average of 33% of the capacity in each cycle, whereas the electrode without the alloy loses 22% per cycle. Indeed, after three cycles this latter electrode delivers a higher charge capacity thanks to a better reversibility of both conversion reactions when the alloying reaction is avoided.

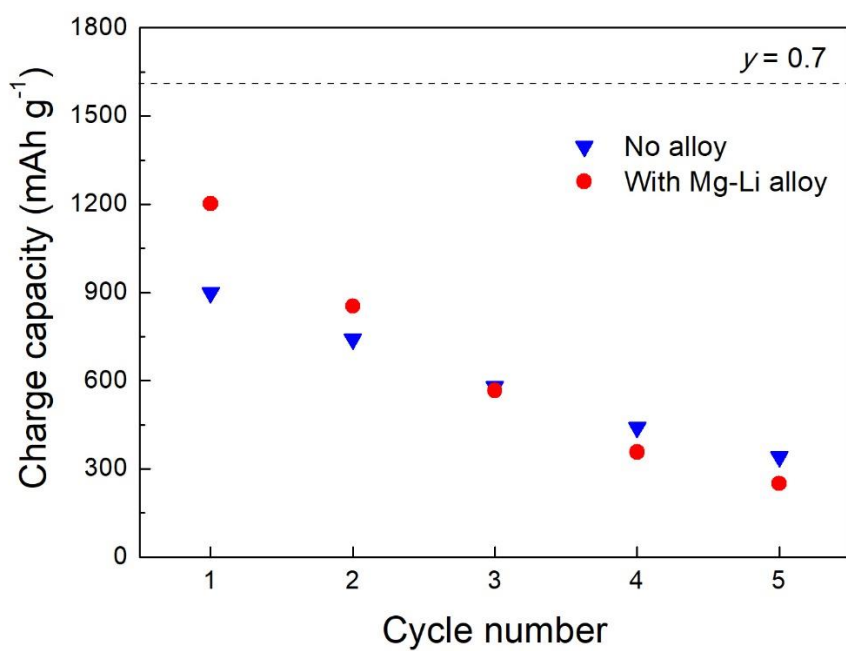


**Figure 4.19.** Evolution of the reversible capacity of  $y = 0.7$  composite on cycling. Red circles: electrode cycled between 5 mV and 1 V (with Mg-Li alloy formation). Blue triangles: electrode cycled between 0.1 V and 1 V (without Mg-Li alloy formation).

## 5 Conclusions

Composites  $y\text{MgH}_2+(1-y)\text{TiH}_2$  with molar composition  $y = 0.2, 0.5, 0.6, 0.7$  and  $0.8$  have been synthesized by mechanical milling under hydrogen pressure. The presence of  $\text{TiH}_2$  during RBM enhances the absorption kinetics of Mg thanks to its abrasive properties and fast H transport. The structural characterization has been carried out by XRD and TEM. In this respect, the main results can be shortened as follow:

- The composites contain two hydrides  $\text{MgH}_2$  and  $\text{TiH}_2$ . For composite  $y = 0.2$ ,  $\text{MgH}_2$  is not found because of its low quantity and poor scattering power of Mg and H elements. However, its presence is detected by HAADF TEM. For the  $\text{MgH}_2$ -rich composite  $y \geq 0.6$ , also the metastable phase  $\gamma\text{-MgH}_2$  is found. No ternary compound is formed during ball milling. The average crystallite sizes ranges between 3 nm to 11 nm and therefore the hydride mixtures are well designed as nanocomposites;
- The nano-structure of the composites is confirmed by TEM analysis, which also shows that for all the composition intimate mixtures of  $\text{MgH}_2$  and  $\text{TiH}_2$  are formed;

These nanocomposites have been tested as anode active materials for Li-ion batteries at RT. The electrochemical activity of the electrodes, as well as the contribution of each single phase during cycling, has been investigated by galvanostatic and cyclic voltammetry measurements. The properties shown by the electrodes can be summarized as follow:

- All the composites can be fully lithiated during the first discharge. This is facilitated by their nanostructure, which creates a high density of grain boundaries and allows for short diffusion paths for the mobility of lithium. The reaction potentials of the hydrides with Li are detected at 0.35 V and 0.1 V for  $\text{MgH}_2$  and  $\text{TiH}_2$  respectively. Below 0.1 V the alloying reaction between Mg and Li occurs;
- The reversibility of the delithiation reaction and so of the hydrides restoration strongly depends on the composition of the electrode. For the Ti-rich composite  $y = 0.2$ , the reformation of any of both hydrides is not detected. For the equimolar mixture  $y = 0.5$ , only  $\text{TiH}_2$  is partially recovered, whereas no signal

due to the reformation of  $\text{MgH}_2$  is found. Finally, for Mg-rich electrodes,  $y \geq 0.6$ , both hydrides are restored, with better reversibility for the  $\text{TiH}_2$  phase;

- The best results have been achieved with the composite  $y = 0.7$ , whereas a reversibility of 56% is achieved during the first cycle. Interestingly, the reversibility of the conversion reactions is better when the cycling potentials are limited to a single hydride phase. This could be attributed to a lower volume expansion during cycling;
- The presence of  $\text{TiH}_2$  has shown pros and cons on the reversibility of  $\text{MgH}_2$  conversion reaction. For high quantity,  $y = 0.2$ , the conversion reaction of both hydrides is irreversible in each potential window investigated. For composite  $y = 0.5$ , the reformation of  $\text{MgH}_2$  is not detected when  $\text{TiH}_2$  undergoes also the conversion reaction. For Mg-rich composites  $y \geq 0.6$ , the restoring of both hydrides during the charge is found, but the reversibility of  $\text{MgH}_2$  increases when cycled alone in the range 0.17 – 1 V. These results suggest that the presence of  $\text{TiH}_2$  can increase both the electric conductivity and the diffusion of H atoms into the electrode, but on the other hand, its conversion reaction limits the cyclability of  $\text{MgH}_2$ . Probably, this is due to the brittleness and volume expansion (~130%) of  $\text{TiH}_2$  phase;
- Mg+LiH strongly enhance the reversibility of  $\text{TiH}_2$ . It is reported in literature [14] that the conversion reaction of  $\text{TiH}_2$  is irreversible after the first lithiation. Here, for  $y = 0.5$ , this hydride is partially reformed, and its reversibility increases with the quantity of  $\text{MgH}_2$ ;
- Cycling  $\text{TiH}_2$  in a restricted potential window (0.1 – 0.45 V) highly increases the reversibility and cycle-life of this phase [25]. Under these conditions, this hydride has shown a reversibility above 90%, with a capacity that slowly decreases with a rate of 3.6% per cycle. This enhancement has been credited to the surrounding Mg+LiH matrix, which guarantees a high density of Ti/LiH interfaces, a good electronic conductivity through the Mg metallic phase, and the accommodation of volume changes within the electrode. This novel strategy for improving the reversibility of metal hydrides as negative electrodes for Li-ion batteries opens new avenues for future research in this field;

- The Mg-Li alloying reaction provides additional capacity during cycling, but it reduces the extent of the conversion reaction of the hydrides, especially  $\text{MgH}_2$ . The alloy reaction has shown to be reversible, hence the extraction of Mg from the alloy is not the main cause of this fade. Likely, the additional volume change caused by this reaction leads to phase segregation and loss of contacts between particles;



## References

1. Ponthieu, M. *et al.* Structural properties and reversible deuterium loading of MgD<sub>2</sub>-TiD<sub>2</sub> nanocomposites. *Journal of Physical Chemistry C* **117**, 18851–18862 (2013).
2. Srinivasan, S. *et al.* Nanostructures of Mg<sub>0.65</sub>Ti<sub>0.35</sub>D<sub>x</sub> studied with x-ray diffraction, neutron diffraction, and magic-angle-spinning <sup>2</sup>H NMR spectroscopy. *Phys. Rev. B - Condens. Matter Mater. Phys.* **81**, 1–10 (2010).
3. Liang, G., Huot, J., Boily, S., Van Neste, a. & Schulz, R. Catalytic effect of transition metals on hydrogen sorption in nanocrystalline ball milled MgH<sub>2</sub>-Tm (Tm=Ti, V, Mn, Fe and Ni) systems. *J. Alloys Compd.* **292**, 247–252 (1999).
4. Zhang, J. *et al.* Highlighting of a single reaction path during reactive ball milling of Mg and TM by quantitative H<sub>2</sub> gas sorption analysis to form ternary complex hydrides (TM = Fe, Co, Ni). *J. Phys. Chem. C* **115**, 4971–4979 (2011).
5. Kobayashi, T. *Strength and Toughness of Materials.* Springer (2004).
6. Wipf, H., Kappesser, B. & Werner, R. Hydrogen diffusion in titanium and zirconium hydrides. *J. Alloys Compd.* **310**, 190–195 (2000).
7. Yao, X., Zhu, Z. H., Cheng, H. M. & Lu, G. Q. Hydrogen diffusion and effect of grain size on hydrogenation kinetics in magnesium hydrides. *J. Mater. Res.* **23**, 336–340 (2008).
8. Cuevas, F., Korablov, D. & Latroche, M. Synthesis, structural and hydrogenation properties of Mg-rich MgH<sub>2</sub>-TiH<sub>2</sub> nanocomposites prepared by reactive ball milling under hydrogen gas. *Phys. Chem. Chem. Phys.* **14**, 1200–1211 (2012).
9. Agubra, V. A. & Fergus, J. W. The formation and stability of the solid electrolyte interface on the graphite anode. *J. Power Sources* **268**, 153–162 (2014).
10. Verma, P., Maire, P. & Novák, P. A review of the features and analyses of the solid electrolyte interphase in Li-ion batteries. *Electrochim. Acta* **55**, 6332–6341 (2010).
11. Oumellal, Y., Rougier, A., Nazri, G. A., Tarascon, J.-M. & Aymard, L. Metal hydrides for lithium-ion batteries. *Nat. Mater.* **7**, 916–921 (2008).
12. Oumellal, Y. *et al.* Bottom-up preparation of MgH<sub>2</sub> nanoparticles with enhanced

- cycle life stability during electrochemical conversion in Li-ion batteries. *Nanoscale* **6**, 14459–14466 (2014).
13. Park, C. M., Kim, Y. U., Kim, H. & Sohn, H. J. Enhancement of the rate capability and cyclability of an Mg-C composite electrode for Li secondary batteries. *J. Power Sources* **158**, 1451–1455 (2006).
  14. Oumellal, Y. *et al.* Reactivity of TiH<sub>2</sub> hydride with lithium ion: Evidence for a new conversion mechanism. *Int. J. Hydrogen Energy* **37**, 7831–7835 (2012).
  15. Mizuno, K., Furuya, Y., Hirano, K. & Okamoto, H. Hydrogen diffusion in titanium-hydride observed by the diffraction-enhanced X-ray imaging method. *Phys. Status Solidi Appl. Mater. Sci.* **204**, 2734–2739 (2007).
  16. Manchester, F.D. Phase Diagrams of Binary Hydrogen Alloys. *ASM International* (2000).
  17. Vermeulen, P., Niessen, R. a. H. & Notten, P. H. L. Hydrogen storage in metastable Mg<sub>y</sub>Ti<sub>(1-y)</sub> thin films. *Electrochem. commun.* **8**, 27–32 (2006).
  18. Asano, K., Enoki, H. & Akiba, E. Synthesis of HCP, FCC and BCC structure alloys in the Mg-Ti binary system by means of ball milling. *J. Alloys Compd.* **480**, 558–563 (2009).
  19. Kyoï, D. *et al.* A new ternary magnesium-titanium hydride Mg<sub>7</sub>TiH<sub>x</sub> with hydrogen desorption properties better than both binary magnesium and titanium hydrides. *J. Alloys Compd.* **372**, 213–217 (2004).
  20. Oumellal Y. *Réactivité électrochimique des hydrures métalliques vis-à-vis du lithium: Electrodes negatives pour batteries Li-ion: Stockage de l'hydrogène par voie solide-gaz.* Ph.D. Thesis, Université de Picardie, Jules Verne (2009).
  21. Aymard, L., Oumellal, Y. & Bonnet, J. P. Metal hydrides: An innovative and challenging conversion reaction anode for lithium-ion batteries. *Beilstein J. Nanotechnol.* **6**, 1821–1839 (2015).
  22. Oumellal, Y., Rougier, A., Tarascon, J. M. & Aymard, L. 2LiH + M (M = Mg, Ti): New concept of negative electrode for rechargeable lithium-ion batteries. *J. Power Sources* **192**, 698–702 (2009).

23. Huang, L., Aymard, L. & Bonnet, J.-P. MgH<sub>2</sub>-TiH<sub>2</sub> mixture as an anode for lithium-ion batteries: synergic enhancement of the conversion electrode electrochemical performance. *J. Mater. Chem. A* **3**, 15091–15096 (2015).
24. Ito, M. *et al.* Electrical and thermal properties of titanium hydrides. *J. Alloys Compd.* **420**, 25–28 (2006).
25. Berti, N., Cuevas, F., Zhang, J. & Latroche, M. Enhanced reversibility of the electrochemical Li conversion reaction with MgH<sub>2</sub>-TiH<sub>2</sub> nanocomposites. *Int. J. Hydrogen Energy* **42**, 22615-22621 (2017). doi:10.1016/j.ijhydene.2017.03.048

# **CHAPTER 5**

All solid-state Li-ion battery



# Content

<b>1</b>	<b>LiBH<sub>4</sub> as solid electrolyte for Li-ion batteries</b>	<b>156</b>
<b>2</b>	<b>MgH<sub>2</sub> and TiH<sub>2</sub> as electrode materials in LiBH<sub>4</sub> solid-state half cells</b>	<b>159</b>
2.1	Cycling of pure MgH <sub>2</sub> electrode	159
2.2	Cycling of pure TiH <sub>2</sub> electrode	160
2.3	Cycling of MgH <sub>2</sub> +TiH <sub>2</sub> nanocomposites	161
<b>3</b>	<b>Solid-state metal hydride-sulphur Li-ion battery</b>	<b>165</b>
<b>4</b>	<b>Discussion</b>	<b>167</b>
4.1	Cycle-life of MgH <sub>2</sub> and TiH <sub>2</sub> in LiBH <sub>4</sub> solid half-cells	167
4.1.1	Single phase MgH <sub>2</sub> and TiH <sub>2</sub>	167
4.1.2	MgH <sub>2</sub> +TiH <sub>2</sub> composites	168
4.2	Cycle-life of solid-state Li-ion battery	170
<b>5</b>	<b>Conclusions</b>	<b>172</b>
	<b>References</b>	<b>174</b>



All solid-state Li-ion batteries are also good candidates for future energy storage applications to overcome safety issues, such as dendrites growth and liquid electrolyte decomposition or leaking. However, to achieve discharge/charge cycling with good kinetics, electrolytes with an ionic conductivity in the order of  $10^{-3}$  S cm<sup>-1</sup> under operating conditions are required.

In the past years, several kinds of solid electrolytes for Li-ion batteries have been investigated [1–10]. In this thesis, we studied the electrochemical behaviour of solid-state cells using LiBH<sub>4</sub> as solid electrolyte. LiBH<sub>4</sub> has shown to possess a high ionic conductivity around 120 °C [11–13], and also to enhance the mobility of H<sup>-</sup> in MgH<sub>2</sub> for hydrogen storage applications [14–16]. For these reasons, LiBH<sub>4</sub> is a promising material to be used in a metal hydride solid-state battery.

In this chapter, the structural and conductivity properties of LiBH<sub>4</sub> are investigated by X-ray diffraction (XRD) and electrochemical impedance spectroscopy (EIS). Half-cells with LiBH<sub>4</sub> as solid electrolyte are prepared to study the performance of MgH<sub>2</sub>, TiH<sub>2</sub> and  $y\text{MgH}_2+(1-y)\text{TiH}_2$  nanocomposites as electrode materials during galvanostatic cycling. Furthermore, a complete solid-state battery is assembled using composite 0.8MgH<sub>2</sub>-0.2TiH<sub>2</sub> and Li<sub>2</sub>S as anode and cathode materials respectively. This latter work has been carried out in collaboration with Dr. Pedro López-Aranguren and Anh Ha Dao in SAFT Co. (Bordeaux).



## 1 LiBH<sub>4</sub> as solid electrolyte for Li-ion batteries

Bulk LiBH<sub>4</sub> was provided by Rockwood Lithium Co. (ECOSTORE partner). Its XRD pattern is shown in Figure 5.1. At room temperature, LiBH<sub>4</sub> crystallizes in orthorhombic structure, with space group *Pnma*. In this low temperature (LT) structure, each (BH<sub>4</sub>)<sup>-</sup> anion is surrounded by four Li<sup>+</sup> cations, and each Li<sup>+</sup> cation by four (BH<sub>4</sub>)<sup>-</sup> anions, both in tetrahedral configurations [17].

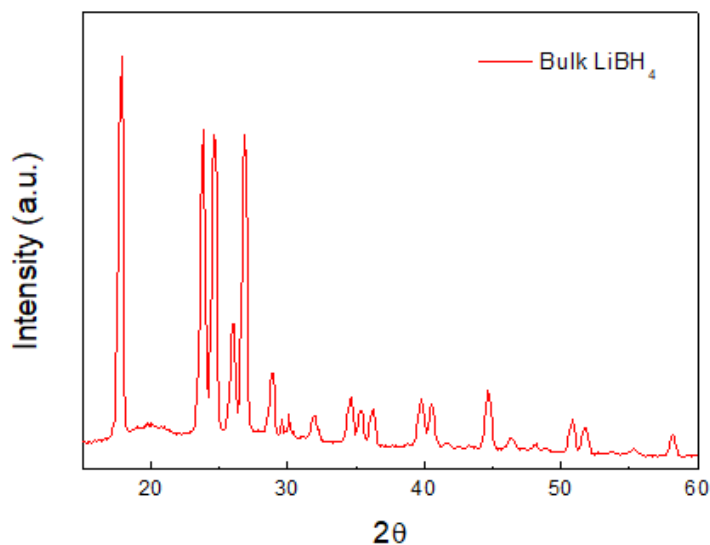


**Figure 5.1.** XRD pattern at room temperature of as-received LiBH<sub>4</sub>.

The conductivity of LiBH<sub>4</sub> has been evaluated by EIS in a temperature range from 60 °C to 140 °C. For this purpose, the solid electrolyte has been pelletized in an 8-mm die, and placed in a Swagelok cell between two Li foil disks. The calculated conductivity values (see Chapter 2 section 3.3 for the calculation) are reported in Figure 5.2.

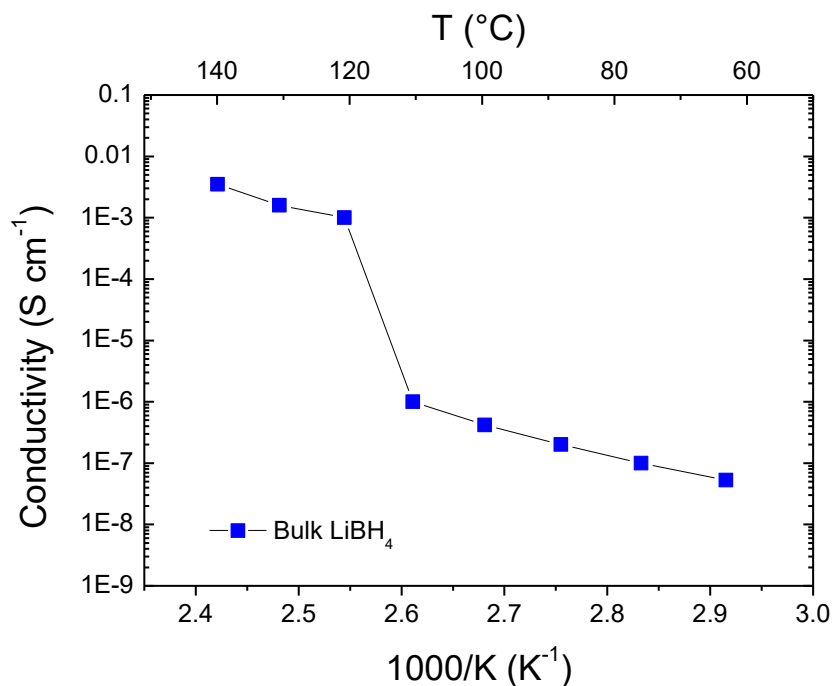


**Figure 5.2.** Ionic conductivity of bulk LiBH<sub>4</sub> from 60 °C to 140 °C.

From 80 °C to 110 °C, bulk LiBH<sub>4</sub> shows a conductivity below 10<sup>-6</sup> S cm<sup>-1</sup>, preventing any practical application. However, above 110 °C a discontinuous jump is observed, leading to a conductivity of 10<sup>-3</sup> S cm<sup>-1</sup> at 120 °C. At higher temperatures, the conductivity gradually increases. These results are in agreement with the work of Matsuo *et al.*, which have demonstrated that this conductivity is actually due to the Li ionic motion [11], hence we can refer to it as ionic conductivity. This increase in the ionic conductivity is due to a first order phase transition which LiBH<sub>4</sub> undergoes at high temperature. As shown in Figure 5.3 (top), during Differential scanning calorimetry (DSC) measurement an endothermic peak (*i.e.* negative heat flow) is observed around 118 °C while heating the sample. This peak corresponds to a transition from the orthorhombic to hexagonal structure. Compared to the orthorhombic phase (Figure 5.3 bottom), the high temperature (HT) hexagonal phase possess a space group  $P6_3mc$  in which the tetrahedral (BH<sub>4</sub>)<sup>-</sup> anions are less disordered. Consequently, one of the four nearest (BH<sub>4</sub>)<sup>-</sup> is shifted away from Li<sup>+</sup>, and the other three are shifted towards it [17]. The high mobility of Li ions in the HT phase has been attributed to the fact that both Li<sup>+</sup> and (BH<sub>4</sub>)<sup>-</sup> line up along the *a* and *b* axes, allowing the migrations of Li ions along the *a* and *c* directions [12].

While cooling, LiBH<sub>4</sub> comes back to the orthorhombic structure, providing an exothermic peak around 102 °C.

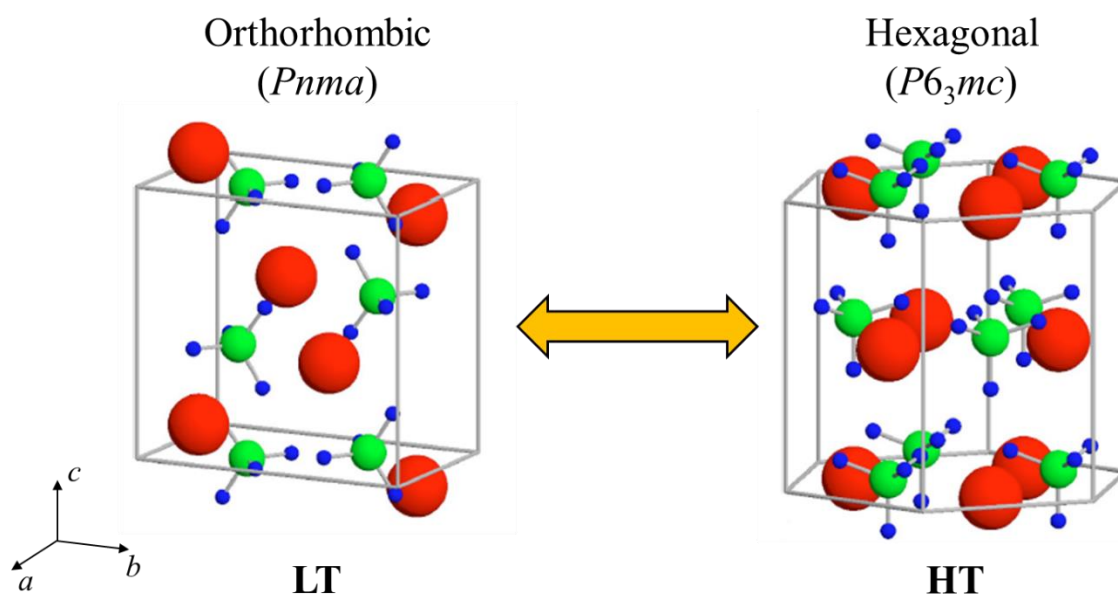
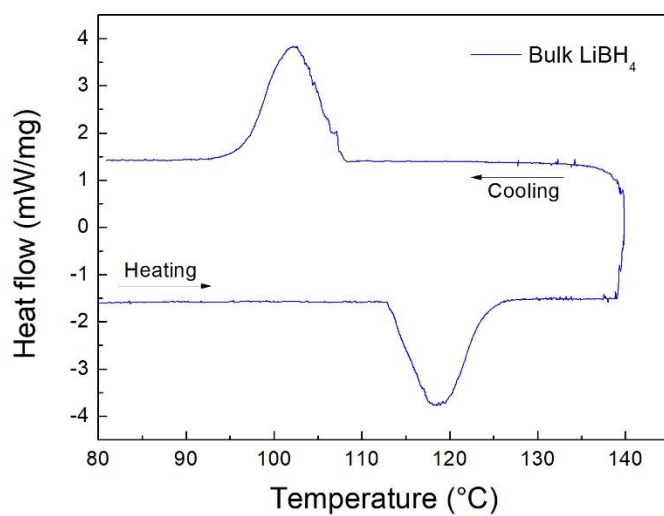


**Figure 5.3.** Top: DSC measurement of  $\text{LiBH}_4$  in the range 80 – 140  $^{\circ}\text{C}$ , with a heat flow of 5  $^{\circ}\text{C}$  per minute. Bottom: Comparison between the LT and HT structures, where Li atoms are the red spheres, H the blues, and B the green ones (Readapted from ref [18]).

## 2 MgH<sub>2</sub> and TiH<sub>2</sub> as electrode materials in LiBH<sub>4</sub> solid-state half cells

Electrodes with MgH<sub>2</sub> and TiH<sub>2</sub> have been prepared, as described in Chapter 2 section 4.2.2, by ball milling the active material with carbon Super P and LiBH<sub>4</sub> in weight ratio 35:20:45 respectively. The solid-state half-cells  $M\text{H}_2+\text{SP}+\text{LiBH}_4 \parallel \text{LiBH}_4 \parallel \text{Li}$  (with  $M = \text{Mg}$  and  $\text{Ti}$ ) have been placed in an oil bath at 120 °C and cycled with a kinetics regime of C/50.

### 2.1 Cycling of pure MgH<sub>2</sub> electrode

Electrodes based on MgH<sub>2</sub> have been cycled in a potential window between 0.2 V and 1 V, in order to avoid both the Mg-Li alloying reaction that occurs below 0.1 V, and the reaction between MgH<sub>2</sub> and LiBH<sub>4</sub> above 1 V [19]. Figure 5.4 shows the initial galvanostatic cycles for MgH<sub>2</sub> electrodes in a solid-state half-cell at 120 °C.

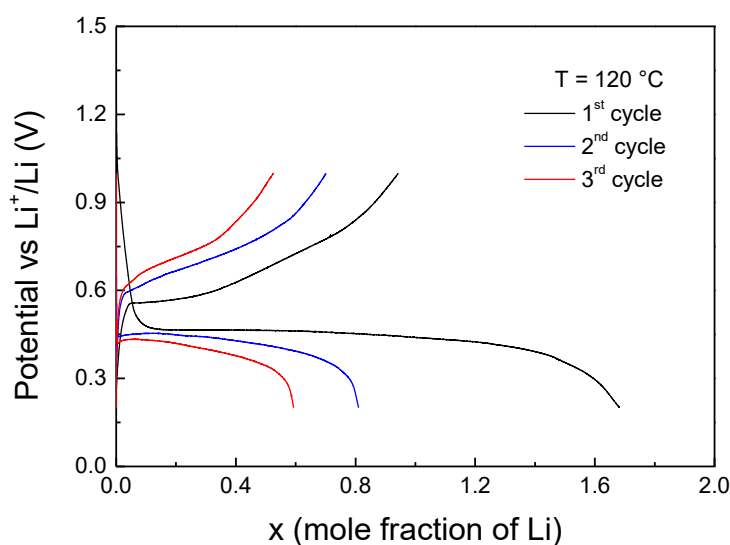


**Figure 5.4.** First galvanostatic discharge-charge curves for MgH<sub>2</sub> electrode between 0.2 V and 1 V, with a C-rate of C/50.

The initial slope, up to  $x = 0.15$  during the discharge has been attributed to the formation of a SEI. As reported by Unemoto *et al.* [20], during the first discharge LiBH<sub>4</sub> decomposes on the surface of the electrode forming a stable new phase, which likely includes Li<sub>2</sub>B<sub>12</sub>H<sub>12</sub>. After the slope, a well-defined plateau is found at 0.45 V attributed to the reaction of MgH<sub>2</sub> with Li. The content of lithium store during the discharge is 1.7 (*i.e.*

1730 mAh g<sup>-1</sup>), hence the lithiation is not complete. During the delithiation, the extraction of lithium is observed at 0.57 V, recovering almost 1 Li, therefore the electrode exhibits a reversibility of 56%.

In the subsequent cycles the capacity decreases with a smaller decay compared to the first cycles. As reported in Table 5.1, because the loss in capacity is smaller after the first cycle, the Coulombic efficiency increases for the second and third cycles.

**Table 5.1.** Coulombic efficiency and discharge/charge capacities attained during cycling of MgH<sub>2</sub> electrode in a solid-state half-cell.

	1 <sup>st</sup> cycle	2 <sup>nd</sup> cycle	3 <sup>rd</sup> cycle
Coulombic efficiency (%)	56	88	87
Discharge capacity (mAh g <sup>-1</sup> )	1730	815	610
Charge capacity (mAh g <sup>-1</sup> )	970	715	530

## 2.2 Cycling of pure TiH<sub>2</sub> electrode

The potential vs. composition profiles of TiH<sub>2</sub> electrode in a solid-state half-cell during galvanostatic cycling at 120 °C, in a potential window 5mV to 1 V, are shown in Figure 5.5.

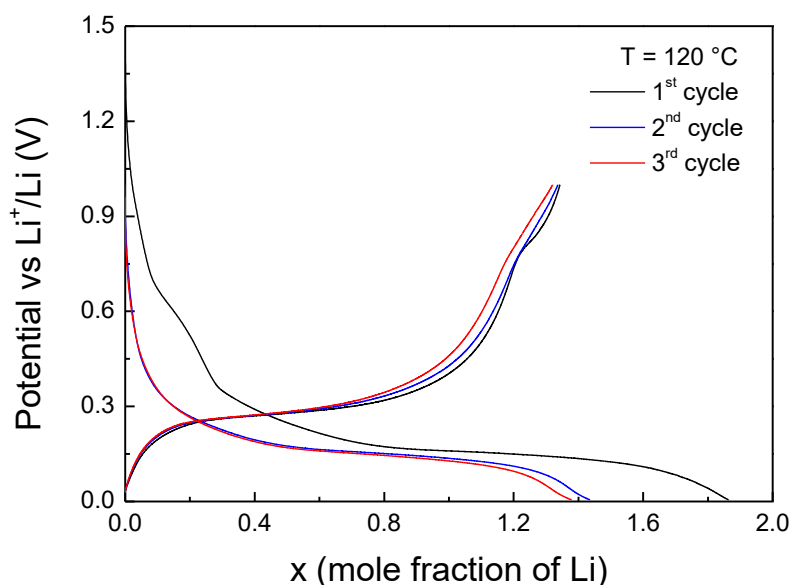


**Figure 5.5.** Evolution of the potential as a function of the mole fraction of Li ( $x$ ) during the discharge-charge cycles for TiH<sub>2</sub> electrode at a kinetics regime of C/50.

On lithiation, three different signals are found in the discharge curve of the half cell. A shoulder is found around 0.7 V, which can be associated to the decomposition of  $\text{LiBH}_4$  forming the SEI. Next, a slope is noticed between 0.3 V and 0.16 V, followed by a plateau around 0.15 V. Previous work on  $\text{TiH}_2$  as electrode material in Li-ion batteries [21] has shown that a single-step reaction cannot be used to describe the conversion reaction of this hydride. Indeed, the slope is attributed to the formation of  $\delta\text{-TiH}_{2-x}$  solid solution, which subsequently is dehydrogenated during the plateau, reaching the complete conversion to Ti and LiH. At the end of the first discharge, 1.9 Li are stored into the electrode, achieving a capacity of  $1000 \text{ mAh g}^{-1}$ . On delithiation, 71% of the lithium is extracted (1.3 Li) during the oxidation at 0.3 V.

As summarized in Table 5.2, after a decrease in capacity in the second cycle ( $770 \text{ mAh g}^{-1}$  on lithiation), the electrode exhibits a high Coulombic efficiency above 90% in the subsequent cycles.

**Table 5.2.** Coulombic efficiency and discharge/charge capacities attained during cycling of  $\text{TiH}_2$  electrode in a solid-state half-cell.

	1 <sup>st</sup> cycle	2 <sup>nd</sup> cycle	3 <sup>rd</sup> cycle
Coulombic efficiency (%)	72	91	93
Discharge capacity ( $\text{mAh g}^{-1}$ )	1000	770	740
Charge capacity ( $\text{mAh g}^{-1}$ )	720	700	690

It is worth to notice that  $\text{TiH}_2$ , whose conversion reaction was irreversible at room temperature using a classical liquid electrolyte, here shows good reversibility at  $120 \text{ }^\circ\text{C}$  using  $\text{LiBH}_4$  as solid electrolyte. Moreover, the reversibility and Coulombic efficiency during cycling are better than for  $\text{MgH}_2$  electrode (Figure 5.4).

### 2.3 Cycling of $\text{MgH}_2+\text{TiH}_2$ nanocomposites

$y\text{MgH}_2+(1-y)\text{TiH}_2$  nanocomposites, with molar ratio  $y = 0.2, 0.5, 0.6, 0.7$  and  $0.8$ , have been investigated as active materials in solid-state half-cells. Galvanostatic cycling has been performed in the potential window  $0.1 - 1 \text{ V}$  in order to avoid the alloying reaction between Mg and Li at potentials lower than  $0.1 \text{ V}$ . Figure 5.6 shows the first discharge/charge cycle for all the composites at a kinetics regime of C/50.

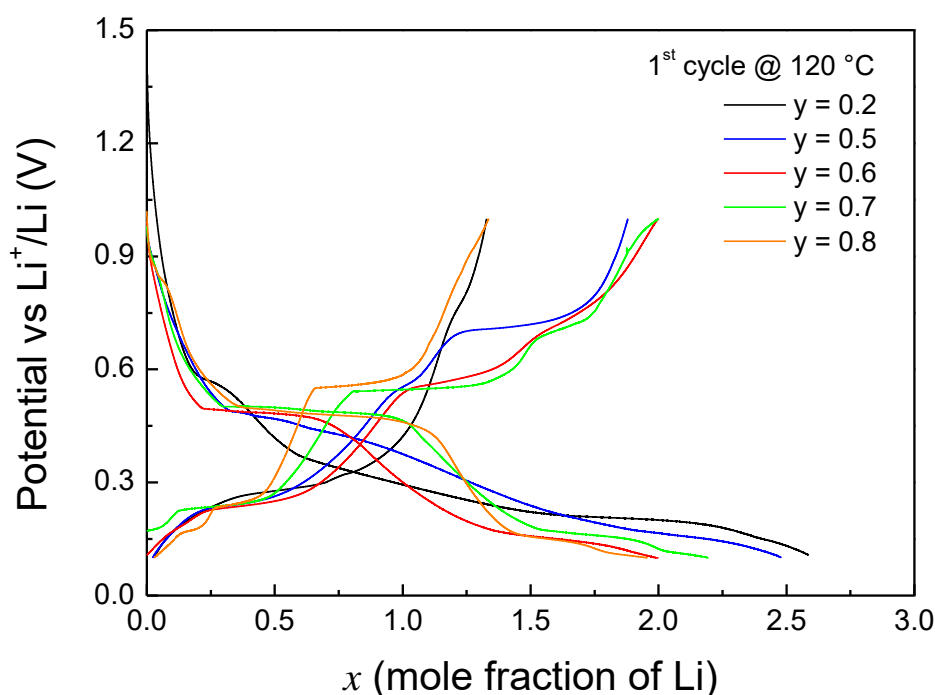


**Figure 5.6.** Evolution of the potential as a function of the mole fraction of Li ( $x$ ) during the first discharge-charge cycle for the  $y\text{MgH}_2+(1-y)\text{TiH}_2$  nanocomposites ( $y = 0.2, 0.5, 0.6, 0.7$  and  $0.8$ ) in half-cells with bulk  $\text{LiBH}_4$  as solid electrolyte.

During the first discharge, after the formation of the SEI, all the electrodes show two plateaus around  $0.50 - 0.45$  V and  $0.20 - 0.15$  V, assigned to the reaction of  $\text{MgH}_2$  and  $\text{TiH}_2$  with Li, respectively. The quantity of lithium stored at the end of the lithiation is comprised between 2 and 2.6 Li. It is worth to notice that the composite electrodes show a lithium content of at least 2 Li, whereas the single hydride electrodes do not reach a full lithiated state (Figure 5.4 and 5.5).

Interestingly, the molar ratio of the composites seems to affect the plateau potential value of the hydrides. Indeed, the conversion reaction of  $\text{MgH}_2$  occurs at higher potential in Mg-rich composites  $y \geq 0.6$  ( $\sim 0.5$  V) compared to  $y = 0.2$  and  $0.5$  ( $\sim 0.3$  V and  $\sim 0.4$  V, respectively). On the other hand, the conversion reaction of  $\text{TiH}_2$  occurs at higher potential in Ti-rich composite  $y = 0.2$  ( $\sim 0.2$  V) compared to Mg-rich electrodes ( $\sim 0.17$  V for  $y = 0.5$ , and  $\sim 0.16$  V for  $y \geq 0.6$ ). These results suggest that the conversion reaction of a hydride possesses a smaller overpotential when it is the most abundant phase in the electrode.

On delithiation, the reformation of  $\text{TiH}_2$  from Ti and LiH is around 0.24 V for all composites except for the Ti-richest one ( $y = 0.2$ ) whose plateau is slightly higher (0.30 V).

Then, the restoring of  $\text{MgH}_2$  is found at 0.56 V. The shoulder noticed at 0.7 – 0.8 V is also found by other authors working with  $\text{MgH}_2$  and  $\text{TiH}_2$  in cells containing  $\text{LiBH}_4$  as solid electrolyte [22, 23], but the nature of this signal is still unclear. However, its extension seems not to depend on the molar ratio of the composites.

Different amounts of Li are extracted from the electrodes during the first charge. The performances achieved during cycling are reported in Table 5.3 below. Composite  $y = 0.2$  loses 32% of its calculated capacity during the first delithiation, but in the subsequent cycles exhibits a stable capacity around  $800 \text{ mAh g}^{-1}$ , achieving the highest reversibility among all the composites. Electrodes  $y = 0.6$  and  $0.7$  show a complete delithiation recovering 2 Li during the first charge, however their capacity decreases while cycling. It is worth to notice that the capacity lost within ten cycles increases with the amount of  $\text{MgH}_2$  into the composite. Indeed, although Mg-rich electrode  $y = 0.8$  shows a good reversibility, it has lost the larger capacity during cycling ( $918 \text{ mAh g}^{-1}$ ). On the other hand, Ti-rich electrode  $y = 0.2$  exhibits the smaller loss ( $365 \text{ mAh g}^{-1}$ ). Previously, it was shown that the cycle-life of pure  $\text{TiH}_2$  was better than pure  $\text{MgH}_2$  electrode (Figure 5.5 vs. 5.4, respectively). This could explain the good capacity retention of composite  $y = 0.2$  compared to  $y = 0.8$ . It is also worth to notice that composite  $y = 0.7$  shows the smaller capacity loss ( $548 \text{ mAh g}^{-1}$ ) among the Mg-rich composites, delivering more than  $1000 \text{ mAh g}^{-1}$  after ten cycles (reversibility 66%). The performance of this composite was highlighted also with liquid electrolyte (Chapter 4 section 3.3), suggesting that even at high temperature the molar ratio between the hydrides plays a relevant role in the electrochemical activity of the cell.



**Table 5.3.** Charge capacities, reversibility, and capacity lost of  $\gamma\text{MgH}_2+(1-\gamma)\text{TiH}_2$  composites using  $\text{LiBH}_4$  as solid electrolyte.

Composite ( $\gamma$ )	Calculated capacity ( $\text{mAh g}^{-1}$ )	Charge capacity 1 <sup>st</sup> cycle ( $\text{mAh g}^{-1}$ )	Charge capacity 5 <sup>th</sup> cycle ( $\text{mAh g}^{-1}$ )	Charge capacity 10 <sup>th</sup> cycle ( $\text{mAh g}^{-1}$ )	Reversibility 1 <sup>st</sup> vs. 10 <sup>th</sup> cycles (%)	Irreversible capacity lost in 10 cycles ( $\text{mAh g}^{-1}$ )
0.2	1185	800	810	820	103	365
0.5	1405	1310	880	800	61	605
0.6	1493	1493	890	805	54	688
0.7	1608	1608	1280	1060	66	548
0.8	1718	1130	920	800	71	918

### 3 Solid-state metal hydride-sulphur Li-ion battery

$\text{MgH}_2+\text{TiH}_2$  composites have shown good electrochemical performance while cycled at high temperature with  $\text{LiBH}_4$  as solid electrolyte, suggesting a possible application in solid batteries in the next future. However, to accomplish their implementation in a full cell it is necessary to find suitable lithium-based positive materials with similar capacities and chemical compatibility with the solid electrolyte. Promising results have been achieved by Unemoto *et al.* [24] using sulphur as active material in a solid-state half-cell with  $\text{LiBH}_4$  as electrolyte. Theoretically, sulphur can be lithiated up to  $\text{Li}_2\text{S}$ , providing a capacity of  $1672 \text{ mAh g}^{-1}$  at a potential around  $2.2 \text{ V vs. Li}^+/\text{Li}$ . Thanks to its high capacity and working potential, sulphur might be coupled with a  $\text{MgH}_2+\text{TiH}_2$  composite with the purpose of assembling a complete solid-state battery.

For this work,  $0.8\text{MgH}_2+0.2\text{TiH}_2$  was chosen as negative material, and  $\text{Li}_2\text{S}$  was prepared in situ and used as positive material. As described in Chapter 2 section 4.2.3, to prepared the positive material a mixture of S, carbon KB and  $\text{LiBH}_4$  (wt% 25:25:50, respectively) was lithiated in a solid-state half-cell at  $120 \text{ }^\circ\text{C}$ , with a C-rate of C/50. Figure 5.7 shows the lithiation curve of this half-cell in the potential window  $1 - 3 \text{ V}$ .

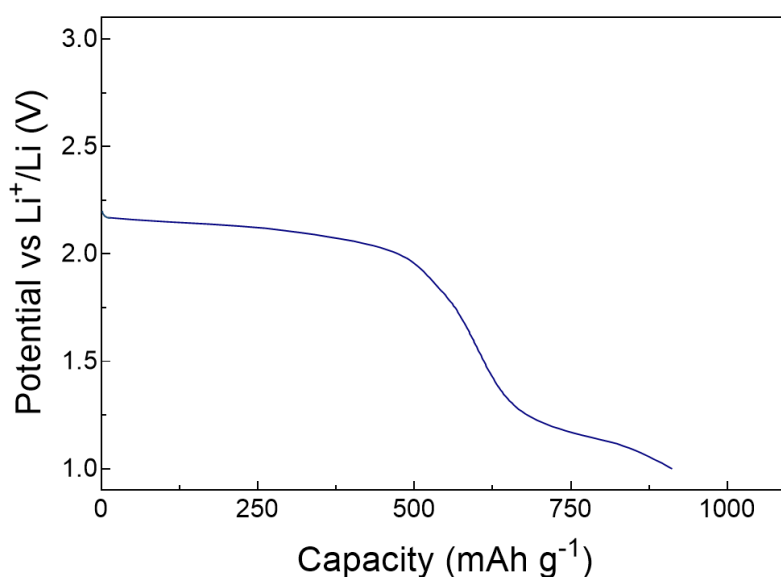


**Figure 5.7.** Lithiation of sulphur electrode in a solid-state half-cell at  $120 \text{ }^\circ\text{C}$ , with C/50 in a potential window between  $1 \text{ V}$  and  $3 \text{ V}$ .

The profile of the sulphur half-cell displays a plateau around  $2.2 \text{ V}$ , reaching a capacity of  $920 \text{ mAh g}^{-1}$ , implying a lithiation of 55% of sulphur. The results are in

agreement with Unemoto *et al.* [24], which obtained similar profile and capacity. Once lithiated, the working electrode was recovered from the cell.

To assemble the complete solid-state battery, the positive material was added in ~ 30% molar excess to compensate the lower capacity of partially lithiated  $\text{Li}_2\text{S}$  compared to  $0.8\text{MgH}_2+0.2\text{TiH}_2$ . Galvanostatic cycling was carried out in a potential window between 0.8 V and 2.5 V at 120 °C, with C/50. Figure 5.8 shows the first five cycles, and the overall redox reaction.

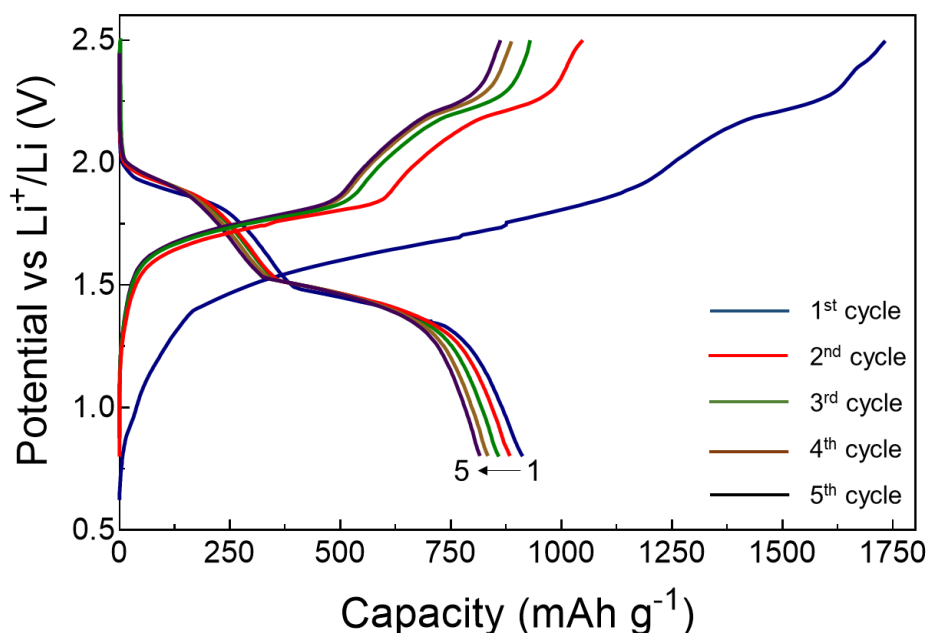
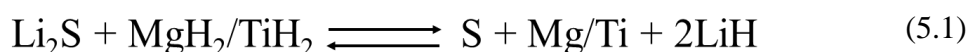


**Figure 5.8.** Discharge/charge profiles of the complete solid-state Li-ion battery  $\text{Li}_2\text{S}/0.8\text{MgH}_2+0.2\text{TiH}_2$  performed at 120 °C, with C/50, in a potential window 0.8 – 2.5 V.

The initial charging process (*i.e.* lithium from the positive to the negative electrode) shows a first large plateau around 1.8 V followed by a smaller one at ~ 2.2 V, corresponding to the reduction of  $\text{MgH}_2$  and  $\text{TiH}_2$  respectively. The additional capacity above 2.3 V has been attributed to the alloying reaction between Mg and Li. The final capacity, 1750 mAh  $\text{g}^{-1}$ , suggests a complete lithiation of the negative electrode.

During the discharge, the battery displays two plateaus at 1.8 V and 1.4 V for the restoring of  $\text{TiH}_2$  and  $\text{MgH}_2$  respectively, achieving a capacity of 920 mAh  $\text{g}^{-1}$ . In the

subsequent cycles the capacity slowly decreases, providing 820 mAh g<sup>-1</sup> during the fifth discharge. It is worth to notice that the capacity retention after five cycles is higher in the complete Li-ion battery than in the half-cell, 89% vs. 81% respectively.

## 4 Discussion

Lithium borohydride has been used as electrolyte to investigate the electrochemical activity of MgH<sub>2</sub> and TiH<sub>2</sub> in solid-state cells. Because LiBH<sub>4</sub> exhibits a high ionic conductivity (10<sup>-3</sup> S cm<sup>-1</sup>) only at high temperature, the cycling of the cells has been carried out at 120 °C. Later, a complete solid-state Li-ion has been assembled using 0.8MgH<sub>2</sub>+0.2TiH<sub>2</sub> composite as negative electrode, and Li<sub>2</sub>S as positive electrode.

### 4.1 Cycle-life of MgH<sub>2</sub> and TiH<sub>2</sub> in LiBH<sub>4</sub> solid half-cells

#### 4.1.1 Single phase MgH<sub>2</sub> and TiH<sub>2</sub>

Electrodes prepared from single MgH<sub>2</sub> and TiH<sub>2</sub> phases showed a partial lithiation during galvanostatic discharge, *i.e.* no one of these hydrides achieved a full conversion with lithium  $x = 2$ . Interestingly, TiH<sub>2</sub> exhibited a higher reversibility compared to MgH<sub>2</sub> during the first cycle, 72% vs. 56% respectively (Figure 5.5 vs. 5.4). Moreover, the capacity retention is higher for TiH<sub>2</sub>, losing only 2% of its capacity in each subsequent cycle.

Similar results can be found in the literature comparing the paper of Zeng *et al.* about MgH<sub>2</sub> catalyzed with Nb<sub>2</sub>O<sub>5</sub> [19]. However, higher reversibility, and so longer cycle life, are obtained by Zeng and coworkers, especially when the active material was ball milled with vapour grown carbon nanofibers (VGCF) [22]. Such performance might be attributed to the different electrode preparation (*i.e.* different conductive carbon, catalytic effect of Nb<sub>2</sub>O<sub>5</sub>, different ball milling conditions and pellet preparation), suggesting that additional studies on the electrode formulation and preparation could lead to further improvements of MgH<sub>2</sub> in solid-state cells. Also Ikeda *et al.* investigated the properties of MgH<sub>2</sub> catalyzed with Nb<sub>2</sub>O<sub>5</sub> [25] and Al<sub>2</sub>O<sub>3</sub> [26], using as solid electrolyte 80Li<sub>2</sub>S-20P<sub>2</sub>S<sub>5</sub> composite at 100 °C. However, these electrodes showed a reversibility of 41% and 51% respectively.

A high Coulombic efficiency for TiH<sub>2</sub> in LiBH<sub>4</sub> solid cells was also found by Kawahito *et al.* [23], which obtained a reversibility of 88% after the first cycle.

Comparing all these papers, it is worth to notice that, in order to exhibit a capacity retention during cycling,  $\text{MgH}_2$  needs a catalyst and also a carbon support (VGCF), whereas  $\text{TiH}_2$  does not require specific additives. These results suggest that  $\text{TiH}_2$  shows a better cycle-life than  $\text{MgH}_2$  at 120 °C because of its better electrical conductivity and hydrogen mobility.

#### 4.1.2 $\text{MgH}_2+\text{TiH}_2$ composites

Composite  $\text{MgH}_2+\text{TiH}_2$  electrodes have shown to achieve a quantity of Li stored during the first discharge higher than the single hydride cells ( $x \geq 2$ ), suggesting a better reactivity of the composites. In the first cycle, electrodes  $y = 0.6$  and  $0.7$  showed the highest reversibility, with the extraction of 2 Li during delithiation (Figure 5.6), implying the complete reformation of both hydrides. However, after ten cycles, Ti-rich electrode  $y = 0.2$  exhibits the highest capacity retention, providing an almost constant capacity around 800  $\text{mAh g}^{-1}$ . On the other hand, Mg-rich composites showed a large capacity loss compared to their first discharge (Table 5.3). Even if  $y = 0.8$  shows the highest reversibility (71%) among the Mg-rich composites, after ten cycles it has lost 918  $\text{mAh g}^{-1}$  (*i.e.* 53% of its calculated capacity), implying a poor capacity retention. These results suggest that also in  $\text{MgH}_2+\text{TiH}_2$  composites  $\text{TiH}_2$  phase possesses a better capacity retention than  $\text{MgH}_2$  phase. This is demonstrated in Figure 5.9, where the cycling of electrodes  $y = 0.2$  and  $0.8$  are compared.

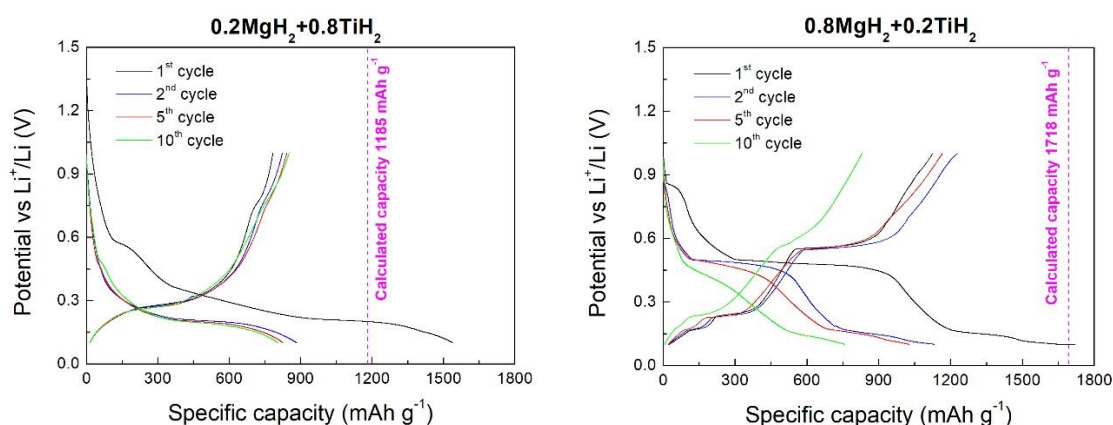


**Figure 5.9.** Discharge/charge potential profiles during cycling of  $y\text{MgH}_2+(1-y)\text{TiH}_2$  electrodes with  $y = 0.2$  (left) and  $y = 0.8$  (right), studied at 120 °C in half-cells with  $\text{LiBH}_4$  as solid electrolyte.

After the lithiation, Ti-rich composite  $y = 0.2$  (Figure 5.9 left) shows a pseudo-plateau around 0.3 V during delithiation for the restoration of  $\text{TiH}_2$ . The reformation of  $\text{MgH}_2$ , expected around 0.6 V, is not clearly detected, probably because of its poor contribution and reversibility compared to the main phase  $\text{TiH}_2$ . Then, after an initial loss of capacity within the first cycle, the electrode exhibits discharge/charge curves around 800  $\text{mAh g}^{-1}$  during the subsequent cycles, implying a good capacity retention.

For the Mg-rich composite  $y = 0.8$  (Figure 5.9 right), after its lithiation, two plateaus are found during the delithiation at 0.23 V and 0.55 V for the reformation of  $\text{TiH}_2$  and  $\text{MgH}_2$  respectively. During cycling, the capacity provided by the electrode decreases, suggesting a poor capacity retention. It is worth to notice that during cycling the extents of the  $\text{MgH}_2$  contribution, both in discharge and charge, drastically decreases compared to the plateaus of  $\text{TiH}_2$  conversion reaction. Indeed, during the tenth cycle, the plateaus of  $\text{MgH}_2$  are barely detected, demonstrating the poor capacity retention of this phase.

If electrode  $y = 0.2$  exhibits the highest capacity retention, on the other hand electrode  $y = 0.7$  provides the highest capacity after ten cycles ( $1060 \text{ mAh g}^{-1}$ ), with a capacity retention of 66%. Because of these results, their electrochemical activity was further investigated cycling at different C-rate. Figure 5.10 shows a comparison between the charge capacities and retention of these two composites cycled in potential window 0.1 – 1 V at 120 °C with different kinetics regimes.

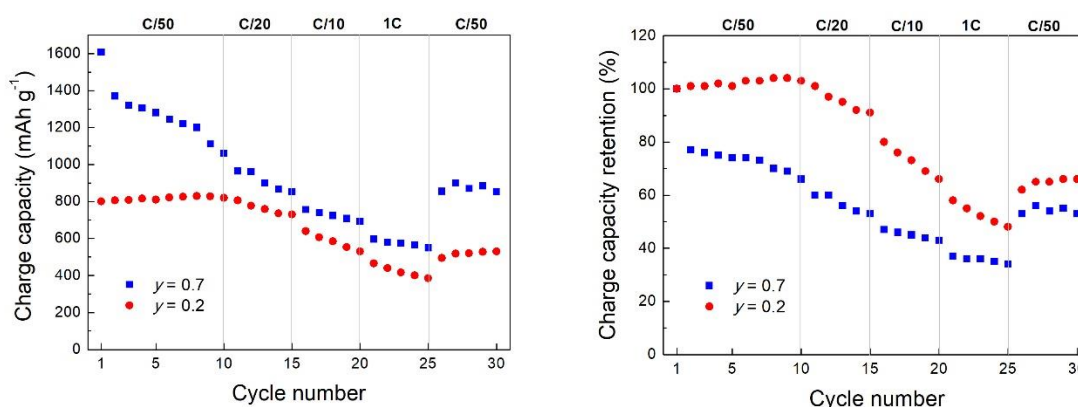


**Figure 5.10.** Charge capacities (left) and retention (right) of composites  $y = 0.2$  (red circles) and 0.7 (blue squares) during cycling at different C-rates.

As previously shown (Figure 5.6), during the first delithiation of composite  $y = 0.7$  the hydrides are fully recovered ( $1608 \text{ mAh g}^{-1}$ , *i.e.* 2 Li). However, in the subsequent cycles at C/50 the capacity decreases, attaining 66% of the initial capacity after ten cycles. When the C-rate is increased a clear drop in the capacity is noticed, which implies kinetics limitations of the electrode. After cycling at C/20, C/10 and 1C, the cell is set back to C/50, recovering a charge capacity of  $855 \text{ mAh g}^{-1}$  (*i.e.* 53% capacity retention), implying a loss of  $205 \text{ mAh g}^{-1}$ .

On the other hand, electrode  $y = 0.2$  achieves a partial delithiation during the first charge ( $800 \text{ mAh g}^{-1}$ , *i.e.* 1.46 Li). Though, the capacity provided in the subsequent cycles at C/50 is almost constant, implying a capacity retention around 100%. When cycled at faster C-rates, composite  $y = 0.2$  shows a remarkable drop in the capacity retention, from 100% to 48% at 1C. Moreover, when back at C/50, the electrode is not able to recover the initial capacity, delivering  $495 \text{ mAh g}^{-1}$  (*i.e.* 62% capacity retention), denoting a loss of  $325 \text{ mAh g}^{-1}$ .

At the light of these results, it is possible to notice that composite  $y = 0.7$  provides high capacity even being cycled at fast C-rates, however its capacity retention decreases during cycling. On the contrary, composite  $y = 0.2$  shows a remarkable capacity drop at high C-rates, but when cycled at C/50 exhibits an almost constant capacity retention around 100%.

## 4.2 Cycle-life of solid-state Li-ion battery

A complete solid-state Li-ion battery has been assembled with  $\text{LiBH}_4$  as solid electrolyte,  $0.8\text{MgH}_2+0.2\text{TiH}_2$  as negative electrode, and  $\text{Li}_2\text{S}$  as positive electrode. After the first cycle,  $920 \text{ mAh g}^{-1}$  are attained from the battery (Figure 5.8). In the subsequent cycles at C/50 the battery has shown a good capacity retention, delivering  $820 \text{ mAh g}^{-1}$  in the fifth cycle (*i.e.*  $100 \text{ mAh g}^{-1}$  lost, 11% of the initial capacity). Owing its good cycle-life, the complete battery has been studied during galvanostatic cycling at  $120^\circ\text{C}$  increasing the C-rate every five cycles. Figure 5.11 display the discharge/charge capacities, and the Coulombic efficiency obtained during cycling in the potential window 0.8 – 2.5 V.

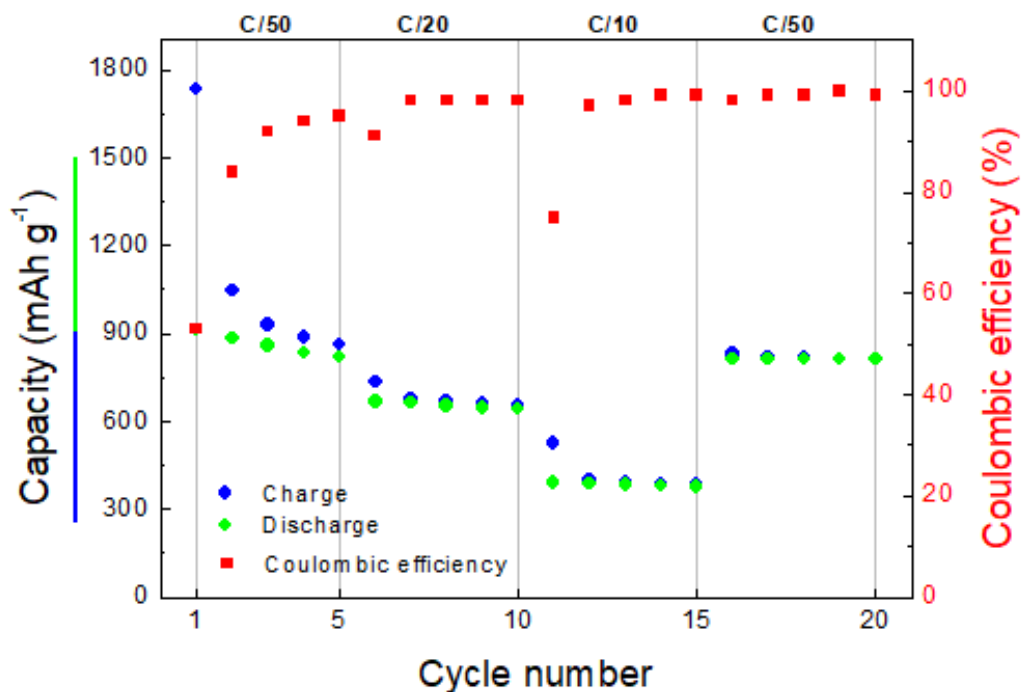


**Figure 5.11.** Discharge/charge capacity of the complete solid-state Li-ion battery  $\text{Li}_2\text{S}/0.8\text{MgH}_2+0.2\text{TiH}_2$  over cycling at  $120^\circ\text{C}$  at different C-rates.

After an initial capacity loss of  $820\text{ mAh g}^{-1}$  within the first cycle (53% Coulombic efficiency), the battery shown an increase in the Coulombic efficiency in the subsequent cycles, with both discharge/charge capacities slowly decreasing in the range between  $900$  and  $800\text{ mAh g}^{-1}$ . Each time the C-rate is increased the battery shows a drop in the capacity, due to kinetics limitations in accomplishing a complete discharge/charge cycle in less time. However, after the first loss, the capacity is almost constant during cycling, showing a Coulombic efficiency above 95%. When the C-rate is set back to C/50, the capacity increases to initial high values. Indeed, the charge capacity achieved in the fifth cycle at C/50 is  $862\text{ mAh g}^{-1}$ , whereas in the sixteenth cycle is  $830\text{ mAh g}^{-1}$ , *i.e.* only 4% of the capacity is lost after the cycling at high kinetics regimes.



## 5 Conclusions

Lithium borohydride has been used as electrolyte in all-solid-state cells. Bulk  $\text{LiBH}_4$  exhibited a high ionic conductivity at high temperatures thanks to the transition at  $118\text{ }^\circ\text{C}$  from the orthorhombic to hexagonal phase.  $\text{MgH}_2$ ,  $\text{TiH}_2$  and composites of these hydrides have been studied as electrode materials at  $120\text{ }^\circ\text{C}$ . The galvanostatic analyses have highlighted the following properties:

- Both hydrides react with lithium at potential values close to the theoretical ones, implying a small overpotential in solid-state cells;
- Full lithiation in single hydride electrodes is not achieved, suggesting that further studies on formulation and preparation of the solid-state cell are required to enhance the performance;
- Compared to room temperature cycling,  $\text{MgH}_2$  and  $\text{TiH}_2$  exhibit a higher capacity retention and a longer cycle-life at  $120\text{ }^\circ\text{C}$ , likely due to the mobility of species at high temperatures;
- $\text{TiH}_2$  shows a better capacity retention than  $\text{MgH}_2$ , with a Coulombic efficiency above 90%;
- All  $\text{MgH}_2+\text{TiH}_2$  nanocomposites can reach the complete lithiation during the first discharge, suggesting a better reactivity towards lithium compared to the single hydride electrodes;
- Composites  $y = 0.6$  and  $0.7$  achieve a complete delithiation (*i.e.* recovering 2 Li) during the first charge;
- Ti-rich composite  $y = 0.2$  exhibits the highest capacity retention during cycling, thanks to the abundance of the  $\text{TiH}_2$  phase. However, when cycled at high C-rates its capacity retention drastically drops;
- Mg-rich composites lose a large capacity within the first cycles because of the poor capacity retention of  $\text{MgH}_2$  phase;
- Electrodes  $y = 0.7$  provides the highest capacity among the composites while cycling, even at fast C-rates;

A complete solid-state Li-ion battery has been assembled coupling  $0.8\text{MgH}_2+0.2\text{TiH}_2$  with  $\text{Li}_2\text{S}$  as negative and positive electrode respectively. The battery, cycled at  $120\text{ }^\circ\text{C}$  in the potential window  $0.8 - 2.5\text{ V}$ , has shown the following properties:

- The composite is fully lithiated during the first charge of the battery;
- After an initial loss in the first cycle (53% Coulombic efficiency), the battery provides a capacity which slowly decreases in the range 900 – 800 mAh g<sup>-1</sup>;
- Compared to the half-cell, the composite exhibits a higher capacity retention (89% vs. 81%) within the first five cycles, implying a better cycle-life in a complete Li-ion battery;
- At high C-rates (*i.e.* C/20 and C/10), the battery shows a drop in the capacity due to kinetics limitations, however the Coulombic efficiency exhibited during cycling was above 90%. When a C-rate of C/50 is re-established, the battery recovers its capacity, delivering more than 800 mAh g<sup>-1</sup>;

Overall, LiBH<sub>4</sub> has shown to be a potential candidate as electrolyte for all solid-state lithium-ion batteries. The main issue comes from the temperature required to achieve the transition to the conductivity phase, limiting its use to high temperature applications. Moreover, without solvents LiBH<sub>4</sub> cannot permeate into the electrode, so a proper preparation of the electrodes mixture is mandatory. Thus, engineered structures are necessary in order to obtain a high density of LiBH<sub>4</sub>/active material interfaces.

However, also other Li-conducting compounds might be studied as solid electrolyte, providing new solutions for the implementation of metal hydrides in solid-state Li-ion batteries.

## References

1. Fergus, J. W. Ceramic and polymeric solid electrolytes for lithium-ion batteries. *J. Power Sources* **195**, 4554–4569 (2010).
2. Stoldt, C. & Lee, S. Glass-Ceramic  $\text{Li}_2\text{S}$ – $\text{P}_2\text{S}_5$  Electrolytes Prepared by a Single Step Ball Milling Process and their Application for all-solid-state lithium – ion batteries. *Electrochem. Commun.* **11**, 1830-1833 (2009).  
doi:10.1016/j.elecom.2009.07.028
3. Tatsumisago, M., Mizuno, F. & Hayashi, A. All-solid-state lithium secondary batteries using sulfide-based glass – ceramic electrolytes. *J. Power Sources* **159**, 193–199 (2006).
4. Soc, J. E., A-a, P. & System, T. L. S. S. Lithium Ionic Conductor Thio-LISICON : The  $\text{Li}_2\text{S}$   $\text{GeS}_2$   $\text{P}_2\text{S}_5$  System. *J. Electrochem. Soc.* **148**, 5–10 (2001).
5. Liu, Z., Huang, F., Yang, J., Wang, B. & Sun, J. New lithium ion conductor , thio-LISICON lithium zirconium sulfide system. *Solid State Ion.* **179**, 1714–1716 (2008).
6. Liang, C. C. Conduction Characteristics of the Lithium Iodide – Aluminum Oxide Solid Electrolytes. *J. Electrochem. Soc.* **120**, 1289–1292 (1973).
7. Varez, A., Leon, C. & Torres-martínez, L. M. Influence of composition on the structure and conductivity of the fast ionic. *Solid State Ion.* **134**, 219-228 (2017).  
doi:10.1016/S0167-2738(00)00761-X
8. Society, T. E., Thokchom, J. & Battery, J. Superionic Conductivity in a Lithium Aluminum Germanium Phosphate Glass – Ceramic. *J. Electrochem. Soc.* **155**, 1–7 (2016). doi:10.1149/1.2988731
9. Inaguma, Y., *et al.* High ionic conductivity in lithium lanthanum titanate. *Solid State Commun.* **86**, 689–693 (1993).
10. Croce, F., Appetecchi, G. B., Persi, L. & Scrosati, B. Nanocomposite polymer electrolytes for lithium batteries. *Nature* **394**, 456–458 (1998).
11. Matsuo, M., Nakamori, Y., Orimo, S. I., Maekawa, H. & Takamura, H. Lithium superionic conduction in lithium borohydride accompanied by structural transition.

- Appl. Phys. Lett.* **91**, 1–4 (2007).
12. Ikeshoji, T. *et al.* Fast-ionic conductivity of Li<sup>+</sup> in LiBH<sub>4</sub>. *Phys. Rev. B - Condens. Matter Mater. Phys.* **83**, 1–5 (2011).
  13. Takahashi, K., Hattori, K., Yamazaki, T., Takada, K. & Matsuo, M. All-solid-state lithium battery with LiBH<sub>4</sub> solid electrolyte. *J. Power Sources* **226**, 61–64 (2013).
  14. Bo, U. *et al.* Hydrogen sorption properties of MgH<sub>2</sub>–LiBH<sub>4</sub> composites. *Acta Mater.* **55**, 3951–3958 (2007).
  15. Vajo, J. J., Salguero, T. T., Gross, A. F., Skeith, S. L. & Olson, G. L. Thermodynamic destabilization and reaction kinetics in light metal hydride systems. *J. Alloys Compd.* **447**, 409–414 (2007).
  16. Zeng, L., Miyaoka, H., Ichikawa, T. & Kojima, Y. Superior Hydrogen Exchange Effect in the MgH<sub>2</sub>-LiBH<sub>4</sub> System. *J. Phys. Chem. C* **114**, 13132–13135 (2010).
  17. Crystal, I. & Soulie, J. Lithium boro-hydride LiBH<sub>4</sub> I. Crystal structure. *J. Alloys Compd.* **346**, 200–205 (2002).
  18. Miwa, K., Ohba, N., Towata, S. I., Nakamori, Y. & Orimo, S. I. First-principles study on lithium borohydride LiBH<sub>4</sub>. *Phys. Rev. B - Condens. Matter Mater. Phys.* **69**, 1–8 (2004).
  19. Zeng, L. *et al.* Metal hydride-based materials towards high performance negative electrodes for all-solid-state lithium-ion batteries. *Chem. Commun.* **51**, 9773–9776 (2015).
  20. Unemoto, A. *et al.* Stable Interface Formation between TiS<sub>2</sub> and LiBH<sub>4</sub> in Bulk-Type All-Solid-State Lithium Batteries. *Chem. Mater.* **27**, 5407–5416 (2015).
  21. Oumellal, Y. *et al.* Reactivity of TiH<sub>2</sub> hydride with lithium ion: Evidence for a new conversion mechanism. *Int. J. Hydrogen Energy* **37**, 7831–7835 (2012).
  22. Zeng, L., Ichikawa, T., Kawahito, K., Miyaoka, H. & Kojima, Y. Bulk-Type all-solid-state lithium-ion batteries: Remarkable performances of a carbon nanofiber-supported MgH<sub>2</sub> composite electrode. *ACS Appl. Mater. Interfaces* **9**, 2261–2266 (2017).
  23. Kawahito, K., Zeng, L., Ichikawa, T., Miyaoka, H. & Kojima, Y. Electrochemical

- Performance of Titanium Hydride for Bulk-Type All-Solid-State Lithium-Ion Batteries. *Mater. Trans.* **57**, 755–757 (2016).
24. Unemoto, A. *et al.* Development of bulk-type all-solid-state lithium-sulfur battery using  $\text{LiBH}_4$  electrolyte. *Appl. Phys. Lett.* **105**, (2014).
  25. Ikeda, S. *et al.* Anode properties of magnesium hydride catalyzed with niobium oxide for an all solid-state lithium-ion battery. *Chem Commun* **49**, 7174–7176 (2013).
  26. Ikeda, S. *et al.* Anode properties of  $\text{Al}_2\text{O}_3$ -added  $\text{MgH}_2$  for all-solid-state lithium-ion batteries. *J. Solid State Electrochem.* **19**, 3639–3644 (2015).

# **CHAPTER 6**

Conclusions and  
Outlook



## 1 Conclusions based on our research

The progress in lithium ion batteries over the past decades has made them the leading technology for mobile applications. Despite all the improvements, the available energy content is limiting the development in new fields, such as electric vehicles and power grid systems, where a high energy is required. With the purpose of replacing the electrodes currently used in commercial Li-ion batteries, new materials with better electrochemical properties are under investigation worldwide. A good electrode material candidate should reversibly react with lithium for as many as possible discharge/charge cycles, providing a high capacity. Even other properties, such as cost, safety, and toxicity must be taken into account.

Among the studied materials, metal hydrides have been suggested as possible candidate for negative electrodes. Theoretically, several metal hydrides can react with lithium at potentials below 1 V vs.  $\text{Li}^+/\text{Li}$ , providing capacities in the order of thousands of  $\text{mAh g}^{-1}$ , thus they could replace graphite ( $372 \text{ mAh g}^{-1}$ ) as electrode material. However, practical applications are still hindered because of the poor reversibility of the conversion reaction at room temperature.

This thesis was an effort to understand the factors that limit the performance and so the cycle-life of metal hydrides in Li-ion batteries, trying to find possible strategies to overcome these issues. For our research,  $\text{MgH}_2$  and  $\text{TiH}_2$  have been chosen as active materials, and their electrochemical properties have been investigated in cells with both liquid and solid electrolytes.

In half-cells cycled at room temperature, these hydrides have shown to deliver a high capacity,  $2000 \text{ mAh g}^{-1}$  for  $\text{MgH}_2$  and  $1000 \text{ mAh g}^{-1}$  for  $\text{TiH}_2$  respectively. However, a large capacity loss occurs within the first cycle, with  $\text{MgH}_2$  exhibiting a reversibility below 30%, and  $\text{TiH}_2$  being completely irreversible (*i.e.* no reformation of the hydride during the charge). Interestingly, we have noticed that during cycling, the drop in capacity occurs during the charge. Indeed, the quantity of lithium extracted can be fully re-introduced into the electrode in the subsequent cycle, but the quantity of lithium recovered during delithiation decreases at each charge. This suggest that some mechanism occurring during the lithiation hinders the subsequent extraction of lithium from the electrode. Previous authors have tried to explain this poor reversibility shown by the hydrides highlighting the facts that all hydrides undergo a conversion reaction which leads to sever



volume change during cycling, producing also LiH, which is an insulator. Moreover, metal hydrides possess a sluggish kinetics at room temperature. Thus, they stated as possible issues the cracks and loss in contacts due to the expansion, the poor electric conductivity due to LiH, and the poor mass transport within the electrode. To better understand which of these phenomena could be the main cause to the poor reversibility, the morphology and composition of the electrode has been studied at different discharge/charge steps. For this purpose, MgH<sub>2</sub> thin films, prepared by reactive plasma sputtering, have been used as working electrode. During lithiation, the conversion of MgH<sub>2</sub> to Mg+LiH starts on top of the thin film, proceeding to the bottom. This leads to a volume expansion, especially along the Z-axis because of the clamping of the film on the copper substrate. On contrast, during delithiation the thin film shrinks, partially coming back to MgH<sub>2</sub>. However, neither cracks, voids, nor detachment of the thin film from the substrate are noticed, suggesting that all these phenomena cannot be the main cause of the large capacity loss that occurs within the first cycle. After that, electrical conductivity has been taken into account as possible issue. Impedance spectroscopy has been performed on the thin film at different conversion reaction steps. The results showed that the highest electrical resistance is found in the pristine thin film, *i.e.* pure MgH<sub>2</sub>. During lithiation, LiH is produced, whoever the overall resistance decreases thanks to the conversion of MgH<sub>2</sub> to Mg. Indeed, the fully lithiated electrode showed the smaller resistance, implying that the extraction of lithium cannot be due to a poor electrical conductivity.

At the light of these results, most of the previous issues hypothesized as possible causes of the poor reversibility are discarded, suggesting that kinetics and mass transport are the main problems to increase the cycle-life of metal hydride electrodes. Even if these two issues are time expensive, and out of the scope of this thesis to be fully investigated, is still possible to take some consideration. Lithium, hydrogen, and magnesium are the species involved in the conversion reaction. Lithium is used in commercial Li-ion batteries, so is rather impossible to hypothesize as main issue the diffusion of lithium ions within the electrode. Hydrogen is the lightest element, so at room temperature its diffusion should not be a problem. However, it is known that its mobility is limited in MgH<sub>2</sub>. Therefore, if the reformation of MgH<sub>2</sub> starts on the surface of Mg particles, the diffusion of hydrogen towards magnesium decreases with the increase of MgH<sub>2</sub> thickness, limiting the complete reformation of the hydride. On the other hand, magnesium is the heaviest specie in the electrode (*e.g.* Mg: 24.3 u *vs.* Li: 6.9 u), so it could possess a poor mobility at room temperature, hindering the conversion reaction. Consequently, the mobility of hydrogen

and heavy species within the electrode might be the main issues that limit the reversibility of the conversion reaction at room temperature.

The fact that the kinetics of metal hydrides is the main issue for their reversibility has been confirmed by experiments at high temperatures. Solid-state half-cells have been prepared using  $\text{LiBH}_4$  as solid electrolyte, investigating the properties of  $\text{MgH}_2$  and  $\text{TiH}_2$  at  $120\text{ }^\circ\text{C}$ . The results have shown that the conversion reaction of  $\text{TiH}_2$  at this temperature is reversible. Moreover, also  $\text{MgH}_2$ , compared to room temperature half-cells, has shown a higher reversibility and so a longer cycle-life. This higher reversibility can be attributed mainly to the enhanced mobility of the species at high temperature compared to the previous studies. Interestingly, at  $120\text{ }^\circ\text{C}$   $\text{TiH}_2$  exhibited a higher capacity retention during cycling compared to  $\text{MgH}_2$ . Confronting our results with other authors, it is clear that the better performance of  $\text{TiH}_2$  compared to  $\text{MgH}_2$  comes from its higher electrical conductivity. This evidences that minor issues, such as conductivity, and probably also volume expansion, are not relevant during the first discharge/charge cycles, but rather later. Hence, in order to achieve a cycle-life comparable with commercial batteries, also these issues must be taken into account, with a proper electrode formulation.

Owing the cooperative effect between  $\text{MgH}_2$  and  $\text{TiH}_2$  reported for hydrogen storage applications, different  $y\text{MgH}_2+(1-y)\text{TiH}_2$  mixtures, with molar ratio  $y = 0.2, 0.5, 0.6, 0.7,$  and  $0.8$ , have been studied as composite materials with the purpose of increasing the performance of the electrode. From previous experiments on thin films, we have found that passivating layers of contaminants, such as metal-oxides, on the surface of the hydride strongly hinder the conversion reaction with lithium. For this reason, the composites have been synthesized from metallic Mg and Ti in a ball mill under  $\text{H}_2$  atmosphere. Moreover, ball milling technique has shown to produce homogeneous mixtures of hydrides, with nanocrystallite domains. All the nanocomposites have been fully lithiated during the first discharge. This good reactivity has been attributed to both pure metal hydride surfaces and nanostructured particles, which provides short diffusion paths enhancing the mobility of species within the electrode. However, the reversibility of the composites has shown to strongly depend on the molar ratio. Indeed, Ti-rich electrode  $y = 0.2$  has shown to be irreversible, with both  $\text{MgH}_2$  and  $\text{TiH}_2$  not reformed during the delithiation. This suggests that, not only  $\text{TiH}_2$  in high quantity is irreversible, but also it hinders the conversion reaction of  $\text{MgH}_2$ . On contrary, the reversibility of the electrodes increased with the quantity of  $\text{MgH}_2$ , with composite  $y = 0.7$  exhibiting the best reversibility and cycle-life. Further

investigations on  $0.7\text{MgH}_2+0.3\text{TiH}_2$  have shown that the reversibility of  $\text{TiH}_2$  phase was higher than  $\text{MgH}_2$  phase. Limiting the conversion reaction to only  $\text{TiH}_2$  has led to a recover of this hydride above 90% during the first cycle. In the subsequent cycles, the electrode showed a capacity that slowly decreased with a loss of  $\sim 3\%$  at each discharge/charge cycle. This enhancement of the cycle-life has been attributed to the surrounding  $\text{Mg}+\text{LiH}$  matrix, which guarantees a high density of  $\text{Ti}/\text{LiH}$  interfaces, a good electronic conductivity, and the accommodation of volume changes within the electrode.

These results have demonstrated short diffusion paths and high interfaces density are mandatory to achieve a higher reversibility and longer cycle-life for metal hydrides as negative materials for Li-ion batteries. From here, new strategies for a proper electrode formulation can be obtained in future with further research.

Finally, a complete solid-state Li-ion battery has been assembled using  $0.8\text{MgH}_2+0.2\text{TiH}_2$  as negative material,  $\text{Li}_2\text{S}$  as positive material, and  $\text{LiBH}_4$  as solid electrolyte. Experimental cycling has been carried out at  $120\text{ }^\circ\text{C}$ . A complete lithiation of the negative material is achieved during the first charge. After an initial capacity drop, the battery provided a capacity which slowly decreases in the range  $900 - 800\text{ mAh g}^{-1}$ . Compared to the solid-state half-cell, composite  $y = 0.8$  has exhibited a higher capacity retention, implying a better cycle-life in a complete Li-ion battery. Moreover, also at fast kinetics regimes, the battery has shown a Coulombic efficiency above 90% during cycling.

These results show that metal hydrides might be coupled with new positive materials to achieve a high energy density. Interestingly, in a complete battery  $\text{MgH}_2+\text{TiH}_2$  composite has shown to achieve better performance than in half-cells, promising excellent results for the future experiments. Thanks to the high temperature, the main issue related to the poor kinetics of metal hydrides is here partially resolved, suggesting that first practical application of metal hydrides in Li-ion battery might begin in the field of high temperature applications.

## 2 Outlook

In our work, we have demonstrated crucial importance of the interfaces within the battery to achieve a better reactivity towards lithium. In order to achieve a performance that allows the introduction of these batteries in the market, further experiments on the electrode design are required. Materials cost and industrial production are also factors to consider.

The sluggish kinetics at room temperature still remains the main issue for a high reversibility and long cycle-life. However, we have shown that a good capacity retention is obtained when short diffusion paths and high interfaces density is provided. Therefore, better performances can be attained with a proper electrode formulation, opening new studies on additives and active material preparation.

Moreover, we have demonstrated that metal hydrides can be used also for solid-state batteries. Owing the high ionic conductivity of  $\text{LiBH}_4$  at high temperatures,  $\text{MgH}_2$  and  $\text{TiH}_2$  have been studied at  $120\text{ }^\circ\text{C}$ . Because of the temperature, the reversibility achieved was higher compared to cells with organic solvents, with  $\text{TiH}_2$  exhibiting a good capacity retention during cycling. These results suggest that practical applications of metal hydride electrodes might come initially for high temperature batteries, where they already show promising performance thanks to the high capacity delivered during cycling. The main advantages these devices can provide are their stability and safety compared to liquid electrolyte cells, leading to a remarkable breakthrough in the field of Li-ion batteries. Besides  $\text{LiBH}_4$ , also other compounds can be investigated as solid electrolyte, especially those with a high ionic conductivity at low temperatures.

Sulphur has shown to be a good candidate as positive material to be coupled with metal hydrides. Thanks to their theoretical capacities in the order of thousands of  $\text{mAh g}^{-1}$  it might be possible to obtain batteries with high energy densities, spreading the use of Li-ion batteries also in new application fields, such as power grid and new electric vehicles.

Concluding, metal hydrides can also react with sodium through the same conversion reaction, forming their metal and  $\text{NaH}$  instead of  $\text{LiH}$ . Hence, metal hydrides can be investigated as electrode materials for sodium batteries, whose interest has increased in the last years. Research can be done with both liquid and solid sodium electrolytes.

For all these reasons, we strongly consider metal hydrides as valid candidates as electrode materials for the new generation of rechargeable batteries.